LEABHARLANN CHOLÁISTE NA TRÍONÓIDE, BAILE ÁTHA CLIATH | TRINITY COLLEGE LIBRARY DUBLIN
Ollscoil Átha Cliath | The University of Dublin

Terms and Conditions of Use of Digitised Theses from Trinity College Library Dublin

Copyright statement

All material supplied by Trinity College Library is protected by copyright (under the Copyright and Related Rights Act, 2000 as amended) and other relevant Intellectual Property Rights. By accessing and using a Digitised Thesis from Trinity College Library you acknowledge that all Intellectual Property Rights in any Works supplied are the sole and exclusive property of the copyright and/or other IPR holder. Specific copyright holders may not be explicitly identified. Use of materials from other sources within a thesis should not be construed as a claim over them.

A non-exclusive, non-transferable licence is hereby granted to those using or reproducing, in whole or in part, the material for valid purposes, providing the copyright owners are acknowledged using the normal conventions. Where specific permission to use material is required, this is identified and such permission must be sought from the copyright holder or agency cited.

Liability statement

By using a Digitised Thesis, I accept that Trinity College Dublin bears no legal responsibility for the accuracy, legality or comprehensiveness of materials contained within the thesis, and that Trinity College Dublin accepts no liability for indirect, consequential, or incidental, damages or losses arising from use of the thesis for whatever reason. Information located in a thesis may be subject to specific use constraints, details of which may not be explicitly described. It is the responsibility of potential and actual users to be aware of such constraints and to abide by them. By making use of material from a digitised thesis, you accept these copyright and disclaimer provisions. Where it is brought to the attention of Trinity College Library that there may be a breach of copyright or other restraint, it is the policy to withdraw or take down access to a thesis while the issue is being resolved.

Access Agreement

By using a Digitised Thesis from Trinity College Library you are bound by the following Terms & Conditions. Please read them carefully.

I have read and I understand the following statement: All material supplied via a Digitised Thesis from Trinity College Library is protected by copyright and other intellectual property rights, and duplication or sale of all or part of any of a thesis is not permitted, except that material may be duplicated by you for your research use or for educational purposes in electronic or print form providing the copyright owners are acknowledged using the normal conventions. You must obtain permission for any other use. Electronic or print copies may not be offered, whether for sale or otherwise to anyone. This copy has been supplied on the understanding that it is copyright material and that no quotation from the thesis may be published without proper acknowledgement.

Unlocking the Structure-Property Relationships of Conjugated Polyelectrolytes and Photoactive Surfactants to Design Functional Responsive Materials

Judith E. Houston
MChem (Hons.)



Thesis submitted to the University of Dublin
for the degree of Doctor of Philosophy

Under the supervision of Dr Rachel C. Evans

School of Chemistry
Trinity College Dublin
Ireland

2017

TRINITY LIBRARY
0 8 AUG 2017
DUBLIN

Thesis 11351

Declaration

I declare that this thesis has not been submitted as an exercise for a degree at this or any other university and it is entirely my own work, except where otherwise cited, referenced, acknowledged or accredited.

I agree to deposit this thesis in the University's open access institutional repository or allow the library to do so on my behalf, subject to Irish Copyright Legislation and Trinity College Library conditions of use and acknowledgement.

Acknowledgements

Firstly, I would like to apologise for making such a huge deal about everyone else's acknowledgements, turns out these are less fun to write than they are to read. Thankfully, is easy to know where to start. I am indebted to my supervisor Dr Rachel Evans. I know that both academically and socially, I have been extremely lucky. From day one she has been exceptionally encouraging for anything I wanted to do (I've still got my sights set on that cat hotel) and has helped to install a healthy dose of competitiveness (where are my office turtles?). In all seriousness though, I am unbelievably grateful for such a fantastic role-model, who has been remarkably patient and generous with her guidance, support and friendship.

The work in this thesis has been the culmination of several experiments and collaborations from outside of Trinity. I am indebted to Drs Sébastian Clément, Amandine Thomas, Michèlle Chevrier, Mario Kraft and Prof. Ullrich Scherf for providing the polymers used. As well as Drs Steve King, Richard Heenan and Ann Terry for their help with SANS measurements and data analysis. I was also lucky enough to spend a small portion of my final year at the FORTH institute in Crete. For that I have to thank the COST network HINT and Dr Kiriaki Chrissopoulou in particular for putting me up, as well as Tasos, Hellen, Spiros and Elena for helping me confirm that I definitely can't drink raki.

Within Trinity, I wouldn't have been able to do a lot of the work over the past four years without the help of the excellent technical staff. Particular thanks have to be given to Drs John O'Brien and Manuel Ruether for bumping me up the NMR queue and helping me use the instruments. (A little less to John for choosing the worst moments to inform me I had "broken" an instrument and extra thanks for Manuel for then calming me down.) My thanks also go to Drs Martin Freeman, Clive Downing, Clodagh Dooley and Gavin McManus for additional specialised measurements that have been extremely valuable in this work.

I would also like to thank Helen and Tess for making me smile. Niamh and I have been talking, and we haven't seen you guys around in a while, did you go on another secret holiday without us? It's ok we can plan another one ;) My thanks also go to Anne-Marie, Fred, Noelle and, in particular, Patsy. He has been endlessly helpful in the face of so many annoying requests. I can also forgive him my ridiculously high golf handicaps, considering the number of times he has kindly bandaged me up.

Over the past four years, I have also had the fortune to have an "interesting" assortment of flatmates, but it would be unjust if I didn't mention two in particular, my fish. Thanks lads for beating the odds and not dying immediately. In addition, my Portobello housemates, as well as Claire, Lauren, and Michelle (the only one crazy enough to do it twice) who were a treat to live with. Finally, thanks to Conal, it was an unlikely alliance but I knew it would work when he agreed to the fish.

To all the members of the Evans Group: Barry, Ilaria, Camille, Steve, Lorcan, Adarsh, Elaine and numerous students (particularly Ian Mooney for buying my love with Maoam) it has been a delight to work with all of you and it wouldn't have been half the experience in another group. Thanks for embracing (or tolerating) chemistry arts and craft and as I am leaving now, you can all have your stolen pens and office football back.

I have been lucky to pick up some other friends along the way, including Fergus, Helen, Rob, Bryan, Colm, (Australian) Lauren, Joao and Dee. I also have a few close friends at home who have supported me through every part of this process, and who either really like me or just saw the opportunity to visit Ireland. Either way, I would be lost without Emma, Heather, David and Dana.

Adam and Niamh have been my little rocks through the past four years. Niamh took me under her wing, taught me the ways of the Pav, and introduced to some of the worst hangovers of my life. Adam, you big dope, sorry for me and Niamh yelling at you so much, but in all honestly I kind of miss it. Thanks so much to the both of you for putting up with me through my freak-outs, supporting me through the nun/swan incidents and providing constant entertainment. You are both stuck with me now, thanks for reading my thesis! Finally, Beth, you are star and I am delighted to call you my friend.

Lastly, I would like to thank my ever-growing family. I look forward to spending the next few years cementing my position as the favourite auntie - puppies for everyone! Finally, to my mum, dad and granddad, thank you for your endless support and love along the way.

Abstract

Self-assembly is an elegant method for the preparation of functional responsive materials. This thesis focuses on understanding the self-assembly properties of photoactive soft matter systems (*e.g.* polymers, polyelectrolytes, phospholipids, liquid crystals). The goal has been to identify key structure-property relationships that facilitate the rational design of functional materials for organic solar cells, bio-imaging and bio-sensing platforms.

Conjugated polyelectrolytes (CPEs) have shown promise in a range of applications from optical sensors to organic photovoltaic devices (OPVs), due to their exceptional optoelectronic properties, low cost and solution processability. Chapters 4-6 focus on exploiting different solvents and counter-ions to modulate the aggregated structure of CPEs in solution, and the subsequently prepared thin films, for use as interfacial layers in OPVs. Specifically, the ability to tune the nanoscale organisation of aggregates of amphiphilic diblock copolymers in solution *via* solvent- and surfactant-mediation is shown to be a simple and effective method to control the film morphology. Furthermore, the incorporation of poly(thiophene)-surfactant complexes as a cathodic interfacial layers in OPV devices resulted in a 20% increase in the power conversion efficiency.

Chapter 6 presents the first demonstration of CPE-polyoxometalate supramolecular networks formed *via* electrostatic associations. The dimensionality of the hybrid networks could be tuned by the chain length and steric charge distribution on the CPE. These complexes could be transferred from solution to the solid-state with retention of their nanoscale organisation, which is critical for potential device applications.

CPEs also have potential as biologically-relevant sensors due to their self-assembly with a variety of biological species. In Chapter 7 the optical properties of poly[3-(6-sulfothioatehexyl)-thiophene)] (P3Anionic) were measured upon self-assembly with phospholipid bilayers allowing the identification of three key phase transition temperatures of dipalmitoylphosphatidylcholine (DPPC) vesicles. A series of strategic studies revealed that charge-mediation is a simple and elegant approach to control the specific localisation of CPEs within membrane bilayers. The nature of the CPE incorporation enabled the selective detection of phase transition changes across bilayer membranes, which may prove valuable in the development of improved theranostic platforms.

Similar to CPE aggregates, photosurfactants (PS) can self-organise into polymolecular assemblies with the added advantage that PS can change their self-assembled shape upon irradiation with light. "Regular" surfactants are known to self-assemble into a variety of thermodynamically stable 2D or 3D lyotropic liquid crystalline (LLC) phases. Such LLC phases using surfactants have previously been employed as sacrificial, soft templates to template nanostructured materials. However, there have been limited reports of LLC phase formation by PS. In Chapter 8, a series of neutral azobenzene PS were rationally designed and synthesised. A combination of techniques were used to monitor the self-assembly and growth of the PS aggregates from isolated micelles to LLC phases and to determine the effect of photoisomerisation on the aggregate structure formed. The surfactants and conditions identified as forming desirable LLC phases will be used as novel photoresponsive to templates for inorganic sol-gel matrixes.

These studies demonstrate that self-assembly is an elegant method for the preparation of functional responsive materials. The potential use of conjugated polyelectrolytes as materials for improving the efficiency of polymer photovoltaic cells and as bioimaging and sensing devices has been demonstrated. Self-assembled systems are naturally dynamic, and therefore it is possible to induce significant changes in the organised structures formed by subtly altering environmental factors. The focus here has been on exploiting solvent, counterions, temperature and light to tune the aggregated structure of CPEs and surfactants in solution and thin films. The structure-property relationships identified will be critical in directing future studies of conjugated polyelectrolytes and photoactive surfactants.

Table of Contents

Declaration i

Acknowledgements ii

Abstract iii

Table of Contents v

Preface xi

Abbreviations xiii

List of Symbols xvii

Chapter 1 – Introduction 1

1.1 Introduction 3

1.2 Conjugated Polymers and Conjugated Polyelectrolytes 3

1.2.1 Self-Assembly of CPEs in Solution 5

1.3 Application of CPEs 7

1.3.1 Organic Photovoltaic Devices 7

1.3.1.1 Device Structure of OPVS 8

1.3.1.2 Optimisation of OPV Devices 9

1.3.1.3 Interfacial Layers 9

1.3.1.4 Role of the Interfacial Layer 9

1.3.1.5 CP/CPE Interfacial Layers 10

1.3.2 Bioimaging and Sensing 11

1.4 Surfactants 12

1.4.1 Self-Assembly of Surfactants 13

1.4.2 Lyotropic Liquid Crystal (LLC) Phases 14

1.4.3 Templates for Inorganic Host Matrices 15

1.5 Photoactive Surfactants 17

1.5.1 Photoswitchable Moieties 18

1.5.2 Azobenzene 18

1.5.3 Spectroscopy of Azobenzene 19

1.5.4 Self-Assembly of Photosurfactants 19

1.5.5 Photosurfactants and LLC phases 21

1.5.6 Applications of Photosurfactants 22

1.6 Aims of Thesis 23

1.7 References 24

Chapter 2 – Theory **29**

2.1 The Interaction of Light with Matter 31

2.1.1 Properties of Light 31

2.1.2 Formation of Excited State 31

2.1.3 Classification of Electronic States 32

2.1.4 Selection Rules for Absorption 32

2.1.5 Optical Transitions – The Franck-Condon Principle 33

2.1.6 Beer-Lambert Law 34

2.1.7 Deactivation of Excited States 35

2.1.8 Excited-State Lifetime 36

2.1.9 Quenching 36

2.1.10 Energy Transfer 37

2.1.11 Photochemical Deactivation of Excited Species 39

2.2 Scattering Technqiues 40

2.2.1 Elastic *vs*. Inelastic Scattering 40

2.2.2 Properties of Light, Neutron and X-ray Radiation 42

2.2.3 Light Scattering 43

2.2.4 Neutron and X-ray Experiments 46

2.2.5 SAS Theory 48

2.2.6 Form Factor ($P(q)$) 50

2.2.7 Structure Factor ($S(q)$) 52

2.2.8 Structure Factor Models 53

2.3 References 54

Chapter 3 – Experimental **57**

3.1 Materials 59

3.1.1 Chemicals 59

3.1.2 Polymers 59

3.2 Instrumentation 59

3.2.1 UV/Vis Absorption Spectroscopy 59

3.2.2 Photoluminescence (PL) Spectroscopy 60

3.2.3 Electrospray Ionisation Mass Spectrometry (ESI-MS) 60

3.2.4 Fourier Transform Infrared (FTIR) Spectroscopy 60

3.2.5 ^{1}H and ^{13}C Nuclear Magnetic Resonance (NMR) Spectroscopy 60

3.2.6 Melting Point Analysis 61

3.2.7 Linear Dichroism (LD) 61

3.2.8 Differential Scanning Calorimetry (DSC) 62

3.2.9 Epifluorescence Microscopy 62
3.2.10 Polarised Optical Microscopy (POM) 62
3.2.11 Atomic force microscopy (AFM) 63
3.2.12 Scanning Electron Microscopy (SEM) and Cryo-SEM 64
3.2.13 Dynamic Light Scattering (DLS) and Zeta Potential (ζ) Measurements 64
3.2.14 Multi-Angle Dynamic Light Scattering (MALS) 65
3.2.15 Small-Angle Neutron Scattering (SANS) 65
3.3 Data Analysis 66
3.3.1 Non-Linear Least Squares (NLLS) Fits 66
3.3.2 Procedure to Check SANS Model Fits 66
3.3.3 SANS Form Factor Models 66
3.3.4 Aggregation numbers 71
3.4 References 71

Chapter 4 – Solvent-Mediated Self-Assembly of Polythiophene-Polythiophene All-Conjugated Diblock Polyelectrolytes 73

4.1 Introduction 75
4.1.1 Aims of this work 76
4.2 Experimental Section 77
4.2.1 Materials 77
4.2.2 Methods 77
4.3 Results 78
4.3.1 UV/Vis Absorption and Steady-State PL Spectroscopy 78
4.3.2 Solution-Phase Structures 80
4.4 Discussion 85
4.5 Conclusions 87
4.6 References 88

Chapter 5 – Optimising the Molecular Organisation and Nanoscale Morphology of Homo- and Diblock-Polythiophenes using Surfactant- and Solvent-Mediation for High Performance Polymer Solar Cells 91

5.1 Introduction 93
5.1.1 Aims of this work 94
5.2 Experimental 95
5.2.1 Materials 95
5.2.2 Methods 95

5.3 Results 96
5.3.1 Optical Characterisation 96
5.3.2 Solution-Phase Structures 102
5.3.3 Thin Film Morphology 109
5.3.4 Proposed Self-Assembly Structures 112
5.3.5 Implications for Device Performance 114
5.4 Conclusions and Outlook 117
5.5 References 119

Chapter 6 – Charge-Modulated Self-Assembly and Growth of Conjugated Polyelectrolyte-Polyoxometalate Hybrid Networks 121

6.1 Introduction 123
6.1.1 Aims of this work 124
6.2 Experimental 125
6.2.1 Materials 125
6.2.2 Methods 125
6.3 Results and Discussion 126
6.3.1 UV/Vis Absorption and PL Studies 126
6.3.2 Binding Mode Studies 129
6.3.3 Aggregate Size in Solution 130
6.3.4 Thin Film Morphology 131
6.4 Proposed Mechanism of Self-Assembly 132
6.5 Conclusions 133
6.6 References 134

Chapter 7 – Charge-Mediated Localisation of Conjugated Polythiophenes Enabling the Sequential Detection of Multiple Phase Transitions in Model Membranes 135

7.1 Introduction 137
7.1.1 Aims 138
7.2 Experimental 139
7.2.1 Materials 139
7.2.2 Methods 140
7.3 Results 141
7.3.1 Temperature Dependence Studies 141
7.3.2 Binding Mode Studies 144

7.4 Conclusions 157
7.5 References 159

Chapter 8 – The Development of Photodeformable Self-Assembly Templates using Photoactive Surfactants 163

8.1 Introduction 165
8.1.1 Aims 166
8.2 Experimental 167
8.2.1 Materials 167
8.2.2 Instrumentation 167
8.2.3 Methods 168
8.2.4 Synthesis and Characterisation of Photosurfactants 170
8.3 Results and Discussion 174
8.3.1 Observation of Photoisomerisation by UV/Vis Absorption Spectroscopy 174
8.3.2 Kinetics Study of Photo- and Thermal-Isomerisation Processes 175
8.3.3 Critical Micelle Concentrations 177
8.4 Micellar Solution-State Structures 179
8.4.1 Multi-Angle Light Scattering 179
8.4.2 Small-Angle Neutron Scattering 181
8.4.3 Cryo-Scanning Electron Microscopy (Cryo-SEM) 186
8.4.4 Discussion of the Nanoscale Organisation of Dilute Solutions of PS 187
8.5 Lyotropic Liquid Crystalline Phase Formation 189
8.5.1 Identification of LLC Phases using POM 189
8.5.2 Proposed Binary Phase Diagrams 194
8.6 Conclusions and Outlook 195
8.7 References 196

Chapter 9 – Conclusions and Outlook 199
9.1 References 204

Appendix I-XXXIX

Preface

The work described in this thesis was carried out through the support of a Trinity Award Studentship. The majority of this work was undertaken at Trinity College Dublin.

The original work presented here has been published as part of a number of peer-reviewed articles:

Chapter 4: A. Thomas, J. E. Houston, N. Van den Brande, J. De Winter, M. Chevrier, R. K. Heenan, A. E. Terry, S. Richeter, A. Mehdi, B. Van Mele, P. Dubois, R. Lazzaroni, P. Gerbaux, R. C. Evans and S. Clément, All-Conjugated Cationic Copolythiophene "Rod-Rod" Block Copolyelectrolytes: Synthesis, Optical Properties and Solvent-Dependent Assembly, *Polym. Chem.*, 2014, **5**, 3352-3362.

Chapter 5: M. Chevrier, J. E. Houston, J. Kesters, N. Van den Brande, A. E. Terry, S. Richeter, A. Mehdi, O. Coulembier, P. Dubois, R. Lazzaroni, B. Van Mele, W. Maes, R. C. Evans and S. Clément, Self-Assembled Conjugated Polyelectrolyte-Surfactant Complexes as Efficient Electron Transport Materials for Bulk Heterojunction Organic Solar Cells, *J. Mater. Chem. A*, 2015, **3**, 23905-23916.

Chapter 6: J. E. Houston, A. R. Patterson, A. C. Jayasundera, W. Schmitt and R. C. Evans, Charge-modulated self-Assembly and Growth of Conjugated Polyelectrolyte–Polyoxometalate Hybrid Networks, *Chem. Commun.*, 2014, **50**, 5233-5235.

Chapter 7: (a) J. E. Houston, M. Kraft, I. Mooney, A. E. Terry, U. Scherf and R. C. Evans, Charge-Mediated Localization of Conjugated Polythiophenes in Zwitterionic Model Cell Membranes, *Langmuir*, 2016, **32**, 8141-8153. (b) J. E. Houston, M. Kraft, U. Scherf and R. C. Evans, Sequential Detection of Multiple Phase Transitions in Model Biological Membranes Using a Red-Emitting Conjugated Polyelectrolyte, *Phys. Chem. Chem. Phys.*, 2016, **18**, 12423-12427.

Abbreviations

1D	One-dimensional
2D	Two-dimensional
3D	Three-dimensional
AFM	Atomic force microscopy
ATR	Attenuated total reflection
AZMS	4-Alkylazobenzene-4′-(oxy-2-hydroxypropyl)-trimethylammoniummethylsulfate
AzoTMA	4-Butyl-4′-(3-trimethyl-ammoniumpropoxy)phenylazobenzene
AZOT-S4	4-butylphenyldiazenylphenoxybutane-1-sulfonate
BHJ	Bulk heterojunction
$C_4AzoOC_2E_2$	Triethyleneglycol mono(4-butylazo-benzene)ether
C_4AzoOC_4Br	(*E*)-1-(4-(4-Bromobutoxy)phenyl)-2-(4-butylphenyl)diazene
$C_4AzoOC_4E_2$	(*E*)-Diethylene glycol mono(4′,4-butyloxybutyl-azobenzene)
$C_4AzoOC_4E_4$	(*E*)-16-(4-((4-butylphenyl)diazenyl)phenoxy)-3,6,9,12-tetraoxahexadecan-1-ol
$C_4AzoOC_4E_6$	(*E*)-22-(4-((4-butylphenyl)diazenyl)phenoxy)-3,6,9,12,15,18-hexaoxadocosan-1-ol
C_4AzoOH	(*E*)-4-((4-Butylphenyl)diazenyl)phenol
Cmc	Critical micelle concentration
CP	Conjugated polymer
CPE	Conjugated polyelectrolyte
CTAB	Cetyltrimethylammonium bromide
D_2O	Deuterium oxide
d_4-MeOD	Deuterated methanol
DCM	Dichloromethane
DFT	Density functional theory
DLS	Dynamic light scattering
DMPG	1,2-Dimyristoyl-*sn*-glycero-3-phosphoglycerol
DNA	Deoxyribonucleic acid
DOPC	Dioleoyl-*sn*-glycero-3-phosphocholine
DOTAP	1,2-Dioleoyl-3-trimethylammonium-propane
DPPC	Dipalmitoylphosphatidylcholine
DPPG	1,2-Dipalmitoyl-*sn*-glycero-3-phosphoglycerol
DSC	Differential scanning calorimetry
EISA	Evaporation-induced self-assembly
EQE	External quantum efficiency
ESI-MS	Electrospray ionisation mass spectrometry
ETL	Electron transport layer
EtOH	Ethanol
FF	Fill factor
FTIR	Fourier transform infrared
FRET	Förster resonance energy transfer
FWHM	Full-width-at-half-maximum
GiSAXS	Grazing-incidence small-angle X-ray scattering
GiWAXS	Grazing-incidence wide-angle X-ray scattering
H_2O	Water
HCl	Hydrochloric acid

HEPES	*N*-(2-hydroxyethyl)piperazine-*N'*-(2-ethanesulfonic acid)
HOMO	Highest occupied molecular orbital
HPLC	High performance liquid chromatography
HTL	Hole transport layer
HTMA-PFP	Poly[9,9-bis[6-(*N*, *N*, *N*-trimethylammonium)hexyl]fluorene-2,7-diyl-*alt*-1,4-phenylene]
IC	Internal conversion
ID	Isomerisation degree
Im	Imidazolium
ISC	Intersystem crossing
ITO	Indium tin oxide
IUPAC	International Union of Pure and Applied Chemistry
LD	Linear dichroism
LED	Light-emitting diode
LLC	Lyotropic liquid crystal
LUMO	Lowest unoccupied molecular orbital
LUV	Large unilamellar vesicle
MeCN	Acetonitrile
MeOH	Methanol
MKP	Modified Kratky-Porod
MO	Molecular orbital
m.p.	Melting point
MPS-PPV	Poly-[5-methoxy-2-(3-sulfopropoxy)-1,4-phenylene-vinylene]
NET	Poly[(2,5-bis(2-(*N*,*N*-diethylammoniumbromide)ethoxy)-1,4-phenylene)-*alt*-1,4-phenylene)]
NLLS	Non-linear least square
NMR	Nuclear magnetic resonance
OD	Optical density
OFET	Organic field-effect transistor
OLED	Organic light-emitting diode
OPV	Organic photovoltaic
P123	Poly(ethylene glycol)-*b*-poly(propylene glycol)-*b*-poly(ethylene glycol)
P2	Poly[2,5-bis[3-(*N,N,N*-triethylammonium)-1-oxapropyl]-1,4-phenylenevinylene]-dibromide
P3Anionic	Poly[3-(6-sulfothioatehexyl)thiophene)]
P3BHT	Poly(3-butylthiophene)-*b*-poly(3-hexylthiophene)
P3DTTP	Poly[(benzo[1,2-*b*:4,5-*b'*]dithiophene-*alt*-(4*H*-thieno[3,4-*c*]pyrrole-4,6(5*H*) dione)]
P3HT	Poly(3-hexylthiophene)
P3HT-*b*-P3HTBr	Poly[3-hexylthiophene-*b*-3-(6-bromohexyl)thiophene]
P3HT-*b*-P3HTIm	Poly[(3-hexylthiophene-2,5-diyl)-*b*-((1-methylimidazolium-3-yl)hexylthiophene-2,5-diyl)]
P3HT-*b*-P3HTNMe$_3$	Poly[(3-hexylthiophene-2,5-diyl)-*b*-((trimethylammoniumhexyl)thiophene-2,5-diyl)]
P3HT-*b*-P3HTPMe$_3$	Poly[(3-hexylthiophene-2,5-diyl)-*b*-((trimethylphosphoniumyl-hexyl)thiophene-2,5-diyl)]
P3HT-*b*-P3HTPy	Poly[(3-hexylthiophene-2,5-diyl)-*b*-((pyridiniumhexyl)thiophene-2,5-diyl)]
P3HTPMe$_3$	Poly[trimethyl-phosphoniumylhexylthiophene-2,5-diyl] bromide
P3TMAHT	Poly[3-(6-triethylammoniumhexyl)thiophene] bromide

P3Zwit	Poly[3-(*N*-(4-sulfonato-1-butyl)-*N*,*N*-diethylammonium)hexyl-2,5-thiophene)
PBS-PFP	Poly[9,9-bis(4-sulfonylbutoxyphenyl) fluorene-2,7-diyl-*alt*-1,4-phenylene]
$PC_{61}BM$	[6,6]-Phenyl-C_{61}-butyric acid methyl ester
$PC_{71}BM$	[6,6]-Phenyl-C_{71}-butyric acid methyl ester
PCE	Power conversion efficiency
PCS	Photon correlation spectroscopy
PDI	Polydispersity
PEDOT	Poly(3,4-ethylenedioxythiophene)
PEO	Polyethylene oxide
PF	Polyfluorene
PF2/6-*b*-P3TMAHT	Poly[9,9-bis(2-ethylhexyl)fluorene)-*b*-poly[3-(6-triethylammoniumhexyl)thiophene] bromide
PFOS	Heptadecafluorooctanesulfonic acid
PFP	Poly[(9,9-di(3,3′-*N*,*N*′-trimethylammonium)propylfluorenyl-2,7-diyl)-*alt*-(1,4-phenylene)]
$PFPB_x$	Poly[(9,9-bis(6′-*N*,*N*,*N*-trimethylammonium bromide)-hexyl)fluorene-*co*-*alt*-1,4-phenylene]
PL	Photoluminescence
PLED	Polymer light-emitting diode
POM	Polarised optical microscopy *or* Polyoxometalate
POM	$K_8[SiW_{10}O_{36}]$
PPE	Poly(phenylene ethynylene)
ppm	Parts per million
PPV	Poly(*p*-phenylene vinylene)
Prodan	6-Propionyl-2-dimethylaminonaphthalene
PS	Photosurfactant
PS_m-*b*-PAA_n	Polystyrene-*b*-poly(acrylic acid)
PSS	Poly(styrene-sulfonic acid)
PT	Polythiophene
PTPA	2,5-Poly(thiophene-3-propionic acid)
Py	Pyridinium
RT	Room temperature
r.u.	Repeat unit
SANS	Small-angle neutron scattering
SAS	Small-angle scattering
SAXS	Small-angle X-ray scattering
SDS	Sodium dodecyl sulfate
SEM	Scanning electron microscopy
SLD	Scattering length density
SOS	Sodium octyl sulfate
SV	Stern-Volmer
TEM	Transmission electron microscopy
THF	Tetrahydrofuran
TMS	Tetramethylsilane
TOF	Time-of-flight
TPP	Tetraphenylporphyrin
UV	Ultraviolet
Vis	Visible

List of Symbols

$[F^*]_0$	Concentration of the excited state molecules at $t = 0$
$[F^*]$	Time dependant concentration of the excited state
$[Q]$	Concentration of the quencher
$\partial\sigma/\partial\Omega$	Scattering cross-section
α	Angle between the transition moment
$\alpha(n_b)$	The expression factor
A	Acceptor
$A^{\perp}$	Absorption perpendicular to the sample
$A(\lambda)$	Absorbance at wavelength, λ
$A^{\parallel}$	Absorption parallel to the sample
B_{inc}	Isotropic incoherent background signal
γ_L	Molar volume of phospholipid
c	Speed of light
C_w	Mass of solid sample in the solution
δ	Electrical double layer thickness
δ_C	Carbon chemical shift
δ_{CD}	Charge density
ΔE	Difference of energy
δ_H	Chemical shift of protons
$\Delta\rho$	Difference in scattering length density between the scatterer and the solvent
d	Lamellar spacing
D	Diffusion coefficient
D_{bulk}	Bulk density of the scattering body
D_H	Hydrodynamic diameter
ε^0	Permittivity of free space
E	Efficiency of energy transfer
ε_A	Molar absorption coefficient
φ_{dry}	Mass volume of the dry material represented by the fit
Φ_F	Fluorescence quantum yield
F	Force
F_D	Intensity of donor emission spectrum
f_{ic}	The calculated value predicted by the model
$G(t)$	Autocorrelation function
h	Planck's constant
$I(q)$	Intensity of scattering
I_0	Initial intensity
I_{max}	Maximum emission intensity
I_p	Persistence length
I_t	Transmitted intensity
I_w	Emission intensity of the CPE
I_{WC}	Scattering function
$j_1(x)$	Bessel function
J_{DA}	Donor-acceptor spectral overlap
J_{sc}	Short-circuit current density
J-V	Current density - voltage
κ	Orientation factor

κ^{-1}	Debye's screening length
k	Spring constant
K_B	Boltzmann constant
k_F	Fluorescence rate constant
k_{IC}	Internal conversion rate constant
k_{nr}	Non-radiative rate constant
k_{obs}	Observed rate constant in the absence of a quencher
K_p	Water/lipid partition coefficient
k_{Phos}	Rate constant for phosphorescence
k_q	Bimolecular quenching constant
k_{rad}	Radiative rate constant
K_a	Association constant for static quenching
K_{SV}	Stern-Volmer constant
λ_{dm}	Dichroic mirror wavelength
λ_{em}	Emission wavelength
λ_{ex}	Excitation wavelength
λ_{max}	Absorbance maximum
L	Sample-detector distance *or* the length of the cylinder
L_c	Liquid crystal phase
L_{con}	Contour length of a flexible cylinder
L_{core}	Length of a cylinder core
L_{Kuhn}	Kuhn length
L_α	Fluid phase
L_β	Lamellar gel phase
μ	Electrophoretic mobility
$\hat{\mu}$	Electric dipole moment
$M_{1,2}$	Dipole moment
M_n	Number-average molecular weight
M_w	Weight-averaged molecular weight
η	Solvent viscosity
n	Refractive index
N	Number of particles per unit volume
n	Number of data points
N_A	Avogadro's number
N_{agg}	Aggregation number
n_{cp}	Refractive index of the solvent in which the compound is dissolved
n_{ref}	Refractive index of the solvent in which the reference is dissolved
θ	Scattering angle
θ_c	Critical angle
θ_i	Angle of incidence
OD_{cp}	Optical density of the compound
OD_{ref}	Optical density of the reference
ψ	Time-dependant wavefunction
p	Linear momentum
$P(q)$	Form or "shape" factor
$P_{CS}(q,R_{CS})$	Scattering function from the cross section of a rigid rod

P_m	Density of the sample mixture
P_s	Density of the solid
P_β	Gel phase
Q	Quencher
q	Scattering vector
ρ	Scattering length density
ρ_c	Scattering length density of the core
ρ_i	Scattering length density of the shell, *i*
ρ_s	Scattering length density of the shell
ρ_{solv}	Scattering length density of the solvent
r	Distance between a donor and acceptor
r	Radius of a sphere or cylinder
R_0	Förster distance
r_{core}	Radius of the core
R_{CS}	Circular cross-sectional radius
R_g	Radius of gyration
R_H	Hydrodynamic radius
r_s	Radius of the core and shell
σ_i	Standard deviation
S	Total spin angular momentum or scaling factor (the orientation factor)
$S(q)$	Structure factor
S_{Debye}	Debye function
s_i	Spin angular momentum
$\int I(\lambda)^{cp} d\lambda$	Integrated area of the emission spectrum of the compound
$\int I(\lambda)^{ref} d\lambda$	Integrated area of the emission spectrum of the reference
S_n	the n^{th} singlet excited state
$S_{WC}(q, L_{con}, L_{Kuhn})$	Scattering function of a single semi-flexible chain
τ_0	Fluorescence lifetime in the absence of a quencher
τ_i	Characteristic lifetime for the i^{th} component of a fluorophore
τ_{obs}	Observed lifetime
t	Time
t_i	Radii of the shells in the model
T_m	Main transition temperature
T_n	the *n*th triplet state
T_{pre}	Pre-transition temperature
T_{sheet}	Thickness of the sheet
T_{shell}	Thickness of the shell
T_{sub}	Sub-transition temperature
$\nu_{N\text{-}H}$	Nitrogen-hydrogen stretch
ν	Frequency
V	Volume of the aggregate
v/v	Percentage per volume
V_c	Volume of the core
V_{DA}	Electronic coupling of the donor and acceptor
$V_{dry\text{-}aggregate}$	Volume of the dry aggregate

$V_{\text{dry-core}}$	Volume of the dry core
$V_{\text{dry-shell}}$	Volume of the dry shell
V_{i}	Volume of each shell
V_L	Volume of phospholipid
V_{molar}	Molar volume
V_{s}	Total volume of the outer shell
V_W	Total volume
$w(qR_{\text{g}})$	Empirical crossover function
χ^2	Chi squared statistic
x	Cantilever deflection
y_i	Measured data value
ζ	Zeta Potential

Chapter 1

Introduction

1.1 Introduction

Self-assembly is the spontaneous organisation of components, from molecules to galaxies, into patterns or structures without intervention from an outside source. It is an elegant method for the preparation of functional responsive materials which is mediated by non-covalent driving forces between molecules such as electrostatic, van der Waals, π-π stacking and hydrogen bonding.[1] These processes are ubiquitous throughout nature, such as the self-assembly of lipid bilayer membranes or the light harvesting systems in plant cells. In recent years, there has been a drive to imitate nature, and create novel molecules with the ability to self-assemble into supramolecular structures for nanotechnology. Structures formed in this manner are naturally dynamic, resulting in the potential to induce significant changes to systems by subtly altering environmental factors such as pH, solvent and counter-ions. The major aim of this work is to understand and design systems which will spontaneously organise into functional materials based on conjugated polyelectrolytes and photoactive surfactants. Initial work will investigate how the solvent and counter-ions can be exploited to encourage or inhibit interchain interactions of conjugated polyelectrolytes and thereby modulate their aggregated structure in solution and the subsequently prepared thin films. The potential application of these materials for improving the efficiency of polymer photovoltaic cells and for bio-imaging and sensing will also be demonstrated. The final part of this thesis will investigate novel surfactants which contain photo-isomerisable groups to be used as a tool for controlling the self-assembled structure of surfactant aggregates in solution and hybrid materials, with a view to their use as responsive templates to fabricate porous hybrid materials.

1.2 Conjugated Polymers and Conjugated Polyelectrolytes

Conjugated polymers (CPs) are polymers with extended π-conjugation along their molecular backbone. The conjugated backbone gives rise to optoelectronic properties which can be exploited for applications such as light-emitting diodes (LEDs),[2, 3] organic photovoltaic cells (OPVs),[4, 5] organic field-effect transistors (OFETs)[6, 7] and optical sensors.[8] The linear combination of π-orbitals gives rise to a band structure which allows CPs to be described as semiconductors. Upon excitation, an electron is excited from the highest occupied band (the π band) to the lowest unoccupied band (the π* band), resulting in the formation of an exciton pair (a weakly bound excited electron and the oppositely-charged 'hole', which is the empty state in the π-band). When the electron and hole recombine, a photon of energy can be emitted as photoluminescence (PL).[9] The wavelength of the emitted photon is determined by the difference between the lowest energy excited state and the ground state. The size of this energy gap is highly dependent on the nature of the monomer unit in the CP backbone. For example, the poly(thiophene), poly[3-(6-trimethylammoniumhexyl)thiophene] bromide (P3TMAHT), is a red-emitter,[10] in contrast, the

poly(fluorene), poly(9,9-bis(6-*N,N,N*-trimethylammonium)-hexyl)fluorene phenylene) bromide (HTMA-PFP), is a blue-emitter (Figure 1.1).[11]

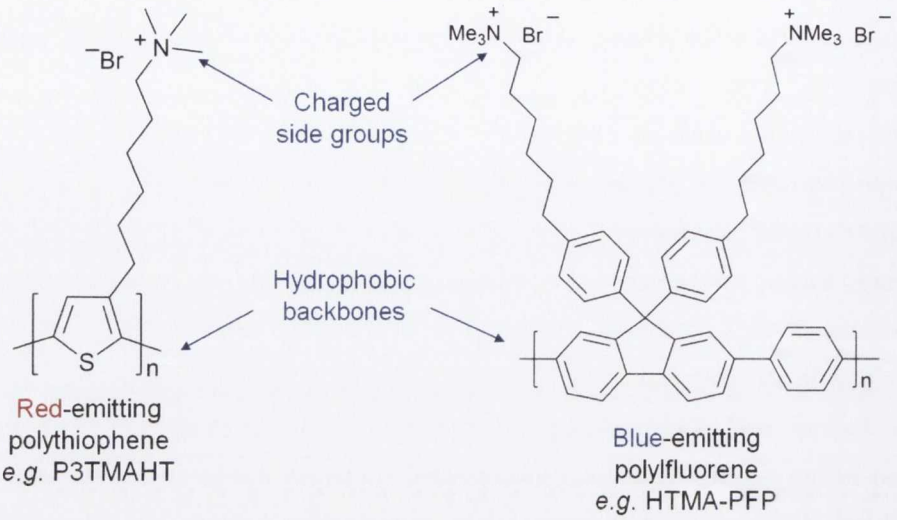


Figure 1.1 Chemical structures of the red-emitting poly(thiophene), P3TMAHT, and the blue-emitting poly(fluorene), HTMA-PFP.

Before further discussion it is pertinent to briefly define some polymer nomenclature. Polymers can be defined in terms of the number and sequence of repeat units, as shown schematically in Figure 1.2. Homopolymers consist of only one type of repeat unit, whereas a co-polymer consists of two or more monomeric species. Copolymerisation gives rise to a variety of polymer structures. For example, a *random* copolymer is comprised of two or more monomer units connected in a completely random arrangement. *Alternate* copolymers are made-up of alternating monomer units, *block* copolymers consist of two or more homopolymer blocks linked together by a covalent bond and *graft* copolymers contain a main chain polymer consisting of one type of monomer with branches made up of other monomers. Polymers can also be defined by whether they are simply linear chains (*linear* polymers) or more complicated structures such as stars or brushes (*branched* polymers). The sheer variety of structures available offers a wealth of opportunities to tune the formation of complex self-assembly structures.

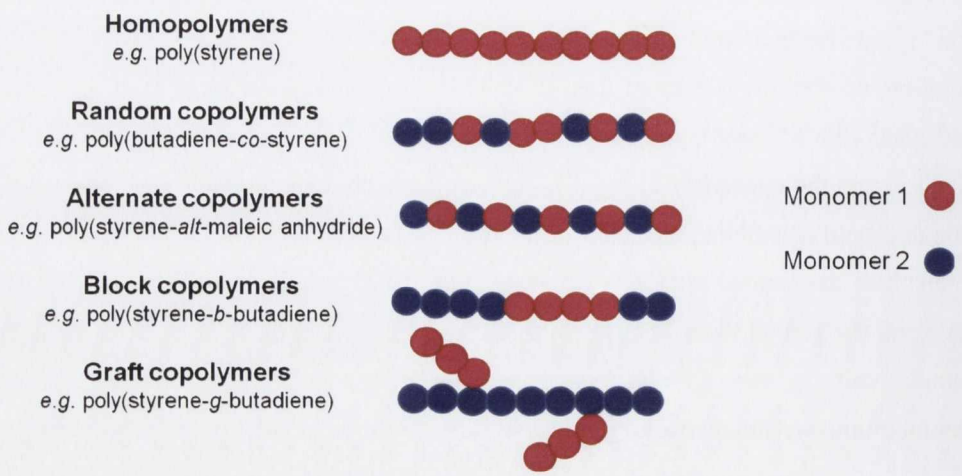


Figure 1.2 Schematic representation of repeat unit arrangements in a selection of polymers.

The CP backbone is hydrophobic and structurally rigid and as such CPs exhibit low solubility in polar solvents.[12] Conjugated polyelectrolytes (CPEs) are conjugated polymers that have pendant ionic functionalities anchored to the π-conjugated backbone. The ionic nature of CPEs allows them to be soluble in polar solvents, including water.[13] However, due to their hydrophobic backbones and hydrophilic side groups (Figure 1.1), CPEs are inherently amphiphilic which introduces a solubility gradient across the polymer leading to aggregation in solution. The aggregation of CPs and CPEs leads to increased intrachain interactions giving rise to an increased conjugation length, leading to a red-shift in polymer emission and decreased emission quantum yield.[14] For example, Tan *et al.* found that the polyphenylethynylene (PPE) with sulfonate-terminated side chains (PPE-SO_3^-) existed as molecularly dissolved chains in the "good" solvent, methanol, and as aggregates in the "bad" solvent, water.[15] Consequently, the sharp, structured, narrow emission band in methanol was replaced by a broad, featureless band which was significantly red-shifted in water. This study highlights how the organisation of the polymer backbone affects the electronic properties of the CP,[16] and is therefore extremely important for their application in optoelectronic devices.

1.2.1 Self-Assembly of CPEs in Solution

One elegant approach to control the organisation of CPEs in solution is to use amphiphilic, all-conjugated polyelectrolyte block copolymers, which are composed of at least two different conjugated blocks, one (or more) of which is an ionic polyelectrolyte block.[17-20] The inherent incompatibility between the solubility of the blocks leads naturally to self-assembled nano-domains with sizes in the range of 5-100 nm. Nanoscale phase separation is particularly attractive for solar cell technology, and as a result there has been a surge in research in this area, which will be described in detail later in this chapter. The morphology of the aggregate structures formed is dependent on the relative volume fraction of one block with respect to the other.[19] A selection of potential aggregate structures for block copolymers are shown in Figure 1.3 for the copolymer polystyrene-*b*-poly(acrylic acid) (PS_m-*b*-PAA_n, where *m* and *n* denote the degrees of polymerisation of PS and PAA, respectively).[21]

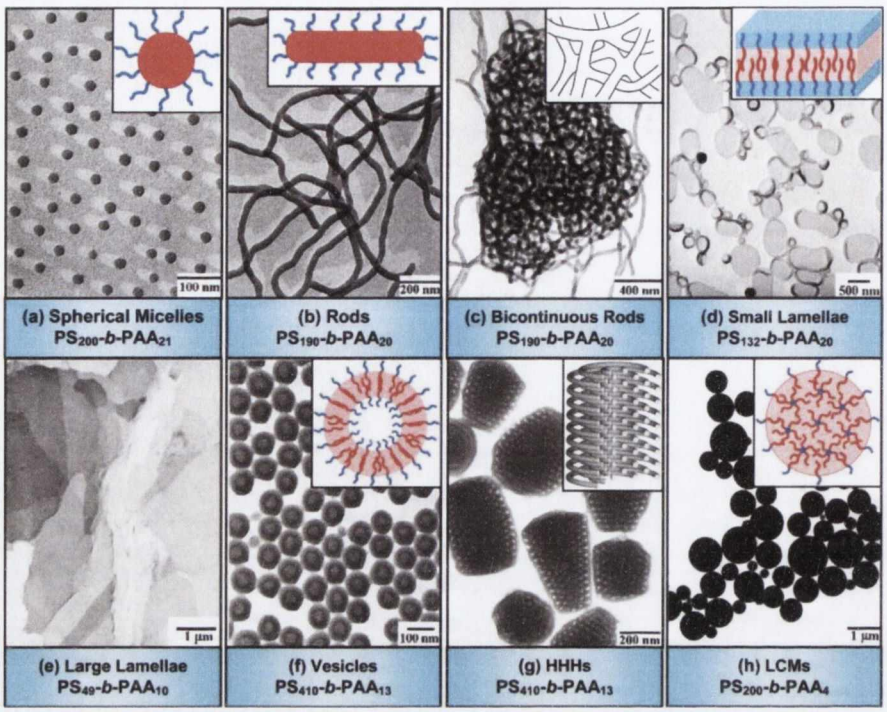


Figure 1.3 The influence of the relative volume fraction of individual blocks on the morphology of polymer aggregates formed. Transmission electron microscopy (TEM) micrographs and corresponding schematic diagrams of various morphologies formed from amphiphilic PS_m-*b*-PAA_n copolymers. Note: *m* and *n* denote the degrees of polymerisation of PS and PAA, respectively. In the schematic diagrams, red represents hydrophobic PS parts, while blue denotes hydrophilic PAA segments. HHHs: hexagonally packed hollow hoops; LCMs: large compound micelles, in which inverse micelles consist of a PAA core surrounded by PS coronal chains. Figure taken from Reference 21.

Further structural control can be achieved by the addition of neutral or oppositely charged surfactants. For example, in water the anionic copolymer poly{1,4-phenylene-[9,9-bis(4-phenoxy-butylsulfonate)] fluorene-2,7-diyl} (PBS-PFP), forms a metastable dispersion of polymer clusters.[22, 23] These aggregates were shown to be broken-up by the addition of the non-ionic surfactant *n*-dodecylpentaoxyethylene glycol ether ($C_{12}E_5$). Small-angle neutron scattering (SANS) and nuclear magnetic resonance (NMR) spectroscopy were used to show the incorporation of isolated CPE chains into polymer-surfactant aggregates.

Alternatively, oppositely-charged surfactants can co-assemble with the CPEs to form discrete, organised structures.[10, 24-28] For example, the cationic poly(thiophene) P3TMAHT is known to form spherical aggregates with interparticle order in water.[10] SANS studies revealed that with increasing charge ratio (x) of sodium dodecyl sulfate (SDS), P3TMAHT self-organises into different supramolecular structures ranging from micelles ($x = 0$) to rods ($x = 0.2$) to lamellar sheets ($x = 1$). These structural transitions were accompanied by changes in colour, from red, to deep violet, to yellow, respectively, as a result of the changes in chain configuration and, therefore, π-conjugation length.

1.3 Applications of CPEs

1.3.1 Organic Photovoltaic Devices

Photovoltaic devices, which directly convert absorbed sunlight into electricity, have emerged as a promising candidate for affordable, clean and renewable energy.[29, 30] OPVs are an emerging alternative to current crystalline silicon solar cell technology due to their compatibility with lightweight flexible substrates, and ease of processing through solution-based techniques, such as spin-coating, combining ease of fabrication with low-cost production.[30] A basic OPV device consists of thin films of a donor material (to absorb light) and an acceptor material (to mediate charge generation), which are sandwiched between two electrodes. The function, design and optimisation of these components will be discussed in greater detail below.

Conjugated polymers, such as poly(3-hexylthiophene) (P3HT), are attractive semi-conductor donor materials in OPV devices due to their large absorption overlap with the solar spectrum, good charge carrier mobilities and large molar absorption coefficients (ε ~10,000 mol^{-1} dm^3 cm^{-1}).[31] These features enable OPV devices to absorb most of the incident photons of sunlight by using a photoactive layer only 10-100 nm thick, which removes a number of potential routes for charge recombination which lower the device performance.[30] Upon photoexcitation, excitons are generated in the CP. These excitons are transported along the polymer chains until either they recombine (and are lost) or reach the donor/acceptor (*D*/*A*) interface where they can dissociate into free charges (and generate an electric current). The free charges generated at the *D*/*A* interface diffuse to the anode and cathode where charge carrier extraction and collection occur. The acceptor material chosen for OPV devices is typically a fullerene derivative, such as [6,6]-phenyl-C_{61}-butyric acid methyl ester ($PC_{61}BM$), due to its reversible electrochemical reduction, excellent electron transport characteristics and anisotropic charge transport.[32] In addition, $PC_{61}BM$ has been found to have an optimal energy level overlap between its lowest unoccupied molecular orbital (LUMO) and the highest occupied molecular orbital (HOMO) of many typical polymer donors,[33] which acts as the driving energy (ΔE) for charge transfer between the *D* and *A*.

The metric typically used to evaluate the performance of a solar cell is its power conversion efficiency (PCE):[32]

$$\text{PCE (\%)} = \frac{I_{sc} V_{oc} FF}{P_{inc} A} \tag{1.1}$$

where I_{sc} is the short circuit current, V_{oc} is the open circuit voltage, P_{inc} is the incident power density and A is the active area of the device. The fill factor (*FF*) is the ratio of actual maximum power output to theoretical power output if both I_{sc} and V_{oc} are maximum. The short circuit current density (J_{sc}) is defined as the I_{sc}/A, and is directly related to the efficiencies of light absorption, exciton generation and dissociation, charge transport and charge collection at the electrodes. V_{oc} is related to the difference between the highest occupied molecular orbital (HOMO) of the donor and

the LUMO of the acceptor in the OPV. *FF* is governed by both the parasitic series resistance (R_s) and the shunt resistance (R_p) of the solar cell. R_s is determined by the bulk conductivity of the electrodes, active and interfacial layers, and the contact resistance between them. R_p is controlled by the quality of the layers of the device and their interfaces. However, simply put, the PCE is the portion of incident photons of light converted into electricity by the device. Although recently OPV devices have been reported with PCEs exceeding 11%,[34, 35] they are yet to be competitive with the best performing inorganic-based solar cell materials (>43%).[36]

1.3.1.1 Device Structure of OPVs

The design of OPV devices has advanced significantly since their invention thirty years ago. In 1986, Tang reported the first OPV device, shown schematically in Figure 1.4a, with a bilayer architecture and a relatively modest PCE of 1%.[37] It is known that excitons within conjugated polymers suffer from a limited diffusion range as charge-recombination occurs within a small spatial volume of 10-20 nm.[38] As a result, the PCE of many early device architectures was low largely due the small contact area between the donor/acceptor interfaces.[39] Soon after in 1992, Sariciftci *et al.* reported the discovery of ultrafast photoinduced electron transfer (within 100 fs) from a CP to a fullerene (C_{60}).[40] This result laid the foundation for the device architecture now referred to as *bulk heterojunction* (BHJ) solar cells.[41] The active layer in a BHJ solar cell is an interpenetrating mixture of conjugated polymer (the donor) with a fullerene derivative (the acceptor).[39, 42] An interpenetrated network of internal donor-acceptor heterojunctions maximises the contact area between the donor and acceptor, thus, increasing the efficiency of the electron and hole transport.[39] Tuning the morphology of the CP is an attractive approach to further optimise this *D/A* interface.[43]

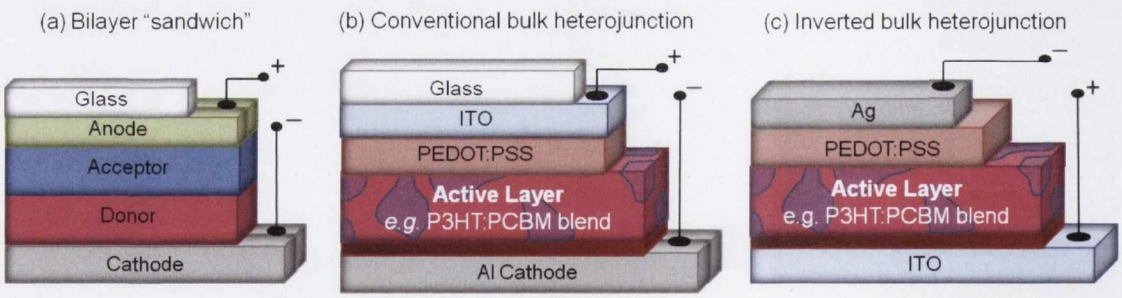


Figure 1.4 Schematic representations of some of the most common OPV device configurations currently under investigation. (a) Bilayer, (b) conventional and (c) inverted bulk heterojunction (BHJ) OPV configurations. ITO is indium tin oxide, PEDOT is poly(3,4-ethylenedioxythiophene), PSS is poly(styrenesulfonic acid), P3HT is poly(3-hexylthiophene) and $PC_{61}BM$ is [6,6]-phenyl-C_{61}-butyric acid methyl ester. The red lines in (b) and (c) represent optional electron transport layers (ETLs).

In a typical BHJ OPV, the photoactive layer blend is sandwiched between an indium tin oxide (ITO) electrode (anode) and the metal electrode (cathode) *e.g.* Al. Normally, a poly(3,4-ethylenedioxythiophene) (PEDOT)/poly(styrene-sulfonic acid) (PSS) layer is also included to assist hole transport (Figure 1.4b).[42] Unfortunately, this conventional device architecture has

encountered problems with stability due to contamination[44] and permeation of moisture and oxygen into the device.[45] Inverted solar cells are a promising alternative configuration to enhance the lifetime of the cell.[44, 46] In this design an air-stable high work function metal, such as Ag or Au, is used as the anode and ITO is used as the cathode (Figure 1.4c). However, these devices suffer from limited solar absorption.[47] Consequently, the structure of an OPV device still needs to be honed before optimum performance can be realised.

1.3.1.2 Optimisation of OPV Devices

Device optimisation is a multi-component problem. In addition to device configuration, the performance of organic solar cells containing P3HT/fullerene blends is known to be highly correlated to the ordered arrangement of P3HT chains within the active layer.[42, 48] P3HT is known to self-organise into semi-crystalline structures involving lamellar packing induced by π-stacking of the thienyl backbones.[48] Enhanced crystallinity has been found to increase light absorption and improve the hole mobility and charge transport.[42] A number of ways exist to tune the self-assembled nanostructure of the conjugated polymer. These methods include varying the polymer:fullerene ratio, film thickness, processing solvent, the use of additives and post-deposition solvents.[49, 50]

1.3.1.3 Interfacial Layers

To further optimise OPV device performance various n-type electron transport layers (ETLs) have been introduced at the metal/active layer (standard cell), or transparent metal oxide/active layer (inverted cell) interfaces, *e.g.* metals (Mg,[51] Ca[52]), metal salts (LiF,[53] Cs_2CO_3[54]), fullerene derivatives[55] and, notably, CPEs.[56-58] ETLs have afforded remarkable improvements in device parameters, such as V_{oc}, J_{sc}, *FF* and final PCEs. However, to date, much debate still remains about the precise role and function of ETLs in OPV devices.[52, 59, 60] In addition to facilitating electron transport and collection (and blocking hole transport), they are believed to diminish detrimental factors such as leakage current, bad interface tuning, charge recombination, *etc.* The role of interfacial layers will be discussed in greater detail below.

1.3.1.4 Role of the Interfacial Layer

Interfacial layers are used in various locations within an OPV device to improve J_{sc}, V_{oc} and *FF*, and thus, the overall device PCE. Firstly, the interfacial layer can greatly lower the interfacial contact resistance between the hydrophilic metal cathode and the hydrophobic layers by reducing their inherent incompatibility, promoting Ohmic contact and, thus, improving the fill factor.[24, 61] ETLs can also induce interfacial dipoles pointing from the cathode to the active layer, serving to reduce the work function of cathodes and increasing the built-in potential of OPVs.[62, 63] Heimel *et al.* used Density Functional Theory (DFT) calculations to show that the orientation of polymer chains with respect to the organic/organic or inorganic/organic interfaces has a decisive

impact on energy level alignment at these heterojunctions.[64] For example, they found that the edge-on orientation of fluorinated P3HT chains, with their electron withdrawing substituents at the exposed surfaces, dramatically lowers the energy levels of the organic semiconductors through collective electrostatic effects. The orientation dependence was attributed to the intrinsic surface dipoles of planar π-conjugated systems and the intramolecular polar bonds.[64] Consequently, control of the molecular orientation of conjugated polymers is a valuable tool for the optimisation of ETLs in OPV devices.

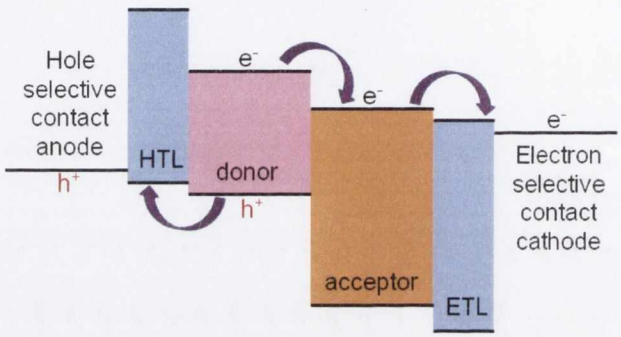


Figure 1.5 Schematic illustration of an OPV cell in extraction mode. Excitons are generated and diffuse to the donor/acceptor interface where they dissociate into free charge carriers (electrons (e^-) and holes (h^+)). The charge carriers are then transported to the electrodes and are extracted by the interfacial layers to the respective electrode. HTL and ETL are hole- and electron-transport layers, respectively.

Additionally, interfacial layer materials have been used as optical spacers to enhance photon absorption in highly efficient OPVs,[65] or to depress surface/interfacial recombination.[60] Finally, interfacial layers also play a critical role in terms of improving device stability, which is essential for real-world application. Hydrophobic and dense ETLs can hinder the penetration of water and oxygen and function as scavengers for these species, which increases the durability of OPVs.[66] Interfacial materials form conformal contacts with improved adhesion between the active layer and electrodes which prevent interfacial dewetting and delamination.[67] Furthermore, they effectively block the diffusion of unwanted species from the electrodes, such as metal particles, during device fabrication and operation which are also detrimental to device stability.

1.3.1.5 CP/CPE Interfacial Layers

An ideal interfacial layer material should encompass good chemical and physical stability, solution processability, good film forming properties, be producible at a low cost, and have sufficient conductivity to reduce resistive losses. For OPV applications, poly(thiophene)- and poly(fluorene)-based conjugated polymers with side chains containing polar moieties, such as amines, amine salts, phosphates, and alkoxy groups, are the most commonly investigated systems.[24, 57, 68-71] Due to the surge of interest in this area, there are now numerous examples of CPE ETLs in the literature which regularly achieve a greater than 20% improvement in PCE compared to reference devices. For example, an amphiphilic diblock poly(thiophene)-based cathodic interlayer in a conventional BHJ OPV afforded a 23% improvement in PCE, reaching

9.1%.[69] Chen *et al.* found that increasing the number of polar groups in poly(fluorene)-based ETLs, improved the coverage of favourable interfacial dipoles on the surface of ITO in an inverted OPV device. The dipole formation lead to an enhancement in the electrostatic interaction between the active layer and the electrode, thus minimising the interfacial energy barrier.[68] Finally, Oh *et al.* demonstrated that an ETL based on a water-soluble poly(fluorene) derivative (WPF-oxy-F) can effectively reduce the work function of different metals, including Al, Ag, Cu and Au, resulting in Ohmic contact between the P3HT:$PC_{61}BM$ BHJ and cathode.[71] Since the ordering and orientation of the polymer controls the orientation of the dipole moment,[24] a detailed understanding of the structured organisation of organic interlayers with respect to their charge transport properties is crucial to further optimise OPV devices.

1.3.2 Biomaging and Sensing

CPEs are attractive biological probes due to their water-solubility, biocompatibility, and environment-[72, 73] and aggregation-responsive fluorescence.[5, 26, 27] In addition, when compared to small molecule sensors, conjugated polymers exhibit large signal amplification resulting from their highly efficient intra- and inter-chain energy transfer, shown schematically in Figure 1.6.[8] Consequently, a number of sensory systems have been rationally designed which harness the ability of a CPE to translate the presence of an analyte into an easily measureable optical or electrochemical response.[8]

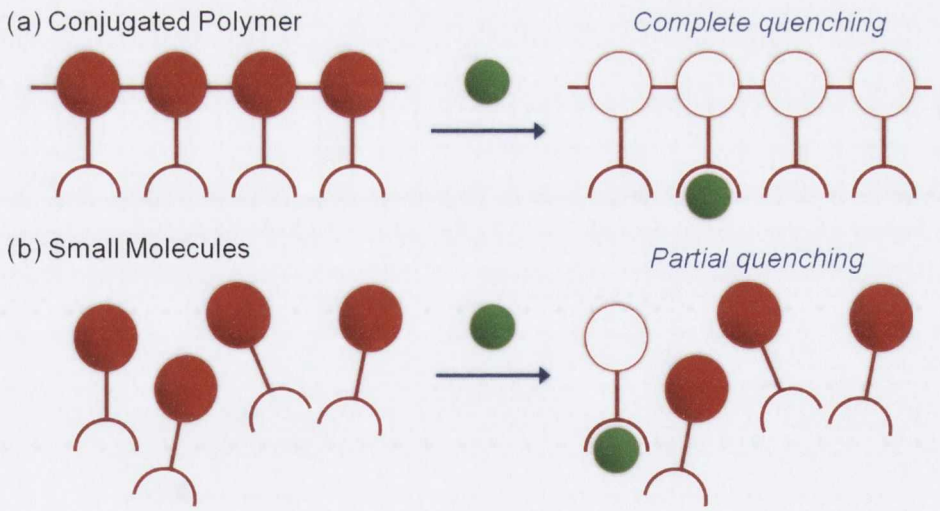


Figure 1.6 Schematic comparison of (a) a conjugated polymer interacting with a small concentration of quencher giving complete quenching of the polymer chain and (b) individual molecular receptors exposed to the same small concentration of quencher, resulting in partial quenching.

CPE-based sensors have been reported for small ions, such as iodide or bromide,[72] enzymes[74] and DNA.[75] For example, Bazan *et al.* used cationic poly[(9,9-bis(6′-*N,N,N*-trimethylammonium bromide)hexyl)fluorene-*co*-*alt*-1,4-phenylene] ($PFPB_x$) to detect and quantitatively measure the concentration of DNA in aqueous solution.[75] They found isolated chains of $PFPB_x$ emitted blue-light, while the DNA-induced aggregation resulted in green-light emission.

The increase in the green-light emission was monitored as a function of the DNA concentration in the system and a calibration curve was prepared to accurately determine unknown DNA concentrations.[75] This system has the potential to be used to monitor the polymerase chain reaction, a common method used in synthetic DNA synthesis.

CPEs have also received a lot of attention as membrane probes in model and live cells. The assembly of CPEs with phospholipid vesicles has yielded a broad range of potential applications for cell biology, including cell imaging,[76] fabrication of sensing devices[73] and formation of biocidal agents.[77] The performance of a CPE probe is dependent on its localisation and orientation within the membrane bilayer. The extent of CPE incorporation within phospholipid vesicles has previously been controlled by varying the nature and number of side-group charges[78] and the length of the polymer chain.[79, 80] Cosa *et al.* investigated the effect of varying the chain length of anionic poly(phenylene ethynylene)s (PPEs) on their interaction with phospholipids of different head-group charge.[79] Regardless of the PPE chain length, the anionic CPE showed no interaction with negatively-charged phospholipid vesicles and associated only to a small extent with zwitterionic phospholipids. In contrast, strong interactions were observed with the cationic phospholipid, 1,2-dioleoyl-3-trimethylammonium-propane (DOTAP), with vesicle fusion being reported exclusively for the longest chain-length PPE. It was proposed that the vesicle fusion may have played a role in the biocidal activity previously reported for PPEs.[80]

1.4 Surfactants

The first part of this introduction has focused primarily on photoresponsive conjugated polymers and it was shown that the aggregate morphology of CPs can be controlled by the addition of simple surfactants to design functional materials. The second portion of work in this thesis will involve surfactants which are inherently photoresponsive. The self-assembly and physicochemical properties of novel photoactive surfactants will be investigated in an effort to design templates for polymeric materials, in which the nanoscale structure is tuneable by light. Both parts of this work are complimentary, as they rely on the forces of self-assembly to create controllable 3D structures in solution.

1.4.1 Self-Assembly of Surfactants

A surfactant, or "surface active agent," is an amphiphilic molecule with a hydrophobic tail and hydrophilic head. Surfactants are often classified by the nature of their hydrophilic component; anionic, cationic and neutral (non-ionic or zwitterionic). Due to their amphiphilic nature, surfactants are pre-programmed to self-organise into a variety of micelle structures in solution including spheres, rods or vesicles, when the concentration exceeds the critical micelle concentration (*cmc*) (Figure 1.7).

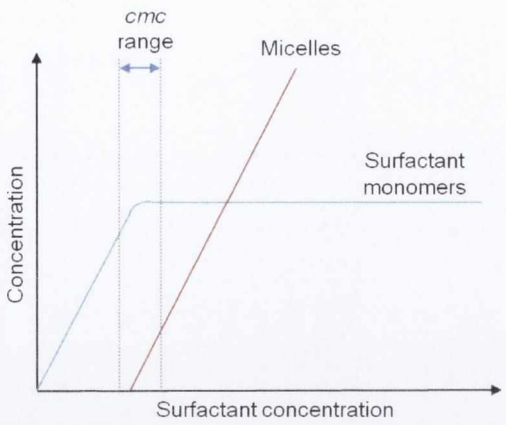


Figure 1.7 Schematic representation of the relationship between the total concentration of surfactant compared to the concentration of free surfactant monomers and micelles. Micelles begin to form when the concentration of surfactant reaches the critical micelle concentration (*cmc*).

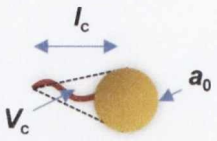
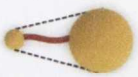
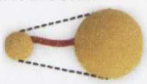
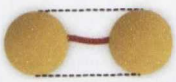
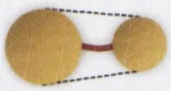
A self-assembled structure forms when a number of surfactant molecules act to minimise either the interaction of their hydrophobic hydrocarbon tails with polar solvents, or their hydrophilic ionic or polar head-groups with organic solvents. Aggregates that form through self-assembly in this manner are the result of the intermolecular forces pushing the chemical system into a low energy minimum on the potential energy surface of the system. Long-range hydrophobic forces act as the driving force to bring surfactant molecules together.[81] While opposing forces, such as the electric double layer, which is the result of interactions between the micelle and the solvent, or hydration forces, repel the surfactants apart and act against the long-range hydrophobic forces.[82] These repulsive forces originate from charge-bearing or hydrated head-groups and are relatively short-range in comparison to the hydrophobic interactions. These two effects vary as a function of the intermolecular distance between two entities, but in opposite ways.[81] Consequently, there is a particular concentration, the *cmc*, in a chemical system at which there is a balance of these opposing forces where micelles are favourably formed. Further addition of surfactant to the bulk solution increases the number of the micelles while the concentration of the surfactant monomer remains constant.

The geometry of the self-assembled structures formed by surfactants can be predicted to some extent by the critical packing parameter (P) of the constituent molecules, given by:[83]

$$P = \frac{V_c}{a_0 l_c} \tag{1.2}$$

where V_c is the volume of the hydrophobic chain, a_0 is the mean cross-sectional surface area of the head-group and l_c is the critical chain length. Table 1.1 shows the relationship between the packing parameter and aggregate morphology. However, the structure is also influenced by external factors, such as the concentration of the surfactant, temperature, pH or solvent.

Table 1.1 Relationship between the effective shape of the surfactant molecule, the packing parameter (P) and the predicted aggregate morphology according to Israelachvili.[83] l_c is the length of the chain, V_c is the volume of the core and a_0 is the mean cross-sectional head-group surface area.

Critical packing parameter (P)	Shape	Aggregate structure
$P < 1/3$	Cone 	Spherical micelle
$1/3 < P < 1/2$	Wedge 	Cylindrical micelle
$1/2 < P < 1$	Truncated cone 	Vesicle
$P = 1$	Cylinder 	Bilayer
$1 < P$	Inverted truncated cone 	Inverted micelle

1.4.2 Lyotropic Liquid Crystal (LLC) Phases

At higher concentrations, the surfactants may undergo a structural reorganisation into a variety of thermodynamically stable 2D or 3D lyotropic liquid crystalline phases, some of which are shown schematically in Figure 1.8. A liquid crystalline phase is an ordered fluid phase with some degree on anisotropy, *i.e.* some degree of directionality to its physical properties, which are the result of molecular-scale interactions.[84] Properties of the phase, such as its optical or electric properties, will differ depending on which orientation of the bulk material is examined.

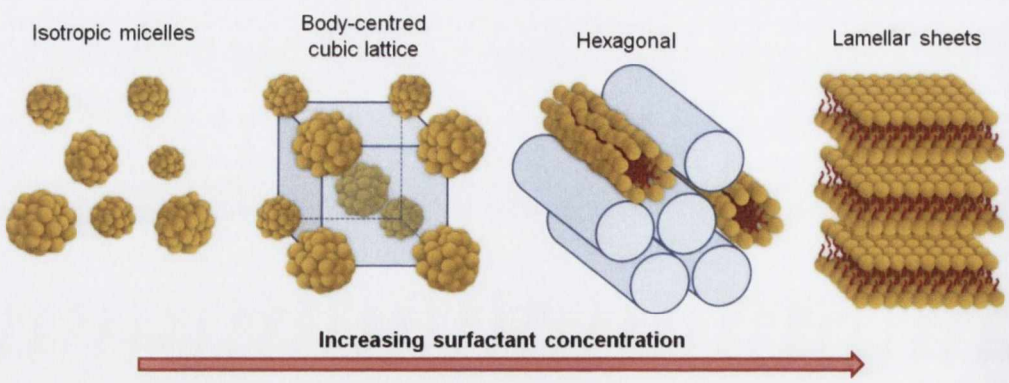


Figure 1.8 Schematic illustrations of some of the lyotropic liquid crystal phases that can be formed by surfactants, and how these phases would be expected to occur as a function of concentration. Body-centred cubic and hexagonal phases are the most efficient ways to pack spherical and cylindrical micelles, occupying 68% and 91% of the available space, respectively.[84]

In liquid crystalline materials bulk anisotropy results in *birefringence*.[84] Birefringence is an optical property of certain materials in which incident light rays of different polarisation are subject to different refractive indexes when passing through the material. For example, when a polarised monochromatic light ray passes into a liquid crystal medium, it will be resolved into two components with orthogonal polarisation directions. As each of these rays will experience a different refractive index, one will travel faster than the other, creating a phase difference between the two.

When polarised white-light passes through a sample, the magnitude of polarisation will vary as a function of the wavelength of light. The transmitted light can be analysed in the presence of a second polarizer (analyser) placed orthogonally to the first. The different wavelengths of light emerge from the liquid crystal with different magnitudes of polarisation. Wavelengths that have a large component of polarisation aligned parallel to the analyser will be observed as the most intense. This effect creates characteristic colours and defect textures typically observed using polarised optical microscopy (POM). POM is a popular technique for the visualisation of liquid crystal textures which takes advantage of their birefringent nature.[85-87] It is often possible to make accurate phase identifications by interpretation of defect textures observed by POM. This technique is described in detail in Section 3.2.10.

1.4.3 Templates for Inorganic Host Matrices

LLC phases of ionic liquids,[88] block copolymers[89] and commercially-available surfactants[90] have all been employed as sacrificial, soft templates for ordered, nanostructured inorganic-organic polymeric materials in the bulk and as thin films. Materials which have been templated by LLC mesophases have attracted considerable attention for electrochemical sensors,[91] OPV devices,[92] catalysis,[93] and gene and drug delivery,[94] owing to the advantage of yielding mesoporous materials with predictable geometry and pore size.

The assembly of the surfactant template into the appropriate phase can be directed through careful selection of the experimental conditions from the phase diagrams (Figure 1.9a)[90] or alternatively, through evaporation-induced self-assembly (EISA).[92, 95, 96] In EISA, preferential evaporation of a volatile solvent results in an increase in the local surfactant concentration, promoting formation of a given LLC phase *in-situ* (Figure 1.9b). In either scenario, a soluble inorganic precursor cooperatively assembles around the surfactant mesophase. Addition of a catalyst initiates hydrolysis resulting in condensation of the inorganic phase, effectively freezing-in the templated architecture. The surfactant is then removed *via* solvent extraction, calcination or UV exposure, leaving the nanostructured morphology intact within the inorganic oxide. The pore size distribution and ordering is determined primarily by the LLC mesophase formed.

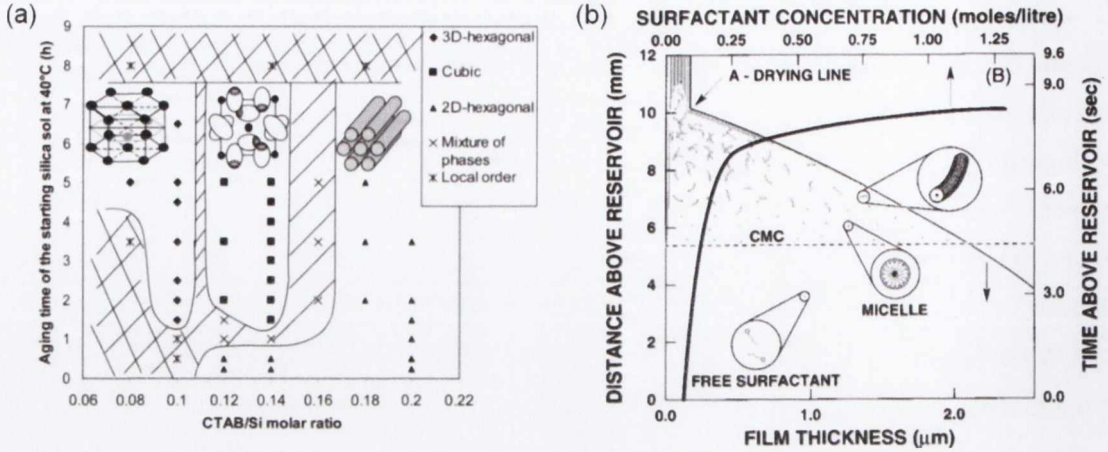


Figure 1.9 (a) Binary phase diagram showing the domains where three distinctive micellar phases of cetyltrimethylammonium bromide (CTAB)-Si exist, as a function of the molar ratio and the aging time of the initial silica sol at 40 °C. Adapted from Reference 90. (b) Steady-state film thinning profile established during dip-coating of a complex fluid comprised of silica, surfactant, alcohol, and water. The initial surfactant concentration is below the *cmc*. However, the surfactant concentration increases with distance above the reservoir surface. Adapted from Reference 95.

Block copolymers which were shown to self-assemble into exotic discrete aggregate structures at lower concentrations in Section 1.2.1, are also known to form exotic LLC phases at higher concentrations.[89] It is possible to use such polymeric LLC phases to template polymeric sol-gel materials. For example, Frey *et al.* demonstrated that Pluronic P123 block copolymer, poly(ethylene glycol)-*b*-poly(propylene glycol)-*b*-poly(ethylene glycol), could be used as structure-directing agent or mesostructured silica films.[89] The solution phase behaviour of the ternary THF-H_2O-P123 system, whose phase diagram is shown in Figure 1.10a, guided the selection of the synthetic conditions. Evaporation of THF during the dip-coating process initiated EISA, by increasing the local concentration of P123. Concomitantly, one H_2O molecule was generated in the condensation of silica to give a Si-O-Si bond. The *in-situ* generation of water molecules over time favoured preferential association with the hydrophilic polyethylene oxide blocks of the surfactant, leading to self-organisation of P123 into liquid-crystal like phases, similar to those observed in the ternary phase diagram. The silica cross-linking network imposed rigidity into the composite films, while, crucially, retaining the highly ordered hexagonal or lamellar mesophases, as identified by grazing-incidence small-angle X-ray scattering (SAXS) and TEM measurements (Figures 1.10b and 1.10c).

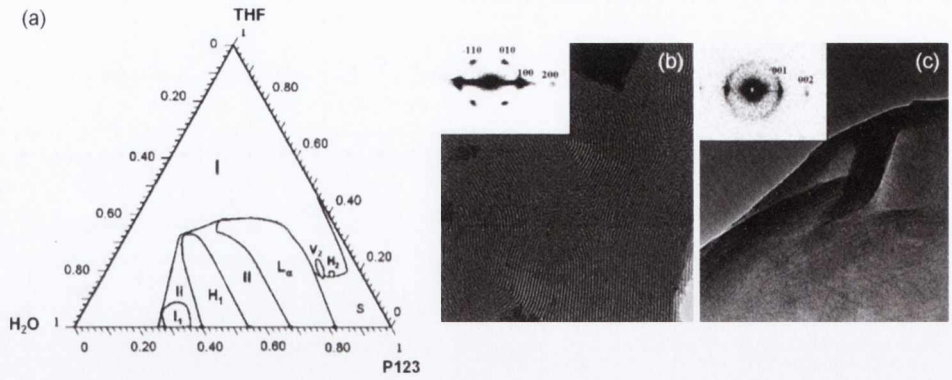


Figure 1.10 Formation of mesostructured silica films using block copolymer templates and an EISA approach. (a) Ternary phase diagram of THF-H_2O-P123 at 298 K (the concentrations are expressed in weight percent). I_1 is a micellar cubic liquid crystal phase, H_1 is a hexagonal phase, L_α is a lamellar phase, V_2 is a reverse bicontinuous cubic phase, and H_2 is a reverse hexagonal phase phase. *II* is a multiphase liquid crystal region, and *S* is a multiphase region containing solid and liquid crystal phases. *I* is an isotropic single-phase region. TEM images and glancing-incidence 2D-SAXS patterns (insets) of silica films deposited from THF sols with TEOS:P123 molar ratios of (b) 1:0.017 and (c) 1:0.033. Figure adapted from Reference 89.

Previously, Frey *et al.* have used a similar approach to prepare hybrid nanostructured donor-acceptor materials for bulk heterojunction solar cells.[92] In this study, they incorporated [2-methoxy-5-(2′-ethylhexyloxy)-1,4-phenylene vinylene] (MEH-PPV) (the *donor*) within cubic mesostructured titania films (the *acceptor*). The films were prepared by the co-assembly of a titania precursor species, titanium tetraethoxide (TEOT), MEH-PPV, and an amphiphilic structure-directing agent, the triblock copolymer, poly(ethylene oxide)$_{106}$-poly(propylene oxide)$_{70}$-poly(ethylene oxide)$_{106}$ (Pluronic F127), from a THF-based precursor solution. This formulation yielded cubic titania thin films incorporated with MEH-PPV. This interpenetrating 3D network had organic-inorganic (*donor-acceptor*) phase separation of 10-15 nm, which is on the same length scale as the polymer exciton diffusion length, a fundamental prerequisite for efficient charge separation in OPV devices, as described in Section 1.3.1. Finally, OPV devices utilising these cubic titania/F127/MEH-PPV films as the active layer material showed reasonable photocurrents (0.2 mA cm^{-2}) and open circuit voltages (0.7-0.8 V). Therefore, this study demonstrated the ability of EISA of polymeric materials and surfactants to form complex high performance devices.

1.5 Photoactive Surfactants

A sub-class of surfactants, photoactive surfactants (PS), contain a photochromic group. Upon illumination with a photon of specific energy, the photochromic group undergoes a structural change. If the concentration of the PS is above the *cmc*, then upon illumination, the change in shape of each molecule can have a congruent effect on the micelle or aggregate structure. This can include a change in the aggregate size or shape,[97] or result in complete dispersion of the aggregated surfactant molecules into solution.[98] PS have received significant attention because of their ability to self-assemble into a range of morphologies, in combination with the structure changing ability of the photochromic group. This means that light can be used as a cheap, clean and non-invasive trigger for switching the structure defining element of a material. Light is an attractive tool because

of the easy mediation of the wavelength, intensity, illumination area and duration of the incident light, all of which are desirable features for device preparation. As such, PS have been increasingly investigated as the basis of stimuli-responsive materials for application in catalysis,[99] drug delivery[100] and microfluidic devices.[101]

1.5.1 Photoswitchable Moieties

Common photochromic groups include spiropyrans, stilbenes and azobenzenes. Azobenzene photosurfactants were chosen as the focus of this project, due to their relatively simple synthetic procedures, and the substantial changes observed in their geometrical configuration without any undersirable side reactions upon photoisomerisation.

1.5.2 Azobenzene

Azobenzene photosurfactants offer simultaneous photoresponsive and interfacial activity from a single molecule. Azobenzenes adopt one of two isomeric states, the *cis*- or *trans*-configuration (Figure 1.11a). Under incident light of appropriate wavelength, photoisomerisation leads to a substantial change in the geometrical configuration and size of the molecule. This process also modifies the delicate hydrophilic-hydrophobic balance, with the *trans*-isomer being considerably more hydrophobic than the *cis*-state (the dipole moments (μ_0) across azobenzenes are ~0 D and ~3 D for *trans* and *cis*, respectively).[102, 103] The *trans*-state is usually >50 kJ mol^{-1} more stable than the *cis*-isomer and therefore is the predominant isomer at thermal equilibrium.[102] Upon photoexcitation, the excited state of the *trans*-isomer decays non-radiatively, either to the ground state of the *trans*- or *cis*-isomer (Figure 1.11b). Similarly, the excited state of the *cis*-isomer may decay non-radiatively, either to the ground state of the *trans*- or *cis*-isomer. In this way a photo-equilibrium known as the photostationary state (PSS) is obtained which is comprised of a mixed population of *trans*- and *cis*-isomers. In the PSS the rate of the forward process equals the rate of the reverse process. The reverse *cis*-to-*trans* process can be driven by either photo- or thermal-excitation. Consequently, if a sample is left in the dark the *cis*-isomer will thermally revert to the *trans*-isomer.

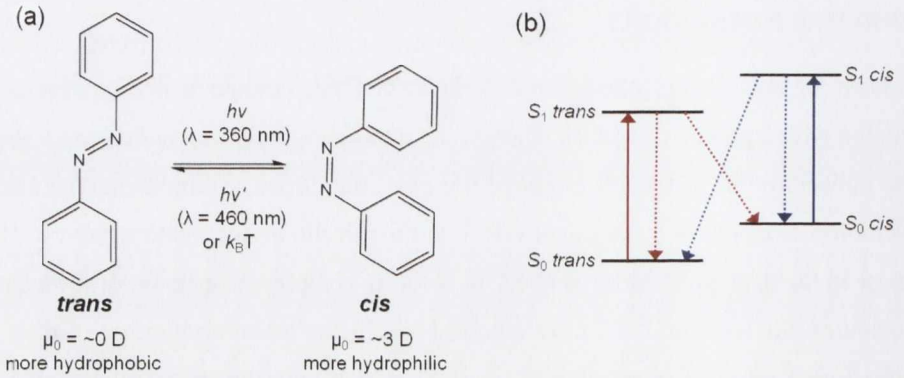


Figure 1.11 Photo- and thermal-isomerisation of azobenzene. (a) *Trans*-to-*cis* isomerisation of azobenzene, μ_0 is the transition dipole moment. (b) Illustration of the electronic excitation (solid lines) and deactivation (dashed lines) of *trans*- and *cis*-isomer.

1.5.3 Spectroscopy of Azobenzene

The *cis*- and *trans*-isomers of azobenzene have two commonly accessible singlet states which correspond to two absorption bands in the UV/Vis absorption spectrum. Figure 1.12 shows a simple Molecular Orbital (MO) diagram describing the -N=N- bond in an azobenzene system, where n_a and n_b are the non-bonding orbitals from the N-atoms (one is higher in energy than the other). The lowest energy transition takes place at ~450 nm which is due to the $n_b \rightarrow \pi^*$ process (which will now be referred to as the $n \rightarrow \pi^*$ transition). The intensity of this transition is different in the *cis*- and *trans*-isomers because the transition is symmetry-forbidden in the planar *trans*-isomer (symmetry group C_{2h}), but allowed in the bent *cis*-isomer (symmetry group C_{2v}). This is due to vibronic coupling of the $n\pi^*$ state in the *trans*-isomer with other low lying molecular states resulting in a relatively intense, forbidden transition with a lack of vibrational structure. The vibronic coupling is also the reason for the inability of nearly all azobenzene compounds to fluoresce.

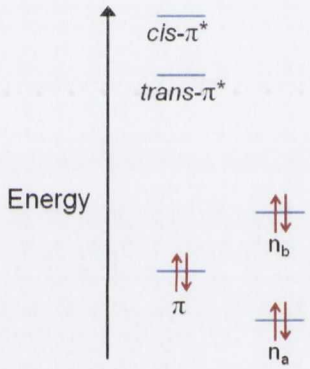


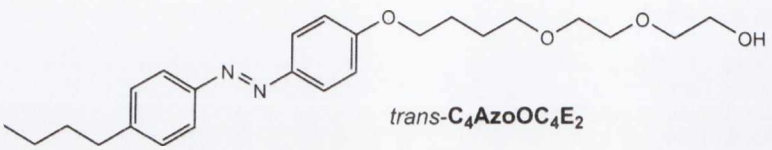
Figure 1.12 A simplified molecular orbital diagram for azobenzene. n_a and n_b are non-bonding orbitals corresponding to the lone pairs of electrons present on each N-atom.

A second transition occurs in the UV region at ~350 nm, attributed to the allowed $\pi \rightarrow \pi^*$ transition, which has a much stronger absorbance than the band at 450 nm. The marked difference in the intensity of this band between the two isomers is due to the non-planar configuration of the *cis*-isomer. In the *cis*-isomer, the non-planarity of the molecule means that conjugation is restricted. This raises the energy of the π^* orbital relative to that of the *trans*-isomer, this increases the energy of the $\pi \rightarrow \pi^*$ transition (Figure 1.12).

1.5.4 Self-Assembly of Photosurfactants

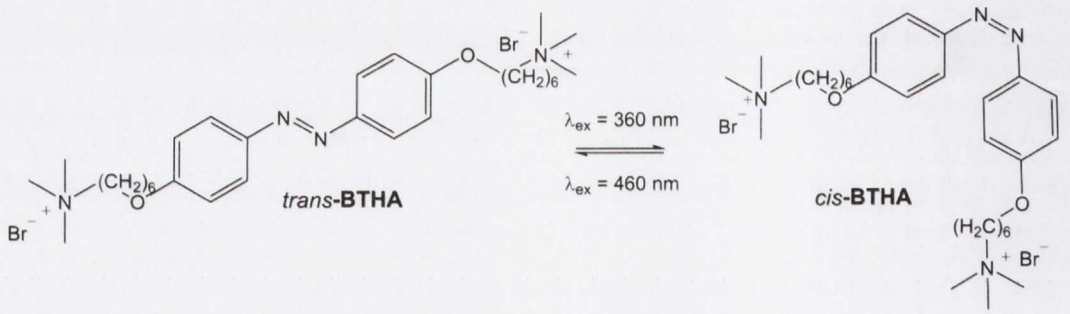
Most studies on PS to date have focussed primarily on exploring PS for a specific application using just a handful of relatively simple surfactant structures. Hatton *et al.* found that the *trans*-isomer of the non-ionic azobenzene PS, diethylene glycol mono(4′,4-butyloxybutyl-azobenzene) ($C_4AzoOC_4E_2$), self-assembled into bilayer vesicles at high concentration. In contrast, the *cis*-isomer formed a bicontinuous phase which was attributed to the change in molecular architecture accompanying the *trans-cis* isomerisation.[104] At concentrations above the *cmc*, $C_4AzoOC_4E_2$ was found to increase in surfactant tension by ~11 mN m^{-1} upon

photoisomerisation.[105] Such changes in their physicochemical behaviour were attributed to the difference in shape and size of azobenzene PS upon photoisomerisation.[105, 106] Similar surfactants could be useful in a variety of surface tension-related applications, including the control of spreading processes and the fluid movement in microfluidic devices.[101]



Scheme 1.1 Chemical structure of the photoactive surfactant, $C_4AzoOC_4E_2$.

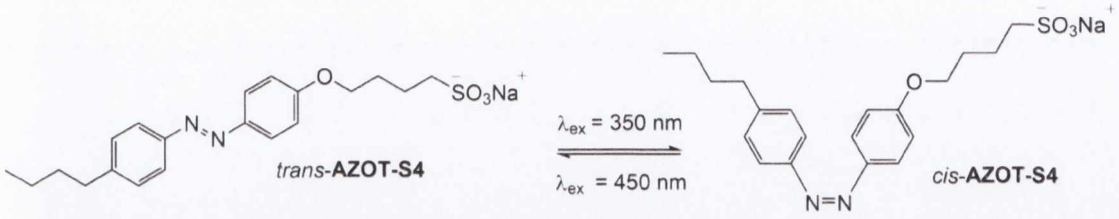
PS have also been used in combination with similarly charged "regular" surfactants (*i.e.* not photoresponsive) to yield photoresponsive self-assembled structures. For example, *trans*-bis(trimethylammoniumhexyloxy)azobenzene dibromide (*trans*-BTHA), was shown to form vesicles in conjunction with sodium dodecyl sulfate (SDS) with diameters of ~1350 Å and bilayer thicknesses of ~35 Å.[107] This layer thickness correlated well with the fully extended *trans*-BTHA molecule length. Upon illumination with UV light (λ_{ex} = 360 nm), BTHA underwent a photoisomerisation to a *cis*-rich photostationary state (80% *cis*-isomer) (Scheme 1.2). This resulted in a dramatic change in the surfactant packing preference, leading to reorganisation of the surfactant molecules from vesicles to cylindrical aggregates with a cross-sectional radii of ~19 Å and a hydrodynamic diameter of 240 Å. Irradiation with visible light (λ_{ex} = 460 nm) leads to the recovery of the *trans*-rich photostationary state of the solution and reformation of the vesicles.[107]



Scheme 1.2 Reversible transition from *trans*-BTHA to *cis*-BTHA using UV and visible light.

Photosurfactants can also exhibit remarkable variations in their bulk phase behaviour upon photoisomerisation. For example, the azobenzene-containing PS, 4-butylphenyldiazenylphenoxybutane-1-sulfonate (AZOT-S4), shown in Scheme 1.3, was used to dope water-in-decane microemulsions, which had been stabilised by the common anionic surfactant sodium bis(2-ethyl-hexyl)sulfosuccinate (AOT).[108] Conversion of AZOT-S4 to the *cis*-form with UV light (λ_{ex} = 350 nm) led to a decrease in the water/decane interfacial tension which resulted in the partitioning of the single phase microemulsion into two co-existing microemulsion phases. Recovery of a single phase microemulsion could be induced by visible light irradiation at 450 nm to regenerate the *trans*-AZOT-S4.[108] The ability to reversibly concentrate

colloids from their solvent has direct applications in recovery of high value synthetic products or for catalytic nanoparticles.



Scheme 1.3 Reversible transformation of *trans*-AZOT-S4 to *cis*-AZOT-S4 using UV and visible light.

1.5.5 Photosurfactants and LLC Phases

While "regular" surfactants are well-known to self-assemble into a variety of thermodynamically stable 2D or 3D lyotropic liquid crystalline phases at concentrations well above the *cmc*, reports for the formation of extended LLC phases in pure PS systems are extremely rare.[86, 87, 109] PS systems which form LLC phases would theoretically have the combined ability to template inorganic sol-gel matrixes and change their shape upon irradiation with light.

Hughes *et al.* were the first to design azobenzene-containing PS capable of forming LLC phases.[87, 109] Two photoresponsive amphiphiles having comparable structures were designed and synthesised consisting of hydrophilic oligooxytheylene units (E), hydrophobic alkyl chains (C) and a light-sensitive azobenzene moiety ($C_{4+n}AzoC_mE_7$, where n = 0, m = 5 or n = 5, m = 0).[87] A combination of differential scanning calorimetry (DSC), POM, SAXS and rheology studies were used to show that the nature of the LLC phases formed could be controlled by varying the position of the azobenzene moiety within the hydrophobic tail (Figure 1.14). Furthermore, *trans-cis* photoisomerisation of the PS with the azobenzene group localised in the middle of the alkyl chain induced significant changes in the self-assembled structure and its bulk properties. In contrast, when the azobenzene unit was directly attached to the hydrophilic domain there were no observable changes in the self-assembled structure upon photoisomerisation. This study demonstrates that the self-assembly and photoresponsive behaviour of photosensitive amphiphiles is extremely sensitive to the position of the photoactive moiety within the surfactants molecular structure.

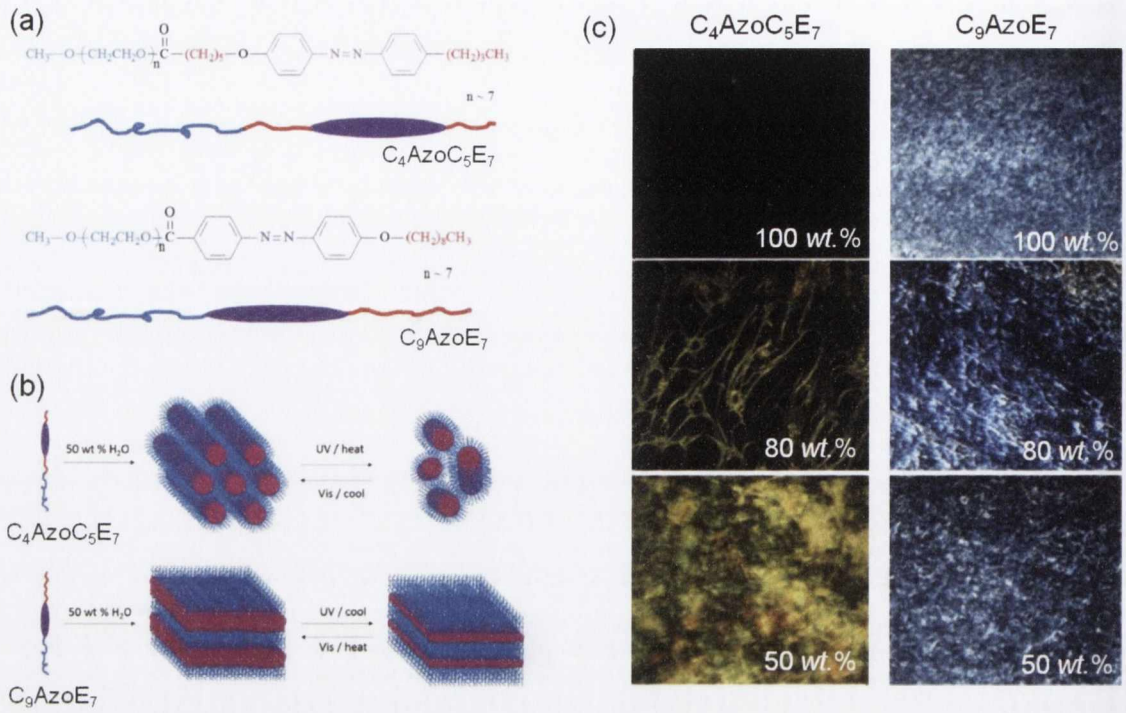


Figure 1.14 The effect of photoisomerisation and concentration on the LLC phases formed from azo-surfactants. (a) Chemical structures and molecular schematics of the azo-surfactants $C_4AzoC_5E_7$ and C_9AzoE_7, with varying positions of azobenzene moiety. (b) Schematic illustrations of the different phase behaviours and stimulus-response of azo-surfactants $C_4AzoC_5E_7$ and C_9AzoE_7 at 50 *wt.*% H_2O content. (c) Polarised optical micrographs of the azo-surfactant-water binary systems at room temperature. Adapted from Reference 87.

Recently, Tschierske *et al.* prepared a series of azobenzene surfactants with three alkyl chains, and hydrophilic groups with or without oligooxyethylene, and hydroxyl or racemic 3-glycerol units as the hydrophilic head-groups ($C_3AzoE_m(OH)_n$, where $m = 3$, $n = 2$ or $m = 3$, $n = 1$ or $m = 0$, $n = 2$).[86] Although this study primarily focused on the formation of thermotropic liquid crystals at high temperatures (greater than 100 °C), they also found that the photosurfactant with the largest polar group ($C_3AzoE_3(OH)_2$) formed a hexagonal phase in water. In contrast, $C_3Azo(OH)_2$ formed a lamellar phase, while the only surfactant not to bear a racemic 3-gylcerol unit, C_3AzoE_3OH, was isotropic. The formation of LLC phases by two of the PS was attributed to the strong hydrogen bonds between the glycerol units. The additional hydrogen bonding acceptor sites along the EO chains were thought to stabilise the higher interfacial curvature of $C_3AzoE_3(OH)_2$. Unfortunately, the effect of photoisomerisation on the LLC phases formed was not investigated in this study.

1.5.6 Applications of Photosurfactants

PS or 'photofoamers' have previously been used to destabilise foams without the necessity of antifoaming agents or using surfactants which are extremely sensitive to temperature.[110] For example, Chevallier *et al.* proposed that the air-water interface of their PS bubbles consisted of the packed *trans*-isomers of the azobenzene trimethylammonium bromide surfactant (*trans*-AzoTMA).

After photoisomerisation with UV light (λ_{ex} = 365 nm) to the *cis*-isomers, the molecules desorbed from the air-water interface due to unfavourable packing. In return, this destabilised the bubble by driving the flow of molecules from the interface. It is thought this approach could be useful for applications such as flotation to collect minerals.[111]

PS have also been developed as vesicles for drug delivery. In 1980, Kano *et al.* incorporated the azobenzene containing surfactants (C2Azo and C4Azo) into dipalmitoylphosphatidylcholine (DPPC) vesicles at various molar ratios.[112] They encapsulated bromothymol blue into the phospholipid bilayer and found that upon illumination with UV light the aggregates formed a *cis*-rich system which resulted in greater leakage of the dye. This opened up a range of targeted drug delivery systems based on simple illumination. For example Patnaik *et al.* produced azo-dextrin-based nanogels in which linear dextran moieties were functionalised with a hydrophobic derivative of azobenzene.[113] These materials self-assembled into nanostructures which could encapsulate model dyes and drugs. Under irradiation with UV light (λ_{ex} = 365 nm), the azobenzene moieties in the nanogels underwent photoisomerisation which lead to the disruption of the stacking and release of the contents. The extent of content release was found to be directly proportional to the irradiation time over 0-300 min.

1.6 Aims of Thesis

The first part of this thesis will examine the self-assembly of fluorescent conjugated polyelectrolytes in different local environments in an effort to optimise their facility as electron transport interlayers in organic photovoltaics and for use as biological sensors.

Chapters 4 and 5 will exploit the solvent- and surfactant-mediated assembly of homo- and diblock-poly(thiophene)s for the purpose of devising new electron transport interlayer materials targeting efficient OPV devices. In Chapter 4 the optical properties, solution-state structures and thin film morphologies of a family of amphiphilic diblock poly(thiophene)s will be investigated as a function of solvent polarity. Following this, in Chapter 5 oppositely-charged surfactants will be used to form self-assembled electrostatic complexes with one of the diblock poly(thiophene)s. To elucidate the role of the neutral block on the organisation of the diblock copolymer assembly, a direct comparison study will be performed with the analogous homopolyelectrolyte. Finally in this chapter preliminary studies will probe whether the CPE-surfactant aggregates can perform as interfacial modifiers between the active layer and cathode of an OPV device, to improve the overall efficiency of the cell.

Polyoxometalates (POMs) are anionic metal-oxide clusters which are frequently used as components in organic-inorganic hybrid materials such as OPV devices due to their rich redox activity, charge transport properties and photoactivity. A proof-of-concept study will be performed in Chapter 6 to determine whether hybrid materials of CPE-POM can be formed by electrostatic co-assembly. The aim is to determine the effect of the CPE structure (number of repeat units, distribution of side-groups) on the structure of the self-assembled aggregates formed.

As discussed previously, CPEs are also attractive materials for imaging and sensing in model and live cell membranes. However, their sensitivity is often critically dependant on their localisation within the cell membrane bilayer. The co-assembly of a series of CPEs bearing cationic, anionic and zwitterionic pendant side-groups with model zwitterionic cell membranes will be investigated in Chapter 7. The first part of this work will determine the effect of membrane fluidity on the fluorescence of the CPE; this will then be correlated to the proposed self-assembly mechanism of each CPE with the zwitterionic vesicle.

The final part of this thesis aims to rationally design photoresponsive surfactants, which will self-organise into desirable patterns that can be controlled by light. In Chapter 8, the synthesis of a family of known and novel photosurfactants will be described. A structure-activity study will then be undertaken to identify the key structural features required to unlock desirable lyotropic liquid crystalline phases. Finally, Chapter 9 looks to summarise the main findings of this thesis and provide an outlook for further studies arising from this work. To provide greater understanding of the background to some of the techniques used and of the nature of the experiments undertaken within this thesis, a brief account of the theoretical and experimental details will precede these results chapters in Chapter 2 and 3, respectively.

1.7 References

1. G. M. Whitesides and B. Grzybowski, *Science*, 2002, **295**, 2418-2421.
2. H. Zheng, Y. Zheng, N. Liu, N. Ai, Q. Wang, S. Wu, J. Zhou, D. Hu, S. Yu, S. Han, W. Xu, C. Luo, Y. Meng, Z. Jiang, Y. Chen, D. Li, F. Huang, J. Wang, J. Peng and Y. Cao, *Nat. Commun.*, 2013, **4**.
3. J. H. Burroughes, D. D. C. Bradley, A. R. Brown, R. N. Marks, K. Mackay, R. H. Friend, P. L. Burns and A. B. Holmes, *Nature*, 1990, **347**, 539-541.
4. J.-H. Kim, S. Wood, J. B. Park, J. Wade, M. Song, S. C. Yoon, I. H. Jung, J.-S. Kim and D.-H. Hwang, *Adv. Funct. Mater.*, 2016, **26**, 1517-1525.
5. N. Zhou, A. S. Dudnik, T. I. N. G. Li, E. F. Manley, T. J. Aldrich, P. Guo, H.-C. Liao, Z. Chen, L. X. Chen, R. P. H. Chang, A. Facchetti, M. Olvera de la Cruz and T. J. Marks, *J. Am. Chem. Soc.*, 2016, **138**, 1240-1251.
6. M. Li, C. An, T. Marszalek, M. Baumgarten, K. Müllen and W. Pisula, *Adv. Mater.*, 2016, **28**, 2245-2252.
7. K. J. Fallon, N. Wijeyasinghe, N. Yaacobi-Gross, R. S. Ashraf, D. M. E. Freeman, R. G. Palgrave, M. Al-Hashimi, T. J. Marks, I. McCulloch, T. D. Anthopoulos and H. Bronstein, *Macromolecules*, 2015, **48**, 5148-5154.
8. S. Rochat and T. M. Swager, *ACS Appl. Mater. Interfaces*, 2013, **5**, 4488-4502.
9. P. S. Heeger and A. J. Heeger, *Proc. Nat. Acad. Sci.*, 1999, **96**, 12219-12221.
10. R. C. Evans, M. Knaapila, N. Willis-Fox, M. Kraft, A. Terry, H. D. Burrows and U. Scherf, *Langmuir*, 2012, **28**, 12348-12356.
11. Z. Kahveci, M. J. Martínez-Tomé, R. Mallavia and C. R. Mateo, *Biomacromolecules*, 2013, **14**, 1990-1998.
12. M. Ballauff, *Angew. Chem. Int. Ed.*, 1989, **28**, 253-267.
13. H. Jiang, P. Taranekar, J. R. Reynolds and K. S. Schanze, *Angew. Chem. Int. Ed.*, 2009, **48**, 4300-4316.

14. C. Tan, E. Atas, J. G. Müller, M. R. Pinto, V. D. Kleiman and K. S. Schanze, *J. Am. Chem. Soc.*, 2004, **126**, 13685-13694.
15. C. Tan, M. R. Pinto and K. S. Schanze, *Chem. Commun.*, 2002, 446-447.
16. T.-Q. Nguyen, I. B. Martini, J. Liu and B. J. Schwartz, *J. Phys. Chem. B*, 1999, **104**, 237-255.
17. A. Gutacker, S. Adamczyk, A. Helfer, L. E. Garner, R. C. Evans, S. M. Fonseca, M. Knaapila, G. C. Bazan, H. D. Burrows and U. Scherf, *J. Mater. Chem.*, 2010, **20**, 1423-1430.
18. M. He, W. Han, J. Ge, Y. Yang, F. Qiu and Z. Lin, *Energy Environ. Sci.*, 2011, **4**, 2894-2902.
19. B. Nandan and A. Horechyy, *ACS Appl. Mater. Interfaces*, 2015, **7**, 12539-12558.
20. L. Ying, P. Zalar, S. D. Collins, Z. Chen, A. A. Mikhailovsky, T.-Q. Nguyen and G. C. Bazan, *Adv. Mater.*, 2012, **24**, 6496-6501.
21. Y. Mai and A. Eisenberg, *Chem. Soc. Rev.*, 2012, **41**, 5969-5985.
22. H. D. Burrows, V. M. M. Lobo, J. Pina, M. L. Ramos, M. J. S. de, A. J. M. Valente, M. J. Tapia, S. Pradhan and U. Scherf, *Macromolecules*, 2004, **37**, 7425-7427.
23. H. D. Burrows, S. M. Fonseca, C. L. Silva, A. A. C. C. Pais, M. J. Tapia, S. Pradhan and U. Scherf, *Phys. Chem. Chem. Phys.*, 2008, **10**, 4420-4428.
24. Y.-M. Chang, R. Zhu, E. Richard, C.-C. Chen, G. Li and Y. Yang, *Adv. Funct. Mater.*, 2012, **22**, 3284-3289.
25. R. C. Evans, *J. Mater. Chem. C*, 2013, **1**, 4190-4200.
26. T. Costa, L. E. Garner, M. Knaapila, A. W. Thomas, S. E. Rogers, G. C. Bazan and H. D. Burrows, *Langmuir*, 2013, **29**, 10047-10058.
27. T. Costa, D. de Azevedo, B. Stewart, M. Knaapila, A. J. M. Valente, M. Kraft, U. Scherf and H. D. Burrows, *Polym. Chem.*, 2015, **6**, 8036-8046.
28. M. Knaapila, R. C. Evans, V. M. Garamus, L. Almásy, N. K. Székely, A. Gutacker, U. Scherf and H. D. Burrows, *Langmuir*, 2010, **26**, 15634-15643.
29. B. Kippelen and J.-L. Bredas, *Energy Environ. Sci.*, 2009, **2**, 251-261.
30. G. Luo, X. Ren, S. Zhang, H. Wu, W. C. H. Choy, Z. He and Y. Cao, *Small*, 2016, **12**, 1547-1571.
31. M. Theander, O. Inganäs, W. Mammo, T. Olinga, M. Svensson and M. R. Andersson, *J. Phys. Chem. B*, 1999, **103**, 7771-7780.
32. A. Facchetti, *Mater. Today*, 2013, **16**, 123-132.
33. R. A. J. Janssen and J. Nelson, *Adv. Mater.*, 2013, **25**, 1847-1858.
34. C.-C. Chen, W.-H. Chang, K. Yoshimura, K. Ohya, J. You, J. Gao, Z. Hong and Y. Yang, *Adv. Mater.*, 2014, **26**, 5670-5677.
35. H. Zhou, Y. Zhang, C.-K. Mai, S. D. Collins, G. C. Bazan, T.-Q. Nguyen and A. J. Heeger, *Adv. Mater.*, 2015, **27**, 1767-1773.
36. M. Steiner, G. Siefer, T. Schmidt, M. Wiesenfarth, F. Dimroth and A. W. Bett, *IEEE J. Photovolt.*, 2016, **6**, 1020-1024.
37. C. W. Tang, *Appl. Phys. Lett.*, 1986, **48**, 183-185.
38. A. Haugeneder, M. Neges, C. Kallinger, W. Spirkl, U. Lemmer, J. Feldmann, U. Scherf, E. Harth, A. Gügel and K. Müllen, *Phys. Rev. B*, 1999, **59**, 15346-15351.
39. G. Yu, J. Gao, J. C. Hummelen, F. Wudl and A. J. Heeger, *Science*, 1995, **270**, 1789-1791.
40. N. S. Sariciftci, L. Smilowitz, A. J. Heeger and F. Wudl, *Science*, 1992, **258**, 1474-1476.
41. M. T. Dang, L. Hirsch, G. Wantz and J. D. Wuest, *Chem. Rev.*, 2013, **113**, 3734-3765.
42. G. Dennler, M. C. Scharber and C. J. Brabec, *Adv. Mater.*, 2009, **21**, 1323-1338.
43. Y. Huang, E. J. Kramer, A. J. Heeger and G. C. Bazan, *Chem. Rev.*, 2014, **114**, 7006-7043.
44. X. Gong, *Polymer*, 2012, **53**, 5437-5448.

45. V. I. Madogni, B. Kounouhéwa, A. Akpo, M. Agbomahéna, S. A. Hounkpatin and C. N. Awanou, *Chem. Phys. Lett.*, 2015, **640**, 201-214.
46. Z. He, C. Zhong, S. Su, M. Xu, H. Wu and Y. Cao, *Nat. Photon*, 2012, **6**, 591-595.
47. H. Bin, Z.-G. Zhang, L. Gao, S. Chen, L. Zhong, L. Xue, C. Yang and Y. Li, *J. Am. Chem. Soc.*, 2016, **138**, 4657-4664.
48. R. Noriega, J. Rivnay, K. Vandewal, F. P. V. Koch, N. Stingelin, P. Smith, M. F. Toney and A. Salleo, *Nat. Mater.*, 2013, **12**, 1038-1044.
49. L. Zeng, C. W. Tang and S. H. Chen, *Appl. Phys. Lett.*, 2010, **97**, 053305.
50. M. He, M. Wang, C. Lin and Z. Lin, *Nanoscale*, 2014, **6**, 3984-3994.
51. M. O. Reese, M. S. White, G. Rumbles, D. S. Ginley and S. E. Shaheen, *Appl. Phys. Lett.*, 2008, **92**, 053307.
52. H. Ju, K. M. Knesting, W. Zhang, X. Pan, C.-H. Wang, Y.-W. Yang, D. S. Ginger and J. Zhu, *ACS Appl. Mater. Interfaces*, 2016, **8**, 2125-2131.
53. M. Gao, J. Subbiah, P. B. Geraghty, M. Chen, B. Purushothaman, X. Chen, T. Qin, D. Vak, F. H. Scholes, S. E. Watkins, M. Skidmore, G. J. Wilson, A. B. Holmes, D. J. Jones and W. W. H. Wong, *Chem. Mater.*, 2016, **28**, 3481-3487.
54. G. Li, C.-W. Chu, V. Shrotriya, J. Huang and Y. Yang, *Appl. Phys. Lett.*, 2006, **88**, 253503.
55. C.-Z. Li, C.-C. Chueh, H.-L. Yip, K. M. O'Malley, W.-C. Chen and A. K. Y. Jen, *J. Mater. Chem.*, 2012, **22**, 8574-8578.
56. J. Kesters, T. Ghoos, H. Penxten, J. Drijkoningen, T. Vangerven, D. M. Lyons, B. Verreet, T. Aernouts, L. Lutsen, D. Vanderzande, J. Manca and W. Maes, *Adv. Energy Mater.*, 2013, **3**, 1180-1185.
57. J. H. Seo, A. Gutacker, Y. Sun, H. Wu, F. Huang, Y. Cao, U. Scherf, A. J. Heeger and G. C. Bazan, *J. Am. Chem. Soc.*, 2011, **133**, 8416-8419.
58. Z. Sun, K. Xiao, J. K. Keum, X. Yu, K. Hong, J. Browning, I. N. Ivanov, J. Chen, J. Alonzo, D. Li, B. G. Sumpter, E. A. Payzant, C. M. Rouleau and D. B. Geohegan, *Adv. Mater.*, 2011, **23**, 5529-5535.
59. B. Cao, X. He, C. R. Fetterly, B. C. Olsen, E. J. Luber and J. M. Buriak, *ACS Appl. Mater. Interfaces*, 2016, **8**, 18238-18248.
60. B. Xiao, H. Wu and Y. Cao, *Mater. Today*, 2015, **18**, 385-394.
61. H. Choi, J. S. Park, E. Jeong, G.-H. Kim, B. R. Lee, S. O. Kim, M. H. Song, H. Y. Woo and J. Y. Kim, *Adv. Mater.*, 2011, **23**, 2759-2763.
62. C. He, C. Zhong, H. Wu, R. Yang, W. Yang, F. Huang, G. C. Bazan and Y. Cao, *J. Mater. Chem.*, 2010, **20**, 2617-2622.
63. S. Chen, J. R. Manders, S.-W. Tsang and F. So, *J. Mater. Chem.*, 2012, **22**, 24202-24212.
64. G. Heimel, I. Salzmann, S. Duhm, J. P. Rabe and N. Koch, *Adv. Funct. Mater.*, 2009, **19**, 3874-3879.
65. M. Gaceur, S. B. Dkhil, D. Duché, F. Bencheikh, J.-J. Simon, L. Escoubas, M. Mansour, A. Guerrero, G. Garcia-Belmonte, X. Liu, M. Fahlman, W. Dachraoui, A. K. Diallo, C. Videlot-Ackermann, O. Margeat and J. Ackermann, *Adv. Funct. Mater.*, 2016, **26**, 243-253.
66. S. Seethamraju, P. C. Ramamurthy and G. Madras, *Phys. Chem. Chem. Phys.*, 2015, **17**, 23165-23172.
67. V. C. Tung, J. Kim, L. J. Cote and J. Huang, *J. Am. Chem. Soc.*, 2011, **133**, 9262-9265.
68. H. Liu, L. Hu, F. Wu, L. Chen and Y. Chen, *ACS Appl. Mater. Interfaces*, 2016, **8**, 9821-9828.

69. J. Kesters, S. Govaerts, G. Pirotte, J. Drijkoningen, M. Chevrier, N. Van den Brande, X. Liu, M. Fahlman, B. Van Mele, L. Lutsen, D. Vanderzande, J. Manca, S. Clément, E. Von Hauff and W. Maes, *ACS Appl. Mater. Interfaces*, 2016, **8**, 6309-6314.
70. T. Yamamoto, D. Komarudin, M. Arai, B.-L. Lee, H. Suganuma, N. Asakawa, Y. Inoue, K. Kubota, S. Sasaki, T. Fukuda and H. Matsuda, *J. Am. Chem. Soc.*, 1998, **120**, 2047-2058.
71. S.-H. Oh, S.-I. Na, J. Jo, B. Lim, D. Vak and D.-Y. Kim, *Adv. Funct. Mater.*, 2010, **20**, 1977-1983.
72. S. M. Fonseca, R. P. Galvão, H. D. Burrows, A. Gutacker, U. Scherf and G. C. Bazan, *Macromol. Rapid Commun.*, 2013, **34**, 717-722.
73. S. Chemburu, E. Ji, Y. Casana, Y. Wu, T. Buranda, K. S. Schanze, G. P. Lopez and D. G. Whitten, *J. Phys. Chem. B*, 2008, **112**, 14492-14499.
74. M. R. Pinto and K. S. Schanze, *Proc. Nat. Acad. Sci.*, 2004, **101**, 7505-7510.
75. J. W. Hong, W. L. Hemme, G. E. Keller, M. T. Rinke and G. C. Bazan, *Adv. Mater.*, 2006, **18**, 878-882.
76. N. Anwar, A. Rix, W. Lederle and A. J. C. Kuehne, *Chem. Commun.*, 2015, **51**, 9358-9361.
77. L. E. Edens, Y. Wang, D. G. Whitten and D. J. Keller, *Langmuir*, 2014, **30**, 10691−10697.
78. L. Ding, E. Y. Chi, S. Chemburu, E. Ji, K. S. Schanze, G. P. Lopez and D. G. Whitten, *Langmuir*, 2009, **25**, 13742-13751.
79. P. Karam, A. A. Hariri, C. F. Calver, X. Zhao, K. S. Schanze and G. Cosa, *Langmuir*, 2014, **30**, 10704-10711.
80. Y. Wang, E. M. Jones, Y. Tang, E. Ji, G. P. Lopez, E. Y. Chi, K. S. Schanze and D. G. Whitten, *Langmuir*, 2011, **27**, 10770-10775.
81. Y. S. Lee, *Self-Assembly and Nanotechnology: A Force Balance Approach* John Whiley & Sons, Inc., Hoboke, New Jersey, 2008.
82. O. G. Us'yarov, *Colloid J.*, 2007, **69**, 95-102.
83. J. N. Israelachvili, D. J. Mitchell and B. W. Ninham, *J. Chem. Soc., Faraday Trans.*, 1976, **72**, 1525-1568.
84. L. S. Hirst, *Fundamentals of Soft Matter Science* CRC Press, Taylor and Francis Group, Boca Raton, U.S.A., 2013, pp. 71-96.
85. T. Inoue, B. Dong and L.-Q. Zheng, *J. Colloid Interface Sci.*, 2007, **307**, 578-581.
86. X. Tan, R. Zhang, C. Guo, X. Cheng, H. Gao, F. Liu, J. R. Bruckner, F. Giesselmann, M. Prehm and C. Tschierske, *J. Mater. Chem. C*, 2015, **3**, 11202-11211.
87. S. Peng, Q. Guo, P. G. Hartley and T. C. Hughes, *J. Mater. Chem. C*, 2014, **2**, 8303-8312.
88. Y. Zhou, J. H. Schattka and M. Antonietti, *Nano Lett.*, 2004, **4**, 477-481.
89. S. Kirmayer, S. Neyshtadt, A. Keller, D. Okopnik and G. L. Frey, *Chem. Mater.*, 2009, **21**, 4387-4396.
90. S. Besson, T. Gacoin, C. Ricolleau, C. Jacquiod and J.-P. Boilot, *J. Mater. Chem.*, 2003, **13**, 404-409.
91. M. Etienne and A. Walcarius, *Electrochem. Commun.*, 2005, **7**, 1449-1456.
92. S. Neyshtadt, M. Kalina and G. L. Frey, *Adv. Mater.*, 2008, **20**, 2541-2546.
93. D. Bernsmeier, E. Ortel, J. Polte, B. Eckhardt, S. Nowag, R. Haag and R. Kraehnert, *J. Mater. Chem. A*, 2014, **2**, 13075-13082.
94. M. Wu, Q. Meng, Y. Chen, Y. Du, L. Zhang, Y. Li, L. Zhang and J. Shi, *Adv. Mater.*, 2015, **27**, 215-222.
95. Y. Lu, R. Ganguli, C. A. Drewien, M. T. Anderson, C. J. Brinker, W. Gong, Y. Guo, H. Soyez, B. Dunn, M. H. Huang and J. I. Zink, *Nature*, 1997, **389**, 364-368.
96. C. J. Brinker, Y. Lu, A. Sellinger and H. Fan, *Adv. Mater.*, 1999, **11**, 579-585.

97. R. F. Tabor, M. J. Pottage, C. J. Garvey and B. L. Wilkinson, *Chem. Commun.*, 2015, **51**, 5509-5512.
98. R. Lund, G. Brun, E. Chevallier, T. Narayanan and C. Tribet, *Langmuir*, 2016, **32**, 2539-2548.
99. Y. Wei, S. Han, J. Kim, S. Soh and B. A. Grzybowski, *J. Am. Chem. Soc.*, 2010, **132**, 11018-11020.
100. Y. Wang, P. Han, H. Xu, Z. Wang, X. Zhang and A. V. Kabanov, *Langmuir*, 2010, **26**, 709-715.
101. A. Venancio-Marques, F. Barbaud and D. Baigl, *J. Am. Chem. Soc.*, 2013, **135**, 3218-3223.
102. K. G. Yager and C. J. Barrett, *J. Photochem. Photobiol. A*, 2006, **182**, 250-261.
103. G. S. Hartley and R. J. W. Le Fevre, *J. Chem. Soc.*,1939, 531-535.
104. T. Shang, K. A. Smith and T. A. Hatton, *Langmuir*, 2006, **22**, 1436-1442.
105. T. Shang, K. A. Smith and T. A. Hatton, *Langmuir*, 2003, **19**, 10764-10773.
106. C. T. Lee, K. A. Smith and T. A. Hatton, *Macromolecules*, 2004, **37**, 5397-5405.
107. M. Bonini, D. Berti, J. M. Di Meglio, M. Almgren, J. Teixeira and P. Baglioni, *Soft Matter*, 2005, **1**, 444-454.
108. R. F. Tabor, R. J. Oakley, J. Eastoe, C. F. J. Faul, I. Grillo and R. K. Heenan, *Soft Matter*, 2009, **5**, 78-80.
109. R. Yang, S. Peng, W. Wan and T. C. Hughes, *J. Mater. Chem. C*, 2014, **2**, 9122-9131.
110. E. Chevallier, C. Monteux, F. Lequeux and C. Tribet, *Langmuir*, 2012, **28**, 2308-2312.
111. P. U. Müller, C. C. Akpo, K. W. Stöckelhuber and E. Weber, *Adv. Colloid Interface Sci.*, 2005, **114–115**, 291-302.
112. K. Kano, Y. Tanaka, T. Ogawa, M. Shimomura, Y. Okahata and T. Kunitake, *Chem. Lett.*, 1980, **9**, 421-424.
113. S. Patnaik, A. K. Sharma, B. S. Garg, R. P. Gandhi and K. C. Gupta, *Int. J. Pharm.*, 2007, **342**, 184-193.

Chapter 2

Theory

2.1 The Interaction of Light with Matter

2.1.1 Properties of Light

Light is only a small fraction of the total energy emitted by the sun. Visible light is a form of electromagnetic radiation and represents only the very narrow group of wavelengths between 380 and 730 nm. In spectroscopy, atoms or molecules absorb, scatter or emit electromagnetic radiation revealing information about the different energy levels therein. The energy levels in atoms and molecules are *quantised* and the separation between energy levels carries information on the electronic structure of the atom or molecule. The specific nature of how radiation interacts with matter is dependent on its wavelength/frequency. For example, within molecules rotational transitions are probed using microwaves ($3 \times 10^6 - 3 \times 10^8$ nm), vibrational transitions are probed with infrared radiation (700 nm – 1 mm) and electronic transitions using visible and ultraviolet light (100 – 730 nm).

Electromagnetic energy exists as discrete/quantised bundles called *photons*. Photons can be absorbed or emitted by a molecule if the energy matches the separation between energy levels in an atom or molecule. In quantum mechanics, the interaction of photons, and any other quantum-mechanical particle, such as an electron, proton or neutron, can be described by considering both their particle-like and wave-like nature. The intrinsic relationship between these two interpretations is shown empirically by the *de Broglie equation*:

$$\lambda = \frac{h}{p} \tag{2.1}$$

This relates the wavelength (λ) of the particle (*wave-like* nature) to its linear momentum (p) (*particle-like* nature) by Planck's constant (h), $h = 6.626 \times 10^{-34}$ J s. Consequently, as each individual photon carries momentum and is always in motion, and since they are travelling at the speed of light in a vacuum (c), $c = 2.997 \times 10^8$ m s^{-1}, the photons have relativistic energy. Energy (E) is related to λ and frequency (v) through Planck's equation:

$$E = h\nu = \frac{hc}{\lambda} \tag{2.2}$$

2.1.2 Formation of Excited States

The formation of the excited state can occur upon absorption of a photon. For a molecule to absorb (or indeed emit) a photon of frequency v, it must possess a dipole oscillating at that frequency. This may be a permanent dipole (for rotational transitions) or transiently-induced dipole created by the oscillating electromagnetic field (for vibrational transitions). In quantum mechanical terms, the transition dipole moment ($M_{1,2}$) describes the transition from state 1 to state 2, where $E_2 > E_1$. $M_{1,2}$ is described by the integral:

$$M_{1,2} = \int \psi_1 \, \hat{\mu} \, \psi_2 \, d\tau \tag{2.3}$$

where Ψ_1 and Ψ_2 are the time-dependant wavefunctions for the electronic ground and excited states, 1 and 2, respectively, and $\hat{\mu}$ is the electric dipole moment operator. As $\hat{\mu}$ is a vector, $M_{1,2}$ needs to be calculated over each axis component (*i.e.* x, y, z) individually, and only one of these needs to be non-zero for a transition to occur. The magnitude of the transition dipole can be regarded as a measure of the charge distribution that accompanies a transition. Therefore, the magnitude of the transition moment is a measure of the amplitude or the intensity of the transition. A transition between states, *e.g.* E_1 and E_2, is only allowed if the amplitude of the transition moment, along at least one of the axes, is non-zero, *i.e.* a transition will only occur if the transition causes a (dipolar) redistribution of charge within the molecule. The probability of a transition occurring is given by the square of the transition dipole moment, $|M_{1,2}|^2$.

2.1.3 Classification of Electronic States

It is sensible at this point to briefly discuss the nomenclature of the electronic states. Singlet (S_n) and triplet (T_n) states are derived using the equation for multiplicity, $2S+1$, where S is the total spin angular momentum ($S = \Sigma s_i$, where the spin angular momentum, s_i, = ±½).[1] Individual spins are denoted as spin up (s = +½) or spin down (s = -½). The spin multiplicity for a ground or excited singlet state is 1 as $S = 0$. In contrast, the spin multiplicity for a ground or excited triplet state is 3, as $S = 1$. The difference between the electron spins of ground- and excited- singlet and triplet states is shown in Figure 2.1. According to Hund's Rule, the triplet state has a lower energy than that of the singlet state of the same configuration.[1]

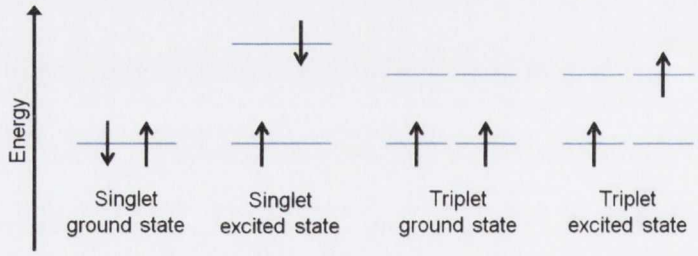


Figure 2.1 Schematic representation of the relative energy levels and the spin configurations of the ground- and excited- singlet and triplet states.

2.1.4 Selection Rules for Absorption

There are two major rules that govern the excitation and relaxation of electronic states in polyatomic organic molecules, which describes the probability of a transition from one state to another. In quantum mechanics, these rules originate from the condition that for a transition to occur the transition dipole moment needs to be non-zero.

(i) *Spin selection rule*: A transition between states of different multiplicities is forbidden as there can be no change in angular momentum for transitions between "pure" states.[2] This means that transitions between singlet and triplet states are formally forbidden ($\Delta S = 0$). However, it is possible for coupling to occur to between the orbital magnetic moment and the spin magnetic moment, which is known as *spin-orbit coupling*. As a result, a singlet (or

triplet) wavefunction always contains a small fraction of the triplet (or singlet) wavefunction. This will allow for a small, yet significant, transition between two states of different multiplicity.

(ii) *Laporte selection rule*: An electronic transition in a polyatomic organic species, such as the conjugated polymers discussed here, can be forbidden for symmetry reasons. Only transitions between states of different parity are allowed, *i.e.* where there is a difference in the symmetry of the wavefunctions involved.[2] For single atoms this means that s → s transitions are forbidden, while s → p transitions are allowed ($\Delta l = \pm 1$, where l is the orbital angular momentum quantum number). The symmetry of larger polyatomic species such as CPs can be related to the symmetry of particular point groups but is beyond the scope of this work. However, it should be noted that this rule only holds for rigid species, while most species undergo vibrational transitions which are enough to disturb the local symmetry. This can distort the molecular structures enough to allow for the transitions to occur which would otherwise be formally forbidden. However, such a transition would have significantly weaker oscillator strength corresponding to a weaker absorbance or emission intensity.

2.1.5 Optical Transitions – The Franck-Condon Principle

The Born-Oppenheimer approximation states that electrons move much faster than the nucleus, with the process of absorption taking ~10^{-15} s and molecular vibrations taking ~10^{-10} to 10^{-12} s.[1] Therefore, it is possible to separate a wavefunction into its electronic, vibrational and rotational components. This observation is the basis of the Franck-Condon principle: an electronic transition is most likely to occur at fixed nuclear coordinates as electronic transitions occur much faster than nuclear motion. Thus, on a potential energy diagram, as shown in Figure 2.2, an electronic transition can be represented by a vertical line between the initial and final states, which are each composed of vibrational wavefunctions. Furthermore, the amplitude of the vibrational wavefunction is directly proportional to the probability of finding the nuclei at a particular internuclear distance, r. According to the Boltzmann distribution, most of the molecules are in the lowest vibrational level of the ground state. A transition to a specific vibrational level is more likely if there is significant overlap between the vibrational wavefunction in the initial state and the vibrational wavefunction of the final state whose amplitude is at a maximum at this internuclear distance (Figure 2.2). For example, the most probable transition in Figure 2.2b is from $v = 0$ (S_0) to $v = 3$ (S_1). Furthermore, the intensity of a vibronic transition is proportional to the square of the overlap integral between the vibrational wavefunctions involved in the transition. As the overlap of the wavefunctions decreases, the transitions become less intense. The wavefunctions for the ground and excited state consist of a nuclear and vibronic component. The transition dipole moment is partly determined by the overlap of the nuclear (vibrational) wavefunctions, known as the Franck-

Condon factor. The Franck-Condon principle can be used to predict the relative probabilities of different vibronic transitions occurring.

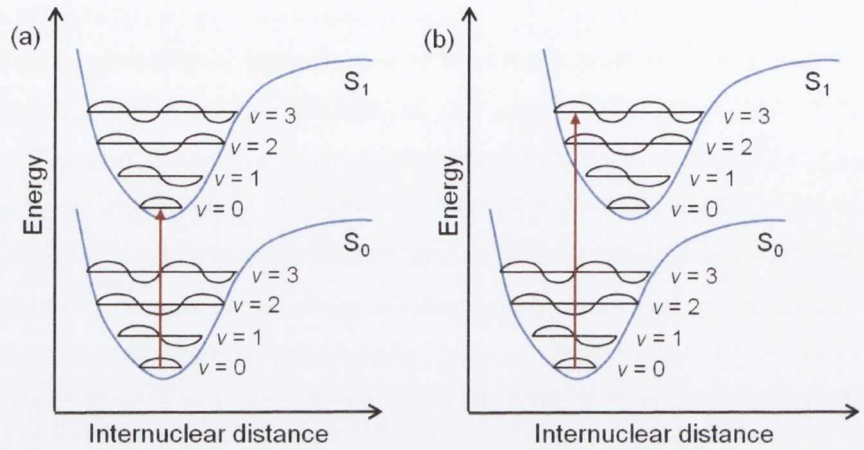


Figure 2.2 Potential energy diagrams showing the basis of the Franck-Condon principle. The vertical arrows represent the most probable transitions between nuclei in (a) the same and (b) different nuclear configurations.

For polyatomic molecules, where numerous transitions take place over a range of energies, the transitions merge to give an absorption spectrum whose shape is determined by the relative intensities of all the transitions. For some rigid aromatic hydrocarbons, such as naphthalene or anthracene, distinct vibrational bands can be resolved in the absorption spectrum. The energy spacing between the vibrational levels combined with the Franck-Condon factors determine the relative intensities of these vibronic bands. However, it should be noted that most fluorescent molecules exhibit broad or structureless absorption bands, as a consequence of two effects: homogeneous and inhomogeneous broadening. Homogeneous broadening arises from the existence of a continuous set of vibrational levels within each electronic state ($v = 0$, $v = 1$, $v = 2$, *etc.*). Inhomogeneous broadening results from changes in the structure of the solvent sheet surrounding the molecule. The distribution of solute-solvent configurations which causes variations in the local electric field of each molecule, leads to a slight distribution of energies of the electronic transitions. These broadening effects also apply to emission bands in the PL spectra. A combination of these two effects can cause the absorption spectra of moderately large and rigid fluorophores in solution to be almost structureless at room temperature.

2.1.6 Beer-Lambert Law

The efficiency of light absorption by an absorbing medium can be measured quantitatively by application of the Beer-Lambert Law:[3]

$$A(\lambda) = \log_{10}\left(\frac{I_0}{I_t}\right) = \varepsilon(\lambda)lc \tag{2.4}$$

where $A(\lambda)$ is the absorbance at wavelength, λ, I_0 is the initial irradiation intensity, I_t is the transmitted intensity, $\varepsilon(\lambda)$ is the molar absorption coefficient at λ, l is the path length of the cell

used in the experiment (usually 1 cm) and c is the concentration of the absorbing material. $\varepsilon(\lambda)$ is a measure of the probability of the electronic transition occurring, whereby a large $\varepsilon(\lambda)$ equates to a high probability of a transition occurring at that wavelength. According to the Beer-Lambert Law, an absorbing species should display a linear relationship between the concentration of the species and the absorbance. Deviations from linearity can often be an indication of aggregate formation at high concentrations or due to the presence of additional absorbing species.[1]

2.1.7 Deactivation of Excited States

Following the absorption of light, a molecule in the excited state relaxes back to the ground state through a combination of radiative and non-radiative processes. For organic molecules, the transitions and processes occurring upon absorption of a photon and the subsequent deactivation pathways of the excited states formed are often illustrated using a *Jablonski diagram* (Figure 2.3).[4]

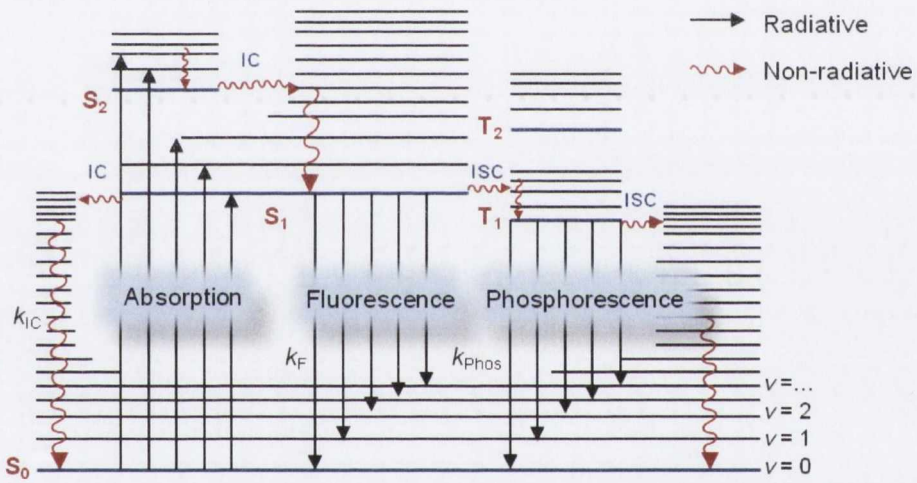


Figure 2.3 Jablonski diagram showing the processes of absorption, fluorescence, phosphorescence, internal conversion (IC) and intersystem crossing (ISC). The radiative processes are represented by black straight lines and the non-radiative processes by red curved arrows. k_{IC}, k_F and k_{Phos} refer to the rate constants for internal conversion, fluorescence and phosphorescence, respectively.

Internal conversion (IC) is a non-radiative transition between two electronic states of the same multiplicity, *e.g.* $S_2 \rightarrow S_1$. In solution, this process is followed by vibrational relaxation towards the lowest vibrational level of the new electronic state. The excess energy is quickly dissipated during collisions with surrounding solvent molecules. IC is more efficient between higher electronic states as the energy gap between any two electronic states is smaller. Thus, other deactivation pathways are often more favourable than IC for the $S_1 \rightarrow S_0$ transition.

Radiative transitions between states of the same multiplicity, *e.g.* $S_1 \rightarrow S_0$, are termed *fluorescence*. Fluorescence typically occurs at longer wavelengths (lower energy) than that of absorption, due to loss of energy from the excited-state through vibrational relaxation. This is a direct consequence of *Kasha's rule* which stipulates that emission only occurs from the lowest excited state of a given multiplicity, thus, emission spectra are usually independent of the

excitation wavelength. The gap between the maximum of the first absorption band and the maximum of the fluorescence emission band is termed the *Stokes shift*.

Molecules in the S_1 excited state can also undergo a non-radiative, spin-forbidden spin-conversion to the first excited triplet state, T_1, through a process termed *intersystem crossing* (ISC). Radiative transitions from the T_1 excited state to the singlet ground state, S_0, known as *phosphorescence*, is also formally a spin-forbidden process. Consequently, radiative rate constants for phosphorescence (k_{phos}) are very small and, thus, vibrational relaxation and internal conversion are highly competitive.

2.1.8 Excited-State Lifetime

Following the absorption of an electron to a higher energy level, all systems will eventually return to their lowest energy, ground state. The length of time a system takes to return to the ground state is termed the *excited-state lifetime*. If we consider a dilute solution of a fluorescent species, F, at a given concentration $[F]$. Following excitation, a certain number of these molecules will be in the excited state, F^*. These molecules will all eventually return to the ground state, radiatively or non-radiatively through a combination of the processes described. The rate of loss of the excited state F^* is given by:[5]

$$-\frac{d[F^*]}{dt} = (k_{rad} + k_{nr})[F^*]_0 \tag{2.5}$$

where k_{rad} is the radiative rate constant and k_{nr} is the sum of the rate constants for all the non-radiative processes. $[F^*]$ is the time dependant concentration of the excited state and $[F^*]_0$ is the concentration of the excited state molecules at $t = 0$, directly after excitation. Integration of Equation 2.4 gives:

$$[F^*] = [F^*]_0 \exp\left(-\frac{t}{\tau_{obs}}\right) \tag{2.6}$$

where τ_{obs} is the observed/measured lifetime of the excited state, given by:

$$\tau_{obs} = \frac{1}{k_{obs}} \tag{2.7}$$

where k_{obs} is the observed decay rate constant and is given by the sum of the rates of all the k_{rad} and k_{nr} processes.

The photoluminescence quantum yield, Φ_{PL}, is the ratio of the number of photons emitted to the number absorbed. The Φ_{PL} is related to the excited state lifetime by:[5]

$$\Phi_{PL} = \frac{k_{rad}}{k_{rad} + k_{nr}} = \tau_{obs} k_{rad} \tag{2.8}$$

2.1.9 Quenching

Quenching refers to any process that decreases the photoluminescence intensity of a sample. The deactivation pathways described in Section 2.1.7 are intrinsic to the excited molecule. However, for a large majority of quenching processes a second species, known as the *quencher,* is also involved. A quencher can decrease the photoluminescence of a molecule by competing with

the intrinsic non-radiative and radiative processes. For such bimolecular processes in solution there are two types of quenching modes: *static* and *dynamic*.[3] A schematic representation of the two different quenching modes in given in Figure 2.4. Both static and dynamic quenching modes require molecular contact between the fluorophore and the quencher. For dynamic quenching, the quencher, Q, must diffuse to the fluorophore, F, within the lifetime of the excited state. On contact, the fluorophore returns to the ground state without emission of a photon, *i.e.* a non-radiative pathway is introduced. In contrast, static quenching is the result of the formation of a non-fluorescent ground-state complex between the fluorophore and the quencher.

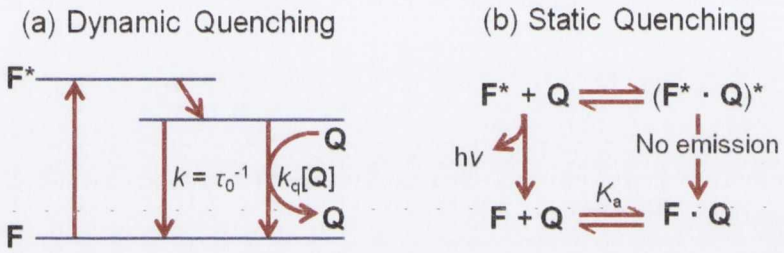


Figure 2.4 Schematic representation of the deactivation of a fluorophore in the excited state by (a) dynamic and (b) static quenching modes. F is the ground-state fluorophore, F^* is the fluorophore in the excited state, Q is the quencher, k is the rate constant for deactivation of the excited state, k_q is the bimolecular quenching rate constant and K_a is the association constant for the static quenching process.

The dynamic quenching of fluorescence can be described by the Stern-Volmer equation:

$$\frac{\tau_0}{\tau} = \frac{I_0}{I} = 1 + K_{SV}[Q] \tag{2.9}$$

where τ_0 and τ are the lifetime of the fluorophore in the absence and presence of the quencher, respectively, and I_0 and I are the fluorescence intensities measured in the absence and presence of the quencher, respectively, and Q is the concentration of the quencher. The Stern-Volmer quenching constant, K_{SV}, is given by $K_{SV} = k_q\tau_0$, where k_q is the bimolecular quenching constant.

In contrast, when non-emission complexes are formed as a consequence of static quenching, the quenching of fluorescence is described by:

$$\frac{I_0}{I} = 1 + K_a[Q] \tag{2.10}$$

where K_a is the association constant for the quenching process, given by:

$$K_a = \frac{[F - Q]}{[F][Q]} \tag{2.11}$$

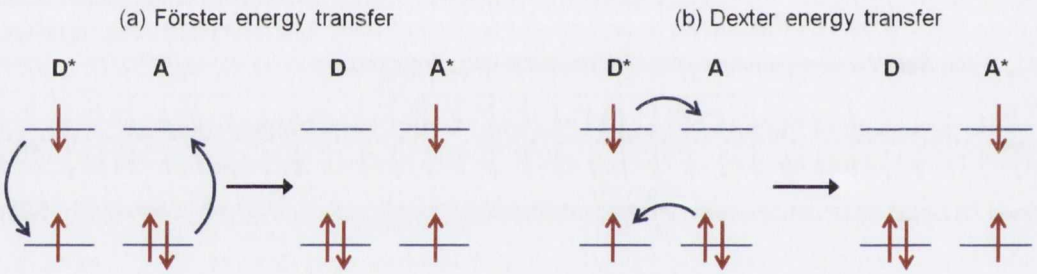
where $[F]$ is the concentration of the un-complexed fluorophore and $[F\text{-}Q]$ is the concentration of the complex.

2.1.10 Energy Transfer

Photoluminescence quenching is a broad term used to describe a decrease in fluorescence (or phosphorescence) intensity which can be brought about through a variety of interactions

between a donor (*D*) and an acceptor (*A*). One potential mechanism for quenching is energy transfer. Excitation energy may be transferred radiatively or non-radiatively. Radiative energy transfer describes the emission of a photon by *D* which is subsequently absorbed by *A*. This form of transfer does not require electronic coupling between *D* and *A*, but depends on the spectral overlap and the concentration of either species. In contrast, non-radiative energy transfer processes require both electronic coupling between the *D* and *A*, and an overlap between the emission spectrum of *D* and the absorption spectrum of *A*.

There are two related mechanisms of non-radiative energy transfer, see Figure 2.5:[4] (1) *Förster resonance energy transfer* (FRET) is a long range dipole-dipole interaction in which the initially excited electron on *D* returns to the ground state orbital, while simultaneously an electron on *A* is promoted into an excited state orbital. Since FRET is a Coulombic interaction it operates over a reasonable distance (~100 Å) and does not require direct contact between the *D* and *A*.[4] (2) *Dexter energy transfer* is a short-range electron exchange in which *D* and *A* exchange an electron between either their singlet or triplet state. As it requires overlap of molecular orbitals, Dexter exchange requires intimate contact between *D* and *A*, and occurs over distances of <10 Å.[4]



(c)

	Förster	Dexter
Spectral overlap	Yes	Yes
Range	<100 Å	<10 Å
Possible excited states	Singlet	Singlet or triplet
Orbital overlap	No	Yes
Distance dependence	r^6	e^{-r}

Figure 2.5 Orbital comparison of an excited state donor (*D**) by a ground state acceptor (*A*) *via* (a) the Förster energy transfer mechanism and (b) the Dexter energy transfer mechanism. (c) Table outlining the requirements and properties of each mechanism. *r* is the distance between donor and acceptor.

The efficiency of energy transfer by dipolar *D*-*A* interactions as described by Förster theory is given by:

$$E = \frac{{R_0}^6}{{R_0}^6 + r^6} \tag{2.12}$$

where *r* is the distance between the donor and the acceptor and R_0 is the Förster distance at which the efficiency of energy transfer, *E*, is 50%. R_0 is given by:

$$R_0^{\,6} = \frac{9000(ln\,10)\kappa^2\phi_D}{128\pi^5 N_A n^4} J_{DA} \tag{2.13}$$

where κ^2 is the orientation factor of two interacting dipoles and is assumed to be 2/3 for randomly orientated dipoles. Φ_D is the fluorescence quantum yield of the donor in the absence of the acceptor, n is the refractive index of the medium, N_A is Avogadro's number and $J_{DA}(\lambda)$ is the spectral overlap integral between the donor emission and acceptor absorption spectra which is given by:

$$J_{DA}(\lambda) = \int_0^\infty F_D(\lambda)\,\varepsilon_A(\lambda)\lambda^4 d\lambda \tag{2.14}$$

where $F_D(\lambda)$ is the fluorescence spectrum of the donor normalised so that $\int_0^\infty F_D(\lambda)\mathrm{d}\lambda = 1$ and $\varepsilon_A(\lambda)$ is the molar absorption coefficient of the acceptor. FRET is commonly employed as a "spectroscopic ruler" for the determination of nanometer-scale distances in biomacromolecules, such as lipid membranes, nucleic acids, proteins, *etc.*[6,7]

2.1.11 Photochemical Deactivation of Excited Species

Some molecules can undergo additional non-radiative de-excitation processes in the form of unimolecular chemical reactions. In contrast to the photophysical processes described above, the deactivated species which follows from a photochemical process is structurally different from that of the initial species. One of the most common types of photochemically driven processes is the *trans-cis* isomerisation about a double bond, as shown in Figure 2.6a for retinal. The structural change is afforded by the energy and electronic configuration of the excited state.[8] In the ground state, the C=C 'π-bond' adopts a planar geometry. However, both the excited S_1- and T_1-states are twisted. This is because the S_1- and T_1-states are classified as ππ*, which means that the excited states have half-filled π- and π*-orbitals. To minimise the repulsion between the two electrons the excited states adopt a twisted structure around the remaining single bond, whereby the two CR_2 groups are mutually perpendicular, which is the lowest energy configuration (Figure 2.6b) for such a molecule. The excited state species can undergo a radiationless transition to S_0, and the molecules reform the double bond in the original geometry or form the other geometric isomer. Other photochemically driven processes include ionisation, dissociation and alternative types of isomerisation.

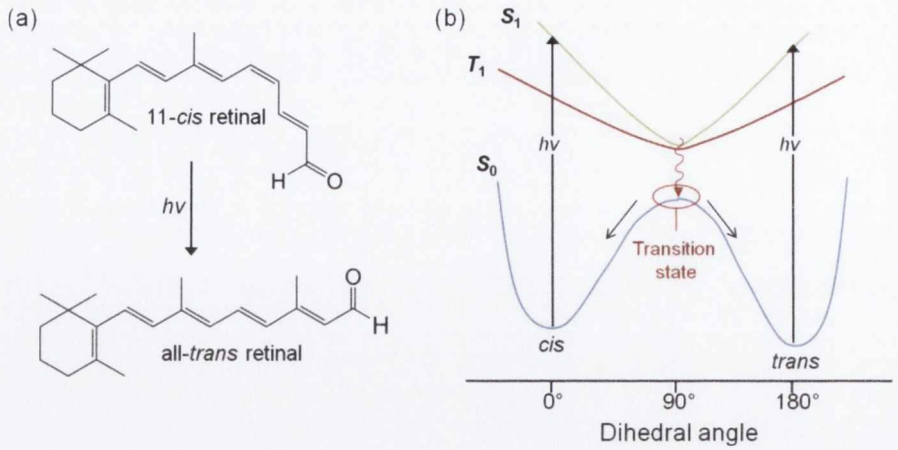


Figure 2.6 (a) *Cis*-to-*trans* photoisomerisation of the C=C bond in retinal. (b) Potential energy diagram of a theoretical *cis*-to-*trans* isomerisation showing that the lowest energy conformation of the excited singlet- and triplet-states has a dihedral angle of 90°.

2.2 Scattering Techniques

Scattering techniques have been utilised extensively for the characterisation of soft and condensed matter to obtain quantitative information on the size, shape and structure of colloidal particles and thin films. Scattering is the process in which electromagnetic radiation, such as X-rays and light, or quantum-mechanical particles, such as neutrons, are deflected from a straight line path *via* the interference of matter.[9] The purpose of this section is to review fundamental scattering theory, universally applicable to electron, light, X-ray and neutron scattering. Particular emphasis will be placed on the scattering techniques and instrumentation used in this thesis.

2.2.1 Elastic *vs.* Inelastic Scattering

Scattering processes can be divided into two categories: elastic (coherent) and inelastic (incoherent).[9] *Inelastic* scattering occurs when an incident photon interacts with an electron within the material and immediately bounces off, in turn, losing a small portion of its energy. In this process, the internal energy levels of atoms and molecules become excited. Therefore, it is possible to probe vibrational bonds of the molecule and thus the electronic structure of materials (*via* Raman scattering). However, this is not usually used to characterise the atomic structure of a material and so will not be discussed in further detail in this chapter.

An *elastic* scattering event occurs when an incident photon (or particle) strikes a material and there is no exchange of energy during the collision. Instead, upon photon collision with the material, the electrons within the material begin to oscillate at the same frequency as the incoming radiation. Neighbouring atoms will oscillate in synchrony with one another and coherent waves are produced. The frequency of the scattered wave is equal to the frequency of the incident wave. The scattered waves produce an interference pattern that contains structural information about the material. The interference may be constructive (*i.e.* in phase), where a bright spot on a detector is observed, or destructive (*i.e.* out of phase), where a dark region on the detector is observed. This phenomenon produces a two dimensional diffraction pattern on the detector.

Furthermore, there are two types of elastic scattering: Mie and Rayleigh. Scattering from very small particles (1/10 of the incident wavelength) is predominantly *Rayleigh* scattering and is essentially isotropic, *i.e.* equal in all directions (Figure 2.7a). The Rayleigh approximation tells us that the intensity of scattered light, I, is inversely proportional to d^6 and λ^4, where d is the particle diameter and λ is the wavelength of the incident light. In contrast, *Mie* scattering predominates for particles with diameters that are comparable or larger than the wavelength of light. Mie scattering occurs primarily in the forward direction and is not strongly wavelength dependant (Figure 2.7b). The greater the particle size, the more intense the Mie scattering is in the forward direction (Figure 2.7c). Therefore, the back-scattering configuration is often preferred in dynamic light scattering experiments to prevent the detector being swamped by larger aggregates (*e.g.* dust).

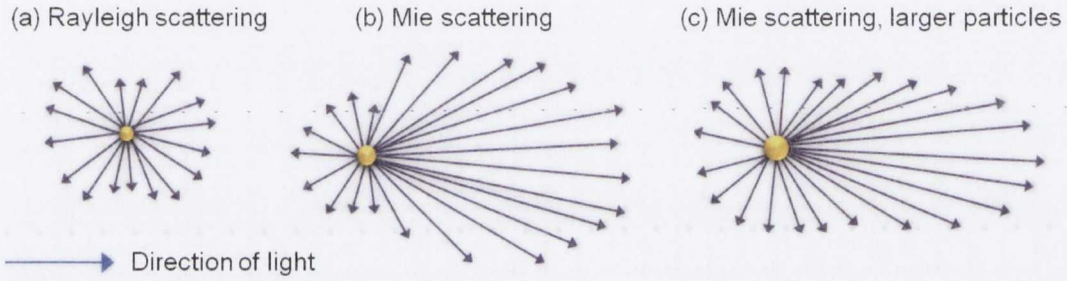


Figure 2.7 A schematic illustration of the patterns of scattered light produced by (a) Rayleigh scattering, when the particles are very small, and by Mie scattering for particles which are (b) comparable or (c) larger in size than the wavelength of incident light.

The geometry of an elastic scattering event is shown in Figure 2.8. Imagine that a photon (or particle) is scattered by a particle so that its trajectory is deflected by an angle, θ. Then, the component of the new trajectory which is aligned in the forward direction is the cosine of θ. The quantity referred to as the *scattering vector*, q, is the modulus of the resultant between the incident ($\boldsymbol{k}_i$) and scattered ($\boldsymbol{k}_s$) wavevectors and is given by:

$$q = |\boldsymbol{q}| = |\boldsymbol{k}_s - \boldsymbol{k}_i| = \frac{4\pi n}{\lambda} sin(\theta/2) \tag{2.15}$$

where n is the refractive index of a material, for neutrons and X-rays this is generally assumed to be 1, λ is the wavelength and θ is the scattering angle. Substituting Equation 2.13 into Bragg's Law of diffraction:

$$\lambda = 2dsin\left(\frac{\theta}{2}\right) \tag{2.16}$$

yields the useful expression:

$$d = \frac{2\pi}{\lambda} \tag{2.17}$$

where d is a distance. Through the combined use of Equations 2.15 and 2.17 it is possible to determine the q-range of the instrument in question and to quickly and rapidly determine the "size" of scattering bodies in a sample from the position of any diffraction peak in the q-space.

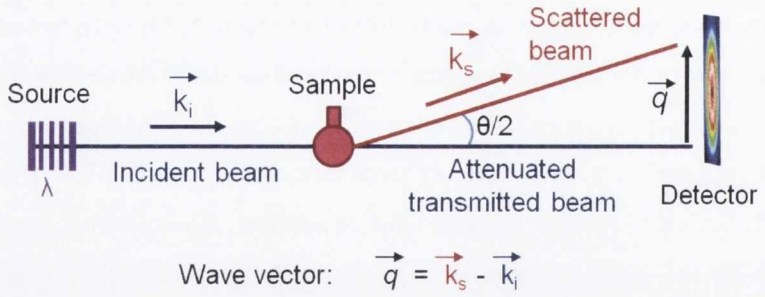


Figure 2.8 Schematic representation of the geometry of an elastic scattering experiment; k_i is the incident wavevector, k_s, is the scattered wavevector, θ is the scattering angle, respectively, and q is the scattering vector.

2.2.2 Properties of Light, Neutron and X-ray Radiation

The most fundamental difference between neutron and electromagnetic radiation (including X-rays and light) is the mechanism by which the incident radiation interacts with matter, as shown in Figure 2.9.[9] Light and X-rays are both scattered by electrons surrounding the atomic nuclei, while neutrons are scattered by the nucleus itself. In the case of light or X-rays, the scattering cross-section of an atom increases proportionally to the number of electrons present, and thus increases with the elemental atomic number, Z. In contrast, the strength of the neutron-nucleus interaction varies completely irregularly with Z. The *neutron scattering cross-section* (σ) is a measure of how "big" the nucleus appears to the neutron and, thus, how strongly the neutrons will be scattered from it.[9] Even isotopes of the same element have different σ. The most significant isotropic variation occurs when $Z = 1$. Hydrogen has a coherent neutron scattering cross-section (σ_{coh}) of 1.75×10^{-24} cm^2, roughly the same as manganese, while for deuterium $\sigma_{coh} = 5.6 \times 10^{-24}$ cm^2, similar to carbon-12.[10] Therefore, neutrons cannot only "see" hydrogen isotopes but distinguish between them. This has important consequences for contrast matching experiments, as described in Section 2.2.6.2.

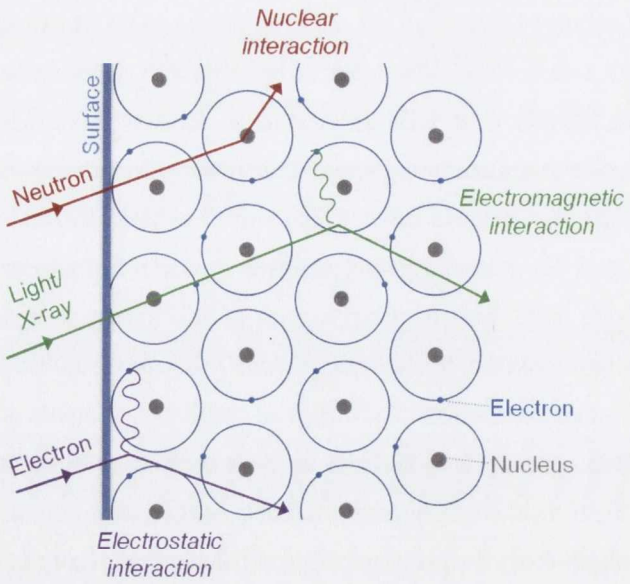


Figure 2.9 A schematic illustration of the principle modes by which electrons, light, X-rays and neutrons are scattered by condensed matter.

A comparison of some of the features of visible light, X-ray and neutron radiation is shown in Table 2.1. Light scattering is typically used as a convenient technique to determine the overall aggregate size of matter on a scale that is typically >10 nm. In contrast, X-rays and neutrons are able to probe structures on nanometre to micrometre length scale. X-ray and neutron scattering techniques reveal information not only about particle size but also particle shape, and when the concentration allows, particle-particle interactions. Small-angle neutron and X-ray scattering are generally thought of as complimentary techniques, each with its own advantages and disadvantages. For example, SAXS experiments generally have a superior q-resolution with significantly faster acquisition times allowing for time-resolved measurements. On the other hand, neutrons are far less energetic than X-rays and not-charged, and thus, are able to penetrate samples further (within complicated experimental set-ups) without causing significant damage. Finally, as neutrons "see" deuterium and hydrogen differently, contrast-matching offers the opportunity to probe the internal structure within the scattering particle. In reality, while the choice of technique is sample dependant, no technique can be used in isolation.

Table 2.1 Properties of light, X-rays and neutron radiation and how they affect scattering experiments.

	Visible light	**X-rays**	**Neutrons**
Type	Electromagnetic wave	Electromagnetic wave	Particle/wave
Wavelength, λ	400-600 nm	0.01-0.2 nm	0.01-2.0 nm
Distance probed	>0.01 μm	nm to μm	nm to μm
Scattering variations are controlled by:	Refractive index	Electron density	Neutron scattering properties

2.2.3 Light Scattering

Light scattering has been used extensively to characterise the structure and dynamics of polymers and colloidal particles. Light scattering principles are based on well-known theories by Einstein, Debye, Raman and Zimm.[11] Dynamic light scattering (DLS), also known as photon correlation spectroscopy (PCS), is useful for determining the average size and size distributions in terms of an hydrodynamic radius (R_H) and polydispersity (PDI). Multi-angle light scattering (MALS) provides information about molecular weight (M_w) and average particle size in terms of a radius of gyration (R_g). R_g is the root mean square value of the radius averaged over the volume of the particles. In a few cases, both DLS and MALS have been combined to yield information about the shape of aggregated polymeric materials. This is possible as the shape of the aggregates are related to a 'q-value' which is determined by the ratio of R_g to R_H.[12]

2.2.3.1 Dynamic Light Scattering

DLS is effectively a method to make a single-angle approximation of the hydrodynamic radius of a particle. In DLS, the speed at which particles diffuse in solution due to Brownian

motion is measured and related to the size of the particles. Brownian motion is the random movement of particles due to bombardment by the solvent molecules that surround them. Smaller particles are "kicked" further by the solvent molecules and move more rapidly. Therefore, the larger the particle, the slower the Brownian motion will be. The velocity of the Brownian motion is defined by a property known as the translational diffusion coefficient (D). D is related to the hydrodynamic radius of the particles through the Stokes-Einstein equation:[13]

$$D = \frac{k_B T}{6\pi\eta R_H} \tag{2.18}$$

where k_B is the Boltzmann constant, T is the temperature and η is the viscosity of the medium. The radius obtained by this technique is the radius of a sphere that has the same diffusion coefficient as the particle.

Experimentally for a DLS measurement, a monochromatic light beam, such as a laser, illuminates an area of particles within a solution. The presence of these particles causes the beam of light to be scattered. The particle size (and magnitude of Brownian motion) will affect the rate at which the intensity of this scattered light fluctuates. A digital auto correlator measures the degree of similarity between the intensity of a scattered light signal at time (t), compares this signal to the intensity at a very small time later ($t+\delta t$), and constructs a correlation function ($G^2(t)$). For larger particles, the signal changes slowly and the correlation will persist for a long time. In contrast, if the particles are small and move rapidly then the correlation will reduce more quickly. The translational diffusion coefficient is determined from a polynomial fit of the logarithm of the correlation function:[14]

$$G^2(t) = \int_0^\infty I(t)I(t+x)dt = B + Ae^{-2q^2Dx} \tag{2.19}$$

where A is the amplitude of the correlation function, q is the wavevector determined from the scattering angle and D is the diffusion coefficient.

2.2.3.2 Multi-Angle Light Scattering

The rate at which the scattered light intensity changes with the scattering angle (or q) will also depend on the size of the particle. MALS is a study of the scattered light intensity as a function of scattering angle, typically over 30-180°. There are two different ways to interpret the data from a MALS experiment which yields either the hydrodynamic radius or the radius of gyration. Firstly, it is possible to acquire a more accurate R_H than with a typical bench-top DLS instrument. To measure this, a similar approach is taken to single-angle DLS. The fluctuation of scattered light over time is recorded at each angle and computed as an intensity correlation function, C(q,t), given by:[15]

$$C(q,t) = Aexp[-(t/\tau)^\beta] \tag{2.20}$$

where t is the start time, τ is the lag time, A is the amplitude of the correlation function and β is a factor that depends on experimental geometry. The lag time represents the time at which the correlation drops off. A stretched exponential is used to fit the correlation function acquired at each scattering angle, enabling the decay rate (Γ) to be determined, where $\Gamma = 1/\tau$. Γ is directly related to the diffusion coefficient of the particles (D) by:

$$\Gamma = q^2 D \tag{2.21}$$

Therefore, a plot of Γ *vs.* q^2 will yield a slope of D, which enables R_H to be determined from the Stokes-Einstein equation (Equation 2.16).

Additionally, for larger particles (>20 nm) the dependence of the scattered intensity on scattering angle (or q) may also be used to determine the radius of gyration of particles. The scattering intensity of light ($I(q)$) is given by:

$$I(q) = kcM(1 + cos^2\theta)(1 - \frac{(qR_g)^2}{3} + ...) \tag{2.22}$$

where c is concentration, M is the molar mass of the particles, k is a collection of constants and '$1 + cos^2\theta$' is the polarisation factor. The polarisation factor results from the physics of the scattering process and is usually removed by an experimental correction. Thus, R_g can be determined from a plot of $I(q)$ against q^2, whose slope = $-R_g^2/3$. This theory is called the Rayleigh-Gans-Debye theory and is applicable when the particle diameter remains less than the wavelength of light.[16] For even larger particles, the scattering pattern becomes extremely complex and Mie theory applies.

2.2.3.3 Small-Angle X-ray and Neutron Scattering

Small-angle scattering (SAS) is the collective name given to small-angle neutron, X-ray and light scattering techniques. For each of these methods, radiation is scattered elastically by the sample and the resulting scattering pattern is analysed to provide information about the particle size, shape and orientation.[9] A typical 1D scattering pattern shows how the scattering intensity varies as a function of q-vector (angle). Small-angle light scattering has already been briefly touched upon in the MALS experiments described above, whereby the intensity of scattered light is measured as function of small to large scattering angles (lowest q-regime), and this relationship is used to determine the particle size. In general, the scattering of radiation in the low q-regime is predominantly sensitive to the size and shape of the particles (as we saw for light scattering), while analysis from scattering of radiation at high q reflects the internal structure of the particles. Considering the range of wavelengths that are accessible using X-rays and neutrons, it becomes necessary to use small angle scattering to obtain the optimum q-range for probing the typical length scales of the aggregates under investigation in soft matter chemistry.

To a large extent SAS techniques are complimentary. However, the length scales, the sample and sample environment probed all depend on the nature of radiation employed. After

accounting for different masses and velocities, the same fundamental theory, such as the basic equations and laws, is applicable to light, X-ray and neutron scattering techniques. The following section will focus primarily on SANS and SAXS.

2.2.4 Neutron and X-ray Experiments

2.2.4.1 Neutron and X-ray Sources

The radiation source used for an X-ray experiment such as SAXS can be either radiation produced at a synchrotron storage ring, *e.g.* Diamond Light Source in Oxford, U.K., or a laboratory X-ray instrument. Unfortunately, in-house instruments typically only achieve a maximum flux of $\sim 10^{11}$ photons s^{-1} and usually require long exposure times, *i.e.* minutes to several hours. In comparison, modern X-ray synchrotron radiation sources have high brilliance and high flux ($\sim 10^{18}$ photons s^{-1}), require extremely short exposure times (seconds) and very little sample. Although it is important to note that radiation damage to the sample can be a serious problem with high-brilliance X-ray beamlines.

Synchrotron facilities can provide X-rays of all wavelengths as a by-product of deflecting and accelerating electrons through large dipole magnets. This acceleration generates *Bremsstrahlung* radiation which is directed into the adjoining beamline instruments. For in-house SAXS instruments, X-ray radiation is generated when electrons, accelerated by an applied voltage, hit an anode, where they are decelerated, resulting in the emission of X-rays.[17] This radiation is also *Bremsstrahlung* and can provide a broad spectrum of wavelengths with energy not exceeding the applied voltage (~30-60 kV). The repetitive bombardment of electrons onto an anode causes aging effects, such as grooves or holes burnt into the anode material. Consequently, rotating anodes are now typically utilised in laboratory SAXS instruments to maximise the lifetime of the instrument by reducing the wear per unit area.

In contrast, neutrons in adequate quantities are only available from a synchrotron radiation source. Even at the most powerful neutron sources, the flux of neutrons reaching a SANS instrument are typically very weak (low brilliance), several orders of magnitude lower than the flux of photons at a synchrotron SAXS beamline.

There are two main sources of neutrons:

(i) *Nuclear reactor*: Neutrons are released by the fission of uranium-235. Each fission reaction releases 2 - 3 neutrons, though one of these is needed to sustain the chain reaction. Currently the most powerful reactor neutron source in the world is the 58 MW High-Flux Reactor at the Institut Laue-Langevin (ILL) in Grenoble, France.[18]

(ii) *Spallation "chipping away" sources*: Particle accelerators and synchrotrons generate intense, high-energy, proton beams which are directed at a target composed of heavy nuclei.[19] Provided that the protons have sufficient kinetic energy to overcome the intrinsic long-range electrostatic and short-range nuclear forces they encounter, they effectively blast the target nuclei apart. One of the most powerful spallation sources in the world is the

ISIS Facility near Oxford in the U.K. It is based around a 200 mA, 800 MeV, proton synchrotron operating at 50 Hz, and uses a tantalum target which releases approximately 12 neutrons for every incident proton.[20]

2.2.4.2 SANS and SAXS Instrumentation

The basic components of SAS apparatus are similar. Neutrons/X-rays scattering at the low q-portion of the scattering vector (where the structural information is found) can be achieved through using small angles or long wavelengths (or both). Generally, the biggest challenge in the design of any SAS instrument is to separate the direct beam from the scattered radiation at small angles (<0.1°). If the incoming beam has a larger divergence than this small-angle requirement then it becomes difficult to distinguish the relatively weak intensity of the scattering pattern from the much higher intensity of the direct beam. Therefore, the divergence of the direct beam must be kept small. Hence, a *collimation system* is required to narrow the beam. This is basically a system of slits or pinholes the beam has to pass through before it reaches the sample.

There are two different types of SANS instruments available to generate the desirable q-range:

(i) *Continuous*: Continuous source instruments control the velocity of the neutrons hitting the sample and thus the scattering angle is the variable factor. These instruments rely on continuous/steady sources of neutrons, *i.e.* from nuclear reactors.

(ii) *Time-of-flight* (*TOF*): TOF instruments use the length of time it takes a neutron to reach the detector to calculate that neutron wavelength, thus, the wavelength is the variable factor. The angle at which each neutron is detected on the 2D detector is then used to calculate the q-vector. TOF instruments are ideal for pulsed sources such as ISIS, U.K.

All the SANS measurements described in this thesis were performed on either the LOQ[19] or SANS2D[21] instruments at the ISIS spallation neutron source in Oxford, U.K. Both instruments are TOF, and therefore, the set-up of a TOF instrument will be discussed in greater detail. In a TOF instrument (Figure 2.10) a pulse of neutrons is released at the 'chopper' with a defined wavelength range (4-20 Å for LOQ, 2-14 Å for SANS2D).[19] The neutron beam then passes through a collimation chamber where it is collimated to a few millimetres in diameter before hitting the sample. Different neutron wavelengths will scatter to different extents depending on the structure and make-up of the sample. A 2D detector, typically a ^{3}He-CF_4 filled scintillation detector, detects the neutrons, the angle at which they have been scattered and the time at which they arrive. By knowing of the exact time at which each neutron left the chopper (pulse start time) and the time each neutron hits the detector, the neutron's speed can be calculated. As speed is linearly related to wavelength and the scattering angle, θ, is identified from the position on which the neutron hits the detector, q can be calculated from Equation 2.15. Therefore, for TOF it is critical to know the precise time the neutrons leave the chopper and arrive at the detector. The problem is that the slowest neutrons from one pulse could arrive at the chopper at the same time as the fastest neutrons in the next pulse. As such, it is important to limit the wavelength range using beam filters, made

from metals such as beryllium which only transmits neutrons with λ >4 Å. An alternative approach is to leave more time between consecutive pulses. However, this means fewer neutrons and therefore longer sample runs or poorer statistics.

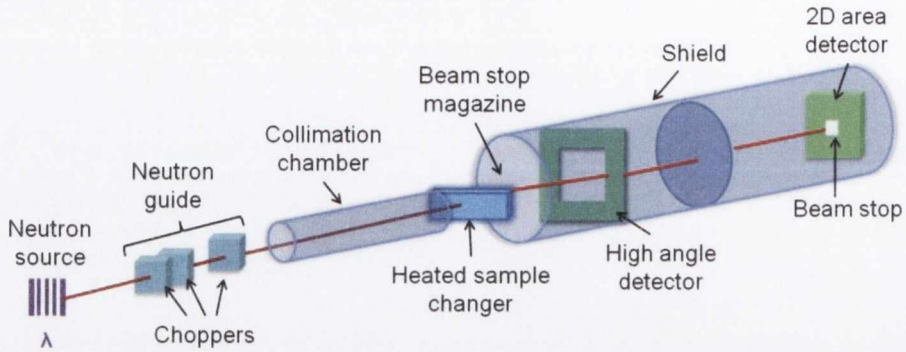


Figure 2.10 Schematic representation of a time-of-flight instrument typically used at a spallation neutron source.

The most complicated part of a SAXS instrument is the sample holder, as a vacuum chamber is required to maintain a low scattering background. The problem is most samples are destroyed when they are placed in a vacuum and need to be kept at ambient conditions. Therefore, special sample holders are necessary to keep the samples fit for the scattering experiments. For example, liquid samples are measured inside a thin-walled capillary. Otherwise, the instrumental set-up for a SAXS experiment is generally the same as a SANS experiment after the sample chamber (Figure 2.10).

2.2.5 SAS Theory

In any SAS experiment, a beam of collimated, although not necessarily monochromatic, radiation is directed at a sample, illuminating a small volume, V.[9] $V = At_s$, where A is the cross-sectional area of the beam and t_s is the path length of the sample, typically volumes are <0.5 cm^3 for solvated samples. Some of the radiation will be transmitted by the sample, some will be absorbed and some will be scattered. A detector of dimension $d_x \times d_y$ is positioned a distance, $\lambda_{\sigma\delta}$, and scattering angle (θ) from the sample and records and translates the flux of radiation scattered into a solid angle element. This flux, $I(\lambda, \theta)$ may be expressed in general terms in the following way:

$$I(\lambda,\theta) = I_0(\lambda)\Delta\Omega\eta(\lambda)TV\frac{\delta\sigma}{\delta\Omega}(q) \tag{2.23}$$

where I_0 is the incident flux, η is the detector efficiency, $\Delta\Omega$ is the flux of radiation scattered into a solid angle element, T is sample transmission and $(\delta\sigma/\delta\Omega)(q)$ is a function known as the microscopic *differential cross-sectional area,* discussed further below. The first three terms of Equation 2.23 are instrument dependant and the last three terms are sample dependant.

2.2.5.1 Scattering Cross-Section

The objective of a SANS or SAXS experiment is to determine the differential cross-section, as it contains all the information on the shape, size and interactions of the scattering bodies (assemblies of scattering centres) in the sample. The differential cross-section ($(\delta\sigma/\delta\Omega)(q)$) is given by:

$$\frac{\delta\sigma}{\delta\Omega}(q) = I(q) = NV^2(\Delta\rho)^2P(q)S(q) + B_{inc} \tag{2.24}$$

where N is the number of scattering bodies per unit volume, V is the volume of one scattering body, $(\Delta\rho)^2$ is the square of the difference in scattering length densities (termed *contrast*), $P(q)$ is the *form* or *shape factor*, $S(q)$ is the *interparticle structure factor* and B_{inc} is the isotropic incoherent background signal. $(\delta\sigma/\delta\Omega)(q)$ has dimensions of (length)$^{-1}$, and for ease, is often written as simply $I(q)$.

2.2.5.2 Contrast and Contrast-Matching Experiments

The contrast in light scattering experiments arises from the difference in refractive indexes between the different components. The contrast in SAXS arises from the differences in electron density. X-ray photons interact with every electron in the sample, and the strength of interaction between an X-ray and an electron (the scattering length) is the Thomson scattering length, b_{Th} = 0.282×10^{-14} m. In neutron scattering, the interaction is nuclear and the contrast arises from differences in neutron scattering length densities. The neutron scattering length density (ρ(r)) of a molecule of i atoms can be determined using:

$$\rho(r) = \sum_i b_i \frac{D_{bulk}N_A}{M_w} \tag{2.25}$$

where b_i is the scattering length of the atom which quantifies the strength of interaction of free neutrons and the bound nucleus, and is the isotope dependant component. D_{bulk} is the bulk density of the scattering body, N_A is Avogadro's number and M_w is its molecular weight. For polymers, it is only necessary to calculate δ for one repeat unit. δ has dimensions of (length)$^{-2}$ and can also be negative. The contrast is simply the difference in δ values between the part of the sample of interest (ρ_p) and the surrounding medium or matrix (ρ_m) all squared, *i.e.* $(\Delta\rho)^2 = (\rho_p - \rho_m)^2$. Clearly if $(\Delta\rho)^2$ is zero then Equation 2.24 is also zero and there will be no SANS scattering profile. When this condition is met the scattering bodies are said to be *contrast-matched*. Since the SANS from a multi-component sample is essentially a contrast-weighted summation of the SANS from each of the individual components, the technique of contrast-matching can be used to dramatically simplify the scattering pattern. Conveniently for neutron scattering scientists there is a large difference between deuterium and hydrogen. Consequently, using deuterated solvents is a relatively convenient way to achieve contrast between the sample and the solvent. Furthermore, by mixing hydrogenous and deuterated forms of the medium in the appropriate ratio, a contrast-match can theoretically be achieved with any part of the species under investigation. Some of the possible

combinations of contrast-matching experiments and the resultant SLD profiles are shown in Figure 2.11. The scattering length densities of some common solvents are shown in Table 2.2.

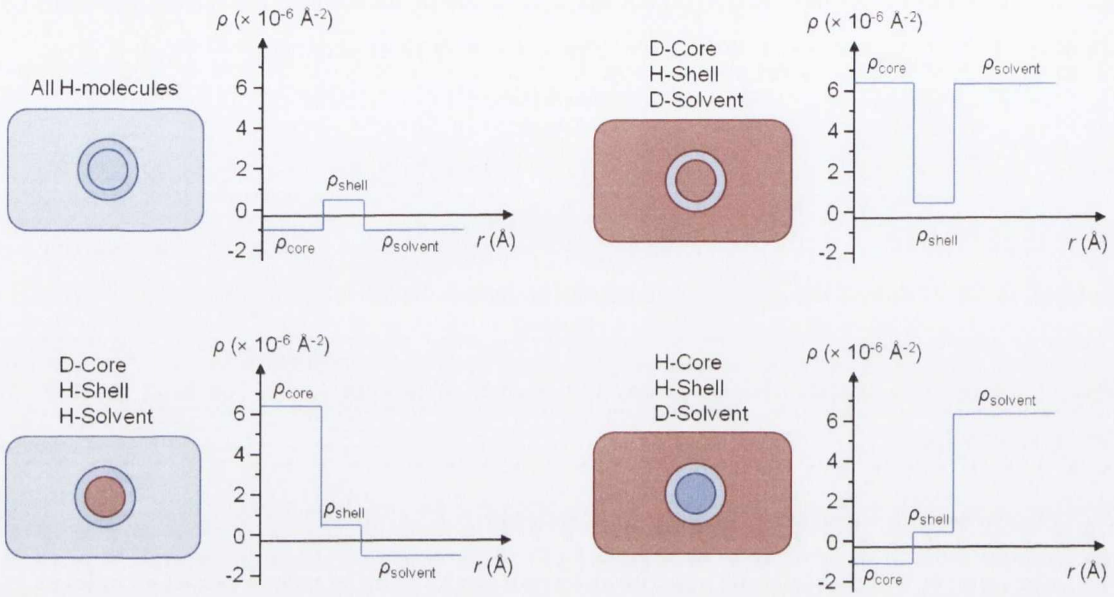


Figure 2.11 Schematic representations of the contrast variation possibilities in a core-shell-solvent microemulsion. The spheres represent a core-shell particle in a surrounding solvent. Red and blue are used for deuterated and hydrogenated materials, respectively. The components in each system with similar scattering length densities (ρ or SLD) (*i.e.* colours) are said to be "contrast-matched". r is the distance from the centre of a droplet.

Table 2.2 Scattering length densities, ρ or SLD, of commonly used solvents in their hydrogenated, H, and deuterated, D, forms.

Solvent	**ρ (H form) ($\times 10^{-6}$ Å^{-2})**	**ρ (D form) ($\times 10^{-6}$ Å^{-2})**
Water	-0.56	+6.38
Methanol	-0.37	+5.80
Chloroform	+2.39	+3.16
Octane	-0.53	+6.43

2.2.6 Form Factor ($P(q)$)

The scattering of one particle, which is made up of many individual atoms, can be explained as the interference pattern produced by all the scattered waves that reach the detector from every electron/atom inside the particle. If all the wave amplitudes at the detector position are combined and squared then the result is an (interference) scattering pattern. This process is known as 1D reduction which is performed by instrumental software such as Mantid[22] or DAWN[23], and will not be discussed in greater detail here. The resulting scattering pattern oscillates in a fashion that is characteristic for the shape (or the form) of the particle as shown in Figure 2.12. It is therefore called the *Form Factor*. It is a "factor" because it must be scaled with a constant in order

to match the experimental intensity units. For structure determination, the scaling factor is not required.

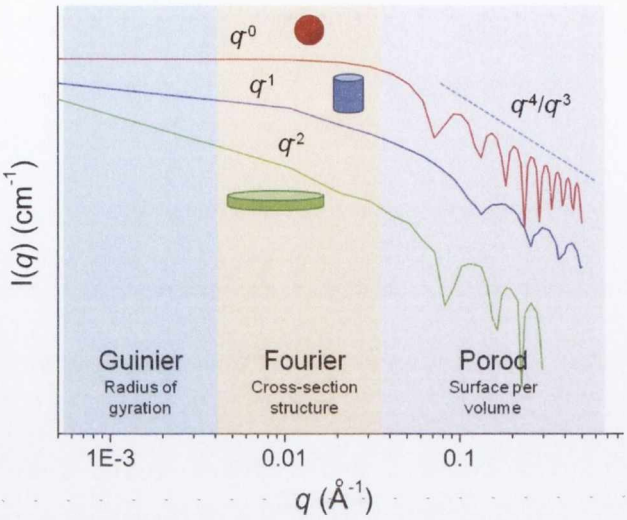


Figure 2.12 The scattering profiles of the form factor for a sphere, rod and disc. The q scale has been divided to demonstrate the approximate regions where particular information may be extracted.

In practical terms, many particles are actually illuminated at the same time and so the observed scattering pattern corresponds to the form factor of one particle only if:

(i) The particles are all identical in shape and size (*i.e.* monodisperse), and,

(ii) The particles are far enough away from each other (*i.e.* dilute solution). If the sample is dilute, then the form factors of all illuminated particles can be summed up. In a dilute sample, the experimental scattering pattern is the form factor multiplied by the number of particles that are in the illuminated area of the incident neutron/X-ray beam.

2.2.6.1 Guinier law

The Guinier law is widely used to determine the basic molecular parameters, such as the radius of gyration, R_g, and the molecular weight, M_W.[24] At low q, when q tends to zero (Guinier regime in Figure 2.12), the single particle form factor, $P(q)$, for a dilute system simplifies to:

$$P(q) = 1 - \frac{1}{3}q^2R_g^2 \tag{2.26}$$

where R_g is the root mean square value of the radius averaged over the volume of the particles, and relates to the shape of the particle. In practice, the Guinier plot, *i.e.* $\ln I(q)$ *vs.* q^2, should include a linear section up to the limit $qR_g < 1$. The associated slope is $-R_g^2/3$, allowing R_g to be determined for any isomeric particle (similar procedure to MALS).

2.2.6.2 *Q*-scaling

The slope of the form factor at small angles is primarily determined by the overall size of the scattering particle and the final slope at large angles bears information about the surface of the

particles. The information about the shape and the internal density distribution lies in the oscillating part in the middle section of the form factor. In particular, the slopes at high q are described by the Porod law whereby the slopes of the *Porod* plot ($\ln I(q)$ *vs.* $\ln q$) represent the interface and scattering dimension of the scattering object.[25, 26] As a result, SAS functions $I(q)$ can be initially interpreted using scaling concepts.[27] The scattering intensity may be considered to scale as:

$$\frac{1}{c} I(q) \approx q^{-\alpha} \tag{2.27}$$

where c is the concentration and the exponent α may be interpreted in terms of an arbitrary particle shape: $\alpha = 1$ for separated rods; $\alpha = 2$ for sheet-like particles; $\alpha = 4$ for smooth 3-dimensional particles, for which the scattering would also level off at low q (Figure 2.13). Slopes between -3 and -4 characterise a rough interface of fractal dimension D. The scatter from such a rough interface drops as $q^{-(6-D)}$.[27]

2.2.7 Structure Factor ($S(q)$)

When particle systems are densely packed (*i.e.* concentrated samples), the distance of the particles relative to each other come into the same order of magnitude as the distances inside. As a result, the interference pattern will contain contributions from neighbouring particles as well. The additional interference multiplies with the form factor of the single particle and is called the *Structure Factor* (Figure 2.13). A decrease in scattering intensity at low q values is typical for repulsive interaction potentials. An intensity increase indicates attractive interactions, which is very similar to aggregation. Eventually this wave can develop into a pronounced peak, when the particles align themselves into highly ordered and periodic (*i.e.* crystalline) arrangement. It is then called the Bragg peak and the position of its maximum (q_{Peak}) indicates the distance (d_{Bragg}) between the aligned particles by using Bragg's law:

$$d_{Bragg} = \frac{2\pi}{q_{Peak}} \tag{2.28}$$

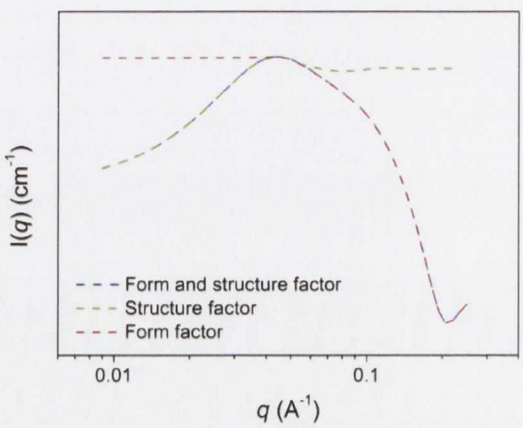


Figure 2.13 The scattering profiles of a form factor (red dashed line), structure factor (green dashed line) and structure and form factor combined (blue dashed line).

2.2.8 Structure Factor Models

In a SANS or SAXS experiment, the main interest is frequently the structure of the building blocks of the sample, therefore, the interference of scattering by different scattering bodies, the structure factor, $S(q)$, is often a complication that is best mitigated by dilution and can then be assumed to be one. However, sometimes with highly polar macromolecules or porous materials the structure factor must be taken into account. The interparticle structure factor is given by:

$$S(q) = 1 + \frac{4\pi N_p}{qV}\int_0^\infty [g(r) - 1]rsin(qr)dr \tag{2.29}$$

$S(q)$ relates scattered intensity to the microstructure through the pair correlation function ($g(r)$) which is related to the probability of finding a particle at a distance r from another particle. The consequence of this is that SAS can be used to gain information about the relative positions of the scattering bodies. The pair correlation function can be determined from the Ornstein-Zernike equation:[28]

$$g(r) = \exp\left(-\frac{U(r)}{k_B T}\right) \tag{2.30}$$

where $U(r)$ is the interaction potential between the neighbouring particles and requires a closure operation to calculate. An alternative approach to fitting the structure factor involves using one of the many approximate model forms of $S(q)$ that have been developed, including:

(i) *Hard-sphere interaction*: The particles can move freely but cannot penetrate each other.[29]

(ii) *Screened coulomb interaction*: Particles that carry any electrical charges can move freely unless their electrical fields start to penetrate and repel each other.[30] This model is described by an effective hard-sphere radius, a concentration, a surface charge and an ionic strength of the solvent (which leads to a layer of counterions that shield the electrical fields of neighbouring particles).

(iii) *Square well interaction*: This model refers to those forces which arise from the polarisation of molecules into dipoles.[28] The polarisation of particles can cause them to become attracted to each other when they reach a minimum distance, this can result in aggregation and condensation. The parameters of this model are the effective hard-sphere radius, concentration and long-range repelling distance.

The approximate interaction potential, $U(r)$, described by each of these structure factor models are shown in Figure 2.14. Each of the structure factor models can fitted to the scattering data in combination with most of the form factor models, which will be described in the following Experimental Chapter.

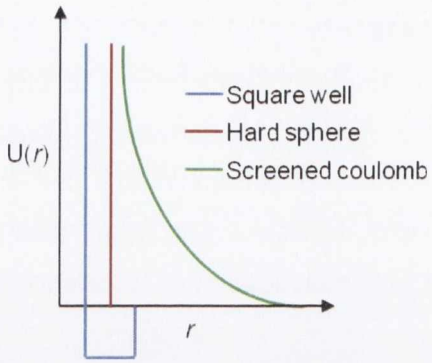


Figure 2.14 A schematic representation of the expected interaction potentials, $U(r)$, as a function of particle-particle distance, r, for different structure factors.

2.3 References

1. B. Valeur, *Molecular Fluorescence: Principles and Applications* Wiley-VCH Verlag GmbH, 2001, pp. 20-33.
2. P. Douglas, H. D. Burrows and R. C. Evans, *Applied Photochemistry*, Springer, 2013, pp. 56-58.
3. J. R. Lakowics, *Principles of Fluorescence Spectroscopy*, Springer, New York, 2006, pp. 331-351.
4. B. Valeur, *Molecular Fluorescence: Principles and Applications*, Wiley-VCH Verlag GmbH, 2001, pp. 34-71.
5. J. R. Lakowicz, *Principles of Fluorescence Spectroscopy*, Springer, New York, 2006, pp. 443-475.
6. C. Ghatak, V. G. Rao, R. Pramanik, S. Sarkar and N. Sarkar, *Phys. Chem. Chem. Phys.*, 2011, **13**, 3711-3720.
7. S. M. Fonseca, R. P. Galvão, H. D. Burrows, A. Gutacker, U. Scherf and G. C. Bazan, *Macromol. Rapid Commun.*, 2013, **34**, 717-722.
8. P. Douglas, H. D. Burrows and R. C. Evans, *Applied Photochemistry*, Springer, 2013, pp. 72-73.
9. D. S. Sivia, *Elementary Scattering Theory for X-ray and Neutron Users*, Oxford University Press, Unilever, Oxford (U.K.), 2011, pp. 1-18.
10. V. F. Sears, *Neutron News*, 1992, **3**, 26-37.
11. B. H. Zimm, *J. Chem. Phys.*, 1948, **16**, 1099-1116.
12. Y. Deng, Y. Li and X. Wang, *Macromolecules*, 2006, **39**, 6590-6598.
13. A. Einstein, *Annalen der Physik*, 1905, **17**.
14. *International Standard ISO22412 Particle Size Analysis - Dynamic Light Scattering*, International Organisation for Standardisation (ISO), 2008.
15. B. J. Frisken, *Appl. Opt.*, 2001, **40**, 4087-4091.
16. R. Apetz and M. P. B. van Bruggen, *J. Am. Ceram. Soc.*, 2003, **86**, 480-486.
17. H. Schnablegger and Y. Singh, *The SAXS Guide*, 3rd edn., Anton Paar Gmbh, Austria, 2013.
18. *https://www.ill.eu.*
19. R. K. Heenan, J. Penfold and S. M. King, *J. Appl. Crystallogr.*, 1997, **30**, 1140-1147.
20. *http://http://www.isis.stfc.ac.uk.*
21. R. K. Heenan, S. E. Rogers, D. Turner, A. E. Terry, J. Treadgold and S. M. King, *Neutron News*, 2011, **22**, 19-21.
22. *http://www.mantidproject.org.*
23. *http://www.dawnsci.org.*

24. A. Guinier and G. Fournet, *Small Angle Scattering of X-rays*, John Wiley and Sons, 1955.
25. G. Porod, *Kolloid-Zeitschrift*, 1951, **124**, 83-114.
26. A. C. Mitropoulos, N. K. Kanellopoulos, K. L. Stefanopoulos and R. K. Heenan, *J. Colloid Interface Sci.*, 1998, **203**, 229-230.
27. P. W. Schmidt, *Some Fundamental Concepts and Techniques Useful in Small-Angle Scattering Studies of Disordered Solids. In Modern Aspects of Small-Angle Scattering*, Kluwer Academic Publishers: Dordrecht, The Netherlands, 1995.
28. S. V. G. Menon, C. Manohar and K. S. Rao, *J. Chem. Phys.*, 1991, **95**, 9186-9190.
29. J. K. Percus and G. J. Yevick, *Phys. Rev.*, 1958, **110**, 1-13.
30. J.-P. Hansen and J. B. Hayter, *Mol. Phys.*, 1982, **46**, 651-656.

Chapter 3

Experimental

3.1 Materials

3.1.1 Chemicals

Sodium dodecyl sulfate (SDS, ≥99.0%), heptadecafluorooctanesulfonic acid (PFOS, ≥98.0%), dipalmitoylphosphatidylcholine (DPPC, ≥99.0%), *N*-(2-hydroxyethyl)piperazine-*N'*-(2-ethanesulfonic acid) (HEPES, ≥99.5%), 6-propionyl-2-dimethylaminonaphthalene (Prodan, ≥98.0%), tetraphenylporphyrin (TPP, >99%) 4-butylaniline (97%), sodium nitrite (≥99.0%), 1,4-dibromobutane (99%), anhydrous potassium carbonate (≥99.0%), potassium iodide (99.0%), sodium sulfite (98%), copper sulfate pentahydrate (≥98.0%), ammonium hydroxide (5.01 N solution in water), hydroxylamine hydrochloride (98%), potassium hydroxide (≥85%), 1,6-dibromohexane (96%), hydrochloric acid (conc. 37%), ethanol (HPLC grade), diethyl ether (≥99.5%), diethylene glycol (99%), tetraethylene glycol (99%), hexaethylene glycol (97%), 4-aminophenol (≥98.0%), dichloromethane, acetone and hexane were purchased from Sigma Aldrich. Deuterated-sodium dodecyl sulfate (d_{25}-SDS) was purchased from Santa Cruz Biotechnology. Sodium hydroxide (≥97%), chloroform (>99%), sodium chloride and chloroform were purchased from Fisher Scientific. Deuterium oxide (D_2O, >99.9%) was purchased from Apollo Scientific Limited. Phenol (>99.0%) was purchased from BDH Chemical Ltd. England. Trimethylamine (24% weight in water) was purchased from ACROS. All reagents and solvents were used as received. All solvents used for reactions were analytical grade and for characterisation were HPLC grade.

3.1.2 Polymers

The experimental information for the polymers used in this thesis is given in the relevant experimental section of each chapter. Due to their polydisperse nature, the concentration of polymers used throughout this thesis are expressed in terms of the concentration of monomer repeat units (r.u.).

3.2 Instrumentation

Some of the instrumentation considered more specialised, or used more frequently, is described in greater detail.

3.2.1 UV/Vis Absorption Spectroscopy

UV/Vis absorption spectra were recorded at room temperature on a Shimadzu UV2401 PC UV-Vis scanning spectrometer with a scanning slit width of 0.5 nm.

The kinetics experiments in Chapter 8 were carried out using an ILT 950 spectroradiometer over a range of 250-1050 nm with a resolution of 1.4 nm and 25 micron slits. Optical data were recorded using SpectraLight III software. A DH-2000 deuterium tungsten halogen light source was used to produce light over 215-2000 nm.

3.2.2 Photoluminescence (PL) Spectroscopy

Steady-state excitation and emission spectra were measured on a Fluorolog-3 (Horiba JobinYvon) spectrophotometer. Dilute samples with optical densities <0.1 were measured in 10 mm path length quartz cuvettes using a right-angle configuration. Concentrated samples were measured in quartz cells with an extremely short path length (0.1 mm) to prevent saturation of the detector signal, using front-face configuration. Spectra were corrected for the wavelength response of the system using correction factors supplied by the manufacturer. The emission and excitation slit widths were varied depending on the nature of the sample being investigated.

3.2.2.1 Fluorescence Quantum Yield

Fluorescence quantum yields (Φ_F) were determined from:[1]

$$\Phi_F^{cp} = \frac{\int I(\lambda)^{cp} d\lambda}{\int I(\lambda)^{ref} d\lambda} \cdot \frac{OD_{cp}}{OD_{ref}} \cdot \frac{n_{cp}^2}{n_{ref}^2} \cdot \Phi_F^{ref} \quad (3.1)$$

where n_{cp} and n_{ref} are the refractive indices of the solvent in which the compound (*cp*) and the reference (*ref*) are dissolved, respectively, OD_{cp} and OD_{ref} are the optical densities of the compound and the reference at the wavelength used and $\int I(\lambda)^x d\lambda$ is the integrated area of the emission spectrum of the compound and the reference. Tetraphenylporphyrin in toluene (λ_{ex} = 500 nm and Φ_F = 0.11) was used as the fluorescence standard.[2] The optical density of all solutions at the excitation wavelength was <0.1.[3]

3.2.3 Electrospray Ionisation Mass Spectrometry (ESI-MS)

ESI-MS were recorded by Dr Martin Feeney on a Bruker microTOF-Q III spectrometer interfaced to a Dionex UltiMate 3000 liquid chromatography system, in negative and positive modes as required. The instrument was calibrated using a tune mix solution (Agilent Technologies ESI-l low concentration tuning mix). Masses were recorded over the range 100-1200 *m/z*. Samples were prepared in HPLC grade solvent.

3.2.4 Fourier Transform Infrared (FTIR) Spectroscopy

FTIR spectra were recorded on a Perkin-Elmer Spectrum 100 FTIR spectrometer using a universal attenuated total reflection (ATR) sampling accessory. All spectra were recorded at room temperature over the range 4000-650 cm^{-1}, with a resolution of 4 cm^{-1}. The following abbreviations are used to describe the intensities: s, strong; m, medium; w, weak and br, broad.

3.2.5 ^1H and ^{13}C Nuclear Magnetic Resonance (NMR) Spectroscopy

Solution NMR spectroscopy was performed on a Bruker DPX 400 NMR instrument at 20 °C. ^1H and ^{13}C NMR spectra were obtained using an operating frequency of 400 and 151 MHz, respectively. Chemical shifts were calibrated against a tetramethylsilane (TMS) signal and are

reported in parts per million (ppm). $CDCl_3$ (δ_H = 7.26 ppm, singlet; δ_C = 77.16 ppm, triplet), D_2O (δ_H = 4.79 ppm, singlet) and d_6-DMSO (δ_H = 2.50 ppm, singlet; δ_C = 39.52 ppm, septuplet) were used as deuterated solvents.[4]

3.2.6 Melting Point Analysis

Measurements were performed on a Stuart SMP3 melting point apparatus. The heating block possesses 3 capillary tube holders. The heating rate was set at 0.5 °C min^{-1}.

3.2.7 Linear Dichroism (LD)

LD spectra were recorded on a Jasco J-815 CD spectrometer. Solutions were loaded into 1 mm path length Couette flow cells. Baseline line spectra were recorded as the LD spectra of the sample in the Couette flow cell with no spin. The baseline was then subtracted from the spectra recorded during a spin rate of ~3600 rpm. All measurements were recorded at 25 °C.

LD is the differential absorption between two orthogonal components of linear polarised light.[5] LD is used on systems that are either intrinsically oriented or can be oriented during the experiment. The orientation of long polymers or macromolecular assemblies in solution is commonly achieved by viscous drag created when the solution is flowed between two narrow walls. [6] A Couette flow LD cell (Figure 3.1a and 3.1b) has proven to be the most sample-efficient method of achieving this. The solution is placed in the annular gap (~500 μm) between two cylindrical cells, one of which rotates and causes alignment of the molecules.[6]

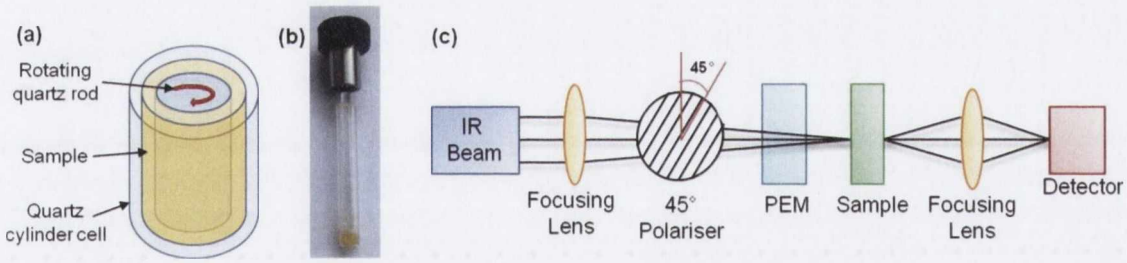


Figure 3.1 (a) Schematic representation and (b) photograph of a Couette flow cell used in the LD experiments. (c) Schematic diagram of the components and operation of LD; PEM – photoelastic modulator.

In an LD experiment, the difference in the absorption of light that is linearly polarised parallel and perpendicular to the orientation axis is measured,

$$LD = A_{\parallel} - A_{\perp} \tag{3.2}$$

where $A_{\parallel}$ is the absorption parallel to sample and $A_{\perp}$ is the absorption perpendicular to the orientation axis of the molecule.[6] The reduced linear dichroism (LD^r) is often a convenient pathlength- and concentration-independent summary of LD data for quantitative analysis:

$$LD^r = \frac{LD}{A} = \frac{A_{\parallel} - A_{\perp}}{A} = \frac{3}{2}S(3\cos^2\alpha - 1) \tag{3.3}$$

where A is the absorption of the sample under isotropic conditions *i.e.* not oriented, and S a scaling factor (the orientation factor) defining the efficiency of the macroscopic orientation. For uniaxial rods, S equals 1 for perfect orientation, and 0 for random orientation. α is defined as the angle between the transition moment responsible for the absorption of light at a particular wavelength and the orientation axis. If a transition moment (the direction of net electron displacement during an electronic transition) is aligned more parallel than perpendicular to the orientation axis, a positive LD signal is observed.[6] Conversely, if the direction of electron movement is more perpendicular than parallel to the orientation axis, a negative LD signal is observed.

3.2.8 Differential Scanning Calorimetry (DSC)

DSC was performed using a Perkin Elmer Pyris Diamond Differential Scanning Calorimeter. All samples were prepared in sealed aluminium crucibles and measurements were performed in a nitrogen atmosphere.

3.2.9 Epifluorescence Microscopy

Epifluorescence microscopy measurements were performed using an Olympus IX71 Epifluorescence Inverted Research Microscope with a Nikon BV-1A filter cube. The filter cube contained an excitation filter (λ_{ex} = 435 nm), dichroic mirror (band pass at λ_{dm} > 455 nm) and an emission (barrier) filter (λ_{em} > 470 nm). The dichroic mirror separates excitation light from fluorescence by reflecting light of one range of wavelengths and transmitting only light of another range of wavelengths.

3.2.10 Polarised Optical Microscopy (POM)

Room temperature POM experiments were carried out on a Nikon Eclipse E400 microscope with a 50 W halogen reflector lamp, equipped with an Olympus DP71 camera. Images were taken using a microscope magnification of 4×, 10× and 40× and a 530 nm polariser. Temperature-controlled POM measurements were carried out at the FORTH institute in Heraklion, Crete on a Zeiss Axio Scope.A.1 polarised optical microscope fitted with a N_2 cooled heat-stage.

POM uses plane-polarised light to analyse structures that are birefringent, *i.e.* structures that have two different refractive indices at right angles to one another.[7] The polarised optical microscope is equipped with two polarisers, one positioned in the light path before the sample, and the second, an analyser, placed in the optical pathway after the objective rear aperture. Image contrast arises from the interaction of plane-polarised light with a birefringent sample to produce two individual wave components that are each polarised in mutually perpendicular planes (Figure 3.2). The velocities of these components are different and vary with the propagation direction through the specimen. After exiting the specimen, the light components are out-of-phase, and interact to produce constructive and destructive interference when they pass through the analyser. As the molecules in a sample are unlikely to phase align in one direction, there will be

varying birefringence across the specimen. Thus, the features, known as *defect textures*, observed in POM images result from defects in molecular packing and the changing orientation of the liquid crystal detector. These characteristic defects and variations in birefringence (colour) can be used to identify different liquid crystalline phases.

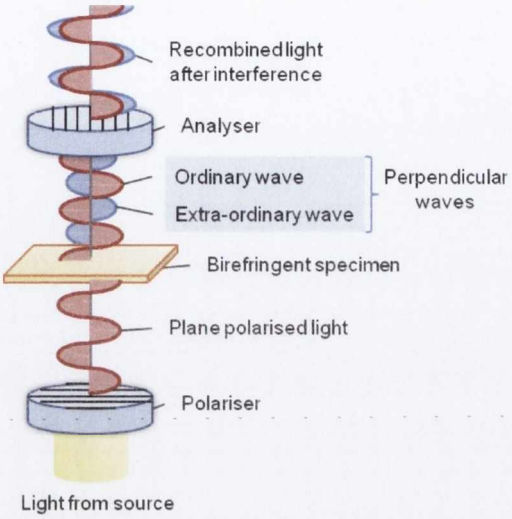


Figure 3.2 Schematic representation of the basic configuration of a polarised optical microscope.

3.2.11 Atomic force microscopy (AFM)

AFM measurements were performed using an Asylum Research MFP-3D™ Atomic Force Microscope mounted on an anti-vibration plinth, in the tapping mode at room temperature under ambient conditions. The silicon cantilevers used were 125 μm in length and had a resonance frequency of approximately 150 kHz. High resolution AFM measurements were performed using sharp diamond tips which were a kind gift from Adama Innovations. The silicon cantilevers had a spring constant of ~110 nN nm^{-1} and a resonance frequency of ~240 kHz. All raw AFM images were visualised and analysed using the Gwyddion 2.31 software.

Figure 3.3 shows the components of an AFM. AFM is a type of scanning probe microscopy that can provide a high resolution 3D profile of a surface by measuring the forces between a sharp probe (*i.e.* the tip) which is mounted on a oscillating cantilever spring.[8] The amount of force between the probe and the sample is dependent on the spring constant of the cantilever. This force is described by Hooke's law:

$$F = -kx \tag{3.4}$$

where F is the force (N), k is the spring constant (N m^{-1}) and x is the cantilever deflection (m). The position of the tip relative to the surface is controlled using a piezoelectronic scanner allowing for the measurement of extremely accurate length scales. As the tip scans across the surface, a laser is focused on the back of the reflective cantilever and the reflection is received by a position-sensitive photodetector, which in turn can be interpreted as topographical information. In tapping mode AFM the cantilever is oscillated over the sample at its resonance frequency, intermittently in

contact with the sample surface. Tapping mode AFM can be employed to produce high resolution images of samples that can be damaged in full contact mode.

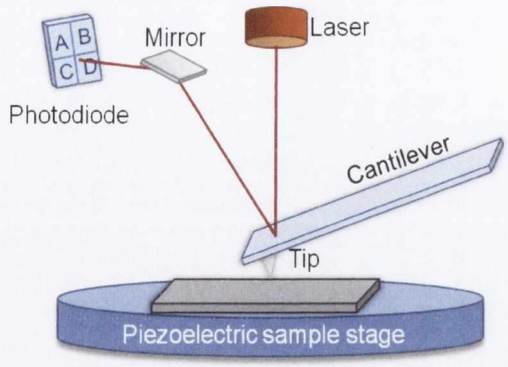


Figure 3.3 A schematic illustration of the components of an AFM.

3.2.12 Scanning Electron Microscopy (SEM) and Cryo-SEM

SEM measurements were performed using a Zeiss-Ultra Scanning Electron Microscope at an accelerating voltage of 2-5 kV using an In-lens (Carl Zeiss) detector. Each silicon wafer was mounted onto a carbon disc and a connection made between wafer and stage with Ag-DAG paint. Samples for cryo-SEM were plunged into sub-cooled N_2 to freeze the samples and then the samples were transferred *in-vacuo* to the cold-stage of the SEM cryo-preparation chamber. SEM measurements were performed by Dr Adam R. Patterson. Cryo-SEM measurements were performed by Dr Clodagh Dooley.

3.2.13 Dynamic Light Scattering (DLS) and Zeta Potential (ζ) Measurements

DLS and ζ measurements were performed using a Zetasizer Nano series nano-ZS (Malvern Instruments, U.K.). The apparatus is equipped with a He-Ne laser emitting at 633 nm and with a 4.0 mW power source. For DLS the instrument was set in the back-scattering configuration (175°). The hydrodynamic diameter (D_H) was calculated by assuming that the diffusing particles were monodispersed spheres. The D_H was averaged from 3 runs of approximately 20 measurements each. The autocorrelation function, $G(t)$, was calculated from the fluctuation of the scattering intensity with time,[9] which was fit with Equation 2.17 to yield the diffusion coefficient (D). The hydrodynamic radius, R_H (or D_H) can then be determined using the Stokes-Einstein equation (Equation 2.16). Cumulants analysis, which is a fit of the logarithm of the correlation function, is used to obtain the diffusion coefficient and a mean value for the size (Z-average) and width parameter of the distribution, the polydispersity index (PDI). As this method is limited to monomodal particle distributions with a Gaussian distribution, the Cumulant method becomes less reliable for multimodal distributions. Therefore, only qualitative observations regarding such systems can be made.

For ζ measurements, electrophoretic mobilities were recorded by a Laser-Doppler facility in the DLS unit. The ζ was calculated from the electrophoretic mobility, μ, using the Henry correction to the Smoluchowski's equation:[10]

$$\zeta = \mu\left(\frac{4\pi\eta}{\varepsilon^0}\right) \tag{3.5}$$

where η is the solvent viscosity and ε^0 is its static dielectric permittivity. Equation 3.5 places no restrictions on the particle shape, except for the assumption that the radii of curvature of the surface are much greater than the Debye's screening length, κ^{-1}. Smoluchowski's approximation holds because the electrical double layer thickness surrounding the vesicles, δ, is much lower than $D_H/2$.[11]

3.2.14 Multi-Angle Dynamic Light Scattering (MALS)

MALS measurements were performed on a Brookhaven multi-angle DLS instrument, equipped with a goniometer, water bath and 637 nm laser. To measure the hydrodynamic radii, R_H, DLS measurements were collected over a series of angles (30-150°), whilst the variation of scattering intensity as a function of scattering angle was collected to determine each radius of gyration. The theory for MALS is described in greater detail in Section 2.2.

3.2.15 Small-Angle Neutron Scattering (SANS)

SANS was carried out on the SANS2D or LOQ small-angle diffractometers at the ISIS Pulsed Neutron Source (STFC Rutherford Appleton Laboratory, Didcot, U.K.).[12] For the Sans2d instrument, a simultaneous q-range of ~0.004–0.6 $Å^{-1}$ was achieved utilising an incident wavelength range of 1.75–16.5 Å separated by time-of-flight and employing an instrument set-up of L1 = L2 = 4 m, where L is the sample-detector distance, with the 1 m^2 detector offset vertically 150 mm and sideways 150 mm. For LOQ, an incident wavelength range of 2.2–10 Å with a sample-to-detector distance of 4.1 m yielded a simultaneous q-range of ~0.009–0.24 $Å^{-1}$, as $q = (4\pi/\lambda)\sin(\theta/2)$, where λ is the wavelength and θ the scattering angle. The theory and instrumentation for SANS are described in greater detail in Section 2.2.

Samples were prepared in deuterated solvents to provide good neutron scattering contrast. Each raw scattering data set was corrected for the detector efficiency, sample transmission and background scattering and converted to scattering cross-section data ($\partial\sigma/\partial\Omega$ *vs.* q) using the instrument-specific software.[13] These data were placed on an absolute scale (cm^{-1}) using the scattering from a standard sample (a solid blend of hydrogenated and perdeuterated polystyrene) in accordance with established procedures.[14]

3.3 Data Analysis

3.3.1 Non-Linear Least Squares (NLLS) Fits

Each of the fitting procedures used throughout this thesis uses the method of NLLS analysis.[15] A NLLS analysis starts with a model that is assumed to describe the data. The goal is to test whether the model is consistent with the data and to obtain the parameter values for the model that provide the best match between the measured data, y_i, and calculated value, f_{ic}, using the assumed parameter values.[15] This is accomplished by minimising the goodness-of-fit parameter, which is given by:

$$\chi^2 = \sum_{i=1}^{n} \frac{(y_i - f_{ic})^2}{\sigma_i^2} \tag{3.6}$$

where σ_i is the standard deviation and n is the number of data points. If the standard deviation of the experimental data from the theoretical model is proportional to the value of the data, the following holds:

$$\sigma_i^2 = y_i$$
$$\chi^2 = \sum_{i=1}^{n} \frac{(y_i - f_{ic})^2}{y_i} \tag{3.7}$$

Thus, the value of χ^2 is the sum of the squared deviations between the measured data, y_i, and the value expected from the model, f_{ic}, each divided by the square of the measured data. The fit is then run in an iterative manner until the smallest sum of the squares is found.[15] Depending on the results and parameters produced by the previous fit, an iterative process involves incremental changes in the fitting parameters for each subsequent fit to find the minimum value of χ^2.

3.3.2 Procedure to Check SANS Model Fits

When possible each fit to the SANS data has been checked by calculating the theoretical volume mass of dry material the fit represents, φ_{dry}. φ_{dry} can be estimated from:

$$\varphi_{dry} = C_w \cdot \frac{P_m}{P_s} \tag{3.8}$$

where C_w is the mass of solid sample in the solution, P_m is the density of the mixture of sample and solvent and P_s is the density of the solid.

3.3.3 SANS Form Factor Models

The SANS scattering profiles in this thesis were modelled in the SasView programme using a non-linear least squares method.[16] The scattered SANS intensity for the following aggregate shapes is given by:

$$I(q) = NV^2P(q)S(q) + B_{inc} \tag{3.9}$$

where N is the number of particles per unit volume, V is the volume of the aggregate, $P(q)$ is the form or shape factor, $S(q)$ is the structure factor and B_{inc} is the isotropic incoherent background signal. Figure 3.4 shows a pictorial representation of the form factor models discussed in this thesis.

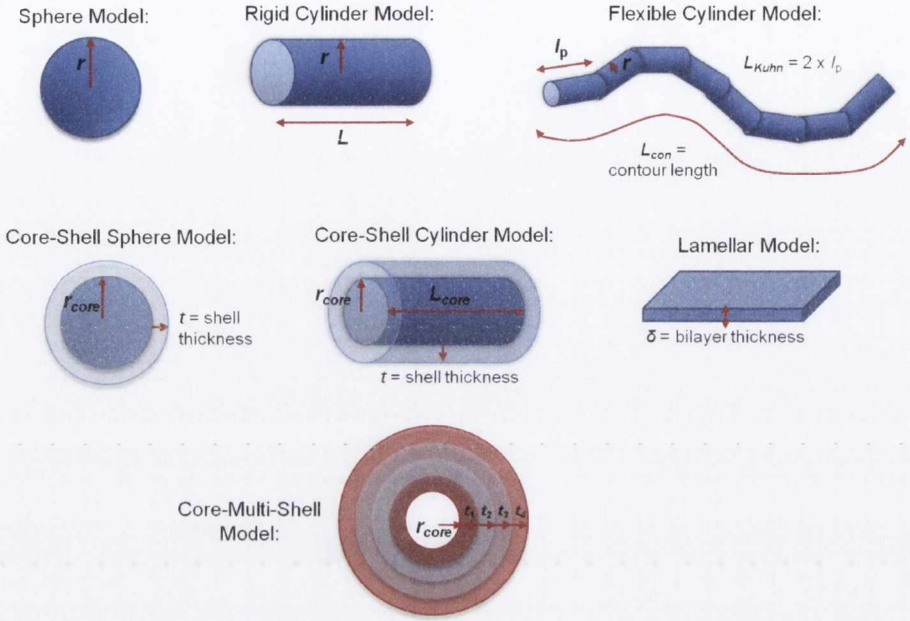


Figure 3.4 Schematic illustrations of the form factors, $P(q)$, used in the SANS fitting procedure. r is the radius of a sphere or cylinder, L is the length of a cylinder, l_p is the persistence length, L_{Kuhn} is the Kuhn length, and r_{core} and L_{core} are the radius and length of a core, respectively.

3.3.3.1 Spherical Model

This model provides the form factor, $P(q)$, for monodisperse spherical particles with uniform scattering length density. The form factor is normalised by the particle volume, V.[17]

$$P(q) = \frac{scale}{V}\left[\frac{3V(\Delta\rho)(\sin(qr) - qr\cos(qr))}{(qr)^3}\right]^2 + B_{inc} \tag{3.10}$$

where *scale* is a volume fraction, r is the radius of the sphere, $\Delta\rho$ (contrast) is the difference in scattering length density (SLD) between the scatterer (sphere) and the solvent and B_{inc} is the isotropic incoherent background signal.

3.3.3.2 Rigid Cylinder Model

The form or shape factor, $P(q, \alpha)$, for the Cylinder model is given by:[17, 18]

$$P(q,\alpha) = \frac{scale}{V}\int_0^{\pi/2} f^2(q)\sin\alpha\, d\alpha + B_{inc} \tag{3.11}$$

where

$$f(q) = 2V(\Delta\rho)\frac{J_1(qr\sin\alpha)}{qr\sin\alpha}\frac{\sin(\frac{qL\cos\alpha}{2})}{\frac{qL\cos\alpha}{2}} \tag{3.12}$$

where α is the angle between the axis of the cylinder and the q-vector, V is the total volume of the cylinder, L is the cylinder length, r is the radius of the cylinder, $\Delta\rho$ (contrast) is the difference in SLD between the scatterer (cylinder) and the solvent. J_1 is the first order Bessel function. The form factor is normalised by the particle volume so that the scale factor of the fit is the total particle volume fraction $\varphi = NV_s$ when $I(q)$ has been correctly reduced to absolute units.

3.3.3.3 Flexible Cylinder Model

The Flexible Cylinder model is based on the form factor for a rigid cylinder. A chain of contour length (total length), L_{con}, can be described as a chain of some number of locally stiff segments of persistence length, l_p. l_p is the length along the cylinder over which the flexible cylinder can be considered a rigid rod. The Kuhn length, L_{Kuhn}, in this model is also used to describe the stiffness of a chain, and is simply $L_{Kuhn} = 2 \times l_p$. The scattering function, $I_{WC}(q, L_{con}, L_{Kuhn}, R_{CS})$, for the Flexible Cylinder model is given by:[19-21]

$$I_{WC}(q, L_{con}, L_{Kuhn}, R_{CS}) = c\Delta\rho_m{}^2 M_W S_{WC}(q, L_{con}, L_{Kuhn}) P_{CS}(q, R_{CS}) + B_{inc} \quad (3.13)$$

where L_{con} is contour length, R_{CS} is the circular cross sectional radius, c is the concentration, M_W gives the average molecular weight of the cylinder, $\Delta\rho$ is the difference in scattering length density between the scatterer and the solvent, and B_{inc} is the background level. $P_{CS}(q, R_{CS})$ is the scattering function from the cross section of a rigid rod given by:

$$P_{CS}(q, R_{CS}) = \left[\frac{2J_1(qR_{CS})}{qR_{CS}}\right]^2 \quad (3.14)$$

where J_1 is the first order Bessel function. S_{WC} (q, L_{con}, L_{Kuhn}) is the scattering function of a single semi-flexible chain with excluded volume effects given by:

$$S_{WC}(q, L_{con}, L_{Kuhn}) = [1 - w(qR_g)] S_{Debye}(q, L_{con}, L_{Kuhn})$$

$$+ w(q, R_g)\left[1.22(qR_g)^{-\frac{1}{0.585}} + 0.4288(qR_g)^{-\frac{2}{0.585}} - 1.651(qR_g)^{-\frac{3}{0.585}}\right]$$

$$+ \frac{C(n_b)}{n_b}\left\{\frac{4}{15} + \frac{7}{15u} - \left(\frac{11}{15} + \frac{7}{15u}\right) \times e^{-u(q, L_{con}, L_{Kuhn})}\right\} \quad (3.15)$$

where R_g is the radius of gyration with excluded volume effects and $w(qR_g)$ is the empirical crossover function:

$$w(x) = \frac{1 + \tanh\left[\frac{x - 1.532}{0.1477}\right]}{2} \quad (3.16)$$

$$n_b = \frac{L_{con}}{L_{Kuhn}} \quad (3.17)$$

For $L_{con} > 10\, L_{Kuhn}$, $C(n_b) = 3.06 n_b^{-0.44}$ and for $L_{con} \leq 10\, L_{Kuhn}$, $C(n_b) = 1$.

S_{Debye} is the Debye function with $u = \langle R_g^2 \rangle q^2$

$$S_{Debye}(q, L_{con}, L_{Kuhn}) = \frac{2}{u(q, L_{con}, L_{Kuhn})}\{e^{-u(q,L_{con},L_{Kuhn})} + u(q, L_{con}, L_{Kuhn}) - 1\} \quad (3.18)$$

$$u(q, L_{con}, L_{Kuhn}) = \frac{L_{con}L_{Kuhn}}{6}\left\{1 - \frac{3}{2n_b} + \frac{3}{2n_b^2} + \frac{3}{4n_b^3}[1 - e^{-2n_b}]\right\} q^2 \quad (3.19)$$

$$\langle R_g^2 \rangle = \alpha(n_b)^2 \frac{L_{con}, L_{Kuhn}}{6} \quad (3.20)$$

$$u(q, L_{con}, L_{Kuhn}) = \alpha(n_b)^2 \frac{L_{con}, L_{Kuhn}}{6} q^2 \quad (3.21)$$

where $\alpha(n_b)$ is the expression factor which follows the following empirical expression:

$$\alpha(x) = \sqrt{\left[1 + \left(\frac{x}{3.12}\right)^2 + \left(\frac{x}{8.67}\right)^3\right]^{0.176/3}} \quad (3.22)$$

3.3.3.4 Core-Shell-Sphere Model

The form factor, $P(q)$, for the Core-Shell-Sphere model is given by:[17]

$$\varphi V_s P(q) = \frac{scale}{V_s} f^2(q) \quad (3.23)$$

where

$$f(q) = 3V_c(\rho_c - \rho_s)\frac{[\sin(qr_c) - qr_c\cos(qr_c)]}{(qr_c)^3}$$

$$+3V_S(\rho_c - \rho_{solv})\frac{[\sin(qr_s) - qr_c\cos(qr_s)]}{(qr_s)^3} \quad (3.24)$$

where V_s is the total volume of the outer shell, V_c is the volume of the core, r_c is the radius of the core, r_s is the radius of the core and shell, $r_s = r_c + t$ where t is the thickness of the shell, and ρ_c, ρ_s and ρ_{solv} are the scattering length densities of the core, shell and solvent, respectively.[17] This model provides the form factor for a sphere with a core-shell SLD profile. The form factor is normalised by the particle volume so that the scale factor of the fit is the total particle volume fraction $\varphi = NV_s$ when $I(q)$ has been correctly reduced to absolute units. The fitting procedure included polydispersity in the radius of the spheres and instrumental q-smearing was applied to provide better fits at the high q end of the SANS data.

3.3.3.5 Core-Shell-Cylinder Model

The form or shape factor, $P(q, \alpha)$, for the Core-Shell-Cylinder model is given by:[22]

$$\varphi V_s P(q, \alpha) = \frac{scale}{V_s}\int_0^{\pi/2} f^2(q)\, d\alpha \quad (3.25)$$

where

$$f(q) = \frac{2(\rho_c - \rho_s)V_c \sin\left[qLcos(\frac{\alpha}{2})\right]}{\left[qLcos\left(\frac{\alpha}{2}\right)\right]\frac{J_1[qrsin\alpha]}{[qrsin\alpha]}} + \frac{2(\rho_s - \rho_{solv})V_s \sin\left[q(L+t)cos(\frac{\alpha}{2})\right]}{\left[q(L+t)cos\left(\frac{\alpha}{2}\right)\right]\frac{J_1[q(r+t)sin\alpha]}{[q(r+t)sin\alpha]}} \quad (3.26)$$

where α is the angle between the axis of the cylinder and the q-vector, V_s is the total volume of the core plus shell, V_c is the volume of the core, L is the length of the core, r is the radius of the core, t is the thickness of the shell, and ρ_c, ρ_s and ρ_{solv} are the SLDs of the core, shell and solvent, respectively.[22] J_1 is the first order Bessel function. This model provides the form factor for a cylinder with a core-shell scattering length density profile. The form factor is normalised by the particle volume.

3.3.3.6 Core Multi-Shell Model

In this model, four shells were used to represent the phospholipid head-group and hydrophobic chain regions of the inner leaflet, and the phospholipid head-group and hydrophobic chain regions of the outer leaflet. The core of the model contains the same solution background as exists outside the vesicles. The scattering intensity from the four-shell model is given by:[23]

$$I(q) = A\left[\sum_{i=1}^{4} \frac{3V_i(\rho_i - \rho_0)j_1(qt_i)}{qd_i}\right]^2 S(q) + B_{inc} \quad (3.27)$$

where A is a scaling factor, B_{inc} is the isotropic incoherent background signal, ρ_i are the SLDs of each shell, ρ_0 is the neutron SLD of the core, which is equal to that of the buffer solution, V_i is the volume of each shell and $j_1(x)$ is the Bessel function. The t_i (i = 1,2,3,4) are the radii of the shells in the model, representing the thickness of the head-group and the chain region of the inner leaflet, and the thickness of the head-group and the chain region of the outer leaflet, respectively. $S(q)$ is the structure factor for inter-vesicle interactions and is equal to unity ($S(q)$ = 1) for the dilute vesicle solutions.

3.3.3.7 Lamellar Sheet Model

The scattered SANS intensity in the lamellar model is given by:[24, 25]

$$I(q) = [2\pi VP(q)S(q)]/(dq^2) + B_{inc} \quad (3.28)$$

where V is the scattering volume, d is the lamellar spacing and B_{inc} is the isotropic incoherent background signal. The interparticle structure factor, $S(q)$, which accounts for the interference of scattering from different particles in concentrated suspensions, is assumed to be one. The form factor, $P(q)$, for neutron scattering from lamellar sheets is given by:[24, 25]

$$P(q) = \frac{2\Delta\rho^2}{q^2}\left(1 - \cos(q\delta)\, e^{-\frac{q^2\sigma^2}{2}}\right) \quad (3.29)$$

where $\Delta\rho^2$ is the difference in SLD between the scatterer and the solvent (*i.e.* the contrast), δ is the bilayer thickness and σ is arbitrarily fixed at $\delta/4$.

3.3.4 Aggregation numbers

From the SANS fitting it is possible to calculate the number of polymers or surfactant molecules in an average particle using:

$$N_{agg} = \frac{V_{dry-aggregate}}{V_{molar}} \times N_A \tag{3.30}$$

where N_{agg} is the aggregation number, $V_{dry\text{-}aggregate}$ is the volume of the dry aggregate, V_{molar} is the molar volume and N_A is Avogadro's number, $N_A = 6.0221 \times 10^{23}$ mol^{-1}. Note that in the case of core-shell models; $V_{dry\text{-}aggregate} = V_{dry\text{-}core} + V_{dry\text{-}shell}$, where $V_{dry\text{-}core}$ is the volume of the dry core and $V_{dry\text{-}shell}$ is the volume of the dry shell.

3.4 References

1. A. M. Brouer, *Pure Appl. Chem.*, 2011, **83**, 2213-2218.
2. P. G. Seybold and M. Gouterman, *J. Mol. Spectrosc.*, 1969, **31**, 1-13.
3. M. Knaapila, R. C. Evans, V. M. Garamus, L. s. Almásy, N. m. K. Székely, A. Gutacker, U. Scherf and H. D. Burrows, *Langmuir*, 2010, **26**, 15634-15643.
4. H. E. Gottlieb, V. Kotlyar and A. Nudelman, *J. Org. Chem.*, 1997, **62**, 7512-7515.
5. A. Rodger and B. Nordén, *Circular Dichroism and Linear Dichroism*, Oxford University Press, 1997.
6. A. Rodger, R. Marrington, M. A. Geeves, M. Hicks, L. de Alwis, D. J. Halsall and T. R. Dafforn, *Phys. Chem. Chem. Phys.*, 2006, **8**, 3161-3171.
7. L. S. Hirst, *Fundementals of Soft Matter Science* CRC Press, Taylor and Francis Group, Boca Raton, U.S.A., 2013.
8. G. Binnig, C. F. Quate and C. Gerber, *Phys. Rev. Lett.*, 1986, **56**, 930-933.
9. *International Standard ISO22412 Particle Size Analysis - Dynamic Light Scattering*, International Organisation for Standardisation (ISO), 2008.
10. J. R. Hunter, *Zeta Potential in Colloid Science.*, Academic Press, London, 1981
11. C. Pucci, A. Scipioni and C. La Mesa, *Soft Matter*, 2012, **8**, 9669-9675.
12. R. K. Heenan, S. E. Rogers, D. Turner, A. E. Terry, J. Treadgold and S. M. King, *Neutron News*, 2011, **22**, 19-21.
13. *http://www.mantidproject.org.*
14. G. D. Wignall and F. S. Bates, *J. Appl. Crystallogr.*, 1987, **20**, 28-40.
15. J. R. Lakowicz, *Principles of Fluorescence Spectroscopy*, Third edn., Kluwer Academic Publishers, New York, 2006, pp. 97-115.
16. *http://www.sasview.org/index.html.*
17. A. Guinier and G. Fournet, *Small Angle Scattering of X-rays*, John Wiley and Sons, 1955.
18. A. A. Golosova, J. Adelsberger, A. Sepe, M. A. Niedermeier, P. Lindner, S. S. Funari, R. Jordan and C. M. Papadakis, *J. Phys. Chem. C*, 2012, **116**, 15765-15774.
19. W.-R. Chen, P. D. Butler and L. J. Magid, *Langmuir*, 2006, **22**, 6539-6548.
20. J. S. Pedersen and P. Schurtenberger, *Macromolecules*, 1996, **29**, 7602-7612.
21. K.-S. Jang, H. J. Lee, H.-M. Yang, E. J. An, T.-H. Kim, S.-M. Choi and J.-D. Kim, *Soft Matter*, 2008, **4**, 349-356.
22. I. Livsey, *J. Chem. Soc., Faraday Trans. 2*, 1987, **83**, 1445-1452.
23. S. Qian and W. T. Heller, *J. Phys. Chem. B*, 2011, **115**, 9831-9837.
24. J. Berghausen, J. Zipfel, P. Lindner and W. Richtering, *J. Phys. Chem. B*, 2001, **105**, 11081-11088.

25. F. Nallet, R. Laversanne and D. Roux, *J. Phys. II France*, 1993, **3**, 487-502.

Chapter 4

Solvent-Mediated Self-Assembly of Polythiophene-Polythiophene All-Conjugated Diblock Polyelectrolytes

The work presented in this chapter has been published in part in:

A. Thomas, J. E. Houston, N. Van den Brande, J. De Winter, M. Chevrier, R. K. Heenan, A. E. Terry, S. Richeter, A. Mehdi, B. Van Mele, P. Dubois, R. Lazzaroni, P. Gerbaux, R. C. Evans and S. Clément, All-Conjugated Cationic Copolythiophene "Rod-Rod" Block Copolyelectrolytes: Synthesis, Optical Properties and Solvent-Dependent Assembly, *Polym. Chem.*, 2014, **5**, 3352-3362.

4.1 Introduction

All-conjugated block copolymers have emerged as promising materials for optoelectronic devices due to the unique combination of their inherent semiconducting properties and their ability to self-assemble at the nanoscale.[1] Block copolymers are composed of at least two different conjugated blocks which are covalently linked. The combination of one ionic polyelectrolyte block and at least one neutral block leads to amphiphilic block copolymers.[2] Such block copolyelectrolytes exhibit a natural tendency to self-assemble into nanodomains due to the different solubilities of the respective blocks.[3] As a result, the polarity of the solvent medium can be used to control the nanostructures formed, often yielding exotic self-assembly structures, such as core-shell spheres,[4] cylinders,[5] toroids[6] and gyroids.[7]

In di- or tri-block copolymers, the extent of phase separation is directly related to the chemical structure and length of the various blocks. Scherf *et al.* developed a family of amphiphilic all-conjugated poly(thiophene) (PT)-poly(fluorene) (PF) diblock copolymers, which contained an identical hydrophobic PF block, poly[9,9-bis(2-ethylhexyl)fluorene] (PF2/6), and different hydrophilic PT blocks in which the ionic pendant groups were varied.[2, 3] One analogue contained a cationic ammonium group (PF2/6-P3TMAHT) and another contained a cationic pyridyl group (PF2/6-P3PyHT), both of which were studied in H_2O/THF[2] and H_2O/MeOH[8] mixtures. THF and MeOH were chosen as non-selective solvents for either block, while H_2O was chosen as a selective solvent for the hydrophilic charged PT blocks. In these studies, the amphiphilic combination of hydrophobic and hydrophilic blocks in a single polymer was found to successfully drive phase separation and self-assembly into core-shell vesicles (polymersomes) with the charged PT blocks located in the outer shells. At higher concentrations a transition into lamellar aggregates was observed using AFM.

Amphiphilic all-conjugated diblock copolymers have attracted particular attention as the donor material in BHJ solar cells (Figure 1.4b).[9] Simple blends of the *D* and *A* exhibit significant structural disorder as they rely on random phase separation of the constituents. Consequently, many domains are too large (exciton loss), too small (charge recombination) or discontinuous (poor carrier mobility), leading to a reduced device perfomance.[10, 11] Therefore, amphiphilic diblock copolymers, with the ability to spontaneously phase separate into controlled exotic architectures on the nanometre scale, have been utilised to provide a versatile approach to manipulate the morphology of the active layer and achieve highly efficient devices.[12]

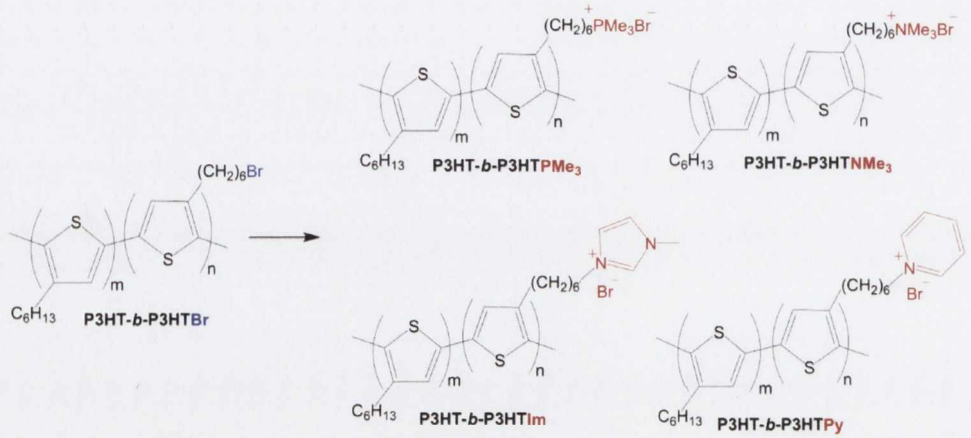
Poly(thiophene)s, such as those in the CPEs mentioned above, make excellent donor materials in polymer solar cells due to their good optical absorption overlap with the solar spectrum, large molar absorption coefficients and high charge carrier mobilities.[13] Consequently, all-conjugated diblock poly(thiophene)-poly(thiophene) copolymers, such as poly(3-butylthiophene)-*b*-poly(3-hexylthiophene) (P3BHT-*b*-P3HT), have been exploited as donor materials exhibiting excellent control over the molecular organisation and nanoscale morphology

within BHJ OPVs.[14] A blend of P3BHT with the fullerene-derivative [6,6]-phenyl-C_{71}-butyric acid methyl ester ($PC_{71}BM$) in a photovoltaic device yielded a reasonable power conversion efficiency of 4.02% which was attributed to the formation of small crystalline domains (10.4 nm) which are comparable to the exciton diffusion length in poly(thiophene)s.[15] Furthermore, the refined phase separation on the nanoscale resulted in a more homogeneous polymer/fullerene interface which is understood to maximise charge generation.

Charge carriers typically move faster in crystalline regions of CP films than in the amorphous regions due to the high degree of π-π stacking within the crystalline region.[16] However, CPs displaying high-crystallinity have proven inadequate for soft electronic applications due to their poor mechanical resilience.[17] In contrast, the random polymer chain orientation in purely amorphous regions reduces interaction between the conjugated backbones and hinders charge transport.[18] Son *et al.* found that the random copolymer, poly(3-hexylthiophene-*co*-thiophene) (RP33), which exhibits low crystallinity, displayed a greatly enhanced field-effect mobility (1.37 $cm^2\ V^{-1}\ s^{-1}$) when compared to the highly crystalline pure P3HT (0.19 $cm^2\ V^{-1}\ s^{-1}$).[16] It was suggested that localised aggregates of well-ordered polymer chains (*i.e.* crystalline regions) increased interchain charge transport.[16] These aggregates effectively act as transport junctions between the conjugated backbones, enhancing charge carrier delocalisation in the amorphous regions. Therefore, the development of molecular design strategies to simultaneously form and connect regions of structural order (across the nano-micrometre scale) in P3HT-type materials could play a key role in the design of the next generation of OPV devices exhibiting high PCEs.

4.1.1 Aims of this work

In this chapter the use of solvent mediation to control the self-assembly of a family amphiphillic diblock poly(thiophene)-poly(thiophene) copolymers for potential use as electron donor materials in OPV devices will be investigated. The diblock copolymers all contain the same neutral hydrophobic P3HT block, but the identity of the pendant cationic group on the hydrophillic block is varied (Scheme 4.1).



Scheme 4.1 Chemical structures of the bromide precursor, P3HT-*b*-P3HTBr, and the all-conjugated diblock poly(thiophene)s, **P3HT-*b*-P3HTPMe$_3$**, **P3HT-*b*-P3HTNMe$_3$**, **P3HT-*b*-P3HTIm** and **P3HT-*b*-P3HTPy**, used in this study.

The specific aims include:

- to investigate the spectral and photophysical behaviour of cationic, all-conjugated poly(thiophene)-poly(thiophene) diblock copolymers in methanolic and aqueous solutions. MeOH and H_2O are expected to be non-selective solvents for the non-charged P3HT block. In contrast, both solvents should be selective solvents for the charged CPE block, but to a greater extent for H_2O. MeOH and H_2O are non-toxic and are extremely attractive for solution-based processing of OPV devices;
- to explore whether the polarity of the medium offers control over the CPE nanostructure. CPEs have hydrophobic backbones and hydrophilic side-chains, which is known to lead to aggregation and self-assembly in solution;
- to study the effect of the ionic strength of different cationic pendant groups on the self-assembly of these CPEs in solution;
- to determine if the nanoscale structure of aggregates formed in the solution phase is retained in the subsequently prepared thin films.

4.2 Experimental Section

4.2.1 Materials

Poly[(3-hexylthiophene-2,5-diyl)-*b*-((1-methylimidazolium-3-yl)hexylthiophene-2,5-diyl)] (**P3HT-*b*-P3HTIm**), poly[(3-hexylthiophene-2,5-diyl)-*b*-((pyridiniumhexyl)thiophene-2,5-diyl)] (**P3HT-*b*-P3HTPy**), poly[(3-hexylthiophene-2,5-diyl)-*b*-((trimethylammoniumhexyl)thiophene-2,5-diyl)] (**P3HT-*b*-P3HTNMe$_3$**) and poly[(3-hexylthiophene-2,5-diyl)-*b*-((trimethylphosphoniumyl-hexyl)thiophene-2,5-diyl)] (**P3HT-*b*-P3HTPMe$_3$**) were a kind gift from Dr Amandine Thomas and Dr Sébastian Clément at the Institut Charles Gerhardt, Université de Montpellier. The all-conjugated diblock copolyelectrolytes were synthesised from the bromide precursor (P3HT-*b*-P3HTBr) with a number-average molecular weight (M_n) 11,000 g mol^{-1} and a polydispersity index (weight-averaged molecular weight (M_w)/M_n) of 1.3. It is not possible to measure the exact molecular weight of the **P3HT-*b*-CPEs** due to strong interaction of the polyelectrolytes with the GPC column. All solvents were filtered through a 0.2 μm nylon syringe filter prior to use. Stock solutions (1 mg mL^{-1}) were prepared in 100% MeOH and 100% millipore H_2O. Samples in MeOH required gentle heating to enable them to completely dissolve.

4.2.2 Methods

The instrumentation for UV/Vis absorption and PL spectroscopy, DLS, SANS and AFM are described in Chapter 3.

UV/Vis absorption and PL titration procedure: For each measurement, stock solutions of each CPE (1 mg mL^{-1}) in 100% H_2O and 100% MeOH were diluted until they had a maximum λ_{abs} of ~0.1.

Further dilution with MeOH or H_2O was used to achieve the required H_2O/MeOH volume ratio. Dilution effects were accounted for in the UV/Vis absorption and PL spectra.

DLS titration procedure: Solutions of CPE (0.35 μg mL^{-1}) were prepared and the hydrodynamic diameters (D_H) were taken as an average of 3 runs of approximately 20 measurements each.

AFM measurements: Polymer films were prepared by drop-casting CPE solutions in H_2O (3.5 μg mL^{-1}), MeOH (3.5-7.0 μg mL^{-1}) and 50:50 (*v*/*v*) H_2O/MeOH (3.5 μg mL^{-1}) onto freshly cleaved mica.

SANS measurements: **P3HT-*b*-P3HTIm** and **P3HT-*b*-P3HTPy** samples for SANS measurements were prepared in deuterated solvents (10 mg mL^{-1}) to provide good neutron scattering contrast. The scattering functions were fit using non-linear least-squares analysis to Core-Shell Cylinder and Core-Shell Sphere models using the SasView programme.[19, 20] Full details of the mathematical models can be found in Chapter 2.

4.3 Results

4.3.1 UV/Vis Absorption and Steady-State PL Spectroscopy

CPEs have hydrophobic PT backbones and hydrophilic side-chains, which are known to drive aggregation and self-assembly in solution. Since the optoelectronic properties of poly(thiophene)s are known to be inherently linked to the nanoscale morphology, the optical properties for all copolymers in the **P3HT-*b*-CPEs** series were investigated by UV/Vis absorption and PL spectroscopy. The optical properties for all **P3HT-*b*-CPEs** were similar; as such the spectra for **P3HT-*b*-P3HTPy** are shown as a representative example.

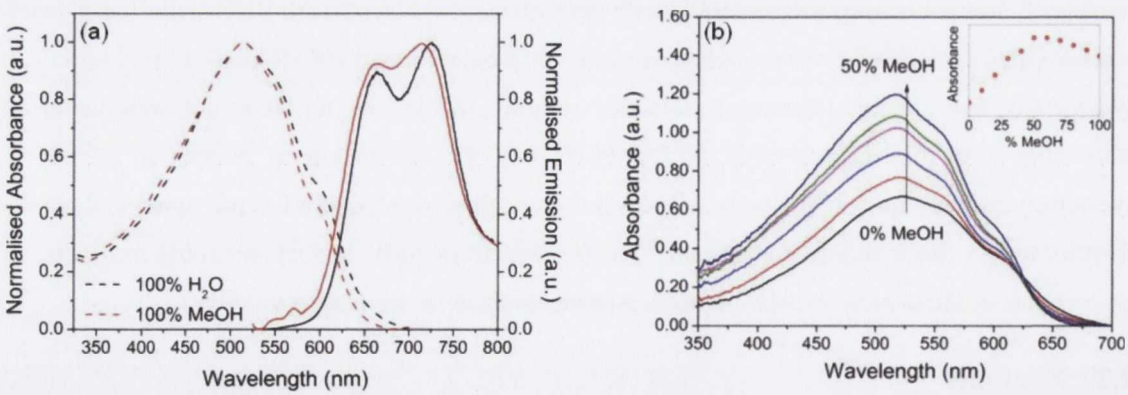


Figure 4.1 (a) Normalised UV/Vis absorption (dashed line) and emission spectra (bold line) for **P3HT-*b*-P3HTPy** in 100% H_2O (black line) and 100% MeOH (red line) (λ_{ex} = 515 nm). (b) UV/Vis absorption spectra of **P3HT-*b*-P3HTPy** in 0% MeOH to 50:50 (*v*/*v*) H_2O/MeOH. Inset: The absorbance at 522 nm for the CPE in each solvent combination.

Figure 4.1a shows the normalised UV/Vis absorption spectra of **P3HT-*b*-P3HTPy** in 100% H_2O and 100% MeOH. A single broad band centred at 522 nm is observed in both solvents,

which is characteristic of poly(thiophene)s and is assigned to the π-π^* electronic transition on the thiophene ring.[21] The UV/Vis absorption spectrum in MeOH is slightly sharper and shows more vibronic structure.[22] This could be attributed to increased packing of one or both of the PT blocks, hindering the free rotation of the thiophene units along the polymer backbone. Figure 4.1b shows the UV/Vis absorption spectra for **P3HT-*b*-P3HTPy** in 100% MeOH and upon subsequent addition of H_2O. The absorbance was found to increase as the percentage of H_2O increased. The greatest absorbance was recorded in the 50:50 (*v*/*v*) MeOH/H_2O mixture (Figure 4.1b inset).

Figure 4.2 shows selected PL and excitation spectra for **P3HT-*b*-P3HTPy** in different MeOH/H_2O mixtures. The optical properties of PTs are known to be very responsive to chain aggregation.[23] The PL spectra for **P3HT-*b*-P3HTPy** show one electronic band with vibronic modes at ~560 nm, ~660 nm and ~730 nm, which can be assigned to vibronic progression of the C=C stretching mode ($\Delta E \approx 0.15$ eV) in the PT backbone of the polymer blocks.[24] As with the UV/Vis absorption spectra, the vibronic structure suggests ordered conformation of the thiophene units along the CPE backbone.[22] Upon addition of H_2O to the 100% MeOH sample, the PL intensity was found to increase, agreeing with the observed changes in the UV/Vis absorption spectra, reaching its maximum at 50:50 (*v*/*v*) MeOH/H_2O. There is no observed shift in the emission maximum in any of the solvent mixtures.

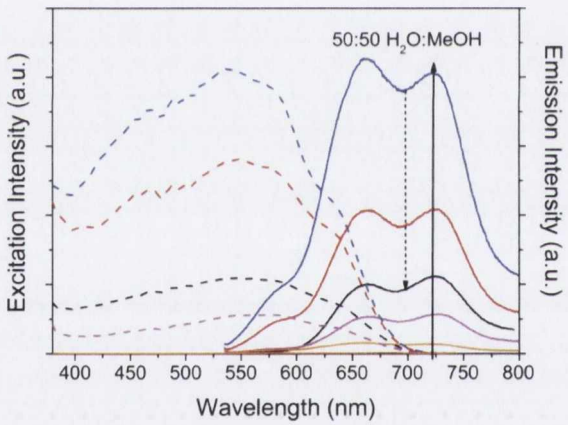


Figure 4.2 Selected excitation (λ_{em} = 730 nm) and PL (λ_{ex} = 515 nm) spectra of **P3HT-*b*-P3HTPy** in 100% MeOH (orange line), 30:70 (*v*/*v*) H_2O/MeOH (pink line), 50:50 (*v*/*v*) H_2O/MeOH (blue line), 70:30 (*v*/*v*) H_2O/MeOH (red line) and 100% H_2O (black line).

Fluorescence quantum yields (Φ_F) were determined to quantify the extent of fluorescence enhancement for the CPEs in MeOH, H_2O and H_2O/MeOH mixtures (Figure 4.3). In general, for **P3HT-*b*-P3HTPy**, **P3HT-*b*-P3HTNMe$_3$** and **P3HT-*b*-P3HTPMe$_3$**, Φ_F ~0.5% were obtained in MeOH and Φ_F ~1.0-1.5% in H_2O. Solvent mixing of MeOH and H_2O leads to an increase in Φ_F, the maximum being recorded at 50:50 (*v*/*v*) MeOH/H_2O (Φ_F ~2.5-5.5%). For **P3HT-*b*-P3HTIm** the case is slightly different with Φ_F ~1.25% at 50:50 (*v*/*v*) MeOH/H_2O and increasing to Φ_F ~3% in 100% MeOH. The increase in Φ_F in mixed solvents suggests improved solubility of the charged and non-charged blocks. The break-up of aggregates leads to decreased exciton mobility and a

decreased probability of electron-hole recombination *via* non-radiative trap sites (non-radiative decay), and hence, the increase in Φ_F.[25] Φ_F values ranging from 0.01 to 0.05 are somewhat typical for PTs in films or poor solvents.[26, 27] In comparison, the Φ_F values recorded for PT in good solvents, such as P3HT in THF, can be as high as 40%.[27]

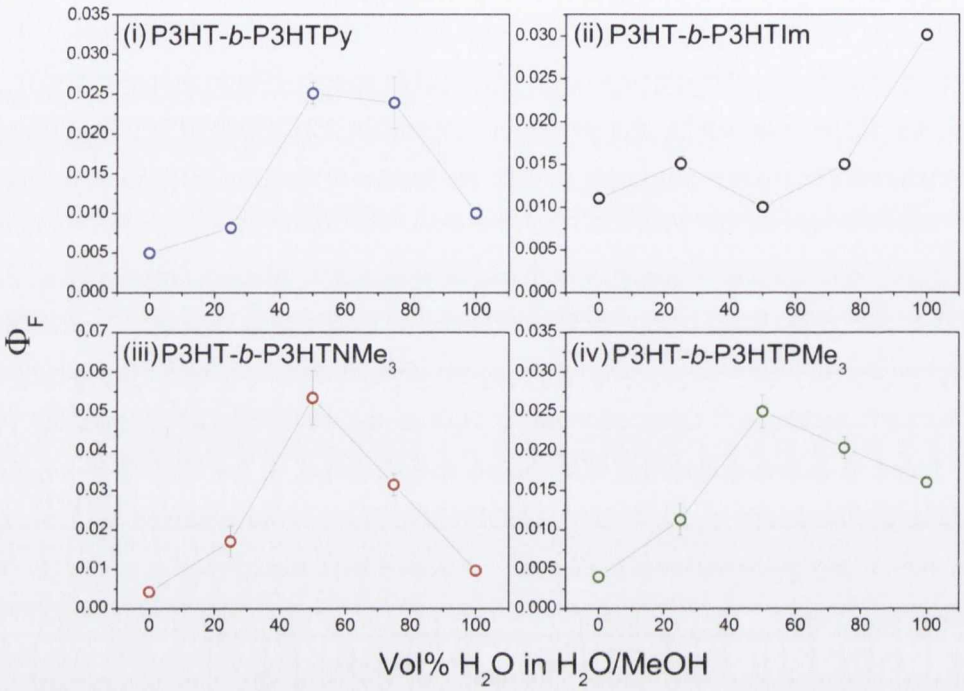


Figure 4.3 Fluorescence quantum yields (Φ_F) of **P3HT-*b*-CPEs** in H_2O/MeOH solvent mixtures. Legend: **P3HT-*b*-P3HTPy** (blue circles), **P3HT-*b*-P3HTIm** (black circles), **P3HT-*b*-P3HTNMe$_3$** (red circles) and **P3HT-*b*-P3HTPMe$_3$** (green circles).

4.3.2 Solution-Phase Structures

It is now well-understood that the nanoscale morphology and optoelectronic properties of CPEs are inherently-linked. Therefore, the UV/Vis absorption and PL studies suggest that solvent variation from H_2O to MeOH corresponds to a change in the preferred geometry of **P3HT-*b*-CPEs** in solution. To investigate this further, DLS and SANS were used to determine their aggregation behaviour in solution.

4.3.2.1 Dynamic Light Scattering

DLS measurements were performed to determine the hydrodynamic diameter (D_H) of the CPE aggregates in MeOH, H_2O and H_2O/MeOH mixtures (Figure 4.4). Samples typically exhibited monomodal distributions of low polydispersity in solution, as calculated using the Cumulants analysis. Generally, the smallest aggregates were obtained in 100% MeOH (~100 nm for **P3HT-*b*-P3HTNMe$_3$**, **P3HT-*b*-P3HTPy** and **P3HT-*b*-P3HTIm** and ~250 nm for **P3HT-*b*-P3HTPMe$_3$**), with slightly larger aggregates in 100% H_2O (~100 nm for **P3HT-*b*-P3HTPy**, ~200 nm for **P3HT-*b*-P3HTIm**, ~300 nm for **P3HT-*b*-P3HTNMe$_3$** and ~260 nm for **P3HT-*b*-P3HTPMe$_3$**). The

largest aggregates (~400-600 nm) were recorded in solvent mixtures between 50-80% (*v*/*v*) H_2O/MeOH for **P3HT-*b*-P3HTNMe$_3$**, **P3HT-*b*-P3HTIm** and **P3HT-*b*-P3HTPMe$_3$** and 20% (*v*/*v*) H_2O/MeOH for **P3HT-*b*-P3HTPy**. This may be due to the increased solubility of both the neutral P3HT block and charged P3HT-CPE blocks, resulting in swelling of the structure and allowing for the chains to become less packed as a result of the associating solvent molecules.

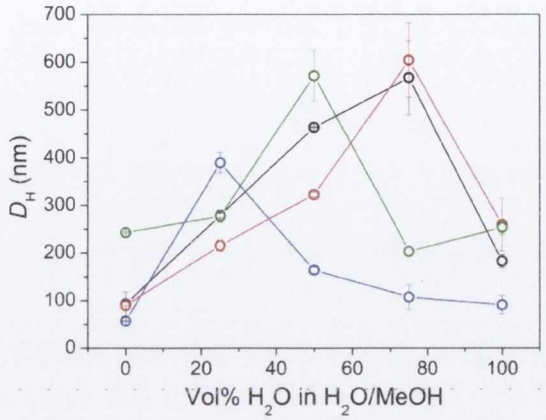


Figure 4.4 DLS studies of the effect of solvent on the size of aggregates of CPE. Hydrodynamic diameter (D_H, *Z*-average) of **P3HT-*b*-CPEs** in H_2O/MeOH solvent mixtures (0.35 μg mL^{-1}). Legend: **P3HT-*b*-P3HTPy** (blue circles), **P3HT-*b*-P3HTIm** (black circles), **P3HT-*b*-P3HTNMe$_3$** (red circles) and **P3HT-*b*-P3HTPMe$_3$** (green circles). The solid lines serve only to guide the eye.

4.3.2.2 Small-Angle Neutron Scattering

SANS was used to obtain deeper insight into the nanoscale organisation of **P3HT-*b*-P3HTPy** in D_2O, d_4-MeOD and 50:50 (*v*/*v*) D_2O/d_4-MeOD. The data were initially interpreted using scaling concepts to provide information on the aggregate shape.[28] Figure 4.5 shows the SANS data for **P3HT-*b*-P3HTPy** in D_2O, d_4-MeOD and their 50:50 (*v*/*v*) mixture. All three solvents yielded similar scattering profiles with a shoulder at q = 0.02 Å^{-1} and an upturn at q = 0.08 Å^{-1}; however, they did differ in the gradient of their slopes. The SANS response at high q (q>0.07) stems from the internal structure of the aggregate. The excess scatter for some samples at q~0.1-0.2 Å^{-1} is likely to be due to internal structure within the aggregates, perhaps due to repulsive interactions between similarly charged polymer chains.[22, 29, 30] The upturn in I(q) at q<0.08 Å^{-1} is indicative of particle aggregation. The power law scaling for the intermediate q region (0.02<q<0.07) varies from $q^{-4.2}$ in d_4-MeOD to $q^{-5.2}$ in D_2O. The low q region (q<0.02) decays as ~$q^{-5/3}$ and is typical of scattering from cylinder aggregates or from individual chains.[31] The observation window of these SANS experiments ranged from 2 to 160 nm, well beyond the length of these CPEs (22.7-25.4 nm).[31] Therefore, fully dissolved rod-rod polymers would be expected to exhibit a monotonic -1 decay, with a Guinier plateau in the low q regime. This was not observed for any of the scattering curves which implied that in all the solvents polymer associations are present.

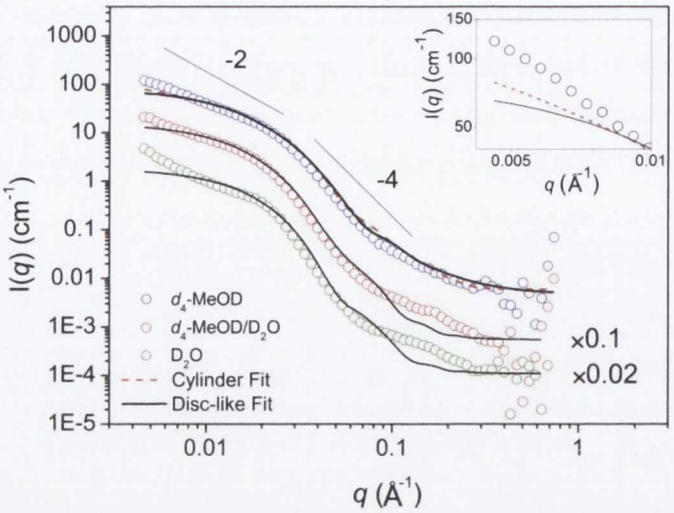


Figure 4.5 SANS data for **P3HT-*b*-P3HTPy** in d_4-MeOD, 50:50 (*v*/*v*) d_4-MeOD/D_2O and D_2O (10 mg mL^{-1}). For clarity, the d_4-MeOD/D_2O and D_2O data have been offset by 0.1 and 0.02, respectively. Straight lines show -2 and -4 decays for comparison. The solid black lines show the disc-like fits obtained using the Core-Shell Cylinder model for each solvent mixture. Only **P3HT-*b*-P3HTPy** in d_4-MeOD was found to be better fit by extended rods at low q, as shown by the red dashed line in the inset.

The SANS data ($0.0046<q<0.6$) in each solvent were fit to a Core-Shell Cylinder model using a non-linear least-squares method, including polydispersity and q-resolution smearing (fits shown as solid lines in Figure 4.5).[19] It was not possible to obtain unique fits to the SANS data, however, the chosen fits all have absolute SANS intensities consistent with the known sample concentrations (~1% vol. dry material). The SANS fitting procedure produced two important variables: (1) the 'wetness' of the aggregate due to incorporation of solvent molecules into the CPE aggregate core and shell; (2) the approximate dimensions, and therefore, shape, of the aggregates including the core cylinder length (L_{core}), core cylinder radius (r_{core}) and the thickness of the shell (T_{shell}).

The scattering length densities of the neutral and charged CPE blocks are both ~1.1×10^{-6} $Å^{-2}$. Therefore, they can only be distinguished by neutron scattering when one block is substantially more solvated than the other (SLD contrast is shown schematically in Figure 2.11). Better dissolved CPE chains would be expected to contain more solvent molecules and thus, have higher calculated SLDs. All the fits for **P3HT-*b*-P3HTPy** showed that the aggregates must contain upwards of 30% solvent, without any significant "dry core". Better fits were obtained with a core plus shell model with a diffuse outer shell (~8 nm) containing 85-95% solvent. The exception to the latter were the samples in pure d_4-MeOD where a thin shell (~2 nm) seemed to have slightly less solvent (~65% solvent) than the core of the aggregate (~80% solvent). There was no clear evidence in the SANS patterns of a sharp core/shell boundary, consequently, a continuous radial variation in solvent composition seemed likely; however, practically this is much more difficult to model.

For **P3HT-*b*-P3HTPy** in d_4-MeOD, depending on the imputed starting values for the model refinement for length and radius, the fits were found to converge to two slightly differing

shapes: (1) an extended rod with core length, L_{core}, of ~80 nm, core radius, r_{core}, of ~6 nm and shell thickness, T_{shell}, of ~2 nm; (2) a disc-like aggregate with L_{core} ~75 nm, r_{core} ~30 nm and T_{shell} ~1 nm. The extended rod core-shell aggregate (1) resulted in an improved fit at low q (Figure 4.5, inset). It should be noted that the upturn at low q could also be the emergence of attractive structure factor, such as the "sticky" square well interaction, described in Section 2.2.8. The SANS data for **P3HT-*b*-P3HTPy** in 50:50 (*v/v*) d_4-MeOD/D_2O were best modelled by a disc-like core-shell aggregate, revealing a wet core with L_{core} ~11 nm and r_{core} ~7.5 nm, and a thick solvated shell (T_{shell} ~9.5 nm). Fitting the SANS data of **P3HT-*b*-P3HTPy** in D_2O similarly yielded a disc-like aggregate with a solvated core (L_{core} ~9 nm, r_{core} ~6 nm) and a very wet shell of T_{shell} ~8 nm. The shell thickness corresponds to the fully extended length of the charged **P3HTPy** block (~9 nm). Therefore, it is likely that the drier core corresponded to the aggregated neutral **P3HT** blocks. The SANS data from the aggregates in d_4-MeOD were, thus, more consistent with elongated, rod-like structures, whilst the others were better fit as "disc-like". The disc-like cases were also equally well fit as polydisperse core/shell spheres, the parameters for which have been shown in Table A.4.1 in the Appendix. The calculated aggregation numbers from these fits are reasonable in the range ~100 to ~300 copolymer molecules. Similar fits were also obtained for **P3HT-*b*-P3HTIm** and can be found with a tabulated summary of the fitting data for both CPEs in Figure A.4.1 and Table A.4.2 in the Appendix.

4.3.2.3 Thin Film Morphology

AFM was used to determine whether the nanoscale morphology of the structured aggregates formed in solution can be transferred to thin films, which is an important requirement for potential device applications. The CPEs in MeOH, H_2O and 50:50 (*v/v*) MeOH/H_2O formed spherical aggregates, the size and surface morphology of which was determined by the deposition solvent. For **P3HT-*b*-P3HTIm** in MeOH (Figure 4.6a) a honeycomb-like texture was observed with an average diameter of 121 (±28) nm. In H_2O (Figure 4.6b) slightly larger and smoother aggregates 147 (±16) nm were observed. In 50:50 (*v/v*) H_2O/MeOH (Figure 4.6c), aggregates appeared as less distinctive spheres and formed extended networks of smaller clusters ~50-80 nm in diameter with smooth surfaces.

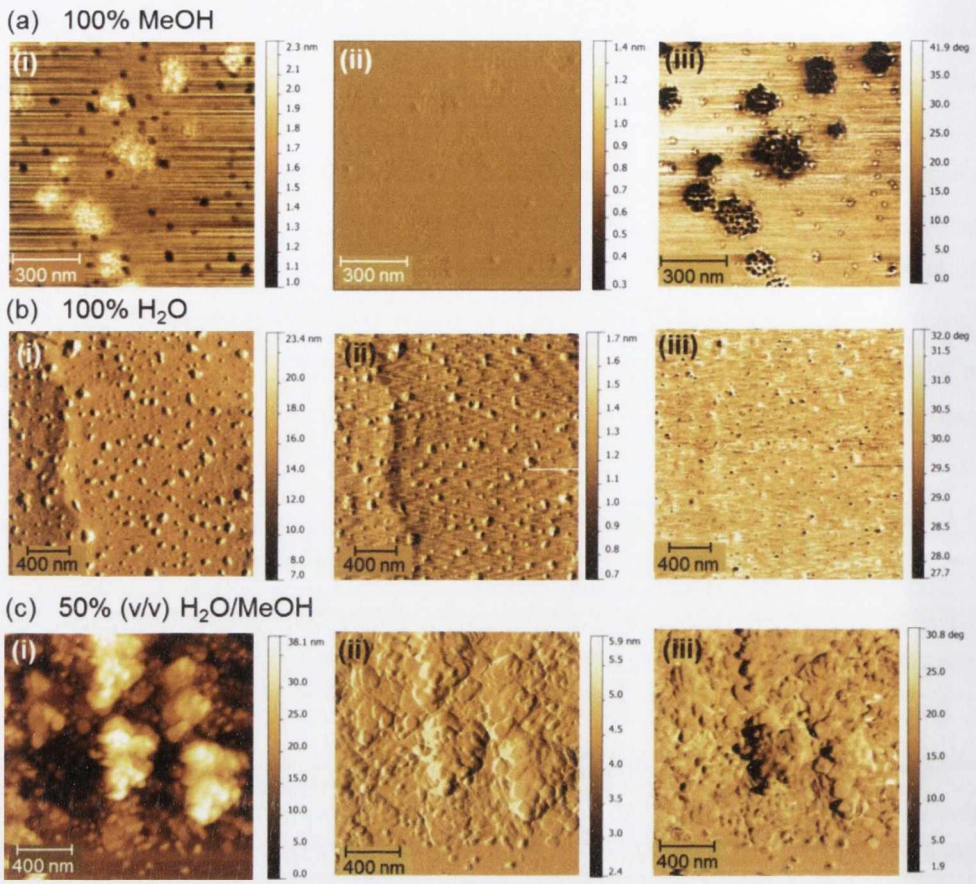


Figure 4.6 AFM tapping mode images of **P3HT-*b*-P3HTIm** films drop-cast from (a) MeOH (7 μg mL^{-1}), (b) H_2O (3.5 μg mL^{-1}) and (c) 50:50 (*v/v*) H_2O/MeOH (3.5 μg mL^{-1}) onto freshly cleaved mica. (i) Height, (ii) amplitude and (iii) phase images, respectively.

Similar trends were also observed for the other **P3HT-*b*-CPEs**, as shown in Figure 4.7. As with **P3HT-*b*-P3HTIm**, the CPEs formed smaller spherical aggregates (~100-300 nm) in MeOH and smooth, slightly larger aggregates in H_2O (~100-400 nm). It should be noted that the SANS data indicate that the core-shell aggregates formed in solution are highly solvated. The corresponding samples prepared as thin films for the AFM measurements were dried prior to imaging. It is conceivable that removal of the solvent during drying led to reorganisation of the aggregate structure due to fluctuations in the solvent gradient.

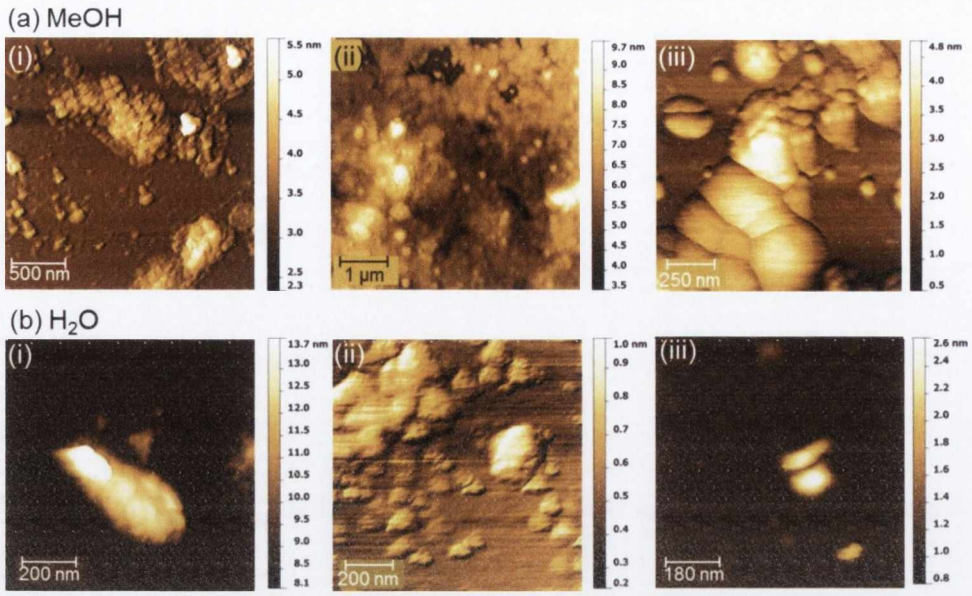


Figure 4.7 AFM height images of **P3HT-*b*-CPEs** drop-cast onto freshly cleaved mica from (a) MeOH and (b) H_2O. (i) **P3HT-*b*-P3HTNMe$_3$** (3.5 μg mL^{-1}), (ii) **P3HT-*b*-P3HTPMe$_3$** (0.1 mg mL^{-1}) and (iii) **P3HT-*b*-P3HTPy** (3.5 μg mL^{-1}).

4.4 Discussion

A combination of techniques has been used to characterise the aggregated morphology of **P3HT-*b*-CPEs** in MeOH/H_2O mixtures. MeOH and H_2O are expected to act as non-selective solvents for the non-charged P3HT block and as selective solvents for the charged CPE block; although H_2O is expected to be a slightly better solvent for the CPE block than MeOH. The increase observed in Φ_F in MeOH/H_2O solvent mixtures indicates a decrease in chain proximity and a decrease in interchain exciton migration, *i.e.* decreased aggregation. This suggests improved solubilisation and at least partial isolation of the polymer chains in one or more of the blocks. The observed increase in the Φ_F was accompanied by an increase in the D_H of the aggregates measured by DLS, further suggesting improved solubilisation of the CPE chains in mixed MeOH/H_2O mixtures.

The fitted SANS data for **P3HT-*b*-P3HTPy** and **P3HT-*b*-P3HTIm** in D_2O suggested the presence of aggregates with highly swollen shells. As D_2O is expected to be a selective solvent for the charged CPE block, the aggregate core was expected to consist predominantly of the neutral P3HT blocks, surrounded by a highly solvated CPE shell. In addition, since D_2O is a non-selective solvent for P3HT, the hydrophobic effect should result in tight packing of the P3HT chains within the aggregate core to minimise interactions with the solvent. In 50:50 (*v*/*v*) d_4-MeOD/D_2O, the core-shell aggregate structure was found to be retained, but the solvent mixture resulted in better solvation of both blocks, leading to an increase in both the core radius and shell thickness. In d_4-MeOD, **P3HT-*b*-P3HTPy** formed more elongated core-shell cylindrical structures, with a solvated core and a drier shell. On the basis of the Hildebrand solubility parameters (δ_H), MeOH is a relatively poor solvent for P3HT (δ_H~19.1 MPa$^{1/2}$ for P3HT and δ_H~29.7 MPa$^{1/2}$ for MeOH,

respectively[32]) and should be a better solvent for the charged CPE block. It is proposed that **P3HT-*b*-P3HTPy** in d_4-MeOD forms core-shell aggregates in which the **P3HT** blocks predominantly occupy the core, but partial mixing of the two blocks across both domains cannot be excluded.

Finally, AFM measurements of films drop-cast from dilute solutions of each CPE showed smooth spherical clusters in H_2O, whilst large extended sheets were observed in H_2O/MeOH mixtures. The reduced electrostatic repulsion may have resulted in long-range assembly of multiple aggregates. This may explain the large D_H obtained by DLS and the textured extended sheets (rather than individual clusters) observed by AFM. In MeOH, smaller aggregates with honeycomb surfaces were found, which could reflect the thin 'dry' shell observed in the SANS fitting.

Figure 4.8 shows a schematic representation of the proposed aggregated structures adopted by **P3HT-*b*-CPEs** in H_2O, MeOH and MeOH/H_2O mixtures.[33] The CPEs in MeOH form the smallest aggregates and exhibit a core-shell cylindrical structure composed of a long 'wet' core and a 'dry' thin shell. In addition, the P3HT and CPE blocks may be mixed across both the core and shell domains. In pure H_2O, slightly larger aggregates in a disc-like conformation are proposed, which consist of a drier core of aggregated neutral P3HT blocks and a wet shell of well-dissolved CPE chains. The CPEs in MeOH/H_2O mixtures have been shown to have the greatest solvation, the largest aggregates and are expected to form discs.

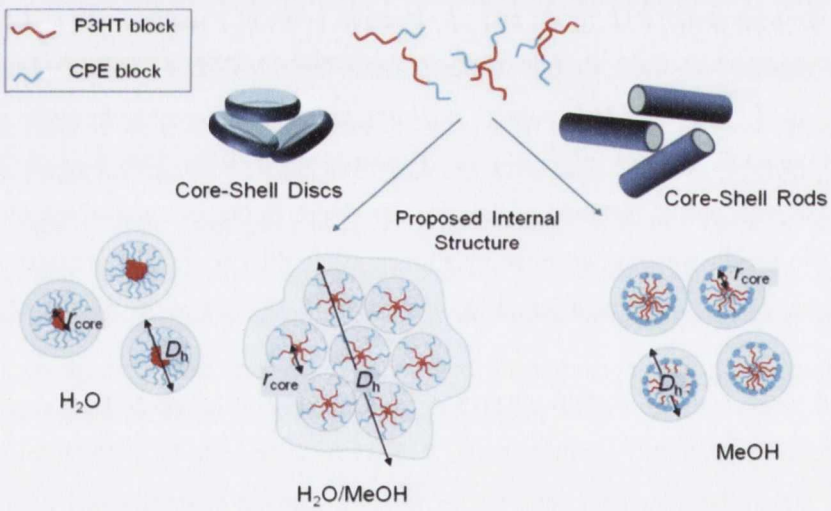


Figure 4.8 A schematic representation of the proposed **P3HT-*b*-CPE** aggregate structures formed in H_2O, MeOH and H_2O/MeOH mixtures. L_{core}, r_{core} and T_{shell} are the core length, core radius and shell thickness obtained from SANS data fitting, respectively. D_H is the hydrodynamic diameter measured by DLS.

The chemical nature of the side chains plays a pivotal role in determining the solubility and conformation of the polymer in a given medium.[22, 29, 30] However, the effect of the cationic groups in these **P3HT-*b*-CPEs** results in only very subtle changes in the photophysical and aggregate properties. For example, the absorbance and PL maximum wavelengths were found to be only slightly different depending on the nature of the CPE block which is likely to be an effect of

the electron donating ability of the side group. In addition, **P3HT-*b*-P3HTPy** was found to form significantly smaller aggregates as characterised by DLS measurements, which may suggest that this CPE is the least soluble. This result could be assigned to the hydrophobic nature of the pyridium cation, as only the imidazolium group is expected to be more hydrophobic.[34]

The absence of any significant difference between the four CPEs suggests that the cation has little effect on the structure of the aggregates formed. In contrast, studies by McCullough *et al.* have suggested that a much greater effect on the nanoscale self-assembly of CPEs when using different counterions.[23, 35] They found that slightly varying the size of the counterion in their carboxylate poly(thiophene), 2,5-poly(thiophene-3-propionic acid) (PTPA), changes the effective steric bulk of the substituent.[35] Small cations were found to favour a self-assembled (purple) state and large cations completely disrupted the aggregated phase to form yellow solutions. Therefore, another approach to controlling the self-assembly structure of CPE aggregates could be *via* the strategic addition of oppositely-charged counterions such as ionic surfactants, which are well-known to induce similar modifications to the photophysical properties as those described for co-solvent systems.[30, 36] Chapter 5 will investigate how the combined use of solvent- and surfactant-mediation can further tune the aggregate morphology of amphiphilic diblock poly(thiophene)s used in this study.

4.5 Conclusions

The solvent dependence of the aggregated structures of all-conjugated poly(thiophene)-poly(thiophene) diblock copolymers has been shown. From UV/Vis absorption and PL studies, the CPEs in pure solvents, in comparison to the mixed solvent systems, were found to have decreased absorption, increased vibronic structure and decreased photoluminescence quantum yields, all of which can be attributed to the increased aggregation of the CPE chains. In H_2O/MeOH mixtures, an enhancement in the Φ_F was accompanied by a corresponding trend in the *Z*-average particle diameter determined by DLS. Small-angle neutron scattering studies revealed that **P3HT-*b*-CPEs** formed core-shell cylindrical aggregates in solution, where the relative thickness and "wetness" of the core and the shell is determined by the solvent system. In H_2O/MeOH mixtures it has been proposed that enhanced solvation of both the core and shell results in aggregate swelling, which promotes disaggregation of localised polymer chains, thereby, increasing Φ_F. AFM studies revealed that the aggregates formed in solution can be transferred as thin films. The thin-film nanoscale morphology of polymer-based devices is a critical component of device operation. Photovoltaic devices require phase separation on the nanometre scale to allow for efficient exciton dissociation and charge transport.[11] In contrast, polymer light emitting diodes generally require a homogenous film with no aggregation or phase separation.[37] Therefore, the ability to tune between different surface morphologies *via* solvent selection could be extremely useful in device preparation.

The elimination of device processing with halogenated solvents is desirable to achieve sustainable large scale fabrication of organic solar cells.[38] In this work the non-toxic solvents, water and methanol, have been utilised to demonstrate an environmentally friendly approach to control the aggregate morphology of diblock poly(thiophene)s. Polar solvents have the added advantage of orthogonal solubility to the organic solvents typically used to deposit the electron acceptor materials layers, such as the fullerene-derivative $PC_{71}BM$ dissolved in chlorobenzene, which is crucial for solution phase processing of multilayer thin film devices.

4.6 References

1. M. J. Robb, S.-Y. Ku and C. J. Hawker, *Adv. Mater.*, 2013, **25**, 5686-5700.
2. G. Tu, H. Li, M. Forster, R. Heiderhoff, L. J. Balk, R. Sigel and U. Scherf, *Small*, 2007, **3**, 1001-1006.
3. U. Scherf, A. Gutacker and N. Koenen, *Acc. Chem. Res.*, 2008, **41**, 1086-1097.
4. C. Ma, P. Pan, G. Shan, Y. Bao, M. Fujita and M. Maeda, *Langmuir*, 2015, **31**, 1527-1536.
5. B. Nandan and A. Horechyy, *ACS Appl. Mater. Interfaces*, 2015, **7**, 12539-12558.
6. X. Xiao, S. He, M. Dan, F. Huo and W. Zhang, *Chem. Commun.*, 2014, **50**, 3969-3972.
7. T. A. Shefelbine, M. E. Vigild, M. W. Matsen, D. A. Hajduk, M. A. Hillmyer, E. L. Cussler and F. S. Bates, *J. Am. Chem. Soc.*, 1999, **121**, 8457-8465.
8. A. Gutacker, N. Koenen, U. Scherf, S. Adamczyk, J. Pina, S. M. Fonseca, A. J. M. Valente, R. C. Evans, J. Seixas de Melo, H. D. Burrows and M. Knaapila, *Polymer*, 2010, **51**, 1898-1903.
9. M. T. Dang, L. Hirsch, G. Wantz and J. D. Wuest, *Chem. Rev.*, 2013, **113**, 3734-3765.
10. G. Zotti and B. Vercelli, *Chem. Mater.*, 2008, **20**, 397-412.
11. I. Botiz and S. B. Darling, *Mater. Today*, 2010, **13**, 42-51.
12. A. Yassar, L. Miozzo, R. Gironda and G. Horowitz, *Prog. Polym. Sci.*, 2013, **38**, 791-844.
13. M. Theander, O. Inganäs, W. Mammo, T. Olinga, M. Svensson and M. R. Andersson, *J. Phys. Chem. B*, 1999, **103**, 7771-7780.
14. M. He, W. Han, J. Ge, Y. Yang, F. Qiu and Z. Lin, *Energy Environ. Sci.*, 2011, **4**, 2894-2902.
15. A. Haugeneder, M. Neges, C. Kallinger, W. Spirkl, U. Lemmer, J. Feldmann, U. Scherf, E. Harth, A. Gügel and K. Müllen, *Phys. Rev. B*, 1999, **59**, 15346-15351.
16. S. Y. Son, Y. Kim, J. Lee, G.-Y. Lee, W.-T. Park, Y.-Y. Noh, C. E. Park and T. Park, *J. Am. Chem. Soc.*, 2016, **138**, 8096-8103.
17. J.-S. Kim, J.-H. Kim, W. Lee, H. Yu, H. J. Kim, I. Song, M. Shin, J. H. Oh, U. Jeong, T.-S. Kim and B. J. Kim, *Macromolecules*, 2015, **48**, 4339-4346.
18. R. Noriega, J. Rivnay, K. Vandewal, F. P. V. Koch, N. Stingelin, P. Smith, M. F. Toney and A. Salleo, *Nat. Mater.*, 2013, **12**, 1038-1044.
19. I. Livsey, *J. Chem. Soc., Faraday Trans.*, 1987, **83**, 1445-1452.
20. A. Guinier and G. Fournet, *Small Angle Scattering of X-rays*, John Wiley and Sons, 1955.
21. L. Angiolini, A. Brazzi, E. Salatelli, K. Van den Bergh and G. Koeckelberghs, *Macromol. Chem. Phys.*, 2013, **214**, 934-942.
22. M. Knaapila, R. C. Evans, V. M. Garamus, L. s. Almásy, N. m. K. Székely, A. Gutacker, U. Scherf and H. D. Burrows, *Langmuir*, 2010, **26**, 15634-15643.
23. K. K. Stokes, K. Heuzé and R. D. McCullough, *Macromolecules*, 2003, **36**, 7114-7118.
24. M. Sundberg, O. Inganäs, S. Stafström, G. Gustafsson and B. Sjögren, *Solid State Commun.*, 1989, **71**, 435-439.

25. C. Tan, E. Atas, J. G. Müller, M. R. Pinto, V. D. Kleiman and K. S. Schanze, *J. Am. Chem. Soc.*, 2004, **126**, 13685-13694.
26. S. Cook, A. Furube and R. Katoh, *Energy Environ. Sci.*, 2008, **1**, 294-299.
27. Y. Li, G. Vamvounis and S. Holdcroft, *Macromolecules*, 2002, **35**, 6900-6906.
28. T. J. Prosa, M. J. Winokur, J. Moulton, P. Smith and A. J. Heeger, *Macromolecules*, 1992, **25**, 4364-4372.
29. M. Knaapila, R. C. Evans, A. Gutacker, V. M. Garamus, N. K. Szekely, U. Scherf and H. D. Burrows, *Soft Matter*, 2011, **7**, 6863-6872.
30. R. C. Evans, M. Knaapila, N. Willis-Fox, M. Kraft, A. Terry, H. D. Burrows and U. Scherf, *Langmuir*, 2012, **28**, 12348-12356.
31. P. W. Schmidt, *Some Fundamental Concepts and Techniques Useful in Small-Angle Scattering Studies of Disordered Solids. In Modern Aspects of Small-Angle Scattering*, Kluwer Academic Publishers: Dordrecht, The Netherlands, 1995.
32. D. W. H. Rankin, *CRC Handbook of Chemistry and Physics*, Taylor & Francis: New York, 2009.
33. A. Thomas, J. E. Houston, N. Van den Brande, J. De Winter, M. Chevrier, R. K. Heenan, A. E. Terry, S. Richeter, A. Mehdi, B. Van Mele, P. Dubois, R. Lazzaroni, P. Gerbaux, R. C. Evans and S. Clément, *Polym. Chem.*, 2014, **5**, 3352-3362.
34. J. Yuan and M. Antonietti, *Polymer*, 2011, **52**, 1469-1482.
35. R. D. McCullough, P. C. Ewbank and R. S. Loewe, *J. Am. Chem. Soc.*, 1997, **119**, 633-634.
36. H. D. Burrows, A. J. M. Valente, T. Costa, B. Stewart, M. J. Tapia and U. Scherf, *J. Mol. Liq.*, 2015, **210**, 82-99.
37. J. H. Seo, A. Gutacker, Y. Sun, H. Wu, F. Huang, Y. Cao, U. Scherf, A. J. Heeger and G. C. Bazan, *J. Am. Chem. Soc.*, 2011, **133**, 8416-8419.
38. K.-S. Chen, H.-L. Yip, C. W. Schlenker, D. S. Ginger and A. K. Y. Jen, *Org. Electron.*, 2012, **13**, 2870-2878.

Chapter 5

Optimising the Molecular Organisation and Nanoscale Morphology of Homo- and Diblock-Polythiophenes using Surfactant- and Solvent-Mediation for High Performance Polymer Solar Cells

The work presented in this chapter has been published in part in:

M. Chevrier, J. E. Houston, J. Kesters, N. Van den Brande, A. E. Terry, S. Richeter, A. Mehdi, O. Coulembier, P. Dubois, R. Lazzaroni, B. Van Mele, W. Maes, R. C. Evans and S. Clément, Self-Assembled Conjugated Polyelectrolyte-Surfactant Complexes as Efficient Electron Transport Materials for Bulk Heterojunction Organic Solar Cells, *J. Mater. Chem. A*, 2015, **3**, 23905-23916.

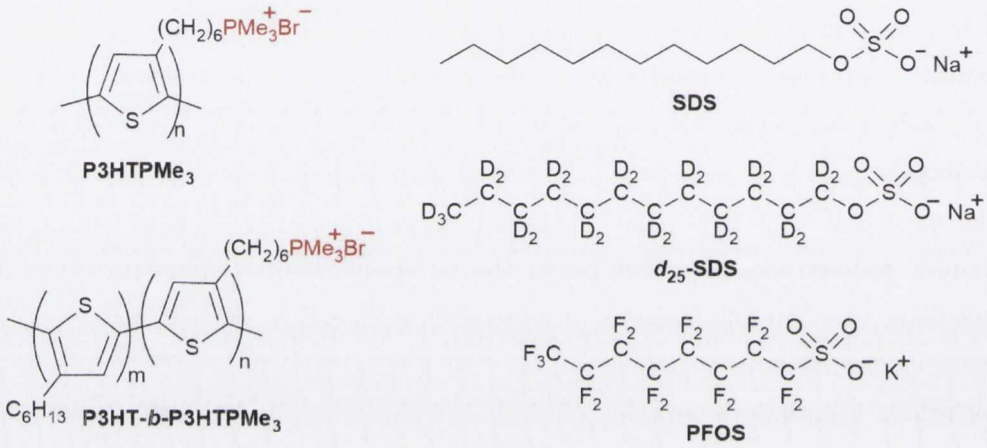
5.1 Introduction

The power conversion efficiency of a polymer solar cell can be significantly improved *via* the incorporation of a CPE interfacial modifier layer in between the active layer and the metal cathode (Figure 1.4).[1, 2] For example, an amphiphilic diblock poly(thiophene) with triethylene glycol and imidazolium-substituted hexyl side chains afforded a PCE of 9.1% when inserted as a cathodic interlayer in a BHJ-OPV device, which was a 23% improvement from the reference device.[3] Although much debate still remains about the precise role and function of interfacial modifier layers in OPV devices,[4-6] it is believed that the additional layers induce the formation and alignment of interfacial dipoles which point from the cathode towards the active layer. Such dipoles serve to reduce the work function of cathodes and increase the built-in potential of OPVs.[7, 8] The ordering and orientation of the polymer has a concomitant effect on the orientation of the dipole moment[9, 10] and thus, a detailed understanding of novel strategies to control the molecular orientation of conjugated polymers is a valuable tool for the optimisation of CPE interfacial layers in OPV devices.

The aim of this study is to harness the well-understood self-assembly behaviour of ionic surfactants (*e.g.* sodium dodecyl sulfate (SDS) and its analogues) to control the short- and intermediate-range intermolecular ordering of poly(thiophene) CPEs in solution and understand how this relates to the nanoscale morphology of the subsequently prepared thin films. The addition of ionic or neutral surfactants to aqueous solutions of CPEs is known to break-up aggregates leading to the formation of hybrid structures with well-defined organisation.[11-15] Such structural transitions result in similar modifications to the photophysical properties as described after the addition of co-solvents as outlined in Chapter 4, such as an increase in the emission intensity,[16, 17] or shift of the emission maximum.[18] Previous work in the Evans group showed that the cationic polymer, poly[3-(6-(*N*-methylimidazolium)hexyl]thiophene] (P3TMAHT), self-assembles into different supramolecular structures depending on the concentration (charge ratio, x) and structure of the anionic surfactants (*e.g.* chain length, head-group, perfluorination).[13] SANS studies revealed that pure P3TMAHT forms charged interacting spherical aggregates. Complexes with SDS were found to form sheets (x = 1) and then upon increasing the charge ratio of SDS, polymer-modified SDS micelles formed (x = 5).[13, 14] This was accompanied by a shift in the colour of the solutions from red to deep violet to yellow. In comparison, sodium octyl sulfate (SOS)-P3TMAHT complexes were found to transform from interacting spheres (x = 0), to sheets (x = 1), to thicker sheets (x = 5) with a congruent surfactochromic red-shift in the absorption maximum from 438 nm (x = 0) to 590 nm (x = 1), before a blue-shift to 420 nm for higher surfactant fractions (x = 5).[13] As such, subtle differences in the surfactant structure were shown to yield extremely different self-assembly structures and consequently different optical properties.

5.1.1 Aims of this work

In Chapter 4 it was shown that the orientation and ordering of amphiphilic diblock copolyelectrolytes containing neutral and cationic poly(thiophene) blocks can be controlled *via* solvent-induced self-assembly.[19] In this chapter, the electrostatic co-assembly of the diblock copolymer poly[(3-hexylthiophene-2,5-diyl)-*b*-((trimethylphosphoniumyl-hexyl)thiophene-2,5-diyl)] (**P3HT-*b*-P3HTPMe$_3$**) and the analogous homopolymer poly(trimethyl-phosphoniumylhexylthiophene-2,5-diyl) bromide (**P3HTPMe$_3$**) will be investigated with the anionic surfactants, SDS, potassium heptadecafluoro-1-octanesulfonate (PFOS) and deuterated-sodium dodecyl sulfate (d_{25}-SDS) (Scheme 5.1) for use as interfacial layers in OPV devices.



Scheme 5.1 Structures of the poly(thiophene)s, **P3HTPMe$_3$** and **P3HT-*b*-P3HTPMe$_3$**, and surfactants, SDS, PFOS and d_{25}-SDS, used in this study.

The specific aims include:

- to investigate the role of the neutral P3HT block on the self-assembly of amphiphilic diblock copolyelectrolytes by direct comparison with the analogous homopolymer;
- to determine the effect of the surfactant structure on the type of co-assembled aggregates formed, including the charge density of the anionic groups by comparing sulfate *vs.* sulfonate head-groups (SDS *vs.* PFOS) and the surfactant rigidity by comparing hydrogenated *vs.* perfluorinated tails (SDS *vs.* PFOS);
- to investigate the internal organisation of the poly(thiophene) within the aggregate structure *via* contrast-matching SANS experiments with d_{25}-SDS;
- to explore whether the polarity of the medium (H_2O *vs.* MeOH) offers some control over the nanostructure of the CPE-surfactant complexes formed;
- to perform preliminary studies on the incorporation of these CPE-surfactant complexes as cathodic interlayers in polymer solar cells.

5.2 Experimental

5.2.1 Materials

P3HTPMe$_3$ and **P3HT-*b*-P3HTPMe$_3$** were a kind gift from Dr Michèle Chevrier and Dr Sébastian Clément at the Institut Charles Gerhardt, Université de Montpellier. The conjugated polymers were synthesised from the bromide precursors, P3HTBr and P3HT-*b*-P3HTBr, with M_n of 13,600 and 15,100 g mol^{-1}, respectively, and polydispersity indexes of 1.36 and 1.12, respectively. It was not possible to measure the exact molecular weight of the CPEs due to strong interaction of the polyelectrolytes with the GPC column. SDS (≥99.0%) and PFOS (≥98.0%) were purchased from Sigma Aldrich and d_{25}-SDS was purchased from Santa Cruz Biotechnology. All surfactants were used as received.

5.2.2 Methods

The instrumentation for UV/Vis absorption and PL spectroscopy, SANS and AFM are described in Chapter 3.

UV/Vis absorption and PL titration procedure: For each measurement, stock solutions of each CPE (10 mg mL^{-1}) were mixed with stock solutions of the surfactants (10 mg mL^{-1}) to obtain the required charge ratio between the CPE monomer units and the anionic surfactant molecules. Samples were measured in quartz cells with an extremely short path length (0.1 mm) to prevent saturation of the detector signal.

AFM measurements: Polymer films of **P3HTPMe$_3$** and **P3HT-*b*-P3HTPMe$_3$** mixed with surfactants were prepared by drop-casting 50 μL aliquots of solutions in H_2O onto silicon substrates. Samples in MeOH were prepared by spin-coating 50 μL aliquots onto silicon substrates (60 s at 1000 revolutions per minute (rpm), 5 s at 4000 rpm). Total concentration = 10 mg mL^{-1}. Samples were dried overnight in an oven at 25 °C. Silicon substrates were cleaned with Piranha solution and dried with N_2 directly before use.

SANS measurements: CPE and CPE-surfactant complexes were prepared in deuterated solvents (10 mg mL^{-1}) to provide good neutron scattering contrast. The scattering curves were fit using non-linear least-squares analysis to Core-Shell Sphere, Core-Shell Cylinder, Rigid Cylinder, Flexible Cylinder, Sphere and Lamellar Sheet models using the SasView programme.[20, 21] Full details of the mathematical models can be found in Chapter 2.

OPV device fabrication: Prototype devices were prepared and characterised by Dr Jurgen Kesters and Prof. Wouter Maes at Hasselt University in Belgium. BHJ polymer solar cells were fabricated using the conventional architecture: glass/ITO/PEDOT:PSS/active layer/CPE/Al, where ITO is indium tin oxide, PEDOT is poly(3,4-ethylenedioxythiophene) and PSS is poly(styrenesulfonic acid). The photoactive layer blend was P3DTTP:$PC_{71}BM$, where P3DTTPD is the low band-gap

copolymer poly[(benzo[1,2-*b*:4,5-*b'*]dithiophene-*alt*-(4*H*-thieno[3,4-*c*]pyrrole-4,6(5*H*)-dione)] and $PC_{71}BM$ is [6,6]-phenyl-C_{71}-butyric acid methyl ester. For the devices employing the interlayer materials, the CPEs were spin-coated from MeOH as a processing solvent (0.25, 0.5 and 1 mg mL^{-1}) to optimise the solar cell parameters.

OPV device characterisation: The current density-voltage (*J-V*) characteristics were measured using a Newport class A solar simulator (model 91195S), calibrated with a silicon solar cell to give an AM 1.5G spectrum. External quantum efficiency (EQE) measurements were performed with a Newport Apex illuminator (100 W Xenon lamp, 6257) as a light source, a Newport Cornerstone 130° monochromator and a Stanford SR830 lock-in amplifier for the current measurements.

5.3 Results

The CPE-surfactant mixtures were prepared over a range of charge ratios, x. These values represent the ratio of surfactant molecules over the number of *charged* CPE monomers. The samples were prepared by mixing 10 mg mL^{-1} solutions of CPE with 10 mg mL^{-1} solutions of surfactant so that the desired charge ratio was reached, with a *total* concentration of 10 mg mL^{-1}. Therefore, the value $x = 1$ corresponds to stoichiometric charge balance. As a representative example, the compositions of polymer-SDS mixtures are given in Appendix Tables A.5.1 and A.5.2.

5.3.1 Optical Characterisation

The optical properties of poly(thiophene)s are well-known to be responsive to intrachain conformational changes and interchain aggregation.[22, 23] The addition of the anionic surfactant SDS to a solution of **P3HTPMe$_3$** in D_2O at different charge ratios, x (total concentration = 10 mg mL^{-1}), resulted in a series of colorimetric transitions, as shown in Figure 5.1. **P3HTPMe$_3$(SDS)$_x$** exhibits a series of well-defined colour transitions, from red ($x = 0$), to wine ($x = 1/5 - 1$), to orange ($x = 5$), and finally, yellow ($x = 20$). A similar series of colorimetric transitions was previously observed when the cationic poly(thiophene) P3TMAHT was combined with SDS at different charge ratios.[13] In contrast, for **P3HT-*b*-P3HTPMe$_3$(SDS)$_x$** a colour transition from purple to red is only observed for $x = 5$ to $x = 20$.[13]

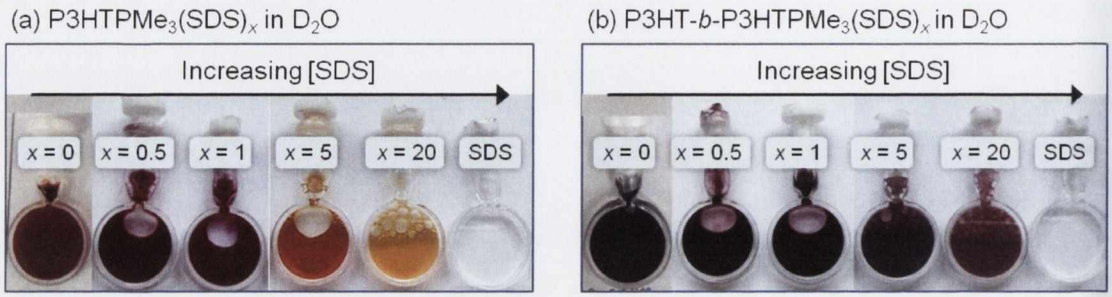


Figure 5.1 Photographs of (a) **P3HTPMe$_3$(SDS)$_x$** and (b) **P3HT-*b*-P3HTPMe$_3$(SDS)$_x$** as a function of SDS composition, x, in D_2O at room temperature.

5.3.1.1 Homo- and Diblock-Copolymer as a Function of Surfactant Charge Ratio

. The colorimetric response can be correlated with changes in the UV/Vis absorption spectrum (Figure 5.2). The absorption spectra of **P3HTPMe$_3$(SDS)$_x$** exhibit similarly pronounced spectral transitions, where the absorption maximum (λ_{abs}) initially undergoes a red-shift from 443 nm (x = 0) to 545 nm (x = 0.5). Upon increasing the SDS charge ratio, a further red-shift is accompanied by the resolution of vibronic structure at the charge compensation point (x = 1 – 2). This is followed by a blue-shift to 429 nm for x > 2. The absorption maximum of the diblock copolymer **P3HT-*b*-P3HTPMe$_3$** is significantly red-shifted (~80 nm) compared to the homopolymer **P3HTPMe$_3$**, which is consistent with increased aggregation of the diblock copolymer.[19] The λ_{abs} maxima remain relatively constant for the **P3HT-*b*-P3HTPMe$_3$(SDS)$_x$** series, however, there is a significant reduction in the absorption bandwidth with increasing x. By x = 5, the absorption band of **P3HT-*b*-P3HTPMe$_3$** also exhibits some moderate vibronic structure, which is consistent with P3HT adopting a "rigid-rod" conformation in block copolymers.[24] Upon dilution of both of the CPE-**SDS** systems by a factor of 100 (total concentration = 0.1 mg mL^{-1}), the UV/Vis absorption spectra exhibit comparable trends to the concentrated samples (Appendix Figure A.5.1). However, **P3HT-*b*-P3HTPMe$_3$** has a significantly narrower band width in the diluted sample as the CPE is less aggregated in this concentration regime.

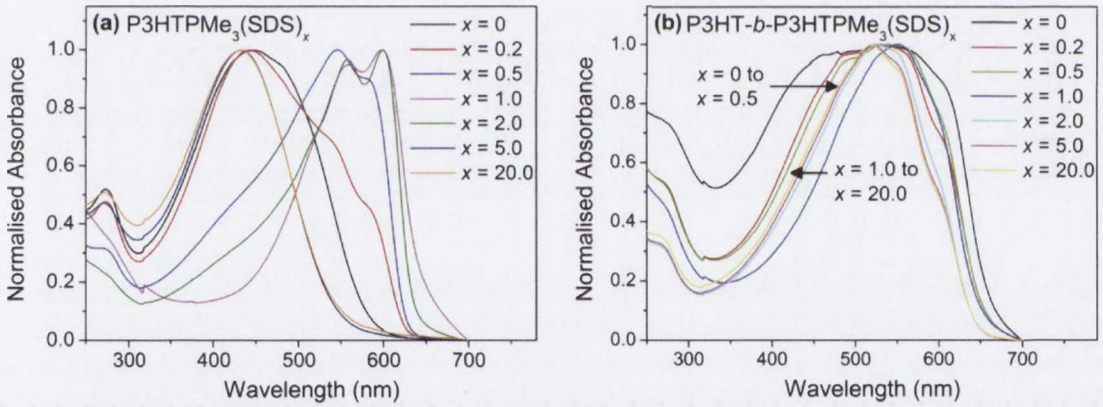


Figure 5.2 Normalised UV/Vis absorption spectra for (a) **P3HTPMe$_3$(SDS)$_x$** and (b) **P3HT-*b*-P3HTPMe$_3$(SDS)$_x$** as a function of SDS composition, x, at room temperature. Total sample concentrations were 10 mg mL^{-1} in D_2O.

The PL properties of the homopolymer and diblock copolymer are also highly sensitive to the charge ratio of surfactant present. Addition of SDS (x = 0.2 – 2) to **P3HTPMe$_3$** triggers both a narrowing of the emission band and the emergence of more resolved vibronic structure (Figure 5.3a), which is assigned to the vibronic progression of the C=C stretching mode ($\Delta E \approx 0.15$ eV).[25] This is also accompanied by a significant red-shift in the emission maximum ($\Delta\lambda_{em}$ = 59 nm) by x = 1. The appearance of vibronic structure in combination with the narrowing of the emission band suggests that **P3HTPMe$_3$** adopts a more planar, ordered conformation in this concentration regime, which prevents free rotation around the polymer backbone.[13, 14] By x = 5, the emission band undergoes a loss in vibronic structure, broadens and undergoes a blue-shift, which

suggests a return to a more twisted conformation along the polymer backbone.[13, 14] In fact, the emission maximum for $x = 5$ is even blue-shifted when compared to that of pure **P3HTPMe$_3$**. This is attributed to a reduction in interchain interactions due to increased screening of the polymer-polymer interactions by the SDS present in charge excess.[13, 14]

Figure 5.3b shows the PL spectrum of **P3HT-*b*-P3HTPMe$_3$**, which exhibits an emission maximum at 734 nm and some vibronic structure. After the initial addition of SDS ($x = 0.2 - 0.5$) there is no significant shift in the emission maximum or change in the vibronic structure, suggesting that no substantial structural reorganisation takes place in this concentration regime. However, for $x = 1$ a significant blue-shift in the emission maximum to 672 nm is observed, which is accompanied by a decrease in the vibronic band at 734 nm and a new band emerges at 637 nm. Increasing the charge ratio further ($x = 2 - 20$) sees a loss of the vibronic structure. Thus, the addition of the surfactant seems to reduce the polymer-polymer interactions.[15] The anionic surfactant is expected to associate exclusively through electrostatic interactions with the cationic P3HTPMe$_3$ block. While the polymer-polymer interactions are expected to persist in the neutral P3HT block domains of the copolymer aggregates. This may explain why some vibronic structure remains until $x = 5$, *i.e.* even when the surfactant is in large excess.

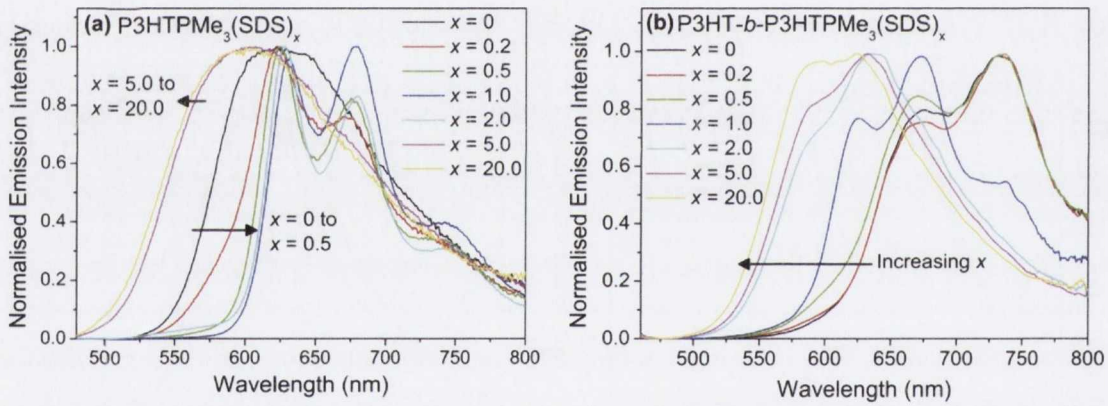


Figure 5.3 Normalised steady-state emission spectra for (a) **P3HTPMe$_3$(SDS)$_x$** and (b) **P3HT-*b*-P3HTPMe$_3$(SDS)$_x$** as a function of SDS charge ratio, x, at room temperature. Total sample concentrations were 10 mg mL^{-1} in D_2O. $\lambda_{ex} = 450$ nm.

5.3.1.2 Homo- and Diblock-Copolymer and a Perfluorinated Surfactant

The results in Chapter 4 suggest that the nature of the cationic side-group on the CPE block did not have a large effect on the self-assembly properties of the diblock copolymers in MeOH and H_2O. However, previous studies within the Evans group have shown that subtle changes in the structure of the associating surfactant can tune the self-assembled aggregate structures formed.[13-15] Therefore, **P3HT-*b*-P3HTPMe$_3$**, and the analogous homopolymer, **P3HTPMe$_3$**, were also mixed with an increasing charge ratio of PFOS (Scheme 5.1). PFOS has a reduced charge density on the head-group and a more rigid hydrophobic tail in comparison to SDS.[26, 27] The normalised UV/Vis absorption and PL spectra of the poly(thiophene)s mixed with a 1:1 charge ratio of PFOS and, for comparison, SDS, are shown in Figure 5.4. The normalised PL

spectra **P3HTPMe$_3$(PFOS)**$_x$ and **P3HT-*b*-P3HTPMe$_3$(PFOS)**$_x$ as a function of PFOS charge ratio, x, are shown in the Appendix Figure A.5.2.

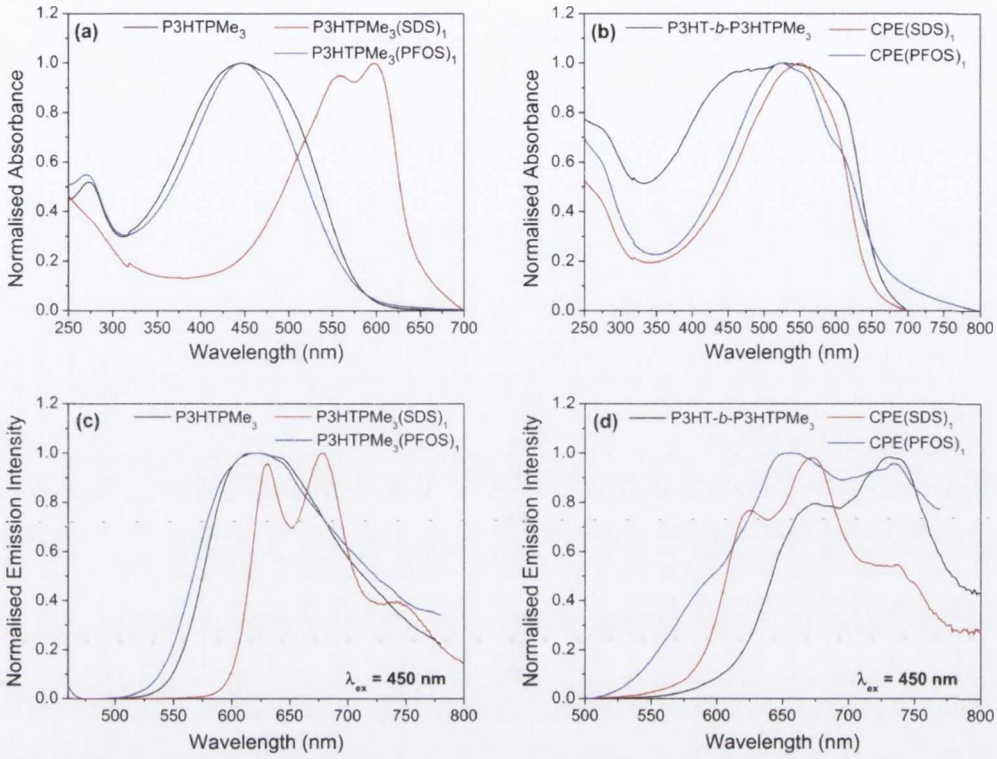


Figure 5.4 Normalised UV/Vis absorption and emission spectra for (a,c) **P3HTPMe$_3$** and (b,d) **P3HT-*b*-P3HTPMe$_3$** with no surfactant (black lines) and 1:1 charge ratio of SDS (red lines) and PFOS (blue lines) at room temperature. Total sample concentrations were 10 mg mL^{-1} in D_2O.

The UV/Vis absorption spectra for **P3HTPMe$_3$(PFOS)**$_1$ and **P3HT-*b*-P3HTPMe$_3$(PFOS)**$_1$ systems are characterised by a single broad absorption band centred at 447 and 523 nm, respectively (Figure 5.4a and 5.4b), similar to the spectra for the pure CPEs. This is in stark contrast to the analogous SDS systems which are red-shifted significantly upon the addition of surfactant, although the emission spectrum for **P3HT-*b*-P3HTPMe$_3$(PFOS)**$_1$ experiences a reduction in the absorbance bandwidth.

The emission spectrum of **P3HTPMe$_3$** is notably insensitive to PFOS, with only a moderate blue-shift observed ($\Delta\lambda_{em}$ = -33 nm) by x = 2, before a red-shift back to the original emission maximum. In contrast, the PL spectrum of **P3HT-*b*-P3HTPMe$_3$** undergoes a large blue-shift (~75 nm) to 657 nm by x = 1. By x = 5, λ_{em} = 614 nm and is accompanied by a complete loss of vibronic structure. The loss of vibronic structure occurs for PFOS at a lower charge ratio (x = 2) than with SDS (x = 5), which suggests that the fluorinated surfactant, with a lower head-group charge density, is more effective at reducing polymer-polymer interactions within the aggregates of **P3HT-*b*-P3HTPMe$_3$** than SDS.[15]

The PL and absorption data of the poly(thiophene)s before and after the addition of surfactant are listed in Table 5.1. To be completely satisfied that the nature of the CPE charge-group had a negligible effect on their co-assembly with oppositely charged surfactants, the UV/Vis

absorption and PL experiments were also performed with the analogous imidazolium (Im) homo- and diblock-copolymer used in Chapter 4. As expected, no significant difference was observed when these measurements were compared to the absorption and PL data for the phosphonium analogues.

Table 5.1 Absorption (λ_{abs}) and PL (λ_{em}) maxima of the poly(thiophene)s in D_2O and d_4-MeOD before and after the addition of SDS and PFOS (1:1 charge ratio). λ_{ex} = 450 nm.

	Solvent	λ_{abs} (nm)	λ_{em} (nm)
P3HTPMe$_3$	D_2O	446	620
	d_4-MeOD	445	592
1:1 SDS	D_2O	598	679
	d_4-MeOD	446	582
1:1 PFOS	D_2O	447	620
	d_4-MeOD	417	572
P3HT-*b*-P3HTPMe$_3$	D_2O	535	732
	d_4-MeOD	518	630
1:1 SDS	D_2O	552	673
	d_4-MeOD	516	636
1:1 PFOS	D_2O	523	657
	d_4-MeOD	518	621

5.3.1.3 CPE and CPE-Surfactant Complexes in Methanol

In Chapter 4 it was shown that the solvent polarity has an effect on the optical properties of the diblock poly(thiophene)s. Therefore, it was anticipated that the solvent polarity may also have a marked effect on the aggregate structure and optical properties of the CPE:surfactant complexes. The normalised UV/Vis absorption spectra of **P3HTPMe$_3$** and **P3HT-*b*-P3HTPMe$_3$** with 1:1 charge ratio of SDS and PFOS in d_4-MeOD (10 mg mL^{-1}) are shown in Figure 5.5a. Similar to D_2O, the absorption maximum of the diblock copoly(thiophene) **P3HT-*b*-P3HTPMe$_3$** is significantly red-shifted (~70 nm) compared to the homopolymer **P3HTPMe$_3$**, which is consistent with an increased aggregation of the diblock copolymer.[19] The absorption band of **P3HT-*b*-P3HTPMe$_3$** also exhibits moderate vibronic structure. Addition of SDS results in a moderate blue-shift in the absorption maximum (~10 nm) and a narrowing of the absorption band for both polymers. This shift is considerably smaller than the blue-shift of ~150 nm observed for **P3HTPMe$_3$(SDS)$_1$** in D_2O which indicates a smaller structural rearrangement in d_4-MeOD. More striking distinctions are observed upon the addition of PFOS to the poly(thiophene)s in d_4-MeOD. The absorption of **P3HTPMe$_3$(PFOS)$_1$** experiences a blue-shift of ~30 nm. While the absorbance band for **P3HT-*b*-P3HTPMe$_3$(PFOS)$_1$** is significantly broader, which implies that the CPE adopts a more planar organisation.

P3HTPMe$_3$ and **P3HT-*b*-P3HTPMe$_3$** in d_4-MeOD also display distinctive PL spectra (Figure 5.5b). **P3HTPMe$_3$** exhibits a broad, featureless emission band centred at 592 nm. While the emission spectrum of **P3HT-*b*-P3HTPMe$_3$** is broader still (520-850 nm) and exhibits well-resolved vibronic structure. Addition of SDS results in the emergence of a vibronic structure for **P3HTPMe$_3$(SDS)$_1$** and **P3HT-*b*-P3HTPMe$_3$(SDS)$_1$**. The addition of PFOS results in a blue-shift in the emission spectra to 572 and 621 nm for **P3HTPMe$_3$** and **P3HT-*b*-P3HTPMe$_3$**, respectively.

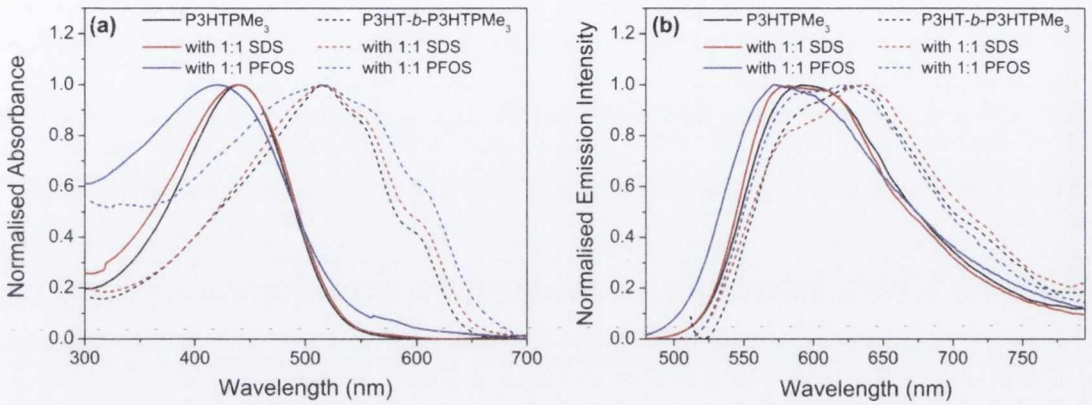


Figure 5.5 Normalised (a) UV/Vis absorption and (b) emission spectra of **P3HTPMe$_3$** (solid lines) and **P3HT-*b*-P3HTPMe$_3$** (dashed lines) as the pure CPE (black) and combined with 1:1 charge ratio of SDS (red lines) and PFOS (blue lines) in d_4-MeOD (10 mg mL^{-1}).

The dodecyl sulfate (DS^-) and heptadecafluorooctanesulfonate ($PFOS^-$) counterions in complexes with **P3HTPMe$_3$** and **P3HT-*b*-P3HTPMe$_3$** in D_2O and d_4-MeOD are likely to hinder polymer-polymer interchain interactions effectively, thereby decreasing the nominal effective conjugation length for exciton migration with significant effects on optical properties.[17] Previously, the complexation of DS^- with the related homopolymers P3TMAHT[13, 14] and poly[3-[6-(*N*-methylimidazolium)hexyl]-2,5-thiophene] bromide (P3ImiHT)[15] was shown to induce significant surfactochromic transitions in aqueous solution, which could also be controlled by varying the surfactant charge ratio. The effect of SDS appears to be greater in D_2O than d_4-MeOD. There are two potential reasons for this: (1) these transitions are controlled to a large extent by the phase diagram of SDS, which differs in methanol[28] and water[29]; (2) the CPEs will also experience different phase transitions in methanol and water, as shown in Chapter 4. MeOH and H_2O are expected to be non-selective solvents for the non-charged P3HT block. In contrast, both solvents should be selective solvents for the charged CPE block, but to a greater extent for H_2O.

Interestingly, PFOS has considerably more effect on the emission properties of **P3HTPMe$_3$** in d_4-MeOD than in D_2O. As with SDS, this is likely to be because of the difference in the critical micelle concentrations of PFOS in MeOH and H_2O[30]. The effect of PFOS is significantly greater for the diblock copolymer *vs.* the homopolymer. The reduced charge density of the sulfonate head-group is likely to mean that PFOS is more able to penetrate the neutral P3HT block core of the aggregates of **P3HT-*b*-P3HTPMe$_3$** than SDS. In contrast, SDS can form stronger

associations with the $P3HTPMe_3$ blocks, thus, explaining why greater changes were observed with the **$P3HTPMe_3(SDS)_x$** series in comparison to the **$P3HTPMe_3(PFOS)_x$** series.

5.3.2 Solution-Phase Structures

Previous SANS experiments have shown that the solution structure of amphiphilic diblock and homopolymer PTs can be modulated by varying the solvent or adding charge compensating surfactants.[13, 19] To obtain a deeper insight into the nanoscale organisation of the polymers in solution, SANS studies were performed on the **$P3HTPMe_3$**-surfactant and **P3HT-*b*-$P3HTPMe_3$**-surfactant complexes in D_2O and d_4-MeOD. Here, differences in the scattering length densities of individual components in the CPE-surfactant systems allow different zones of the complex to be probed. The SLDs of the surfactants differ significantly: SDS is closer to poly(thiophene), while d_{25}-SDS and PFOS are closer to D_2O and d_4-MeOD (Figure 5.6). Therefore, CPE-SDS complexes will appear to the neutrons as single entities, enabling the entire polymer-surfactant complex to be observed. In contrast, scattering from the CPE-d_{25}-SDS and CPE-PFOS systems would originate primarily from the polymer, allowing the polymer organisation within the complex to be investigated.

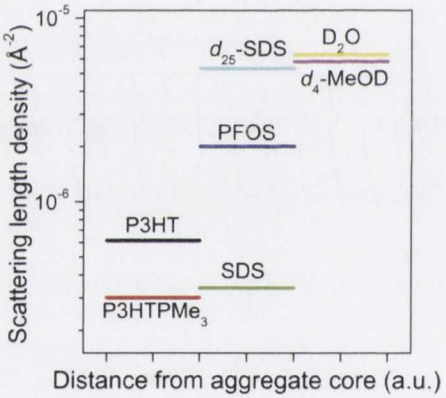


Figure 5.6 Comparison of the estimated neutron scattering length densities for the polymer blocks, surfactants and solvents used in the SANS studies. Materials with similar SLDs are said to be *contrast-matched.*

The observation window of these SANS experiments ranged from 2.6-70 nm, which covers the isolated chain lengths of the CPEs (22.2-30.4 nm) calculated from the length of the thiophene monomer (~4 Å).[31] If the CPEs were dissolved down to the single molecule level, the SANS data would level off as a Guinier plateau at an experimentally obtainable q which is not observed here for any of the CPEs in D_2O or d_4-MeOD. All fits are summarised in Tables A.5.3-A.5.10 in the Appendix. Although it was not possible to obtain unique fits to the SANS data, all the chosen fits have absolute SANS intensities consistent with the known sample concentrations (~1% vol. dry material). For full mathematical models and schematic representations of the models used refer to Section 3.3.3.

5.3.2.1 Homopolymer with Surfactants in D_2O

The solution structure of **P3HTPMe$_3$** is extremely susceptible to changes induced by the addition of anionic surfactant (Figure 5.7). Similar homopolymers in solution, P3TMAHT[13, 14] and P3ImiHT[15], have previously been assigned to spherical aggregates in D_2O. However, a modest upturn at low q ($q < 0.02$ Å^{-1}) of $\sim q^{-1}$ implies that **P3HTPMe$_3$** may experience some degree of aggregation. Fitting of the SANS data ($0.008 < q < 0.32$ Å^{-1}) to the Cylinder Model[21, 32] gave a length of 87.5 Å and radius of 15.3 Å. The hump at $q = 0.03$ Å^{-1}, was accounted for by applying the Hayter-Penfold Structure Factor, see Section 2.2, which allows for particle-particle repulsion interactions.[33-35] Alternatively, using a Guinier plot[21] (Appendix Figure A.5.3) the calculated radius of gyration (R_g) of aggregates of **P3HTPMe$_3$** in D_2O is 21.0 Å.

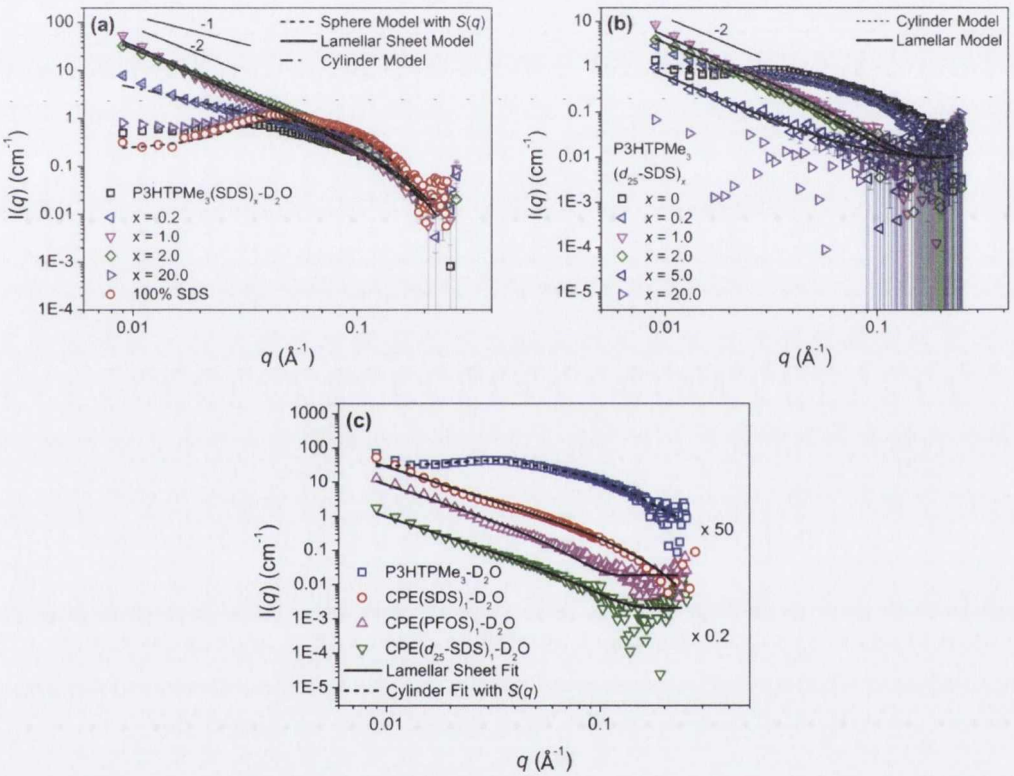


Figure 5.7 SANS data of **P3HTPMe$_3$** in D_2O with selected charge ratios of (a) SDS and (b) d_{25}-SDS. Straight lines show q^{-1} and q^{-2} for comparison. (c) **P3HTPMe$_3$** (blue) in D_2O and with 1:1 charge ratio of SDS (red), PFOS (pink) and d_{25}-SDS (green). Solid, dashed and dot-dashed lines represent the fits described in the text. The overall concentration of each system was 10 mg mL^{-1}. T = 25 °C.

The scattering profile of **P3HTPMe$_3$** upon initial addition of SDS ($x = 0.2$) is qualitatively similar to that of the pure polymer, although the interference maximum at $q = 0.03$ Å^{-1} is somewhat diminished (Figure 5.7a). This means that while **P3HTPMe$_3$** structure is only moderately influenced by SDS at this concentration, only a small amount is required to weaken the interparticle electrostatic ordering.[15] As the charge ratio is increased from $x = 0.5$ to $x = 2$, there is a significant increase in scattering at low q ($q < 0.02$ Å^{-1}). By $x = 1$, the scattering curve decays as $q^{-2.6}$, which is interpreted as the existence of "sheet-like" particles or larger smooth fractal

aggregates, such as vesicles.[36] The power law scaling at high q ($q > 0.1$ Å^{-1}) starts to decay as q^{-4}, thus, marking the thickness of the sheet-like aggregates.[15] The upturn at $q = 0.08$ Å^{-1}, could be repulsion between similarly charged chains or the appearance of free SDS micelles, considering that the concentration is well above the *cmc* of SDS in water (8.2 mM ≈ 2.4 mg mL^{-1}).[29] Fitting with the Lamellar Sheet Model[37, 38] gave sheet thicknesses (T_{sheet}) of 10.0, 20.1 and 13.6 Å for $x = 0.5$, 1 and 2, respectively. These thicknesses correspond to the solid state d-spacing of poly(3-octylthiophene),[31] implying that the polymer and surfactant must be interwoven rather than forming well-defined layers.[15] At higher charge ratios of SDS where $x = 5$ the scattering intensity scales as $q^{-0.5}$. Fitting of this data gave spherical aggregates with radius of 24.8 Å and 65% solvent content. This is only slightly larger than pure SDS micelles which are also spherical with radius of ~19 Å (Figure 5.7a, red circle, dashed line). This suggests that the scattering from the $x = 5$ sample occurs predominantly from SDS micelles, with the **P3HTPMe$_3$** associating to their surfaces, potentially explaining the slightly larger radius. Unsurprisingly, the scattering profile at $x = 20$ also strongly resembles the scattering profile of pure SDS, although the scattering plateaus at low q, which could indicate the presence of a few well-dissolved chains.

Figure 5.7b shows the SANS data and fits for **P3HTPMe$_3$(d_{25}-SDS)$_x$** in D_2O. The contrast between d_{25}-SDS and D_2O is approximately 50 times lower than that between SDS and D_2O. Thus, the contrast mainly arises from **P3HTPMe$_3$** within the **P3HTPMe$_3$(d_{25}-SDS)$_x$** associations. After addition of d_{25}-SDS up to $x = 1$, the SANS data are characterised by a strong upturn at low q, described empirically by a power law scaling of $q^{-2.7}$, strongly resembling that of **P3HTPMe$_3$(SDS)$_1$** (Figure 5.7c). The data with d_{25}-SDS indicate that **P3HTPMe$_3$** forms sheet-like aggregates *within* the sheet-like SDS-CPE associations. Furthermore, the Lamellar Sheet model[37, 38] gave a T_{sheet} of 34.0 Å for **P3HTPMe$_3$(d_{25}-SDS)$_1$**, thicker than **P3HTPMe$_3$(SDS)$_1$** (~20 Å). The slight hump at $q = 0.07$ Å^{-1} in the **P3HTPMe$_3$(SDS)$_1$** scattering profile is likely to be a minor contribution from free SDS micelles.[15] Interestingly, the scattering profile for **P3HTPMe$_3$(d_{25}-SDS)$_5$** is clearly still reminiscent of lamellar sheets ($\sim q^{-2}$). The apparent spherical scattering profile in **P3HTPMe$_3$(SDS)$_5$** is likely to be a consequence of the micelles formed from the excess SDS.

Figure A.5.4 in the Appendix shows the SANS data for **P3HTPMe$_3$(PFOS)$_x$**. After the addition of PFOS to a 1:1 charge ratio (Figure 5.7c), the SANS data is characterised by a strong upturn at low q, described empirically by power law scaling of $q^{-2.3}$, strongly resembling that of **P3HTPMe$_3$(SDS)$_1$**. This implies that the complexes are also forming sheet-like aggregates, however, fitting with the Lamellar Sheet model gave considerably thicker sheets ($T_{sheet} = 48.1$ Å).[37, 38] The increase is potentially a result of the increased rigidity of the surfactant tail and reduced charge density of the sulfonate head-group, making PFOS less able to penetrate the existing **P3HTPMe$_3$** aggregates when compared to SDS or d_{25}-SDS,[13] and resulting in more distinctive **P3HTPMe$_3$**- and PFOS-layers.

5.3.2.2 Diblock Copolymer with Surfactants in D_2O

The SANS data of **P3HT-*b*-P3HTPMe$_3$** in D_2O (Figure 5.8) yields a similar scattering profile to the pyridinium (Py) and imidazolium (Im) **P3HT-*b*-P3HTX** analogues previously studied in D_2O in Chapter 4.[19] The scattering data exhibits a shoulder at $q = 0.02$ Å^{-1} and an upturn at $q = 0.08$ Å^{-1}. At high q ($q > 0.07$ Å^{-1}), the SANS response stems from the internal structure of the aggregate. In D_2O, the low q region ($q < 0.02$ Å^{-1}) decays as $q^{-1.6}$, which is typical of scattering from either cylindrical aggregates or from individual chains.[39] The SANS data ($0.008 < q < 0.2$ Å^{-1}) were fit to a Core-Shell Cylinder model.[20] In D_2O, **P3HT-*b*-P3HTPMe$_3$** forms aggregates with a dry core (~5% solvent) with a radius (r_{core}) of 47.2 Å, length (L_{core}) of 517.9 Å, and a thick, wet shell (~82% solvent) of 69.5 Å. The SLDs of the neutral P3HT and the P3HTPMe$_3$ blocks are both ~1 × 10^{-6} Å^{-2} (Figure 5.6). Therefore, they can only be distinguished by neutron scattering when one block is substantially more solvated than the other. A difference in solubility between amphiphilic copolymer blocks is known to lead to nanoscale phase separation within CPE aggregates.[40] Here, core-shell cylinders with hydrophobic, neutral block cores and solvated, hydrophilic charged block shells are observed.

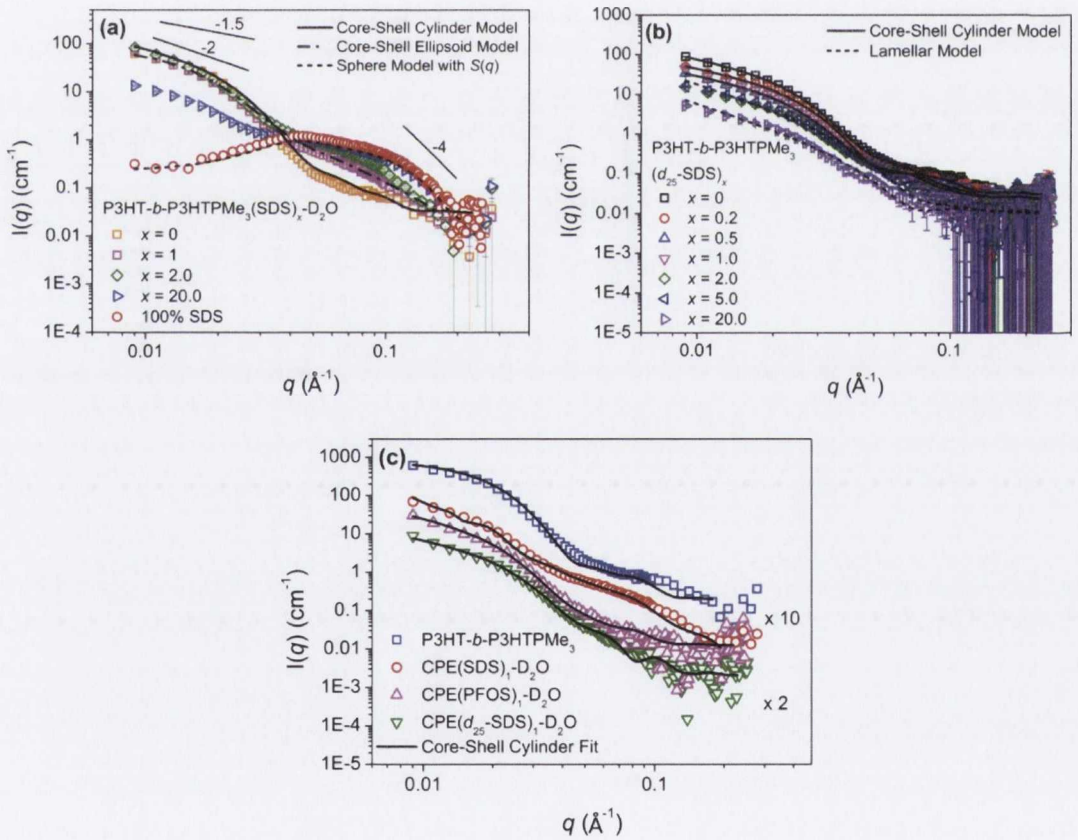


Figure 5.8 SANS data for **P3HT-*b*-P3HTPMe$_3$** in D_2O with increasing charge ratio of (a) SDS and (b) d_{25}-SDS. Straight lines show $q^{-1.5}$, q^{-2} and q^{-4} for comparison. (c) SANS data for **P3HT-*b*-P3HTPMe$_3$** (blue) in D_2O and with 1:1 charge ratio of SDS (red), PFOS (pink) and d_{25}-SDS (green). Solid, dashed and dot-dashed lines represent the fits described in the text. Total concentration of each sample was 10 mg mL^{-1}. T = 25 °C.

Initially, there is practically no change in the scattering profile of **P3HT-*b*-P3HTPMe$_3$** upon addition of SDS (x = 0.2) (Figure 5.8a). However, by further increasing the charge ratio (x = 0.5) an increase in the scattering intensity is observed at q = 0.08 Å^{-1}, indicative of repulsion between similarly charged chains. In addition, by x = 1 the shoulder at q = 0.02 Å^{-1} becomes less pronounced and the profile has a q-scaling of q^{-2}. This implies that the core-shell cylinders of the pure diblock copolymer transform into 2D sheets upon coordination with SDS. At x = 2 and x = 5 the q-scaling decreases to $q^{-1.9}$ and $q^{-1.7}$, respectively. This means that the lamellar sheet structure at x = 1 is progressively lost upon increasing charge ratio. The SANS data (0.008 < q < 0.2 Å^{-1}) of **P3HT-*b*-P3HTPMe$_3$(SDS)**$_x$ were fit to a Core-Shell Cylinder, Lamellar Sheet or Sphere model using SASView, shown in Figure 5.8a and summarised in the Appendix (Table A.5.5).[20] The fits for this system proved particularly difficult. For x = 0.2 and x = 0.5 the samples were fit using the Core-shell Cylinder Model. Although the core lengths and radii are similar to those of the parent diblock copolymer, the shell appears to become thicker and drier. However, it must be noted that these fits were not perfect, and are particularly poor at q = 0.08 Å^{-1}. At x = 1, the charge compensation point, the scattering profile was best fit to the Lamellar Sheet model,[37, 38] with a T_{shet} of 59.4 Å. Although this fit was again not ideal, it was significantly better than the alternative fit using the Core-Shell Cylinder model. For x = 5 and x = 20, fits of satisfactory quality to the entire data were not possible. However, the high q data (0.027 < q < 0.24 Å^{-1}) strongly resembled the scattering from pure SDS micelles. Therefore, for both samples this region was fit to the Spherical model,[21] and resulted in radii which corresponded closely to SDS micelles (26.6 and 23.1 Å for x = 5 and x = 20, respectively). This implies that by x = 5, the **P3HT-*b*-P3HTPMe$_3$(SDS)**$_x$ system exists mainly as SDS micelles, potentially with associating CPE chains on the surface to account for the slight increase in radius from the pure SDS micelles.

Interestingly, when contrast-matching with the deuterated surfactant analogue (d_{25}-SDS) is performed, the scattering profiles of the entire **P3HT-*b*-P3HTPMe$_3$(d_{25}-SDS)**$_x$ series strongly resemble the core-shell cylinder profile of the parent diblock copolymer (Figure 5.8b). Fitting the Core-Shell Cylinder model to each of the scattering profiles was performed and the fits are summarised in the Table A.5.6 in the Appendix. At x = 1, the fitting gave an elongated cylinder with L_{core} of 477.3 Å, r_{core} of 49.5 Å and T_{shell} of 71.4 Å. Each of the fits was greatly improved by adding polydispersity to the core radius. The fact that lamellar sheets are observed with SDS, and yet core-shell cylinders when the surfactant has been contrast-matched, suggests that SDS connects adjacent **P3HT-*b*-P3HTPMe$_3$** cylinders to form two-dimensional, sheet-like arrays.

Fitting with the Core-Shell Cylinder model to the **P3HT-*b*-P3HTPMe$_3$(PFOS)**$_x$ series also gave core-shell cylinders with hydrophobic, neutral block cores and solvated, hydrophilic charged block shells (Appendix, Figure A.5.4b). The SLD of PFOS (2 × 10^{-6} Å^{-2}) is quite well contrast-matched with D_2O, and as a result the scattering is expected to mainly occur from the polymer. At x = 1 the fit gave a wide, (relatively) wet core with r_{core} of 59.0 Å (16% wetness), a shorter L_{core} of

466.3 Å, and thick, wet T_{shell} of 77.7 Å (85% wetness) (Figure 5.8c). Notably, PFOS, unlike SDS, induced a significant increase in the "wetness" of the neutral P3HT block cores.

5.3.2.3 Homopolymer and Diblock Copolymer with SDS in d_4-MeOD

For **P3HTPMe$_3$** in d_4-MeOD the scattering profile scales as $q^{-1.2}$ in the $q < 0.08$ Å^{-1} region, suggesting that the homopolymer adopts a rod-like conformation in solution.[39] The corresponding Holtzer plot (q*I(q) *vs.* q, Figure 5.9a, inset) shows an upturn at low q ($q < 0.02$ Å^{-1}), which is indicative of a semi-flexible rod conformation.[41] The SANS data ($0.009 < q < 0.23$ Å^{-1}) were independently fit to a Rigid Cylinder model[21] and a Flexible Cylinder model[42, 43] using a non-linear least-squares method and included q-resolution smearing. The Rigid Cylinder model describes the length and radius of an unbending, uniform rod- or disc-shaped aggregate, whereas the Flexible Cylinder model is used to describe a non-linear chain consisting of a number of locally stiff segments with persistence length, l_p. The Kuhn length (L_{Kuhn}), or $2*l_p$, describes the stiffness of the chain. This model gave an improved fit to the data at low q with a reasonable L_{Kuhn} (225.6 Å) compared to the total cylinder length (900.5 Å), and a radius of 12.9 Å. From the estimated aggregation number (N_{agg}) (Section 3.3.4 for the calculation of N_{agg}), each cylinder is comprised of 5-10 polymer chains, with L_{Kuhn} corresponding to the length of a single chain (220 Å) and the cylinder diameter (25.8 Å) approximating the thickness of two adjacent chains (~26 Å). The fitting data indicates that the cylinders are well-solvated, containing >85% solvent. The homopolymer **P3HTPMe$_3$** in D_2O forms charged spherical aggregates (R_g ~21 Å) with interparticle interactions. In contrast, **P3HTPMe$_3$** in d_4-MeOD better resembles the scattering profiles obtained when this CPE or the analogous homopolymers, P3TMAHT and P3ImiHT,[13, 14] are combined with a small amount of SDS (CPE/surfactant charge ratio of 1:0.2) in D_2O. In all three systems, the pure CPE aggregates are believed to disassemble and reorganise into CPE-surfactant cylinders.[13, 14] This suggests that **P3HTPMe$_3$** forms more ordered aggregates in d_4-MeOD, with significant packing between CPE chains.

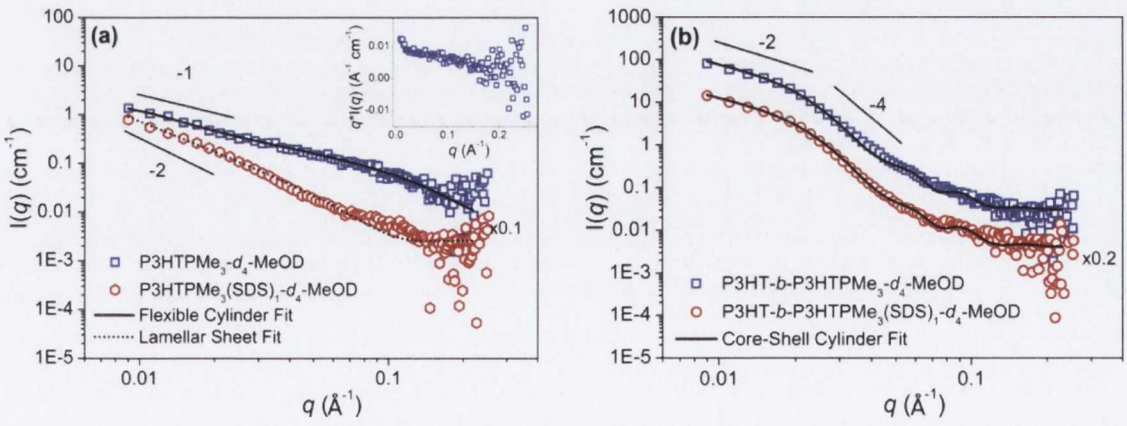


Figure 5.9 SANS data for (a) **P3HTPMe$_3$** and (b) **P3HT-*b*-P3HTPMe$_3$** (blue) with 1:1 charge ratio of SDS (red) in d_4-MeOD. Inset: Holtzer or "bending rod" plot for **P3HTPMe$_3$** in d_4-MeOD. Total concentration of each sample was 10 mg mL^{-1}. Straight lines show -1, -2 and -4 decays for comparison. Solid and dashed lines correspond to the fits to the models described in the text.

Addition of SDS results in a significant change in the scattering profile for **P3HTPMe$_3$(SDS)$_1$**, scaling as $q^{-1.9}$ at low q ($q < 0.02$ Å^{-1}), and becoming steeper in the intermediate q region ($0.02 < q < 0.07$ Å^{-1}), resulting in $q^{-2.21}$, which is indicative of scattering from sheet-like particles.[49] A Lamellar Sheet model provided a reasonable fit to the data (Figure 5.9a, dashed line), yielding a sheet thickness of ~47 Å, with a slightly decreased solvent content (~50%) than obtained for **P3HTPMe$_3$**. **P3HTPMe$_3$** and the related homopolymers, P3TMAHT and P3ImiHT, were also found to form sheet-like aggregates when combined with a 1:1 charge ratio of SDS in D_2O.[13, 14] However, the calculated sheet thicknesses were much thinner (~20 Å), and assigned to interwoven CPE-surfactant structures rather than well-defined layers.[48] In contrast, the sheet thickness obtained here for **P3HTPMe$_3$(SDS)$_1$**-d_4-MeOD (~47 Å) is in excellent agreement with the sum of the length of the individual SDS molecules (~25 Å)[51] and the solid-state *d*-spacing of poly(3-octylthiophene), suggesting that distinct SDS/CPE layers are present. However, due to the similar SLDs of **P3HTPMe$_3$** and SDS (~1 × 10^{-6} Å^{-2}), the individual layers cannot be distinguished by this experiment. Nevertheless, the formation of sheet-like, rigid particles does suggest more efficient packing of the CPE within lamellar sheets, potentially leading to the exclusion of d_4-MeOD molecules and hence the lower solvent content.

The SANS data of **P3HT-*b*-P3HTPMe$_3$** in d_4-MeOD (Figure 5.9b) were fit to the Core-Shell Cylinder model,[20] resulting in a dry core (~15% solvent) with a r_{core} = 53.1 Å, L_{core} = 572.8 Å, and a thick, wet shell (~86% solvent) of 77.4 Å. It should be noted that the phosphonium analogue appears to have a wetter and thicker shell than the Py and Im analogues described in Chapter 4.[19] This result is in good agreement with the significantly larger hydrodynamic diameter obtained by dynamic light scattering for **P3HT-*b*-P3HTPMe$_3$** in comparison to the Py and Im analogues.[19]

Unlike in D_2O, counterion exchange yields only subtle changes in the scattering profile for **P3HT-*b*-P3HTPMe$_3$(SDS)$_1$**-d_4-MeOD, with the core-shell cylinder structure of the parent copolymer retained (Figure 5.9b). The power law scaling for the intermediate q region varies from $q^{-4.4}$ for the parent diblock to $q^{-4.9}$ for **P3HT-*b*-P3HTPMe$_3$(SDS)$_1$**-d_4-MeOD, suggesting a slight change in the internal aggregate morphology. Fitting with the Core-Shell Cylinder model gave moderately elongated cylinder cores, L_{core} = 544.4 Å and r_{core} = 54.3 Å, with a slightly drier shell (~85% solvent) with a shell thickness, T_{shell} = 74.0 Å. The core is slightly more solvated (~19%) than the parent **P3HT-*b*-P3HTPMe$_3$**-d_4-MeOD, which may explain the difference in q-scaling of the intermediate region. The shell thickness for the CPE with and without SDS remains almost constant. The surfactant is expected to associate parallel to the CPE chains extending from the hydrophobic block core. This is consistent with the slightly lower N_{agg} ~230 obtained for **P3HT-*b*-P3HTPMe$_3$(SDS)$_1$**-d_4-MeOD. As such, we do not expect an increase in the thickness of the CPE shell, only in the chain packing/density within the shell, which is suggested by the subtle decrease in 'wetness'. Unfortunately, the similarity between the SLDs of the CPE block and surfactant means that we can only observe the 'global' shell structure. Future studies will involve contrast-matching with d_{25}-SDS to try and pin-point the exact orientation of the CPEs within the CPE-SDS

complexes. Nevertheless, we can conclude the addition of SDS has only a limited effect on the solution structure of **P3HT-*b*-P3HTPMe$_3$(SDS)$_1$**-d_4-MeOD, with the hydrophobic P3HT core apparently retaining the cylindrical morphology of the pure diblock polymer. In comparison, the less-aggregated homopolymer **P3HTPMe$_3$**-d_4-MeOD is able to freely transform from semi-flexible cylinders to rigid sheets upon counterion exchange.

5.3.3 Thin Film Morphology

AFM was used to determine the correlation between the nanoscale organisation of the aggregates formed in solution and the morphology of thin films. Thin films of pure CPEs and CPE/surfactant complexes dissolved in MeOH were spin-coated onto silicon substrates. By adjusting the spin rate and the volume of sample deposited, it is possible to finely control the film thickness and produce films with a more uniform surface than with drop-casting. As both the sample thickness and uniformity have a large effect the device performance,[44] an ideal system would be spin-coated. Unfortunately, it was not possible to get substantial films by spin-coating when using H_2O as a solvent due to the hydrophobicity of the silicon substrates. Consequently, all the films of the H_2O samples were prepared *via* drop-casting. Nevertheless, these studies have provided an indication about the transferability of both samples from solution to thin films.

The surface morphology of the thin films produced was found to be dependent on the type of poly(thiophene) (homo- *vs.* diblock copolymer), solvent and presence and nature of surfactant. Initially, solutions of **P3HTPMe$_3$**, **P3HTPMe$_3$(SDS)$_1$**, **P3HTPMe$_3$(PFOS)$_1$**, **P3HT-*b*-P3HTPMe$_3$**, **P3HT-*b*-P3HTPMe$_3$(SDS)$_1$** and **P3HT-*b*-P3HTPMe$_3$(PFOS)$_1$**, in H_2O (total concentration = 10 mg mL^{-1}) were drop-cast onto silicon substrates. **P3HTPMe$_3$** formed mainly featureless films (Figure 5.10a). This is not surprising since the homopolyelectrolyte is expected to be well-dissolved in H_2O, with minimal assembly into spheres or rods. In contrast, films of **P3HTPMe$_3$(SDS)$_1$** consisted of large aggregates with smooth flat surfaces. The inset phase image in Figure 5.10c shows more clearly the formation of sheet-like domains, with spacing of ~50 nm. **P3HTPMe$_3$(PFOS)$_1$** forms a collection of polydisperse spheres that show no resemblance to the parent homopolymer or **P3HTPMe$_3$(SDS)$_1$**.

P3HT-*b*-P3HTPMe$_3$ formed large clusters of small, polydisperse spheres, with an average diameter of 36.0 ± 7.7 nm (Figure 5.10b). In the image of **P3HT-*b*-P3HTPMe$_3$(SDS)$_1$** (10 mg mL^{-1}) it was difficult to distinguish any clear features within the extremely amorphous surface morphology (Figure 5.10d). However, upon dilution (×100), and using a super-fine AFM tip, we can clearly see spheres, with core-shell structure visible in the phase image (Figure 5.10d inset). The average diameter was 55.0 ± 10.4 nm with an average core diameter of 17.6 ± 3.9 nm. **P3HT-*b*-P3HTPMe$_3$(PFOS)$_1$** forms a significantly less distinct surface, with some small spheres (~30 nm) appearing at the edge of larger, amorphous aggregates.

Given that the concentration of SDS and PFOS in these samples is greater than the surfactant *cmc*s,[29, 30] it is reasonable to expect the coexistence of surfactant micelles. However,

most of CPE-SDS complexes formed films with distinctive morphologies when compared to the films of the pure surfactant (Appendix Figure A.5.5). The only exception was observed for **P3HTPMe$_3$(PFOS)$_1$** which formed a collection of polydisperse spheres which resembled pure PFOS.

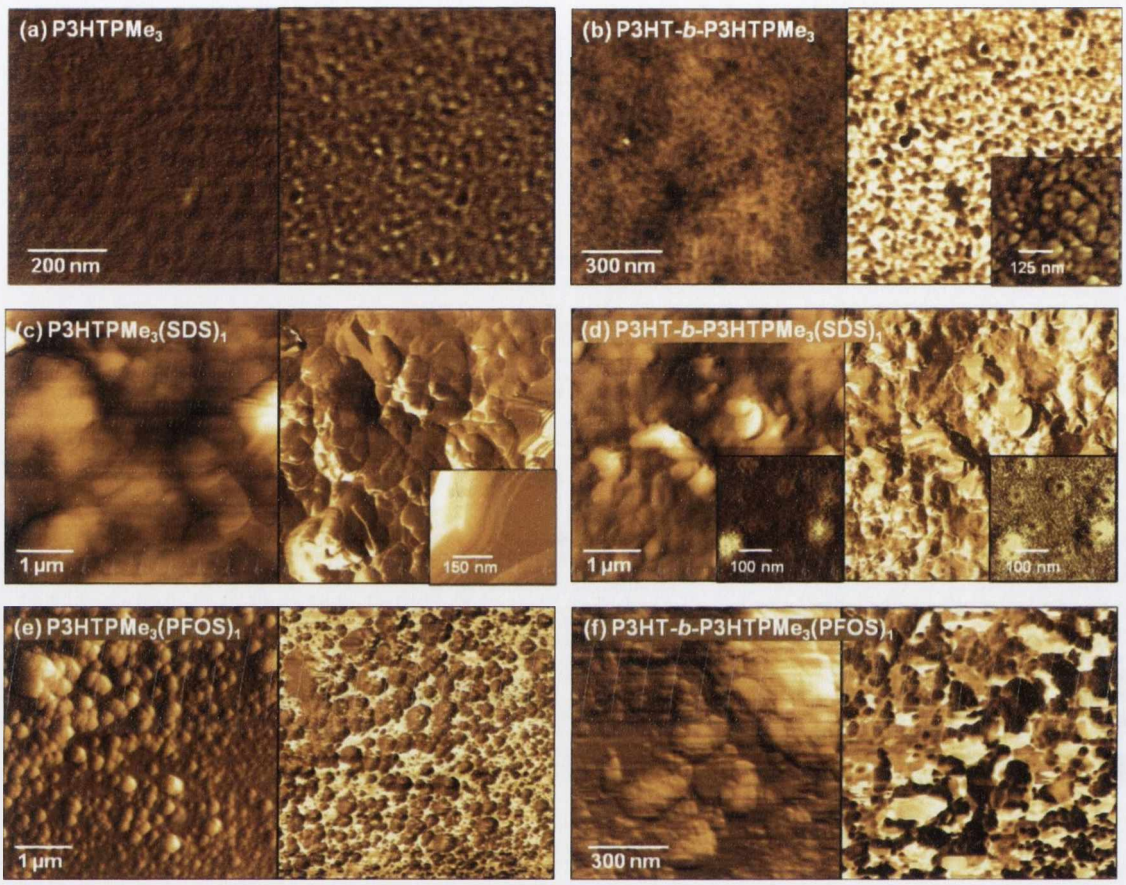


Figure 5.10 AFM tapping mode images of (a) **P3HTPMe$_3$**, (b) **P3HT-*b*-P3HTPMe$_3$** (inset: 0.25 mg mL^{-1} showing spherical structures), (c) **P3HTPMe$_3$(SDS)$_1$** (inset: lamellar structures), (d) **P3HT-*b*-P3HTPMe$_3$(SDS)$_1$** (inset: 0.1 mg mL^{-1} showing core-shell structures), (e) **P3HTPMe$_3$(PFOS)$_1$** and (f) **P3HT-*b*-P3HTPMe$_3$(PFOS)$_1$**. Drop-cast from solutions of CPE and CPE/surfactants in H_2O (10 mg mL^{-1}). Left: height images; right: phase images.

Figure 5.11 shows the tapping mode AFM images of **P3HTPMe$_3$** and **P3HT-*b*-P3HTPMe$_3$** in MeOH (10 mg mL^{-1}) with 1:1 charge ratio of SDS and PFOS. As with H_2O, **P3HTPMe$_3$**-MeOH forms largely featureless films (Figure 5.11a). Small spheres (10-20 nm) are only apparent in the phase image. Complexation with SDS produces large globules (~100 nm), which look from the phase image to be potentially vesicles. Finally, complexes formed with PFOS formed a generally flat plane of spheres, dispersed with significantly larger, flat structures (Figure 5.11e). The high resolution image inset clearly shows lamellar structure within these aggregates.

Thin films of **P3HT-*b*-P3HTPMe$_3$**-MeOH formed quite uniform films of spheres (~30 nm in diameter), which appear to have core-shell structure in the phase image inset. Complexation with SDS, Figure 5.11d, shows some spherical aggregates without any distinctive boundaries. There appears to be a continuous network running through this image, implying that CPE

aggregates are more interdispersed with SDS. In contrast, **P3HT-*b*-P3HTPMe$_3$** with PFOS, which is expected to penetrate the P3HTPMe$_3$ shell slightly less effectively, appears to retain the spherical structure from the parent copolymer more than SDS. However, the spheres of **P3HT-*b*-P3HTPMe$_3$**-PFOS complexes are significantly larger (~60 nm), which is potentially the result of a larger core radius observed from SANS measurements. Blanks films of pure SDS and PFOS prepared from MeOH bore no resemblance to any of the films of the CPE-surfactant (Figure A.5.6).

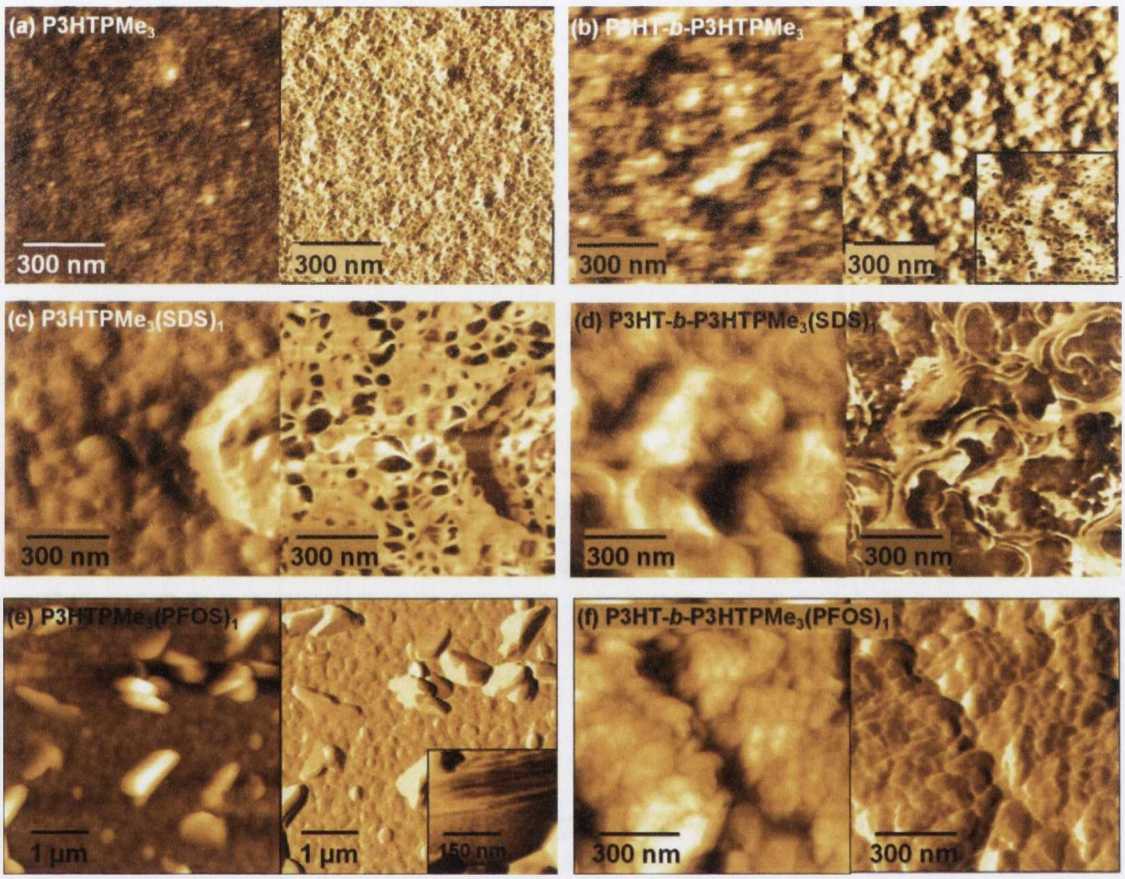


Figure 5.11 AFM tapping mode images of (a) **P3HTPMe$_3$**, (b) **P3HT-*b*-P3HTPMe$_3$** (inset: alternative phase image showing aggregate core-shell structure), (c) **P3HTPMe$_3$(SDS)$_1$**, (d) **P3HT-*b*-P3HTPMe$_3$(SDS)$_1$**, (e) **P3HTPMe$_3$(PFOS)$_1$** (inset: magnification of lamellar structures), (f) **P3HT-*b*-P3HTPMe$_3$(PFOS)$_1$**. Spin-coated onto silicon from solutions of CPEs and CPE/surfactants in MeOH (10 mg mL^{-1}). Left: height images; right: phase images.

In summary, each of the CPE and CPE-surfactant samples investigated formed films with distinctive surface morphologies. The addition of surfactants to solutions of **P3HTPMe$_3$** induced nanoscale phase separation in the film. Interestingly, each of the **P3HTPMe$_3$**-surfactant complexes in MeOH and H_2O were found to resemble lamellar sheets in regions. This corresponds well to the increased organisation suggested by the optical studies and lamellar sheet structures interpreted from the SANS data. The diblock copolymer **P3HT-*b*-P3HTPMe$_3$** deposited from MeOH and H_2O both strongly resembled core-shell spheres. This is in contrast to the core-shell cylinder or lamellar structures indicated from the SANS measurements. However, SANS also indicated that aggregates

of **P3HT-*b*-P3HTPMe$_3$** possessed solvated, wet shells. It is therefore conceivable that the removal of the solvent during drying may lead to partial reorganisation of the aggregate structure. The **P3HT-*b*-P3HTPMe$_3$**-surfactant complexes formed less distinct spherical or sometimes amorphous structures, suggesting complete or partial collapse of the core-shell structure.

5.3.4 Proposed Self-Assembly Structures

A combination of techniques has been used to characterise the aggregate morphologies of **P3HTPMe$_3$** and **P3HT-*b*-P3HTPMe$_3$** in D_2O and d_4-MeOD upon increasing charge ratio of the surfactants SDS, d_{25}-SDS and PFOS. Although previous studies have shown that an anionic surfactant can co-assemble with the cationic CPE chains or blocks, this study provided a direct comparison between the interactions of surfactants with an amphiphilic diblock copolymer and its analogous homopolyelectrolyte. Figure 5.12 shows a schematic representation of the proposed aggregate structures adopted by **P3HTPMe$_3$** and **P3HT-*b*-P3HTPMe$_3$** in D_2O upon increasing charge ratio of SDS. The fitted SANS data for **P3HTPMe$_3$** in D_2O suggest that the homopolyelectrolyte forms either short-cylinders or spherical aggregates, with R_g ~21 Å. After the addition of SDS, a significant colour change is observed, from the red-aggregated phase to a yellow solution of disrupted aggregates. The emergence of vibronic structure in the PL spectra for x = 0.2 – 2, implies the formation of rigid, compact planar aggregates. This observation corresponds well to the SANS data which suggest the formation of sheets comprised of intimate blends of CPE and surfactant. Increasing the concentration of SDS further led to the formation of isolated SDS micelles, although it was evident from the contrast-matching experiments that the **P3HTPMe$_3$**-SDS sheet complexes persist until x = 5.

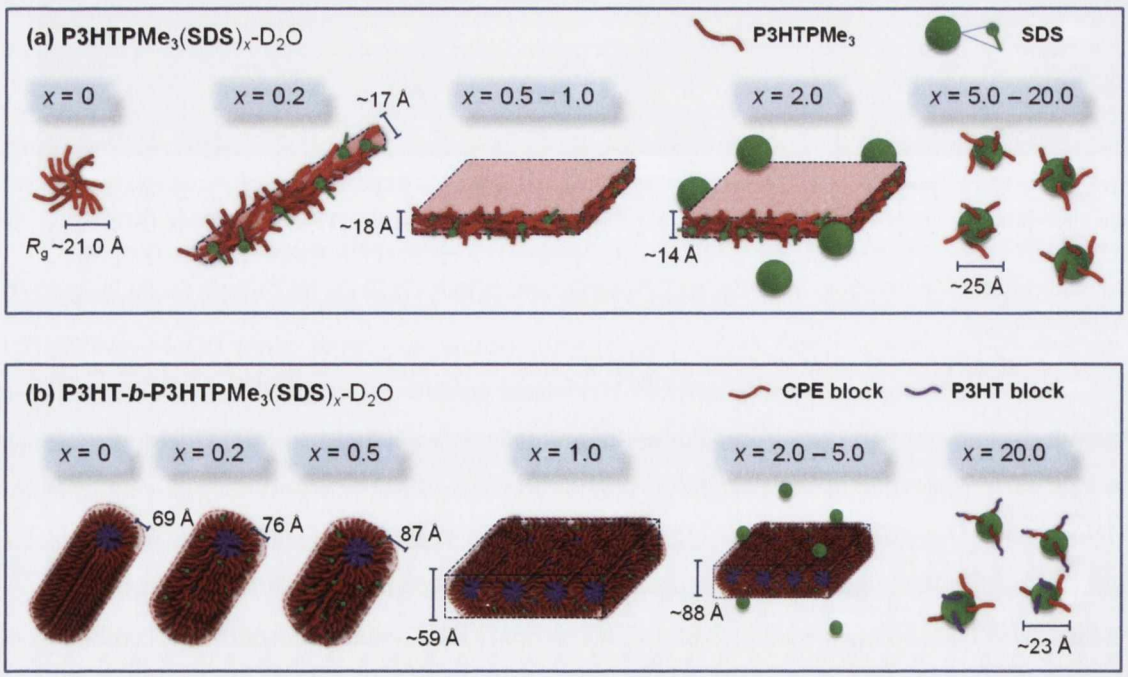


Figure 5.12 Schematic representation of the proposed self-assembly structures of (a) **P3HTPMe$_3$** and (b) **P3HT-*b*-P3HTPMe$_3$** with increasing charge ratios, x, of SDS in D_2O.

In contrast, it was found that SDS has only a limited effect on the solution-state structure of **P3HT-*b*-P3HTPMe$_3$**, with the hydrophobic P3HT core retaining the cylindrical morphology of the pure diblock copolymer. As D_2O is a selective solvent for the charged CPE block, the aggregate core is expected to consist predominantly of the neutral P3HT blocks, surrounded by a highly solvated CPE shell. Optical studies and SANS fitting indicated that polymer-polymer packing within the shell CPE blocks was affected by the presence and concentration of surfactant. Upon addition of SDS, the emission blue-shifts, while some vibronic structure is retained right up until x = 5. From SANS fitting an increase in wetness and thickness of the CPE block shell is observed upon increasing SDS, which corresponds to a reorganisation of P3HTPMe$_3$ chains. In contrast, the dimensions and wetness of the P3HT core did not alter significantly upon addition of SDS, which may account for the retention of some vibronic structure in the PL spectra far past the charge compensation point. The SANS data suggest that **P3HT-*b*-P3HTPMe$_3$** with 1:1 charge ratio of SDS, uniquely adopts a sheet-like structure. However, contrast-matching experiments with d_{25}-SDS make it possible to see how the macromolecular structure within these CPE-surfactant aggregates may be forming. The core-shell cylinder aggregates of **P3HT-*b*-P3HTPMe$_3$-SDS** are proposed to bind together with help of SDS to form lamellar sheets (Figure 5.12b).

Striking differences are also observed between how the homo- and diblock polymers interact with PFOS, a surfactant which differs significantly from SDS in the chemical nature of its head-group and hydrophobic tail. The proposed self-assembly structures of the CPEs with 1:1 charge ratio of PFOS are shown in Figure 5.13a. The PL studies indicated that PFOS had little effect on the conformation of the intrinsic **P3HTPMe$_3$** aggregates, as observed in a comparable P3TMAHT-PFOS study.[13] However, the SANS studies do suggest the formation of sheet-like aggregates. The reduced charge density of the sulfonate group in PFOS compared to the sulfate group in SDS,[27] means that PFOS is less able to penetrate the CPE aggregates. Therefore, electrostatic interactions between **P3HTPMe$_3$** and PFOS occur predominantly at the aggregate surface, where the interaction forms sheet-like aggregates, but does not alter the effective conjugation length of **P3HTPMe$_3$** backbone, thus the optical and electronic properties are essentially unchanged. This corresponds well to the fitted sheet thickness in the SANS measurements which suggested that distinct PFOS/CPE layers are present.

P3HT-*b*-P3HTPMe$_3$ appears to once again retain its core-shell cylinder structure when combined with PFOS. However, there is a striking increase in wetness and radius of the P3HT core at x = 1. When this is taken into consideration with the significantly larger blue-shift in the emission observed with PFOS over SDS, PFOS is proposed to penetrate the neutral P3HT core, causing some degree of structural rearrangement to the neutral polymer-polymer associations. Theoretical studies have shown that sulfate and sulfonate groups differ significantly in their charge density (δ_{CD} = -1.13 and -0.66, respectively)[27]. The inductive effect of the fluorine atoms will decrease this further. Thus, weaker interactions are expected between the phosphonium group of the CPEs and PFOS than with SDS. Therefore, PFOS might also be expected to penetrate more

deeply within the neutral P3HT blocks of the diblock copolymer than SDS due to weaker van der Waals forces.[45]

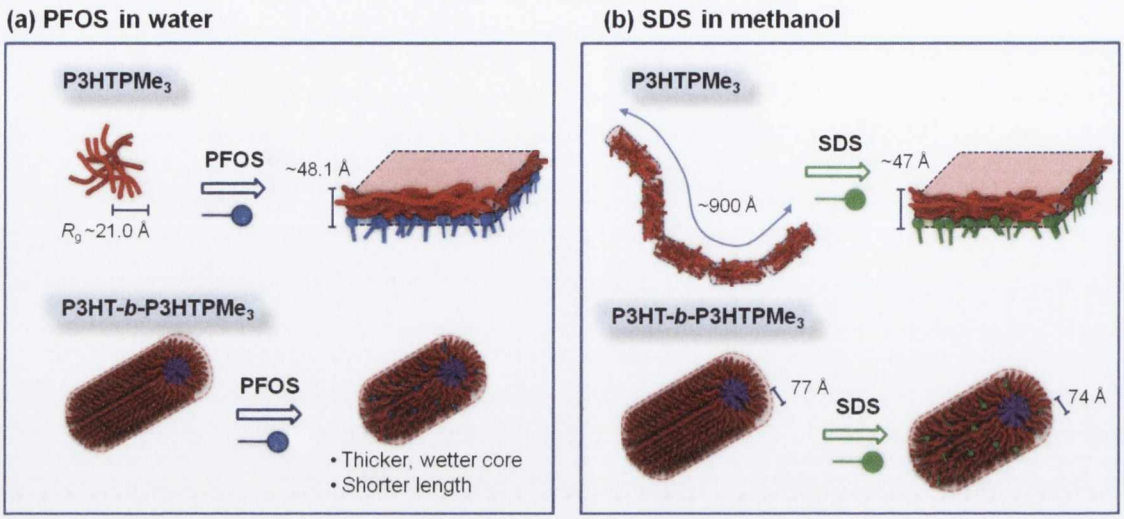


Figure 5.13 (a) Schematic representation of the proposed self-assembly structures of **P3HTPMe$_3$** and **P3HT-*b*-P3HTPMe$_3$** before and after the addition of 1:1 charge ratio of PFOS in water. (b) Schematic representation of the proposed self-assembly structures of **P3HTPMe$_3$** and **P3HT-*b*-P3HTPMe$_3$** before and after the addition of 1:1 charge ratio of SDS in methanol.

In the final study, the effect of solvent polarity on the aggregate structures of the CPE-surfactant complexes was investigated. Methanol is a significantly better solvent for device deposition than water due to its higher volatility. The optical properties of **P3HTPMe$_3$** and **P3HT-*b*-P3HTPMe$_3$** in methanolic solution only showed minor dependence on the nature of the counterion, with the addition of SDS causing a moderate blue-shift in the absorption and the emission maxima. This was attributed to reduced interchain interactions, driven by the presence of the larger counterion (in comparison to Br^-). The aggregate structures formed in MeOH, strongly resemble those in D_2O, although with subtle differences. **P3HTPMe$_3$** in d_4-MeOD formed a flexible rod-like conformation with high solvent content, while **P3HTPMe$_3$(SDS)$_1$** favoured a lamellar-type structure believed to be comprised of distinct, rather than interwoven, **P3HTPMe$_3$** and SDS layers. In contrast, **P3HT-*b*-P3HTPMe$_3$** and **P3HT-*b*-P3HTPMe$_3$(SDS)$_1$** formed core-shell cylinder aggregates in solution, with the core comprising of P3HT and the CPE block (with SDS) forming the shell.

5.3.5 Implications for Device Performance

As discussed previously, CPEs have been widely studied as interfacial charge transport and extraction layers.[3, 9, 46] In collaboration with Dr Jurgen Kesters and Prof. Wouter Maes at Hasselt University in Belgium, a preliminary investigation was performed on the incorporation of these PT-surfactant complexes as cathodic interface layers in polymer solar cells. BHJ polymer solar cells with traditional architecture (glass/ITO/PEDOT:PSS/PBDTTPD:$PC_{71}BM$/CPE/Al) were fabricated (Figure 5.14a). The photoactive layer PBDTTPD:$PC_{71}BM$ (1:1.5) (chemical structures

are shown in Appendix Figure A.5.7) was deposited from a combination of chlorobenzene and 5% (*v*/*v*) chloronaphthalene as the processing solvent. The CPE interlayers were then spin-coated directly on top of the photoactive layer from MeOH solutions in various concentrations (0.25, 0.5 and 1 mg mL^{-1}) to optimise the final device performance. As summarised in Table 5.2 and Figure 5.14b, the incorporation of the surfactant interlayers resulted in an increase in the short-circuit current density (J_{sc}).[47] J_{sc} is the largest current which may be drawn from a solar cell when the voltage across the cell is zero. The increase in J_{sc} resulted in significantly improved (*ca.* 20%) PCEs, from an average value of 7.18 to 8.65 and 8.78% for the homopolymer- and block copolymer-surfactant complexes, respectively (for an interlayer concentration of 0.5 mg mL^{-1}). These values are significantly higher than reported for polymer solar cells incorporating a P3TMAHT-SDS complex as a cathodic interlayer (PCE = 4.01% for P3HT:$PC_{61}BM$ and PCE = 6.47% for poly(thieno[3,4-b]-thiophene-*co*-benzodithiophene) (PTB7):$PC_{71}BM$).[9] A control device with pure MeOH spin-coated on top of the photoactive layer also provided some efficiency increase (7.69% average, 7.89% best PCE), in accordance with previous findings,[1, 47, 48] but the values obtained were still significantly below the PCEs observed upon incorporation of the CPE interlayers.

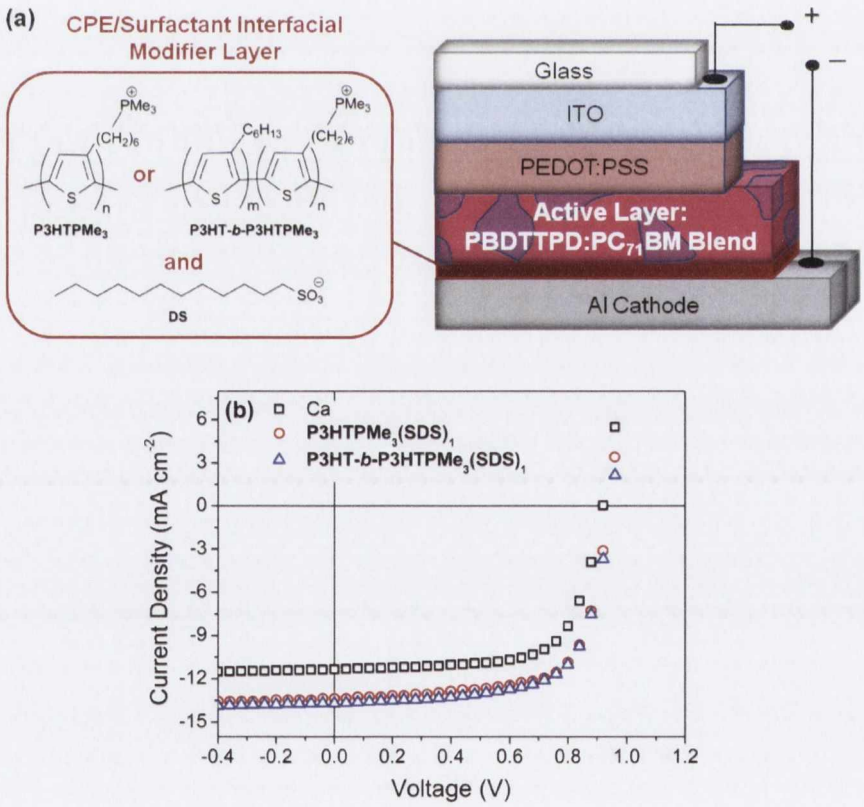


Figure 5.14 OPV device performance studies using CPE and CPE/surfactant interfacial layers. (a) Schematic representation of the bulk heterojunction polymer solar cells with traditional architecture (glass/ITO/PEDOT:PSS/PBDTTPD:$PC_{71}BM$/CPE/Al) used in the preliminary device performance studies. (b) *J-V* curves for average performance PBDTTPD:$PC_{71}BM$ solar cell devices produced with and without CPE interlayers (0.5 mg mL^{-1} deposition solution).

Table 5.2 Photovoltaic performance of PBDTTPD:$PC_{71}BM$ polymer solar cells with and without the incorporation of **P3HTPMe$_3$(SDS)$_1$** or **P3HT-*b*-P3HTPMe$_3$(SDS)$_1$** cathode interfacial layers.[a] V_{oc} is the open circuit voltage, J_{sc} is the short circuit current density, *FF* is the fill factor and PCE is the power conversion efficiency.

Cathodic interlayer	Concentration (mg mL^{-1})	V_{oc} (V)	J_{sc} (mA cm^{-2})	*FF*	Average PCE (%)[b]	Best PCE (%)
Ca		0.93	11.32	0.69	7.18	7.70
\ (Methanol)		0.92	11.73	0.71	7.69	7.89
P3HTPMe$_3$(SDS)$_1$	0.25	0.93	12.52	0.70	8.15	8.49
P3HTPMe$_3$(SDS)$_1$	0.5	0.93	13.20	0.70	8.65	8.83
P3HTPMe$_3$(SDS)$_1$	1	0.95	13.30	0.68	8.60	8.77
P3HT-*b*-P3HTPMe$_3$(SDS)$_1$	0.25	0.93	12.97	0.70	8.41	8.78
P3HT-*b*-P3HTPMe$_3$(SDS)$_1$	0.5	0.93	13.52	0.70	8.78	8.91
P3HT-*b*-P3HTPMe$_3$(SDS)$_1$	1	0.95	12.75	0.68	8.24	8.26

[a] Device structure: glass/ITO/PEDOT:PSS/PBDTTPD:$PC_{71}BM$/Ca or CPE/Al. [b] Average over 4–8 devices.

The external quantum efficiency (EQE) is given by:

$$\text{EQE}(\%) = \frac{\text{Electrons collected as photocurrent } (s^{-1})}{\text{Photons incident } (s^{-1})} \tag{5.1}$$

From the EQE spectrum the amount of current the cell will produce when exposed to sunlight can be evaluated. For our devices, enhanced photocurrent generation over the entire absorption range was observed upon incorporation of the surfactant interlayers (Figure 5.15). A maximum EQE of 65% was obtained for the reference device, whereas this increased to ~80% for the devices with CPE cathodic interlayers. The extracted current densities from the EQE measurements (J_{EQE} = 13.06 and 13.39 mA cm^{-2} for the **P3HTPMe$_3$(SDS)$_1$** and **P3HT-*b*-P3HTPMe$_3$(SDS)$_1$** interlayers, respectively) which correspond well to the measured J_{sc} values. Thus, the CPE-surfactant complexes were successfully employed as cathodic interlayers to enhance the efficiency of solar cells.

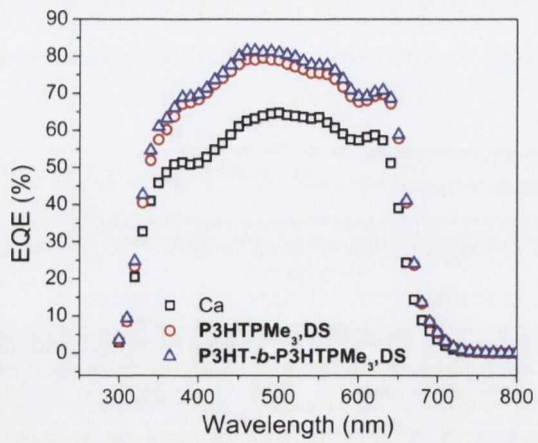


Figure 5.15 External quantum efficiency spectra for average performance PBDTTPD:$PC_{71}BM$ solar cell devices with and without CPE interlayers (0.5 mg mL^{-1} deposition solution).

The incorporation of **P3HT-*b*-P3HTPMe$_3$(SDS)$_1$** as an interfacial layer resulted in an slightly greater enhancement in the performance of the OPV device than **P3HTPMe$_3$(SDS)$_1$**, which highlights the importance of the neutral P3HT block. In addition, the short current densities showed the greatest improvement after inclusion of either interlayer material. The magnitude of this parameter is directly related to the efficiency of light absorption, exciton generation and dissociation, charge transport and charge collection at the electrodes.[49] Previously, enhanced crystallinity within films of conjugated polymers was found to increase light absorption and improve the hole mobility and charge transport.[50] The dry, neutral block cores of the aggregates of **P3HT-*b*-P3HTPMe$_3$(SDS)$_1$**, determined from the fitted SANS data, are expected to consist of well-packed, potentially crystalline P3HT chains, which are potentially the source of the enhanced J_{sc} values observed here. Furthermore, **P3HT-*b*-P3HTPMe$_3$(SDS)$_1$** in MeOH has a significantly broader absorption bandwidth than **P3HTPMe$_3$(SDS)$_1$**, which may also contribute to the increase in J_{sc}. Future measurements are planned on the full range of systems discussed in the solution-phase studies to try and fully determine the origin of the observed enhancement in OPV performance. It should be noted that the SANS and AFM experiments were performed at significantly higher solution concentrations than employed for the film deposition (~10× larger), which needs to be taken into consideration in future studies.

5.4 Conclusions and Outlook

To summarise, the optical properties of **P3HTPMe$_3$** and **P3HT-*b*-P3HTPMe$_3$** show a moderate dependence on the nature of the surfactant counterion, its concentration and the solvent. **P3HTPMe$_3$** has been shown to freely transform from spheres or semi-flexible cylinders to rigid sheets upon association with anionic surfactant, the size and morphology of which is dependent of the surfactant charge density, tail length and stiffness and solvent. In contrast, SDS has only a limited effect on the solution structure of **P3HT-*b*-P3HTPMe$_3$**, with the hydrophobic P3HT core retaining the cylindrical morphology of the pure diblock copolymer. However, contrast-matching SANS experiments with deuterated surfactants have indicated how the macromolecular organisation between CPE-SDS aggregates is formed. Furthermore, the reduced charge density of perfluorinated surfactants may offer an effective route to tune the polymer-polymer packing density within the P3HT-cores. The ability to control the chain packing within the semi-crystalline P3HT blocks could be harnessed to balance the charge carrier ability with other physical properties of the films.[51, 52] For example, greater packing of the polymer chains in solution-state structures could be an optimal route to increase chain-packing in the corresponding thin films and thus increase charge generation in the corresponding OPV devices.

AFM studies revealed that the CPE-surfactant complexes formed films with distinctive surface morphologies from the pure parent polymers. The homopolyelectrolyte **P3HTPMe$_3$** was found to phase separate into organised nanostructures upon surfactant addition. While the structures formed from the diblock copolymers, which already phase separate due to the inherent

incompatibility of the poly(thiophene) blocks, are transformed upon the addition of surfactant. Unfortunately, a direct comparison between films prepared from methanol and water is not possible due to different deposition procedures (spin-coating *vs.* drop-casting, respectively). However, these initial studies have indicated that distinctive morphologies between the two mediums, with the homogeneity and size of the aggregates dependent on the surfactant and solvent used. It is interesting to note that the core-shell structures formed in solution (SANS) are retained in the films spin-coated from methanol, since one potential drawback of spin-coating is that it is known to reduce the crystallinity of P3HT thin films by preventing appropriate alignment of the polymer chains.[52]

A full investigation of the CPE-surfactant complexes incorporated into OPV devices to enhance their PCE efficiencies has yet to be performed. However, preliminary performance studies showed a 20% increase in the PCE of a BHJ-OPV device (with PBDTTPD:$PC_{71}BM$ as the active layer) through the incorporation of poly(thiophene)-dodecyl sulfate complex as a cathodic interfacial layer. Unfortunately, no direct correlation between the solution-phase structure (from SANS, optical spectroscopy), the layer morphology (from AFM) and the observed enhancement in the device performance could be identified from this preliminary study. This is understandable, since the effect of molecular structure, solvent, the role of the spin-coating deposition process in reducing polymer chain alignment, and thermally-induced morphological changes from the heating-cooling cycles inherent to device operation[53] were not probed in any detail. Furthermore, while AFM is a convenient tool to measure the bulk phase separation, it is not a suitable method to probe the crystallinity of the semi-crystalline polymers which is believed to underpin the significant enhancement in the PCEs observed here.[51] Therefore, a strategic structure-property organisation study is now underway to investigate the nano-microstructural order of surfactant-ordered homo- and diblock-poly(thiophene) films using grazing-incidence small-/wide-angle X-ray scattering (GiSAXS/GiWAXS). GiSAXS will be used to probe the long-range connectivity and GiWAXS will investigate the relative degree of polymer crystallinity. Particular emphasis will be placed on identifying how the surfactant controls the nature and extent of face-to-face packing of the conjugated polymer backbones (π-π–stacking) and edge-to-edge packing of the conjugated polymer side chains (*lamellar*-stacking). These studies will also look at thin films which have been prepared by both spin- and drop-casting methods to investigate the effect of the deposition process on the film organisation. Thermal annealing (*ex-situ*) will be performed on some films at a temperature intermediate to the glass transition and melting temperatures of the CPE-surfactant complexes to probe the thermally-induced reorganisation of the film structure. These results will be correlated with complementary microscopy experiments (AFM, TEM) to probe the film morphology and OPV devices will be fabricated and characterised for the most relevant examples. Given the vast tuneability offered by homopolymer and diblock copolymer-surfactant complexes, coupled with their solution processability, further significant enhancements in OPV device performance are to be expected once their structure-property relationships are better understood.

5.5 References

1. J. H. Seo, A. Gutacker, Y. Sun, H. Wu, F. Huang, Y. Cao, U. Scherf, A. J. Heeger and G. C. Bazan, *J. Am. Chem. Soc.*, 2011, **133**, 8416-8419.
2. J. Luo, H. Wu, C. He, A. Li, W. Yang and Y. Cao, *Appl. Phys. Lett.*, 2009, **95**, 222512.
3. J. Kesters, S. Govaerts, G. Pirotte, J. Drijkoningen, M. Chevrier, N. Van den Brande, X. Liu, M. Fahlman, B. Van Mele, L. Lutsen, D. Vanderzande, J. Manca, S. Clément, E. Von Hauff and W. Maes, *ACS Appl. Mater. Interfaces*, 2016, **8**, 6309-6314.
4. B. Cao, X. He, C. R. Fetterly, B. C. Olsen, E. J. Luber and J. M. Buriak, *ACS Appl. Mater. Interfaces*, 2016, **8**, 18238-18248.
5. H. Ju, K. M. Knesting, W. Zhang, X. Pan, C.-H. Wang, Y.-W. Yang, D. S. Ginger and J. Zhu, *ACS Appl. Mater. Interfaces*, 2016, **8**, 2125-2131.
6. B. Xiao, H. Wu and Y. Cao, *Mater. Today*, 2015, **18**, 385-394.
7. C. He, C. Zhong, H. Wu, R. Yang, W. Yang, F. Huang, G. C. Bazan and Y. Cao, *J. Mater. Chem.*, 2010, **20**, 2617-2622.
8. S. Chen, J. R. Manders, S.-W. Tsang and F. So, *J. Mater. Chem.*, 2012, **22**, 24202-24212.
9. Y.-M. Chang, R. Zhu, E. Richard, C.-C. Chen, G. Li and Y. Yang, *Adv. Funct. Mater.*, 2012, **22**, 3284-3289.
10. G. Heimel, I. Salzmann, S. Duhm, J. P. Rabe and N. Koch, *Adv. Funct. Mater.*, 2009, **19**, 3874-3879.
11. H. D. Burrows, M. J. Tapia, C. L. Silva, A. A. C. C. Pais, S. M. Fonseca, J. Pina, J. Seixas de Melo, Y. Wang, E. F. Marques, M. Knaapila, A. P. Monkman, V. M. Garamus, S. Pradhan and U. Scherf, *J. Phys. Chem. B*, 2007, **111**, 4401-4410.
12. L. Chen, S. Xu, D. McBranch and D. Whitten, *J. Am. Chem. Soc.*, 2000, **122**, 9302-9303.
13. R. C. Evans, M. Knaapila, N. Willis-Fox, M. Kraft, A. Terry, H. D. Burrows and U. Scherf, *Langmuir*, 2012, **28**, 12348-12356.
14. M. Knaapila, R. C. Evans, V. M. Garamus, L. s. Almásy, N. m. K. Székely, A. Gutacker, U. Scherf and H. D. Burrows, *Langmuir*, 2010, **26**, 15634-15643.
15. M. Knaapila, R. C. Evans, A. Gutacker, V. M. Garamus, N. K. Szekely, U. Scherf and H. D. Burrows, *Soft Matter*, 2011, **7**, 6863-6872.
16. J. J. Lavigne, D. L. Broughton, J. N. Wilson, B. Erdogan and U. H. F. Bunz, *Macromolecules*, 2003, **36**, 7409-7412.
17. H. D. Burrows, V. M. M. Lobo, J. Pina, M. L. Ramos, M. J. S. de, A. J. M. Valente, M. J. Tapia, S. Pradhan and U. Scherf, *Macromolecules*, 2004, **37**, 7425-7427.
18. M. Knaapila, L. Almásy, V. M. Garamus, C. Pearson, S. Pradhan, M. C. Petty, U. Scherf, H. D. Burrows and A. P. Monkman, *J. Phys. Chem. B*, 2006, **110**, 10248-10257.
19. A. Thomas, J. E. Houston, N. Van den Brande, J. De Winter, M. Chevrier, R. K. Heenan, A. E. Terry, S. Richeter, A. Mehdi, B. Van Mele, P. Dubois, R. Lazzaroni, P. Gerbaux, R. C. Evans and S. Clément, *Polym. Chem.*, 2014, **5**, 3352-3362.
20. I. Livsey, *J. Chem. Soc., Faraday Trans. 2*, 1987, **83**, 1445-1452.
21. A. Guinier and G. Fournet, *Small Angle Scattering of X-rays*, John Wiley and Sons, 1955.
22. K. K. Stokes, K. Heuzé and R. D. McCullough, *Macromolecules*, 2003, **36**, 7114-7118.
23. K. Faied, M. Frechette, M. Ranger, L. Mazerolle, I. Levesque, M. Leclerc, T.-A. Chen and R. D. Rieke, *Chem. Mater.*, 1995, **7**, 1390-1396.
24. Y.-H. Lee, W.-C. Yen, W.-F. Su and C.-A. Dai, *Soft Matter*, 2011, **7**, 10429-10442.
25. M. Sundberg, O. Inganäs, S. Stafström, G. Gustafsson and B. Sjögren, *Solid State Commun.*, 1989, **71**, 435-439.
26. V. M. Sadtler, F. Giulieri, M. P. Krafft and J. G. Riess, *Chem. Eur. J.*, 1998, **4**, 1952-1956.
27. P. D. T. Huibers, *Langmuir*, 1999, **15**, 7546-7550.

28. A. I. Mitsionis and T. C. Vaimakis, *Chem. Phys. Lett.*, 2012, **547**, 110-113.
29. P. Kékicheff, C. Grabielle-Madelmont and M. Ollivon, *J. Colloid Interface Sci.*, 1989, **131**, 112-132.
30. Q. Yuan, R. Ravikrishna and K. T. Valsaraj, *Sep. Purif. Technol.*, 2001, **24**, 309-318.
31. T. J. Prosa, M. J. Winokur, J. Moulton, P. Smith and A. J. Heeger, *Macromolecules*, 1992, **25**, 4364-4372.
32. A. A. Golosova, J. Adelsberger, A. Sepe, M. A. Niedermeier, P. Lindner, S. S. Funari, R. Jordan and C. M. Papadakis, *J. Phys. Chem. C*, 2012, **116**, 15765-15774.
33. J. B. Hayter and J. Penfold, *Mol. Phys.*, 1981, **42**, 109-118.
34. J.-P. Hansen and J. B. Hayter, *Mol. Phys.*, 1982, **46**, 651-656.
35. J. B. Hayter and J. Penfold, *Colloid. Polym. Sci.*, 1983, **261**, 1022-1030.
36. B. Hammouda, *J. Appl. Crystallogr.*, 2010, **43**, 716-719.
37. F. Nallet, R. Laversanne and D. Roux, *J. Phys. II France*, 1993, **3**, 487-502.
38. J. Berghausen, J. Zipfel, P. Lindner and W. Richtering, *J. Phys. Chem. B*, 2001, **105**, 11081-11088.
39. P. W. Schmidt, *Some Fundamental Concepts and Techniques Useful in Small-Angle Scattering Studies of Disordered Solids. In Modern Aspects of Small-Angle Scattering*, Kluwer Academic Publishers: Dordrecht, The Netherlands, 1995.
40. A. Gutacker, S. Adamczyk, A. Helfer, L. E. Garner, R. C. Evans, S. M. Fonseca, M. Knaapila, G. C. Bazan, H. D. Burrows and U. Scherf, *J. Mater. Chem.*, 2010, **20**, 1423-1430.
41. S. R. Kline, *Langmuir*, 1999, **15**, 2726-2732.
42. W.-R. Chen, P. D. Butler and L. J. Magid, *Langmuir*, 2006, **22**, 6539-6548.
43. J. S. Pedersen and P. Schurtenberger, *Macromolecules*, 1996, **29**, 7602-7612.
44. M.-S. Kim, B.-G. Kim and J. Kim, *ACS Appl. Mater. Interfaces*, 2009, **1**, 1264-1269.
45. A. González-Pérez, J. M. Ruso, G. Prieto and F. Sarmiento, *J. Surf. Det.*, 2004, **7**, 387-395.
46. H. Choi, J. S. Park, E. Jeong, G.-H. Kim, B. R. Lee, S. O. Kim, M. H. Song, H. Y. Woo and J. Y. Kim, *Adv. Mater.*, 2011, **23**, 2759-2763.
47. J. Kesters, T. Ghoos, H. Penxten, J. Drijkoningen, T. Vangerven, D. M. Lyons, B. Verreet, T. Aernouts, L. Lutsen, D. Vanderzande, J. Manca and W. Maes, *Adv. Energy Mater.*, 2013, **3**, 1180-1185.
48. H. Zhou, Y. Zhang, J. Seifter, S. D. Collins, C. Luo, G. C. Bazan, T.-Q. Nguyen and A. J. Heeger, *Adv. Mater.*, 2013, **25**, 1646-1652.
49. A. Facchetti, *Mater. Today*, 2013, **16**, 123-132.
50. G. Dennler, M. C. Scharber and C. J. Brabec, *Adv. Mater.*, 2009, **21**, 1323-1338.
51. S. Y. Son, Y. Kim, J. Lee, G.-Y. Lee, W.-T. Park, Y.-Y. Noh, C. E. Park and T. Park, *J. Am. Chem. Soc.*, 2016, **138**, 8096-8103.
52. H. Erothu, J. Kolomanska, P. Johnston, S. Schumann, D. Deribew, D. T. Toolan, A. Gregori, C. Dagron-Lartigau, G. Portale and W. Bras, *Macromolecules*, 2015, **48**, 2107-2117.
53. R. Dattani, J. H. Bannock, Z. Fei, R. C. I. MacKenzie, A. A. Y. Guilbert, M. S. Vezie, J. Nelson, J. C. de Mello, M. Heeney, J. T. Cabral and A. J. Nedoma, *J. Mater. Chem. A*, 2014, **2**, 14711-14719.

Chapter 6

Charge-Modulated Self-Assembly and Growth of Conjugated Polyelectrolyte-Polyoxometalate Hybrid Networks

The work presented in this chapter has been published in part in:

J. E. Houston, A. R. Patterson, A. C. Jayasundera, W. Schmitt and R. C. Evans, Charge-Modulated Self-Assembly and Growth of Conjugated Polyelectrolyte–Polyoxometalate Hybrid Networks, *Chem. Commun.*, 2014, **50**, 5233-5235.

6.1 Introduction

In recent years organic-inorganic hybrid polymer solar cells have drawn increasing attention as they combine the advantages associated with both the organic and the inorganic components, including good mechanical strength, substrate flexibility, low-cost solution-based processing, high carrier mobility, complementary light absorption and environmental stability.[1] Furthermore, with judicious selection of the organic/inorganic building blocks it should be possible to tune the supramolecular organisation and impart enhanced functionality due to synergistic interactions between the two components. A particularly exciting class of hybrid materials include hole-conducting polymers associated with polyoxometalates (POMs).[2] POMs are polyanionic metal-oxide clusters which can be extremely diverse in size, composition, charge and structure and have a wide range of applications from sensing[3] and catalysis[4] to light-emitting devices.[5] They are particularly promising materials for charge-separation and charge-transport in photovoltaic devices,[2] due to their ability to accept and release a specific number of electrons without decomposition or change in their structural arrangements.[3, 6] As such, POMs are potentially superior alternatives to the traditional materials used as the electron acceptor,[7] such as [6,6]-phenyl-C_{61}-butyric acid methyl ester ($PC_{61}BM$).[8] In these envisioned POM-based devices, π-conjugated polymers are the photo-excited electron donors and the POM clusters behave as the electron acceptors.

An early demonstration of a CP-POM photovoltaic cell was developed by Wang *et al.* in 2013.[9] They showed that the spherical keplerate polyoxometalate $[K_{20}\{(W)W_5O_{21}(SO_4)\}_{12}(VO)_{30}(SO_4)(H_2O)_{63}]^{18-}$ ($[W_{72}V_{30}]^{18-}$) could act as the electron acceptor material when combined with the cationic poly(*p*-phenylenevinylene) derivative, poly[2,5-bis[3-(*N,N,N*-triethylammonium)-1-oxapropyl]-1,4-phenylenevinylene]-dibromide (P2) through a layer-by-layer deposition approach.[9] The composite $W_{72}V_{30}$-P2 films showed significant photocurrent response (J_{sc} = 1.68 μA cm^{-2}) when compared to that of the reference device which consisted of composite poly(sodium-*p*-styrenesulfonate) (PSS)-P2 films (J_{sc} = 0.55 μA cm^{-2}), where PSS is simply a conductive polymer. The enhancement was attributed the occurrence of efficient photoinduced electron transfer from P2 to $[W_{72}V_{30}]^{18-}$. More recently, Peng *et al.* investigated three POM-containing hybrid rod-coil diblock copolymers.[10] POM clusters were covalently attached as side-chain pendants to the coil block which itself was attached to a P3HT "rod" block. Differences in solubility between the POM-rich block and the CP block led to phase separation. Thin film studies revealed conduction domains with worm-like textures of < 50 nm - a perfect morphology for BHJ solar cells. However, the devices prepared from these materials were found to have power conversion efficiencies of ~0.055%.[10] The low PCEs were attributed to the lack of direct π-conjugation between the organic P3HT block (the donor) and the coordinated-POM block (the acceptor), leading to inefficient charge transfer. One potential solution to this problem is to covalently attach the POMs directly to the electron donor CP-block. However, this rather difficult

synthetic procedure has yet to yield the desired *D-A* nanoscale morphology required for efficient organic solar cell devices.[2]

POMs have also shown promise as highly efficient interlayer materials in OPV devices, due to their rich redox properties, photoactivity, light-induced electron transfer process, nanostructured morphology and attractive optical properties such as high transparency in the visible region of the light spectrum.[11] For example, the tungsten polyoxometalate, $H_3PW_{12}O_{40}$, was previously employed as a cathodic interfacial layer in a hybrid polymer solar cell.[11] The authors observed a ~40% increase in the J_{sc} of the device modified with the $H_3PW_{12}O_{40}$ interfacial layer, which resulted in a 70% increase in PCE from 1.57% to 2.70%. The LUMO of the $H_3PW_{12}O_{40}$ semiconducting layer was found to be favourably aligned with the Fermi level of the Al cathode, facilitating electron transport and extraction when inserted between the active layer and Al, while its nanostructured morphology was believed to assist charge extraction by increasing the local electric field at the contact area.

6.1.1 Aims of this work

POMs have been used frequently to construct organic-inorganic hybrid materials *via* covalent linkages and ionic self-assembly.[12, 13] However, it is difficult to realise hybrid CP-POM networks *via* covalent bonding with the desired structural organisation, due to the drastic differences in molecular arrangement of the organic and inorganic components. The motivation of this work is to see if POMs could be used in a similar manner to surfactants to form organised structures with CPEs *via* electrostatic assembly.[14] Such an approach would be facile and less energetically demanding than the alternative covalent co-assembly. As POMs are large, anionic clusters, in order to achieve electrostatic self-assembly, the CPEs used need to be cationic. Two commercially available cationic CPEs were chosen, which differ in the nature and number of repeat units (r.u.) and distribution of their side chains. Poly[(2,5-bis(2-(*N*,*N*-diethylammoniumbromide)ethoxy)-1,4-phenylene)-*alt*-1,4-phenylene)] (**NET**) has only 2 r.u. per chain, with a M_w of approximately 1,054 g mol^{-1}. In contrast, poly[(9,9-di(3,3′-*N*,*N*′-trimethylammonium)propylfluorenyl-2,7-diyl)-*alt*-(1,4-phenylene)] (**PFP**) has ~14-22 r.u. per chain with a M_w of 10,000-15,000 g mol^{-1}. Both CPEs contain two ammonium groups per r.u. located in opposite and adjacent positions in **NET** and **PFP**, respectively, as shown in Figure 6.1. As the counter-ion, the γ-Keggin isomer of the well-studied anionic lacunary decatungstosilicate $K_8[SiW_{10}O_{36}]$ (**POM**) was chosen (Figure 6.1).[3, 15] It is anticipated that the difference in the steric charge distribution on the CPEs will control the direction of self-assembly and, thus, the dimensionality of the resulting supramolecular networks.

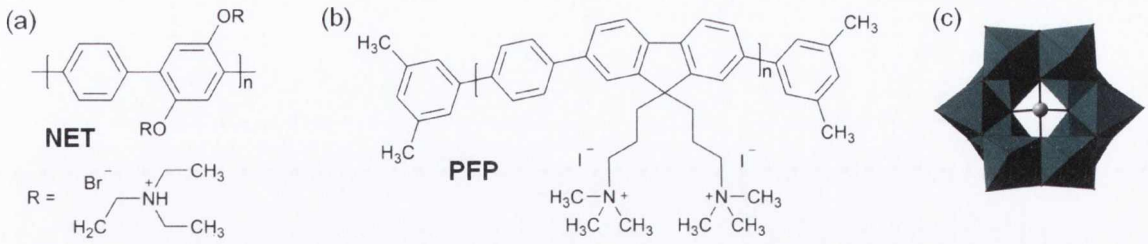


Figure 6.1 Chemical structures of (a) **NET** and (b) **PFP**. (c) Top view of the lacunary $[SiW_{10}O_{36}]^{8-}$ fragment (**POM**) (Si grey and WO_6 octahedra teal).

The specific aims include:

- to obtain POM-CPE hybrid materials through electrostatic co-assembly and fully understand the interactions formed within their structures;
- to determine whether the chemical structure of the CPE can be used to control the dimensionality of the hybrid material;
- to determine if hybrid networks can be transferred from the solution phase to thin films with retention of their nanoscale morphology. This is extremely important if these materials are to be realised for potential device applications.[16]

6.2 Experimental

6.2.1 Materials

Poly[(9,9-di(3,3′-*N*,*N*′-trimethylammonium)propylfluorenyl-2,7-diyl)-*alt*-(1,4-phenyl-ene)]diiodide salt, end-capped with dimethylphenyl (**PFP**), was purchased from American Dye Source, Inc., and has a M_w = 10,000-15,000 g mol^{-1}. Poly[(2,5-bis(2-(*N*,*N*-diethyl-ammonium bromide)ethoxy)-1,4-phenylene)-*alt*-1,4-phenylene] (**NET**) was purchased from Sigma Aldrich, and has an M_w = 1,054 g mol^{-1}, M_n = 745 g mol^{-1} and a PDI = 1.4. $K_8[SiW_{10}O_{36}]\cdot xH_2O$ (**POM**) was synthesised by Dr Anil Jayasundera according to the procedure previously reported in the literature.[15]

6.2.2 Methods

Instrumentation for UV/Vis absorption, PL, FTIR, LD and NMR spectroscopy, DLS and AFM are described in Chapter 3.

UV/Vis absorption and PL titration procedure: A stock solution of **PFP** (1.44 × 10^{-3} M (r.u.)) was prepared in 3:1 (*v*/*v*) Millipore water/MeCN and a stock solution of **NET** (1.84 × 10^{-3} M (r.u.)) was prepared in Millipore water; both solutions were stirred for at least two days before use. Aliquots of an aqueous **POM** solution (0.04 mM) were added to a fixed volume of CPE solution across the concentration range 0 – 1.54 × 10^{-6} M for **NET** and 0 – 7.2 × 10^{-7} M for **PFP**. Dilution effects were accounted for in the UV/Vis absorption and PL spectra and no significant change in pH was observed across the titrations.

DLS titration procedure: Solutions of **PFP** (7.20×10^{-6} M (r.u.)) and **NET** (9.18×10^{-6} M (r.u.)) were prepared in filtered Millipore water. Aliquots of a filtered aqueous **POM** solution (0.04 mM) were added to the solution of CPE across the concentration range $0 - 3.17 \times 10^{-6}$ M for **NET** and $0 - 2.26 \times 10^{-6}$ M for **PFP**. All measurements were performed at 20 °C. It is noted that the solutions were not visibly turbid, nor was any precipitation observed. The *Z*-average hydrodynamic radius was calculated by assuming that the diffusing particles were monodisperse spheres. R_H values were averaged from 3 runs of approximately 20 measurements each.

AFM and SEM sample preparation: Samples for AFM and SEM were prepared in the same way. The concentrations for the blank samples were [**POM**] = 5×10^{-7} M, [**NET**] = 6.4×10^{-7} M (r.u.) and [**PFP**] = 5×10^{-7} M (r.u.) (for AFM, [**PFP**] = 5×10^{-8} M (r.u.)). For the preparation of **POM**/CPE hybrids, the concentration for both CPEs was fixed at [CPE] = 5×10^{-7} M (r.u.). The concentration of **POM** was varied to obtain the desired charge ratio; namely a charge ratio of 1 for **POM/NET** ([**POM**] = 5×10^{-7} M), and a charge ratio of 0.5 for **POM/PFP** ([**POM**] = 6.25×10^{-8} M). For AFM, these stocks were diluted further by a factor of 10. **POM**/CPE films were prepared by drop-casting 20 μL aliquots of the stock solutions onto freshly cleaved mica for AFM and cut silicon wafers for SEM. In both cases, films were left to dry at room temperature.

Linear dichroism: For both CPEs a starting concentration was chosen which gave an optical density of approximately 1.1. Aqueous **POM** solution (0.04 mM) was then added to obtain a **POM**/CPE charge ratio of 1 and 0.5 for **NET** and **PFP**, respectively.

6.3 Results and Discussion

6.3.1 UV/Vis Absorption and PL Studies

The UV/Vis and PL spectra of each CPE in aqueous solution were measured upon titration of the **POM** to investigate the possibility of complex formation. Figures 6.2a and 6.2c show the UV/Vis absorption spectra of aqueous solutions of **NET** and **PFP**, respectively, upon addition of **POM**. In both cases there is an increase in absorbance at 250 nm which can be attributed to **POM** O→W LMCT band.[5] The second observation is the decrease and red-shift in the absorbance maximum of the CPE, from 375 nm to 380 nm for **NET**, and from 331 nm to 344 nm for **PFP**. Simultaneously, red-edge band broadening was observed, which may be attributed to an increase in the effective conjugation length of the CPE.[17] Finally, upon the addition of **POM,** isosbestic points appear at ~303 nm for both CPEs, and a second isosbestic point at 342 nm for **NET** and 402 nm for **PFP**, respectively, which provide a clear indication of CPE-**POM** associations.

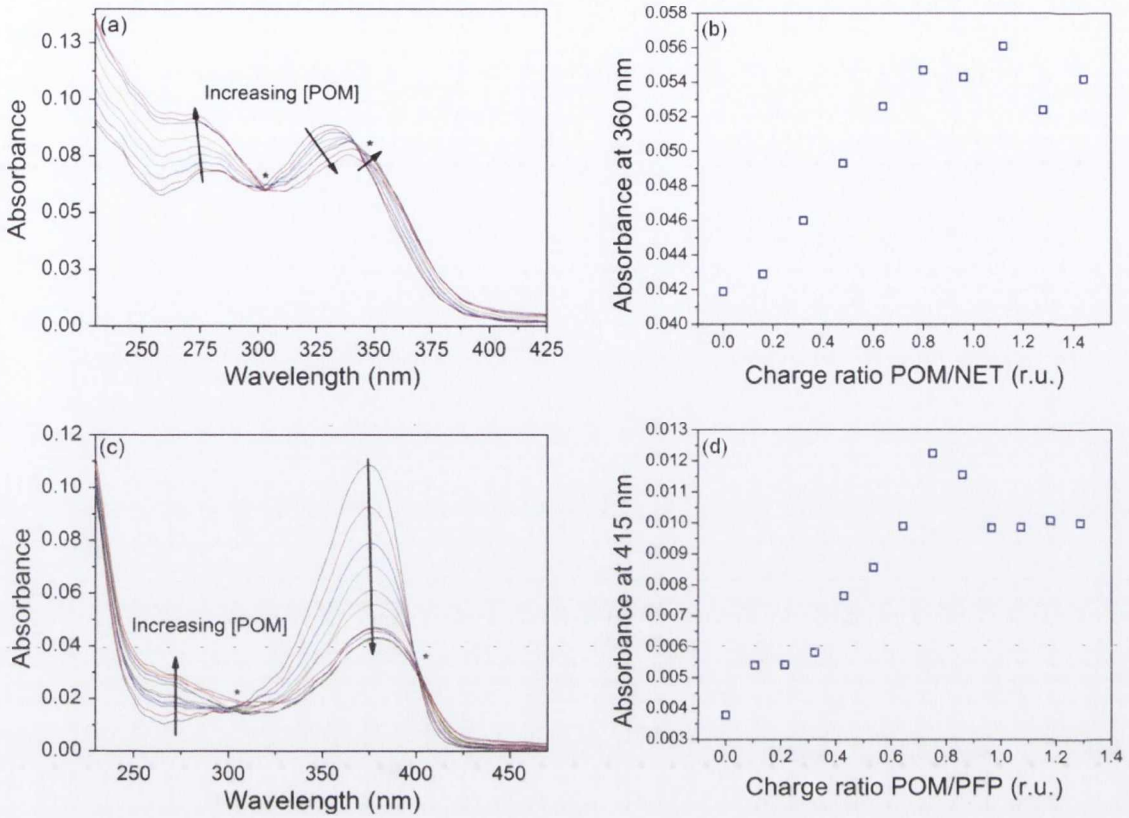


Figure 6.2 UV/Vis absorption spectra of (a) **NET** in water (5×10^{-6} M (r.u.)) on addition of **POM** ($0 - 1.54 \times 10^{-6}$ M) and (c) **PFP** in water (2.4×10^{-6} M (r.u.)) on addition of **POM** ($0 - 7.2 \times 10^{-7}$ M). UV/Vis absorbance maxima of (b) **NET** at 360 nm and (d) **PFP** at 415 nm, plotted as a function of charge ratio.

The CPE:**POM** charge ratio was determined from the number of charges per r.u. of the CPE (+2), the average number of the r.u. per chain, the number of charges on the **POM** (-8) and the molar concentrations of each. Figures 6.2b and 6.2d show the UV/Vis absorbance at 360 nm and 415 nm of **NET** and **PFP**, respectively, upon the addition of **POM**, plotted as a function of charge ratio. The plots show that the trends in the change in UV/Vis absorption plateau at charge neutralisation (**POM**/CPE = 1), after which there is expected to be no more 'free' cationic CPE to associate with the anionic **POM**. This indicates that electrostatic interactions play a major role in the binding affinity.

Figures 6.3a and 6.3c show the corresponding PL spectra of the CPEs upon addition of the **POM**. In water, **NET** exhibits a single broad emission band at $\lambda_{em} = 404$ nm, while **PFP** exhibits an emission maximum at 408 nm with some vibronic structure, which is assigned to the vibronic progression of the C=C stretching mode ($\Delta E \approx 0.15$ eV).[18] The addition of the anionic **POM** leads to quenching of the PL intensity of the cationic CPEs. This quenching process can be described by the Stern-Volmer equation (Equation 2.9). Figures 6.3b and 6.3d show the Stern-Volmer plots for **NET** and **PFP**, respectively. Both plots were found to be linear below the charge neutralisation point with Stern-Volmer constants of $K_{SV} = 5.73\ (\pm 1.54) \times 10^6\ M^{-1}$ for **NET** and $K_{SV} = 1.16\ (\pm 0.52) \times 10^8\ M^{-1}$ for **PFP**. These values are indicative of static quenching, where a non-emissive complex

forms between the CPE and the **POM**. Thus, the slope of the plots, now termed K_a, represents the association constant for the quenching process and can be described by Equation 2.10.

CPs are known to exhibit amplified fluorescence quenching due to efficient exciton migration along the conjugated backbone.[19] Therefore, **PFP** with its higher M_w than **NET**, would be expected to exhibit amplified quenching, typical of CPs. This is also reflected by the lower charge ratio at which the **POM**/CPE quenching (0.67 for **PFP**, 1.12 for **NET**) undergoes further amplification. This is most likely a consequence of the CPE chains being brought into closer proximity with each other upon association with the **POM** which amplifies these quenching interactions.

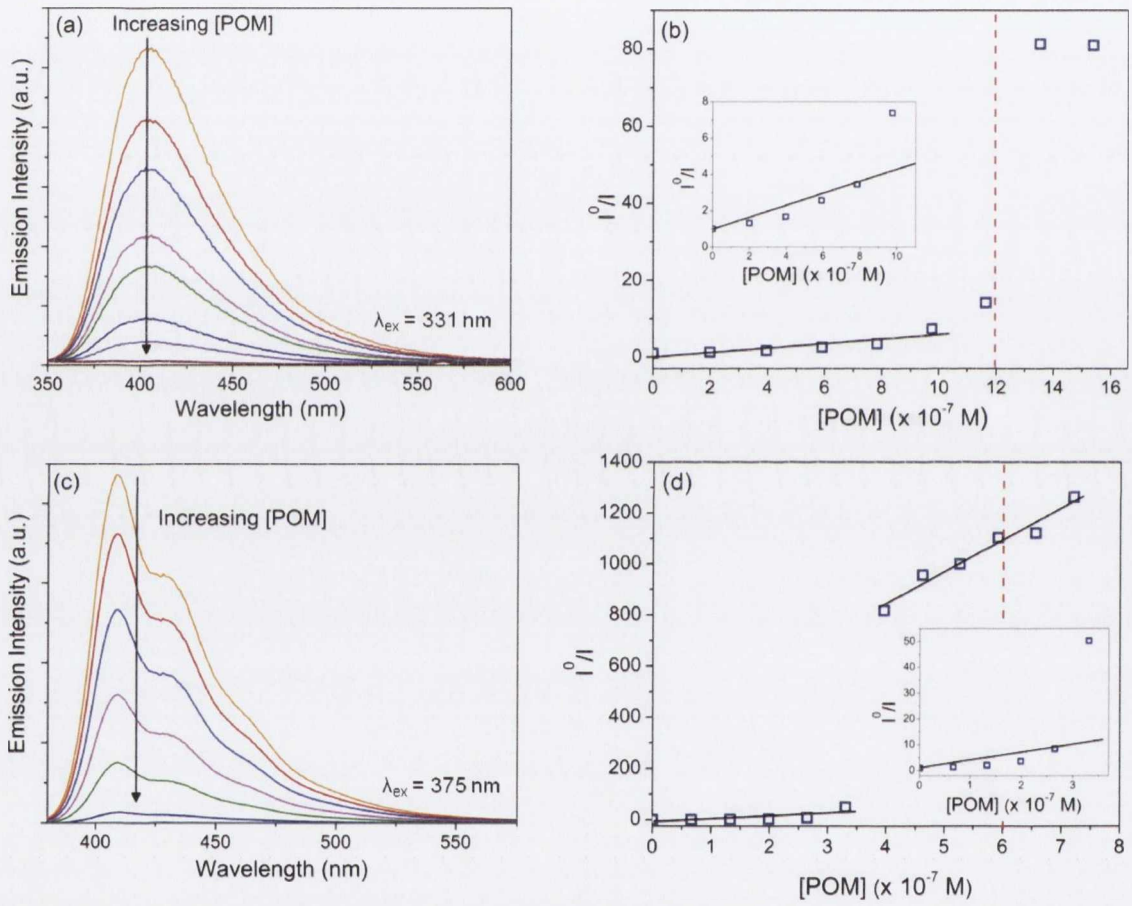


Figure 6.3 PL spectra of (a) **NET** in water (5×10^{-6} M (r.u.)) on addition of **POM** ($0 - 1.54 \times 10^{-6}$ M) and (λ_{ex} = 331 nm) (c) **PFP** in water (2.4×10^{-6} M (r.u.)) on addition of **POM** ($0 - 7.2 \times 10^{-7}$ M) (λ_{ex} = 375 nm). Stern-Volmer plots for (b) **NET** and (d) **PFP** (red dashed line indicates POM/CPE = 1). Insets: Magnification of the Stern-Volmer data below the charge compensation point.

6.3.2 Binding Mode Studies

The addition of the **POM** to aqueous solutions of both CPEs induced changes in the optical properties of the CPEs. Due to the opposing charges of the CPEs and the **POM**, the complexes are expected to form as a result of electrostatic binding. To qualify this assumption, binding mode studies were performed. Initially, the mode of binding was examined by ^{1}H NMR and FTIR spectroscopies. Upon addition of **POM** to **NET**, the ^{1}H NMR signals remained in the same position, which is expected since no formal chemical bonding occurs between the two species (Figure 6.4). However, a broad peak at 9.68 ppm assigned to the N-H proton, was observed to decrease in intensity and became sharper upon addition of the **POM**. This is attributed to electrostatic bonding between the anionic **POM** and the positively-charged nitrogen on the **NET** pendant ionic chain. This observation may be explained by electron donation from the **POM** to the CPE, which is expected to weaken and lengthen the N-H bond. The weaker N-H bond allows the hydrogen to rotate more freely, resulting in the slightly sharper peaks in the NMR spectrum. The FTIR spectra showed a 10 cm^{-1} shift in the $\upsilon_{N\text{-}H}$ stretching mode at ~3384 cm^{-1} upon addition of **POM** (Appendix Figure A.6.1). This further supports the direct association between the **POM** and the N-H on the **NET**. There was no change observed between the ^{1}H NMR or FTIR spectra of **PFP** and **POM/PFP**, probably due to the lack of a proton bonded directly to the nitrogen in the ammonium group.

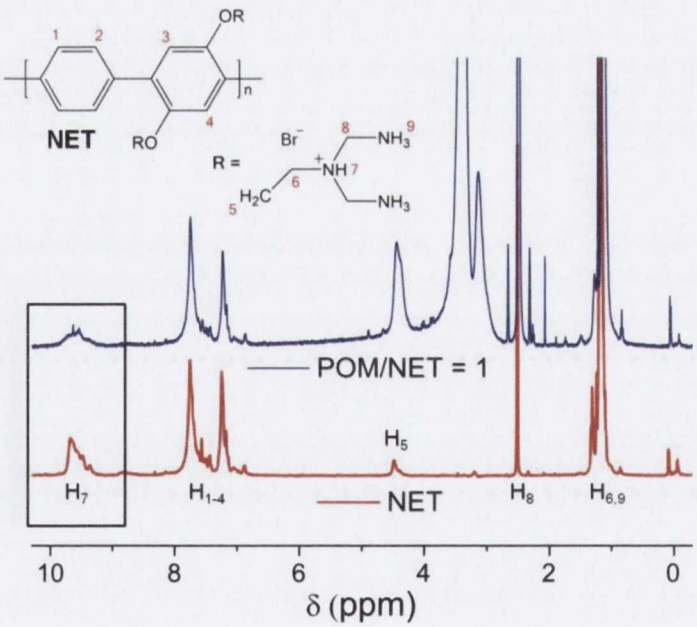


Figure 6.4 ^{1}H NMR binding studies of the **POM-NET** system. ^{1}H NMR spectra of (a) **NET** and (b) **POM/NET**=1 in d_6-DMSO (400 MHz). The black box highlights the N-H proton signal in **NET** and **POM/NET** spectra.

Linear dichroism was also employed as an insightful technique for systems which are intrinsically orientated or can be orientated under shear flow.[20] Figure 6.5 shows the LD spectra of **NET** and **PFP** upon the addition of **POM**. In both cases, in the absence of **POM** comparatively no LD signal was observed. This indicated that the polymer chains were randomly orientated in solution. However, upon addition of **POM**, distinctive LD bands were observed, suggesting that the CPE-**POM** structures aligned upon co-assembly. More specifically, for **POM/NET** = 1 three broad signals were resolved, which provide an indication of the relative orientation of the CPE and **POM** components in the hybrid. Since the transition moment of CPs usually lies parallel to the backbone,[21] the positive LD signals at 350 nm and 443 nm suggest that the **NET** chains are aligned parallel to the local orientation axis. The negative LD signal at 260 nm suggests that bound **POM** clusters lie perpendicular to aligned CPE chains. In the LD spectrum of **POM** added to **PFP** (**POM/PFP** = 0.5), only two broad bands were observed, with the sign of the bands reversed. This may indicate that the CPE in the **POM/PFP** associations are now aligned perpendicular to the local orientation axis.

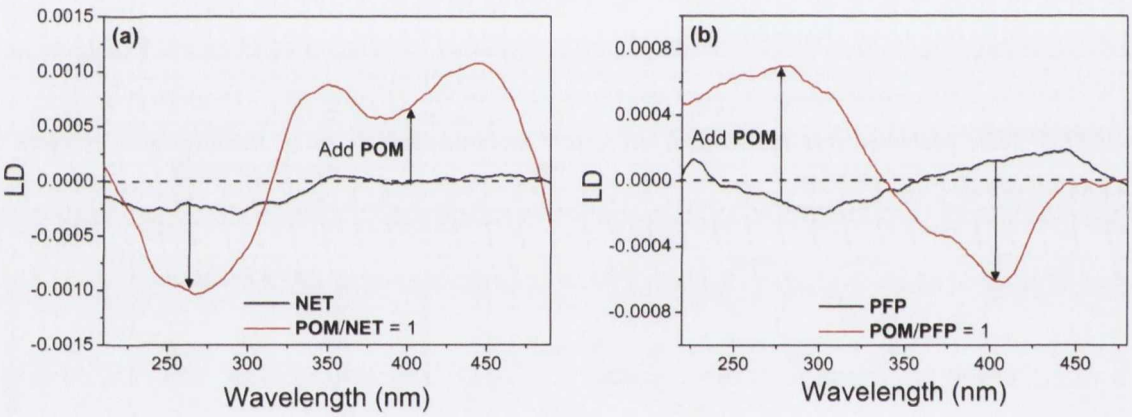


Figure 6.5 LD studies to investigate any orientation CPE chains induced by co-assembly with **POM**. LD spectra for (a) **NET** and **POM/NET** = 1 ([**NET**] = 5.48 × 10^{-5} M (r.u)) and (b) **PFP** and **POM/PFP** = 0.5 ([**PFP**] = 2.14 × 10^{-5} M (r.u)).

6.3.3 Aggregate Size in Solution

Dynamic light scattering was used to determine the hydrodynamic radii of the CPE-**POM** aggregates in aqueous solution (Figure 6.6). The *Z*-average R_H of the individual components were 115 (±9) nm for **POM** (1 × 10^{-6} M), 123 (±36) nm for **NET** (9.18 × 10^{-6} M (r.u.)) and 201 (±23) nm for **PFP** (7.20 × 10^{-6} M (r.u.)), respectively. Addition of **POM** to CPE solutions resulted in a bimodal distribution indicating the presence of both free CPE and **POM**/CPE aggregates. The R_H was determined from a polynomial fit of the logarithm of the correlation function using the Cumulants method. This method becomes less reliable for multimodal distributions[22] and as such only qualitative observations regarding the change in R_H can be made. For both systems, R_H remained constant until a critical **POM**/CPE charge ratio was attained. At this point the global R_H increased to 163 (±23) nm for **POM/NET** = 1 and to 227 (±23) nm for **POM/PFP** = 0.8. Further

addition of **POM** resulted in the formation of larger aggregates, approximately 500-600 nm in size. At these concentrations there were no visible signs of turbidity or precipitation.

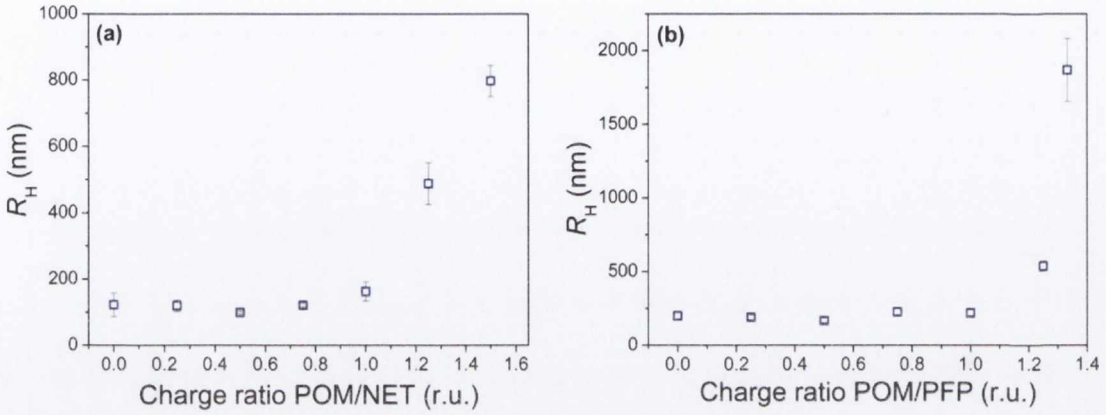


Figure 6.6 DLS studies to determine the effect of the addition of **POM** on the size of aggregates of CPE-**POM** complexes formed. *Z*-average radii determined by DLS of (a) **NET** in aqueous solution (9.18×10^{-6} M (r.u.)) on addition of **POM** ($0 - 3.17 \times 10^{-6}$ M), (b) **PFP** in aqueous solution (7.20×10^{-6} M (r.u.)) on addition of **POM** ($0 - 2.26 \times 10^{-6}$ M), plotted against charge ratio.

6.3.4 Thin Film Morphology

To determine whether the solution phase structure of the CPE/**POM** hybrid materials could be transferred to thin films with the retention of their nanoscale structure, atomic force microscopy and scanning electron microscopy were employed. Films of the CPEs and the **POM** were measured prior to mixing and found to form amorphous clusters of **POM** (~100–300 nm), **NET** (~200–300 nm) and **PFP** (~200–300 nm) (Appendix Figure A.6.2). Upon mixing, **POM** and **NET** retained the amorphous character observed in the blank samples of each, until charge balance was reached. At charge balance (**POM/NET** = 1) 1D strand-like structures (~20–35 nm in diameter) became apparent on the film surface under AFM and SEM (Figure 6.7a). In comparison, stacked, extended plate-like structures, with thicknesses that varied between 40–200 nm emerged at a charge ratio of **POM/PFP** = 0.5 (Figure 6.7b). Further addition of **POM** to either CPE resulted in much larger (700–1500 nm) amorphous aggregates, which suggested a dispersion of the aggregated structures.

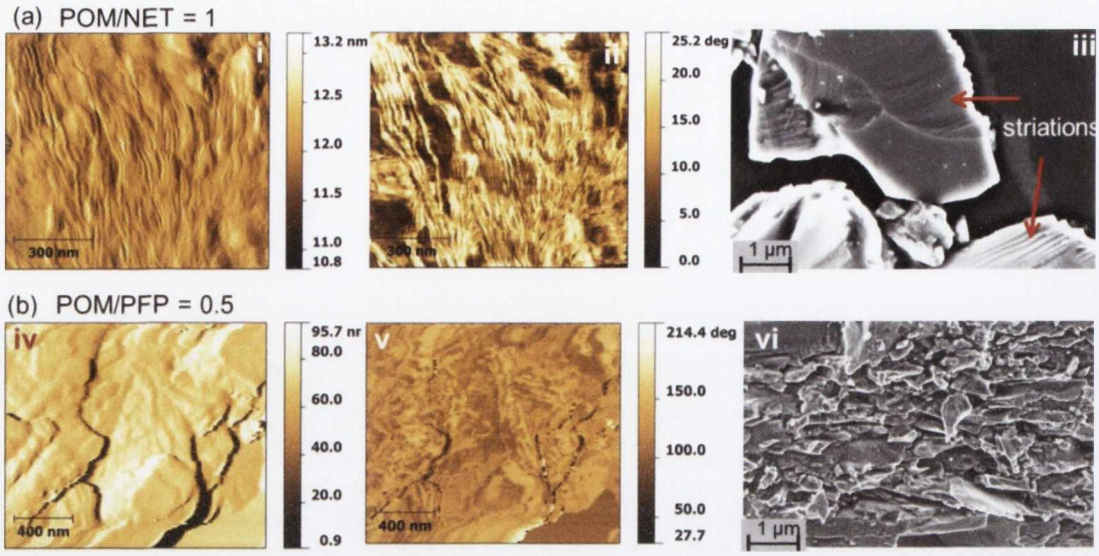


Figure 6.7 Topography images of (a) **POM/NET** = 1 ([**POM**] = 5×10^{-7} M) and (b) **POM/PFP** = 0.5 ([**POM**] = 6.25×10^{-7} M) films obtained from amplitude (i, iv) and phase (ii, v) AFM images and (iii, vi) SEM images. In both cases, [**POM**] = 5×10^{-7} M. SEM measurements were performed by Dr Adam Patterson.

6.4 Proposed Mechanism of Self-Assembly

A combination of techniques have been used to characterise the CPE-**POM** hybrid systems formed in aqueous solution, which suggest distinctive self-assembly patterns for **NET** and **PFP** with the anionic **POM**, $[SiW_{10}O_{36}]^{8-}$. In Figure 6.8 the proposed self-assembly mechanisms for **NET-POM** and **PFP-POM** hybrid systems are shown. For both CPEs, the red-shift in the absorption band and the formation of isosbestic points in the UV/Vis absorption spectra, in combination with the static quenching observed in the photoluminescence, demonstrates electrostatic associations between the CPEs and the **POM**. The onset of self-assembly was found to occur at lower **POM**/CPE charge ratios for **PFP** than **NET** (~0.5-0.8 and 1, respectively). This could be the result of amplified quenching often observed in CPs with high M_w like **PFP** in comparison to **NET**.[19] However, further analysis was required to determine the nanoscale structure of these aggregates.

LD suggested that the aggregates of **NET-POM** form with the **POM** clusters aligning perpendicular to the conjugated backbone of **NET**. This has two important consequences: (1) the **POM** interacts most closely with the ammonium groups on the pendant side chains of the CPE. This interaction was further supported by NMR and FTIR; (2) the ionic chains in **NET** are distributed on either side of the CPE chain, which will promote the growth of alternating **NET-POM** 1D chain-like aggregates (Figure 6.8a). Finally, the **NET** units (~1.4 nm) approximately match the diameter of one **POM** unit (1.0 nm), which is expected to prevent the CPE from cross-linking between adjacent **POM** units. These individual chains were observed in AFM and SEM measurements, where the drop-cast films appeared as individual fibres in a lamellar packing arrangement.

In contrast, the DLS measurements and the amplified quenching of the **PFP** with **POM** suggested increased interchain interactions, which are both consistent with the formation of larger aggregates in the **PFP-POM** system. This was further demonstrated *via* AFM and SEM where the **PFP-POM** films appeared as extended 2D sheets (Figure 6.8b). Therefore, **PFP-POM** hybrids are believed to exist as 2D plate-like arrays, the formation of which is facilitated by the significantly larger CPE chain length (16.0-25.1 nm), which can associate with multiple **POM** units. Simultaneously, hydrophobic and van der Waals interactions are expected to drive the stacking of these layers, as observed in the AFM and SEM images.

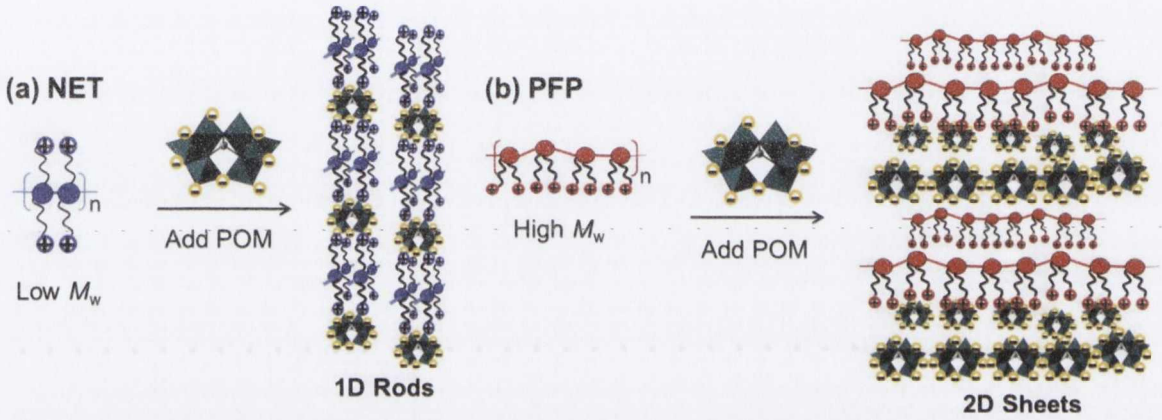


Figure 6.8 Schematic representation of the proposed mechanism of self-assembly of (a) **NET–POM** and (b) **PFP–POM** into hybrid networks.

6.5 Conclusions

In this study, it has been demonstrated for the first time that CPE-**POM** supramolecular networks can be formed *via* electrostatic associations.[14] It was also shown that the dimensionality of the hybrid networks can be tuned by the chain length and steric charge distribution on the CPE. Furthermore, AFM and SEM studies confirmed that the CPE-**POM** complexes could be transferred from solution to the solid-state with retention of their nanoscale organisation, which is critical for potential device applications.[23]

This has been primarily a proof-of-concept study, which used an anionic polyoxometalate ($K_8[SiW_{10}O_{36}]$) and two cationic CPEs (**PFP** and **NET**), to demonstrate that the targeted formation of CPE-POM supramolecular networks can be achieved *via* electrostatic association. In future work, the formation of CPE-**POM** hybrid materials will be easily extended to combine the multitude of different **POM** and CPEs available, with their wealth of molecular topologies, surface charge densities, chemical structures, redox and optical properties, to yield a variety of well-defined, supramolecular architectures with enhanced functionality.

Finally, this study should provide the foundation for future studies in optimised OPV devices. CPEs and POMs are being increasingly reported as interfacial modifying layers and as charge transport materials within the active layer of OPV devices.[9, 11] Given that the optimisation of such devices is strongly correlated to the nanostructure of the material, hybrid systems of CPE-

POMs could satisfy this requirement, while simultaneously offering enhanced functionality due to synergistic interactions between these two components.

6.6 References

1. M. Wright and A. Uddin, *Sol. Energy Mater. Sol. Cells*, 2012, **107**, 87-111.
2. S. Herrmann, C. Ritchie and C. Streb, *Dalton Trans.*, 2015, **44**, 7092-7104.
3. M. Ammam, *J. Mater. Chem. A*, 2013, **1**, 6291-6312.
4. P. He, B. Xu, X. Xu, L. Song and X. Wang, *Chem. Sci.*, 2016, **7**, 1011-1015.
5. T. Ito, H. Yashiro and T. Yamase, *Langmuir*, 2006, **22**, 2806-2810.
6. I. A. Weinstock, *Chem. Rev.*, 1998, **98**, 113-170.
7. M. Vasilopoulou, E. Polydorou, A. M. Douvas, L. C. Palilis, S. Kennou and P. Argitis, *Energy Environ. Sci.*, 2015, **8**, 2448-2463.
8. K. Yuan, L. Chen and Y. Chen, *J. Mater. Chem. C*, 2014, **2**, 3835-3845.
9. G. Jin, S.-M. Wang, W.-L. Chen, C. Qin, Z.-M. Su and E.-B. Wang, *J. Mater. Chem. A*, 2013, **1**, 6727-6730.
10. Y. Li, L. Jin, S. Chakraborty, S. Li, P. Lu, D.-M. Zhu, X. Yan and Z. Peng, *J. Polym. Sci., Part B: Polym. Phys.*, 2014, **52**, 122-133.
11. L. C. Palilis, M. Vasilopoulou, A. M. Douvas, D. G. Georgiadou, S. Kennou, N. A. Stathopoulos, V. Constantoudis and P. Argitis, *Sol. Energy Mater. Sol. Cells*, 2013, **114**, 205-213.
12. M.-P. Santoni, G. S. Hanan and B. Hasenknopf, *Coord. Chem. Rev.*, 2014, **281**, 64-85.
13. P. Yin, D. Li and T. Liu, *Chem. Soc. Rev.*, 2012, **41**, 7368-7383.
14. J. E. Houston, A. R. Patterson, A. C. Jayasundera, W. Schmitt and R. C. Evans, *Chem. Commun.*, 2014, **50**, 5233-5235.
15. J. Canny, A. Teze, R. Thouvenot and G. Herve, *Inorg. Chem.*, 1986, **25**, 2114-2119.
16. R. Berger, A. L. Domanski and S. A. L. Weber, *Eur. Polym. J.*, 2013, **49**, 1907-1915.
17. T. M. Swager, C. J. Gil and M. S. Wrighton, *J. Phys. Chem.*, 1995, **99**, 4886-4893.
18. M. Sundberg, O. Inganäs, S. Stafström, G. Gustafsson and B. Sjögren, *Solid State Commun.*, 1989, **71**, 435-439.
19. P. S. Heeger and A. J. Heeger, *Proc. Nat. Acad. Sci.*, 1999, **96**, 12219-12221.
20. A. Rodger and B. Nordén, *Circular Dichroism and Linear Dichroism*, Oxford University Press, 1997.
21. B. Grimm, C. Risko, J. D. Azoulay, J.-L. Bredas and G. C. Bazan, *Chem. Sci.*, 2013, **4**, 1807-1819.
22. R. Finsy, N. d. Jaeger, R. Sneyers and E. Geladé, *Part. Part. Syst. Char.*, 1992, **9**, 125-137.
23. X. Yang, J. Loos, S. C. Veenstra, W. J. H. Verhees, M. M. Wienk, J. M. Kroon, M. A. J. Michels and R. A. J. Janssen, *Nano Lett.*, 2005, **5**, 579-583.

Chapter 7

Charge-Mediated Localisation of Conjugated Polythiophenes Enabling the Sequential Detection of Multiple Phase Transitions in Model Membranes

The work presented in this chapter has been published in part in:

1. J. E. Houston, M. Kraft, I. Mooney, A. E. Terry, U. Scherf and R. C. Evans, Charge-Mediated Localization of Conjugated Polythiophenes in Zwitterionic Model Cell Membranes, *Langmuir*, 2016, **32**, 8141-8153.

2. J. E. Houston, M. Kraft, U. Scherf and R. C. Evans, Sequential Detection of Multiple Phase Transitions in Model Biological Membranes Using a Red-Emitting Conjugated Polyelectrolyte, *Phys. Chem. Chem. Phys.*, 2016, **18**, 12423-12427.

7.1 Introduction

Within every biological system the cell membrane facilitates the transportation of materials, energy and information between the interior and exterior cell environment, achieved by modification of its structure or phase.[1] However, membrane order is a delicate balance, and unsought changes in membrane permeability *via* phase transitions are thought to be behind a number of degenerative or life-threatening diseases, including age-related neurological conditions, such as Alzheimer's disease,[2] and tumour cell formation.[3] As such, the development of probes capable of accurately elucidating, detecting and monitoring subtle changes in the order of model and live membranes at the nanoscale is crucial for the development of targeted diagnostic and therapeutic platforms.

CPEs are attractive membrane probes due to their water-solubility and environment-[4, 5] and aggregation-responsive fluorescence.[6] Homogenous phospholipid large unilamellar vesicles (LUVs) are commonly used as models for complex plasma membranes.[7] Despite their considerable differences from live cell membranes, the interaction of CPEs with phospholipid vesicles can provide vital information on a range of variables, such as binding affinity, the orientation or localisation of the CPE and its local environment.[7] Complexes of CPE-phospholipid vesicles have previously been exploited for a broad range of potential applications including cell imaging,[8] fabrication of sensing devices,[5] formation of biocidal agents[9] and for the optimisation of power generation in microbial fuel cells.[10]

Phospholipid membranes exist in discrete phases which are defined by their microviscosity and lipid order, these include the liquid crystal phase (L_c), lamellar gel phase (L_β'), gel phase (P_β') and the fluid phase (L_α).[11] All phospholipids have characteristic temperatures at which they undergo a transition between different phases, as shown schematically in Figure 7.1 for dipalmitoylphosphatidylcholine (DPPC).[11] Thus, the ability to induce phase transitions in model membranes as a function of temperature is a convenient tool to test the sensitivity of a phase transition probe.

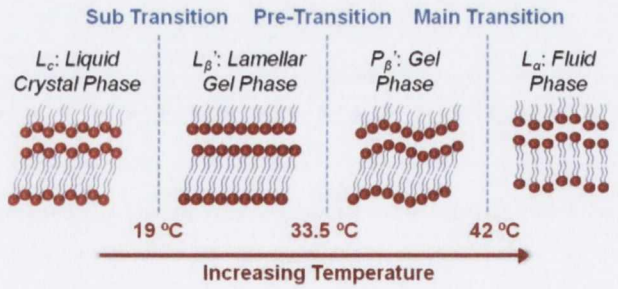


Figure 7.1 Schematic representation of the phase transitions of the phospholipid dipalmitoylphosphatidylcholine (**DPPC**).

Recently, the steady-state emission intensity of the blue-emitting, cationic poly(fluorene), poly[9,9-bis(6′-*N*,*N*,*N*-trimethylammonium)hexyl]fluorene-2,7-diyl-*alt*-1,4-phenylene (HTMA-PFP), was found to be sensitive to *two* phase transitions (the main- and pre-transitions) in the

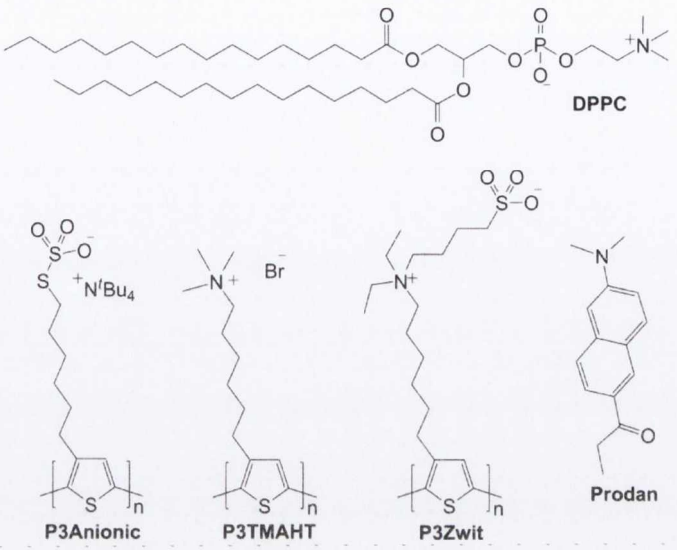
phospholipids DPPC and 1,2-dimyristoyl-*sn*-glycero-3-phosphoglycerol (DMPG).[12] The observed phase sensitivity was attributed to the localisation of the CPE close to the vesicle surface. However, to date there is no CPE probe which is able to detect the less energetically-demanding sub-transition. As physical parameters, such as fluidity, are known to change dramatically across the membrane bilayer,[13] the challenge is to identify CPEs that, through a delicate balance of intermolecular forces, are able to localise specifically at a targeted location within a phospholipid bilayer to enable accurate detection of all phase transitions.

The extent of incorporation of CPEs within phospholipid vesicles has previously been controlled by varying the nature and number of charges on the phospholipid head-group,[14] as well as the nature and number of side-group charges[14] and length of the polymer chain.[15, 16] Karam *et al.* investigated the effect of varying the chain length of anionic poly(phenylene ethynylene)s (PPEs) and their interaction with phospholipids of different head-group charge.[15] Regardless of the PPE chain length, the anionic CPE showed no interaction with negatively-charged phospholipid vesicles and associated only to a small extent with zwitterionic phospholipids. In contrast, strong interactions were observed with the cationic phospholipid, 1,2-dioleoyl-3-trimethylammonium-propane (DOTAP), with vesicle fusion being reported exclusively for the longest chain-length PPE. A comparative study between cationic PPEs and the anionic phospholipid, 1,2-dipalmitoyl-*sn*-glycero-3-phosphoglycerol (DPPG), commonly used as model membranes for bacterial cells, found that the extent of membrane perturbation by the CPEs decreased with increasing size.[16] Mammalian cell membranes predominantly consist of zwitterionic phospholipids,[17] which possess both positive and negative charges in their polar head-groups. However, limited studies exist regarding the effect of zwitterionic surfactants, generally phospholipids, on the solution behaviour of CPEs.[14, 15] Recently, it was shown that the nature of the surfactant (cationic, anionic, zwitterionic, non-ionic) when added to a solution of the zwitterionic CPE, poly[3-(*N*-(4-sulfonato-1-butyl)-*N,N*-diethylammonium)hexyl-2,5-thiophene], had a significant effect on the optical and structural properties of the zwitterion.[18] Specific ionic associations between charged groups and non-specific interactions, such as structural rearrangements to accommodate incorporation of the surfactant tails, were proposed to govern the nanoscale organisation of the CPE. However, no study has probed the interaction between zwitterionic phospholipids and CPEs which contain the same conjugated backbone, but bear different charges on their pendant side-groups.

7.1.1 Aims

In this chapter, a series of poly(thiophene)s bearing zwitterionic, cationic or anionic terminal groups, namely poly[3-(6-trimethylammoniumhexyl)thiophene] (**P3TMAHT**), poly[3-(6-sulfothioatehexyl)thiophene)] (**P3Anionic**) and poly[3-(*N*-(4-sulfonato-1-butyl)-*N,N*-diethylammonium)hexyl-2,5-thiophene) (**P3Zwit**), respectively (Scheme 7.1), will be investigated as phase transition probes using **DPPC** LUVs. Binding mode studies are expected to provide insight into the origin of any phase sensitivity observed, as well as into the effect of charge-

mediation on the membrane perturbation of CPEs which may prove valuable in the development of improved theranostic platforms.



Scheme 7.1 Chemical structures of the phospholipid, **DPPC**, the three poly(thiophene)s investigated (**P3Anionic**, **P3Zwit** and **P3TMAHT**) and the polarity probe (Prodan).

The specific aims include:

- to investigate the fluorescence of CPEs and CPE-**DPPC** mixtures as a function of temperature;
- to study whether emission properties of CPEs are sensitive to the three primary phase transitions in model cell membranes;
- to determine the interaction and depth of penetration of the CPEs within the phospholipid bilayer using a combination of PL, scattering and microscopic techniques;
- to probe the relationship between the localisation of the CPEs within the membrane bilayer and their viability as membrane probes.

7.2 Experimental

7.2.1 Materials

P3TMAHT, **P3Anionic** and **P3Zwit** were a kind gift from Dr Mario Kraft and Prof. Ullrich Scherf at Bergische Universtät in Germany. The conjugated polymers were synthesised from the bromide precursors with M_n of 12,000, 5,000 and 12,000 g mol^{-1}, respectively, and PDIs of 1.1. **DPPC**, *N*-(2-hydroxyethyl)piperazine-*N*'-(2-ethanesulfonic acid) (HEPES, ≥99.5%) and 6-propionyl-2-dimethylaminonaphthalene (Prodan, ≥98.0%) were purchased from Sigma Aldrich. All materials were used as received. Unless otherwise stated, all buffers utilised had the same ionic strength: 10 mM HEPES, 30 mM NaCl, pH 7.3.

7.2.2 Methods

The instrumentation for UV/Vis absorption and PL spectroscopy, SANS, AFM, DSC, DLS, zeta potential measurements and epifluorescence microscopy are described in Chapter 3.

*Preparation of **DPPC** large unilamellar vesicles* (LUVs): **DPPC** powder was dissolved in chloroform to a final concentration of 40 mg mL^{-1}. The solvent was then evaporated while rotating the sample vial to create a thin film on the vial wall. Films were placed under vacuum for at least 1 h to remove excess solvent. Lipid films were hydrated to a final concentration of 20 mM with buffer solution. The lipid suspensions were then subjected to 15 cycles of freeze-thaw-sonicate, where freeze indicates 10 min in the freezer, thaw indicates 1 min in a water bath at 40-50 °C, and sonicate indicates 5 min of sonication at 40-50 °C. The lipid mixtures were subsequently extruded 15 times through a 100 nm pore size polycarbonate membrane. During the extrusion process the samples were maintained above the gel-liquid transition of **DPPC** (42 °C).[19] The vesicle suspensions were stored at 4 °C before use, if they were not used immediately.

Titration procedure: For each measurement, stock solutions of the CPE were mixed with stock solutions of the **DPPC** LUVs to obtain the required charge ratio between the CPE monomer units and the zwitterionic **DPPC**. The M_W's of the CPE monomer units are 519.9, 302.3 and 373.6 g mol^{-1} for **P3Anionic**, **P3TMAHT** and **P3Zwit**, respectively. CPE stock solutions (1.92×10^{-3} M (r.u.), 3.31×10^{-3} M (r.u.) and 2.68×10^{-3} M (r.u.) for **P3Anionic**, **P3TMAHT** and **P3Zwit**, respectively) were prepared in Millipore water and stirred for at least two days before use.

UV/Vis absorption and PL titrations:
(*i*) *Temperature measurements*: **P3Anionic** (1.9×10^{-5} M (r.u.)), **P3TMAHT** (4.2×10^{-5} M (r.u.)) and **P3Zwit** (3.3×10^{-5} M (r.u.)) were prepared from the stock solution in HEPES buffer solution. Aliquots of **DPPC** solution (2 mM) were added to achieve a 1:1 charge ratio of **DPPC**:CPE. The temperature of each solution was controlled at 2.5 °C intervals between 10 and 60 °C using a Wavelength Electronics temperature controller. Each sample was continuously stirred and allowed to equilibrate for 5 min before a spectrum was recorded.

(*ii*) *Concentration measurements*: **P3Anionic** (1.93×10^{-5} M (r.u.)), **P3TMAHT** (4.2×10^{-5} M (r.u.)) and **P3Zwit** (3.3×10^{-5} M (r.u.)) were prepared from the above stock solutions in HEPES buffer. Aliquots of **DPPC** solution (2 mM) were added to a fixed volume of the CPE solution across the concentration range 0 - 9.60×10^{-5} M for **P3TMAHT** and 0 - 4.08×10^{-5} M for **P3Zwit** and **P3Anionic**. Measurements were performed at room temperature. Dilution effects were accounted for in the absorption and PL spectra.

Differential scanning calorimetry: DSC was performed in the range 10-60 °C in a nitrogen atmosphere using a heating rate of 15 °C min^{-1} in an aluminium crucible.

Dynamic light scattering and zeta potential (ζ) measurements procedure: A solution of **P3Anionic** (4.0×10^{-6} M (r.u.)) was prepared in filtered HEPES buffer solution. Aliquots of **DPPC** vesicles were added to the CPE solution to achieve 1:1 charge ratio. All measurements were performed at 20 °C. The pathlength of the light was automatically adjusted by the apparatus in accordance with the sample turbidity. However, it should be noted that the solutions were not visibly turbid, nor was any precipitation observed.

Atomic force microscopy: HEPES buffer solution was filtered through 0.2 μm nylon syringes prior to sample preparation. Concentrations for the blank samples were [**DPPC**] = 1.6×10^{-5} M and [CPE] = 1.0×10^{-5} M (r.u.). The **DPPC**/CPE films were prepared by drop-casting 20 μL aliquots onto freshly cleaved mica and left to dry at room temperature.

Epifluorescence microscopy: **DPPC** multilamellar vesicles (MLVs) were prepared from lipid films hydrated to a final concentration of 20 mM with buffer solution. The lipid suspensions were then subjected to 1 h of sonication at 40-50 °C. **DPPC** MLVs (2.6×10^{-3} M) were titrated with **P3Anionic** (1.3×10^{-3} M (r.u.)), **P3TMAHT** (1.3×10^{-3} M (r.u.)) or **P3Zwit** (1.3×10^{-3} M (r.u.)). The **DPPC**/CPE films were prepared by drop-casting 50 μL aliquots onto microscope slides and left to dry at room temperature.

SANS measurements: CPE-**DPPC** vesicle complexes were prepared in deuterated solvents (10 mg mL^{-1}) to provide good neutron scattering contrast. The thickness of the vesicle bilayer was first analysed using the modified Kratky-Porod (MKP) approach,[20] which relates the radius of gyration to the thickness of the bilayer and is independent of other model fitting. The scattering functions were fit using non-linear least-squares analysis to the Core-Multi-Shell model using the SasView programme.[21, 22] Full details of the mathematical model can be found in Chapter 3. The fits were checked to have absolute SANS intensities consistent with the known sample concentrations (1 vol% dry material).

7.3 Results

7.3.1 Temperature Dependence Studies

In order to establish the sensitivity of the CPEs to membrane order, the temperature dependence of the fluorescence properties of the CPE-**DPPC** complexes was monitored. Dilute samples of the CPE and CPE:**DPPC** mixtures at a 1:1 charge ratio were measured at 2.5 °C intervals between 10-60 °C. For **P3Anionic** (Figure 7.2) three distinct changes were noted in the emission spectra in response to the temperature: (i) an increase in the emission maximum, λ_{em}, and a decrease in emission intensity between 17.5-20 °C, corresponding to the sub-transition temperature (T_s) at 18.8 °C;[11] (ii) an increase in the emission intensity above 32.5 °C, which corresponds to the pre-transition temperature (T_p) of **DPPC** (at 32-35 °C);[23] (iii) the λ_{em} blue-shifts

rapidly above 40 °C, which corresponds to the main phase transition temperature (T_m) of 41.6 °C between the gel and fluid phase.[11]

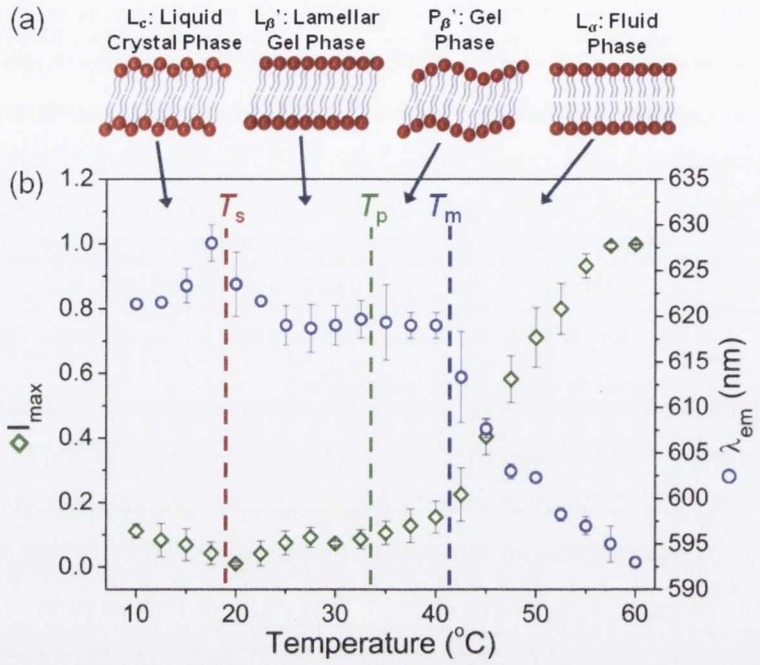


Figure 7.2 (a) Schematic representations of the expected structure of the bilayer phase at different temperatures. (b) Temperature dependence of the maximum emission intensity, I_{max}, (green diamonds) and the emission maximum, λ_{em}, (blue circles) of **P3Anionic-DPPC** at 2.0 × 10^{-5} M (r.u.). The dashed lines indicate the sub- (T_s), pre- (T_p) and main transition temperature (T_m).

The observed enhancement in the emission intensity and blue-shift in λ_{em} are indicative of higher interchain disorder due to distortion of the thienylene building blocks, which leads to a corresponding decreased conjugative interaction in the deaggregated state.[24-26] This suggests that **P3Anionic** is located in a motionally-restricted environment within the lipid bilayer.[27] This response mode contrasts with that of some other microenvironment fluorescent probes, which distinguish phospholipid phases by the penetration depth of water molecules into the lipid bilayer and the degree of lipid packing.[23, 27-29] It should be noted that after equilibrating the CPE:**DPPC** mixture at 4 °C for a few days, the initial emission intensity and λ_{em} were recovered. In contrast, the emission intensity of pure **P3Anionic** in HEPES buffer decreased proportionately as the temperature was increased over this range (Figure 7.3a). Furthermore, there was a slight change in the trend of emission intensity for **P3Zwit** before and after the addition of **DPPC** (Figure 7.3b) with the intensity of emission between 25-35 °C continuing to decrease for **P3Zwit/DPPC**, in contrast to the pure CPE which increased slightly. However, there is no apparent correlation between this observed change and the phase transitions of **DPPC**. **P3TMAHT** showed no sensitivity to the temperature-induced phase transitions of **DPPC** (Figure 7.3c).

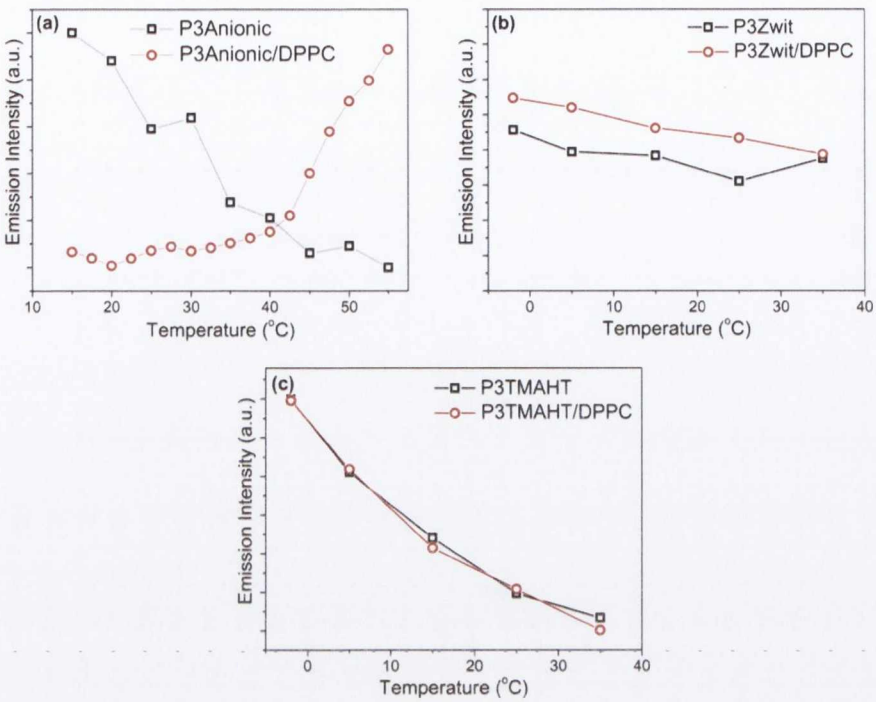


Figure 7.3 Emission intensity maxima as a function of temperature for (a) **P3Anionic** (1.9×10^{-5} M (r.u.)), (b) **P3Zwit** (3.3×10^{-5} M (r.u.)) and (c) **P3TMAHT** (4.2×10^{-5} M (r.u.)) with and without **DPPC** vesicles (1:1 charge ratio) in HEPES buffer.

To confirm that the observed changes in the fluorescence spectrum of **P3Anionic** as a function of temperature correspond to the phase transitions of pure **DPPC**, DSC measurements were performed on the LUVs before and after the addition of **P3Anionic** (Figure 7.4). In both cases, the T_m gave rise to an intense peak at ~42 °C,[11] the T_p is a less intense broad peak at 31-33 °C,[23] while the T_s was not observed in the thermogram, which is common for lipid bilayers.[30] Firstly, this result confirms that the phase transitions specific to **DPPC** are retained upon addition of the CPE and correlate well with the observed spectral changes highlighted in Figure 7.2. In addition, the negligible effect on the shape or position of the T_m profile at ~41 °C upon addition of **P3Anionic** signifies the absence of any substantial lipid reorganisation due to CPE binding.[31] However, an increase in the width of the peak in comparison to the pure **DPPC** vesicles may suggest a slight decrease in cooperativity among the alkyl chains of the **DPPC** bilayers.[32]

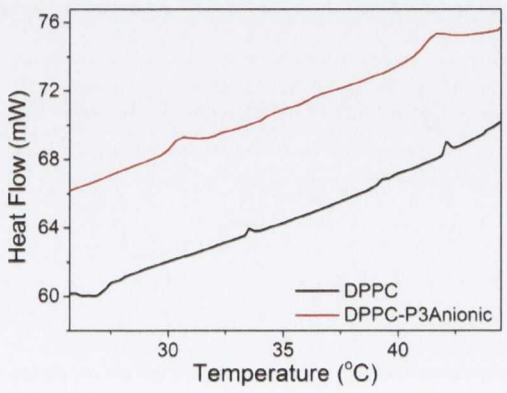


Figure 7.4 DSC thermograms of **DPPC** (2 mM) and **DPPC/ P3Anionic** at 1:1 charge ratio.

7.3.2 Binding Mode Studies

The sensitivity of phase transition probes is directly related to their specific localisation within phospholipid hydrophobic tails and/or hydrophilic head-groups.[27, 33] Therefore, it was proposed that the difference in sensitivity to membrane order by each of the CPEs was a direct consequence of the nature of their localisation within the membrane bilayers. To investigate this further, a series of binding mode studies were performed to determine the mechanism of interaction between the CPEs and **DPPC**.

Due to their inherent charges, electrostatic association between the poly(thiophene)s and the zwitterionic phospholipid head-groups is expected.[18] The UV/Vis absorption and fluorescence spectra of **P3TMAHT**, **P3Zwit** and **P3Anionic** were studied upon titration with increasing concentrations of **DPPC** vesicles in HEPES buffer solution (30 mM NaCl, pH 7.3) at 25 °C. For solutions of the pure CPE, single absorption bands were observed, centred at λ_{abs} = 431 nm for **P3Zwit** and **P3TMAHT** and 435 nm for **P3Anionic**. Upon titration with **DPPC** vesicles, a blue-shift and an increase in the absorbance was observed for all CPEs (Figure 7.5). For **P3Anionic** red-edge band broadening was also observed which is most likely attributed to an increase in conjugation length of the poly(thiophene);[4, 26, 34, 35] however, scattering effects arising from the addition of nanometre sized vesicles to the solution cannot be excluded.

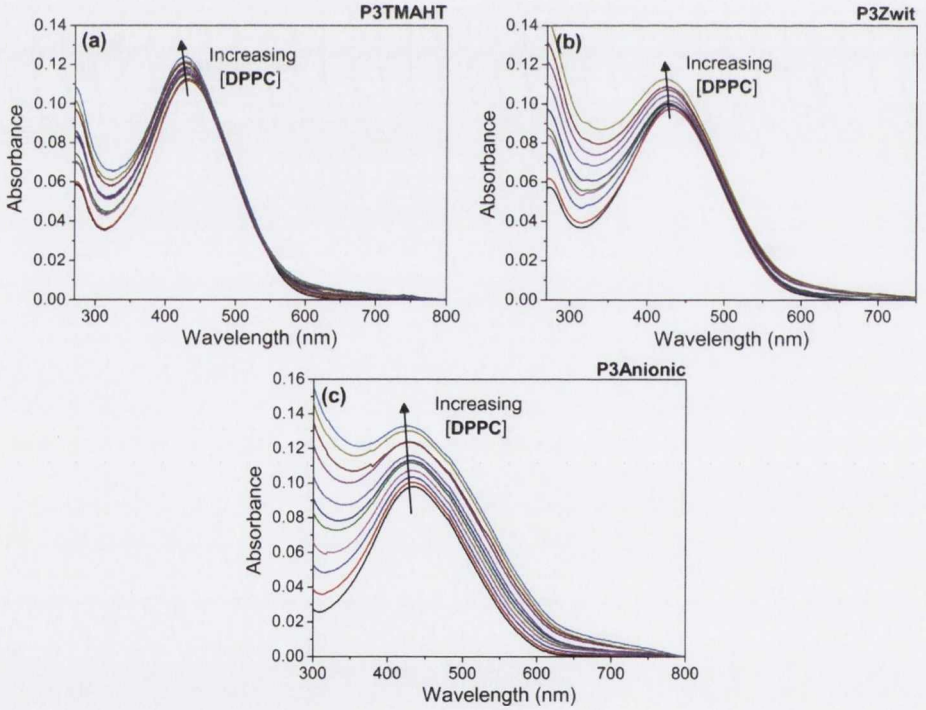


Figure 7.5 UV/Vis absorption spectra of (a) **P3TMAHT** (3.96×10^{-5} M (r.u.)), (b) **P3Zwit** (1.93×10^{-5} M (r.u.)) and (c) **P3Anionic** (1.93×10^{-5} M (r.u.)) upon titration with **DPPC** vesicles (0 - 9.60×10^{-5} M for **P3TMAHT** and 0 - 4.08×10^{-5} M for **P3Zwit** and **P3Anionic**).

Each CPE also exhibits a single broad emission band with λ_{em} centred at 625, 607 and 625 nm for **P3TMAHT**, **P3Anionic** and **P3Zwit**, respectively. The addition of **DPPC** vesicles into a buffered solution of **P3TMAHT** results in the appearance of vibronic structure in the emission

spectrum, a significant blue-shift ($\Delta\lambda_{em}$ = 625-595 nm) and an increase in emission intensity, reaching a three-fold enhancement by a 3:1 **DPPC**:CPE charge ratio (Figure 7.6ai). In contrast, **P3Zwit** and **P3Anionic** exhibit quenching of the emission intensity, with a smaller blue-shift in λ_{em} from 625 to 622 nm for **P3Zwit** (Figure 7.6bi), and 607 to 604 nm for **P3Anionic** (Figure 7.6ci). The excitation spectra are in excellent agreement with the absorption spectra (Figure A.7.1 in the Appendix).

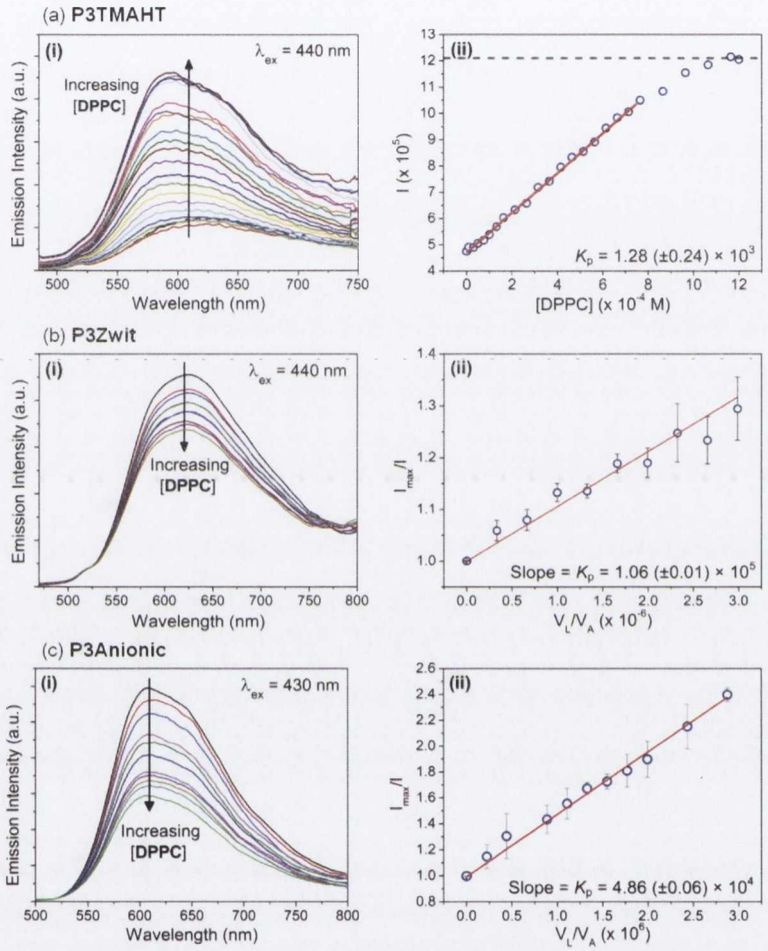


Figure 7.6 PL data for (a) **P3TMAHT** (3.96×10^{-5} M (r.u.)), (b) **P3Zwit** (1.93×10^{-5} M (r.u.)) and (c) **P3Anionic** (1.93×10^{-5} M (r.u.)) upon titration with **DPPC** vesicles (0 - 9.60×10^{-5} M for **P3TMAHT** and 0 - 4.08×10^{-5} M for **P3Zwit** and **P3Anionic**): (i) PL spectra. (ii) Plots for the calculation of the water/lipid partition coefficient, K_p.

The partition coefficient, K_p, provides information about the distribution of the CPE between the phospholipid and water phases of the solutions of phospholipid vesicles, including the approximate number of CPE chains per **DPPC** vesicle. These values can be determined from the fluorescence intensity depending on whether there is quenching or enhancement. For fluorescent molecules that display an *increase* in emission intensity, I, upon the addition of phospholipid vesicles, K_p is determined from:[36, 37]

$$I = \frac{I_w + K_p \gamma_L [L] I_{max}}{1 + K_p \gamma_L [L]} \tag{7.1}$$

where γ_L is the molar volume of phospholipid, I_w is the emission intensity of the CPE in the absence of the vesicles, and I_{max} is the maximum emission intensity that can be achieved upon addition of vesicles to the CPE. A plot of emission intensity at a fixed wavelength against phospholipid concentration, [*L*], will be hyperbolic if $I_{max} > I_w$. In this case the initial slope at [*L*] = 0 mol dm^{-3} is given by:

$$Slope = K_p \gamma_L (I_{max} - I_w) \tag{7.2}$$

Alternatively, if a fluorescent molecule is *quenched* upon titration with phospholipid vesicles, K_p can be calculated from:[38]

$$\frac{I_{max}}{I} = 1 + K_p \alpha \tag{7.3}$$

where $\alpha = V_L/V_w$, V_L is the volume of phospholipid and V_w is the total volume. V_L can be calculated by taking the volume of a molecule of **DPPC** as 1148 Å^3.[39] Eq. 7.1 can be equated to Eq. 7.3 if the limit of emission intensity, I_{max}, is assumed to be zero.[37] A plot of I_{max}/I *vs.* α should be linear, where the slope is equal to the partition coefficient, K_p. The measured λ_{abs} and λ_{em} for the CPEs in the absence and presence of **DPPC** vesicles (at 1:1 charge ratio of CPE:**DPPC**), and the calculated K_p, are summarised in Table 7.1.

Table 7.1 UV/Vis absorption (λ_{abs}) and emission (λ_{em}) maxima for CPEs before and after the addition of **DPPC** vesicles (1:1 charge ratio) in HEPES buffer solution (30 mM NaCl, pH 7.3), the calculated partition coefficients, K_p, and the calculated number of repeat units (and chains) of CPE expected to associate with each **DPPC** vesicle.

CPE	λ_{abs} (nm)		λ_{em} (nm)		K_p	No. of CPE r.u. (*chains*) per DPPC vesicle [a]
	without DPPC	with DPPC	without DPPC	with DPPC		
P3Anionic	431	426	607	604	4.86 (±0.06) × 10^4	8,800 (*419*)
P3Zwit	435	424	625	622	1.06 (±0.01) × 10^5	17,000 (*180*)
P3TMAHT	435	427	625	595	1.28 (±0.24) × 10^3	8,800 (*179*)

[a] The number of CPE r.u. per **DPPC** vesicle is calculated for a concentration of CPE = 1 × 10^{-5} M (r.u.) and **DPPC** = 1 × 10^{-4} M (see the Appendix for calculation details).

The increased emission intensity and blue-shift observed for **P3TMAHT** is common for CPEs when combined with phospholipids,[6, 14, 40] oppositely-charged,[26, 41, 42] or neutral surfactants.[41, 43] Such changes have been attributed to the surfactant-induced break-up of the CPE clusters to form new surfactant-CPE aggregates,[43] where the conformation of the CPE changes from an aggregated to more extended state.[24] The observed emission intensity enhancement and blue-shift in λ_{em} are indicative of higher interchain disorder due to distortion of neighbouring thienylene building blocks, which leads to a corresponding decreased conjugative interaction in the deaggregated state.[24, 25] In addition, the reasonably low K_p value (1.28 (±0.24) × 10^3) suggests that **P3TMAHT** is not significantly incorporated within the phospholipid bilayer of the vesicle. The partition coefficient also allows the ratio of CPE in the phospholipid bilayer *vs.* unassociated CPE

in the buffer solution to be calculated, and as such the approximate number of CPE r.u. (and chains) associating with each vesicle (Table 7.1). For **P3TMAHT**, this is relatively low at ~8,800 r.u. per vesicle or ~179 poly(thiophene) chains.

The observed quenching of the **P3Zwit** and **P3Anionic** emission upon addition of **DPPC** vesicles may be the result of the CPEs embedding within the membrane and forming ground-state complexes with the charged phospholipid head-groups.[4] The large K_p for **P3Zwit** (1.06 (±0.01) × 10^5), which corresponds to ~17,000 r.u. per **DPPC** vesicle, indicates that this CPE is buried deep within the bilayer. In contrast, the lower K_p for **P3Anionic** (4.86 (±0.06) × 10^4) suggests that it is restricted from penetrating as much, with a significantly lower number of associating r.u. (~8,800) per **DPPC** vesicle. It is interesting to note that the shorter chain-length poly(thiophene), **P3Anionic**, (~8 nm) would typically be expected to penetrate further within the phospholipid bilayer than the longer chain-length, **P3Zwit** (~20 nm).[15, 16] This is the first indication that the charge of the CPE side-chain may play a crucial role in controlling the penetration depth within the zwitterionic bilayers.

7.3.2.1 Förster Resonance Energy Transfer (FRET) Studies

Environment-sensitive hydrophobic probes are often used to obtain information about the structure and interactions within biomembranes.[13] The emission spectrum of the probe, Prodan, is highly sensitive to the polarity of the local environment,[44] and was selected to examine more precisely the location of the CPEs within the phospholipid bilayer by FRET. Prodan can be incorporated within the **DPPC** bilayers *via* simple titration before or after vesicle preparation, with a calculated partition coefficient of 1.8 × 10^5 (Figure A.7.2 in the Appendix). In water, Prodan exhibits a broad emission band centred at 525 nm, which shifts to 445 nm upon incorporation/binding with **DPPC** (Figure 7.7a) as the origin of the emission shifts from a charge-transfer to a locally-excited state.[44] Visual inspection of the emission spectrum of Prodan in **DPPC** vesicles (donor) and the absorption spectra of the CPEs (acceptor) reveals excellent overlap, and results in large values for the calculated spectral overlap integral, J_{DA}, as shown in Table 7.2, which suggest that FRET should take place.

Table 7.2 Measured molar absorption coefficients for the CPEs, ε_A, and calculated spectral overlap integrals, J_{DA}, Förster distances, R_0, and Stern-Volmer constants, K_{SV}.

Donor	Acceptor	ε_A at 430 nm (M (r.u.)$^{-1}$ cm^{-1})	J_{DA} (× 10^{-14} M (r.u.)$^{-1}$ cm^3)	R_0 (nm)	K_{SV} (× 10^4 M (r.u.)$^{-1}$)
Prodan	**P3TMAHT**	8,483	2.46	2.82	5.55 (±1.64)
Prodan	**P3Zwit**	13,193	3.84	3.04	3.80 (±0.64)
Prodan	**P3Anionic**	9,242	2.85	2.89	6.38 (±2.22)

As shown in Figure 7.7b for **P3Zwit** (Figure A.7.3 for **P3Anionic** and **P3TMAHT**), following selective excitation of Prodan (λ_{ex} = 340 nm), the emission band at λ_{em} = 435 nm

becomes increasingly quenched upon addition of each CPE, in the preferential order: **P3Anionic** › **P3TMAHT** » **P3Zwit**. Moreover, a congruent increase in the emission intensity at 610 nm, attributed to the poly(thiophene) emission, is observed. The corresponding excitation spectra detected in the CPE emission band reveal a contribution from both the CPE (~450 nm) and the Prodan excitation (~360 nm), confirming that Prodan to CPE energy transfer occurs (Figure 7.7c for **P3Zwit**, Figure A.7.4 for **P3Anionic** and **P3TMAHT**). The corresponding Stern-Volmer plots for quenching of the Prodan emission by the CPE were shown to be linear (Figure 7.7d) and the calculated Stern-Volmer constants are collected in Table 7.2.

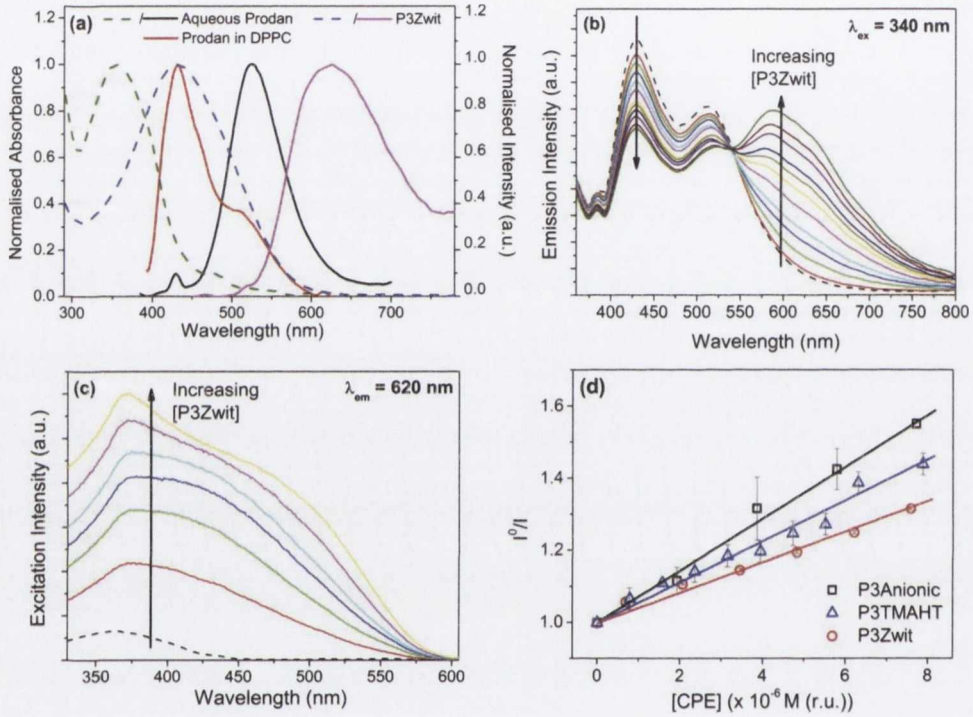


Figure 7.7 FRET studies to determine the precise location of the CPEs within the **DPPC** bilayers. (a) Normalised absorption (dashed lines) and emission (solid lines) spectra of Prodan and **P3Zwit** in HEPES buffer before and after the addition of **DPPC** vesicles, (30 mM NaCl, pH 7.3). (b) Emission and (c) excitation spectra of Prodan (2×10^{-8} M) in **DPPC** (1×10^{-4} M) vesicles upon the addition of **P3Zwit** (0-1.45×10^{-5} M (r.u.)). (d) Stern-Volmer plots of the quenching of Prodan by **P3Anionic** (black squares), **P3TMAHT** (blue triangles) and **P3Zwit** (red circles). To enable direct comparison between CPEs, titrations were performed with a constant concentration of **DPPC**/Prodan stock solution.

Fluorescence quenching is a powerful technique to obtain topographical information about proteins, nucleic acids and biological membrane systems.[4, 45] However, in systems involving membranes it can be difficult to make quantitative conclusions about the precise *D-A* distances as the donor and/or the quencher are likely to be partitioned between the aqueous phase and the phospholipid phase. Nevertheless, from the calculated K_p values, there will be an estimated 10^5 and 10^3–10^5 fold excess of Prodan and the CPEs, respectively, partitioned within the vesicle membrane relative to the aqueous buffer solution. Moreover, control experiments for the analogous CPE/Prodan systems in the absence of **DPPC** vesicles were also performed. In the control samples, the emission spectrum of Prodan in the buffer exhibits minimal spectral overlap with the

absorption spectrum of the CPE (Figure 7.7a). For each system, Prodan to CPE energy transfer was only observed for Prodan concentrations that were 10-100 fold those used in the analogous CPE/Prodan/**DPPC** studies (Figure 7.8a **P3Zwit**, Figure A.7.5 in the Appendix for **P3Anionic** and **P3TMAHT**), thus, revealing that no significant quenching of the Prodan fluorescence occurs at these quencher concentrations. Furthermore, Figure 7.8b for **P3Zwit** (and Figure A.7.6 for **P3Anionic** and **P3TMAHT** in the Appendix) shows that the Prodan (donor) emission intensity increases with increasing concentration, while the CPE (acceptor) emission intensity remains unaffected. This further indicates that energy transfer between free Prodan/CPE molecules in the buffer solution is negligible under these conditions. Therefore, the observed energy transfer in these systems is strongly believed to be primarily associated with donor-acceptor interactions within the **DPPC** bilayer. This allows qualitative deductions to be made about the relative position of the acceptor CPEs in relation to Prodan, which is known to preferentially locate at the boundary between the glycerol head-group and the lipid chains of phospholipids.[46]

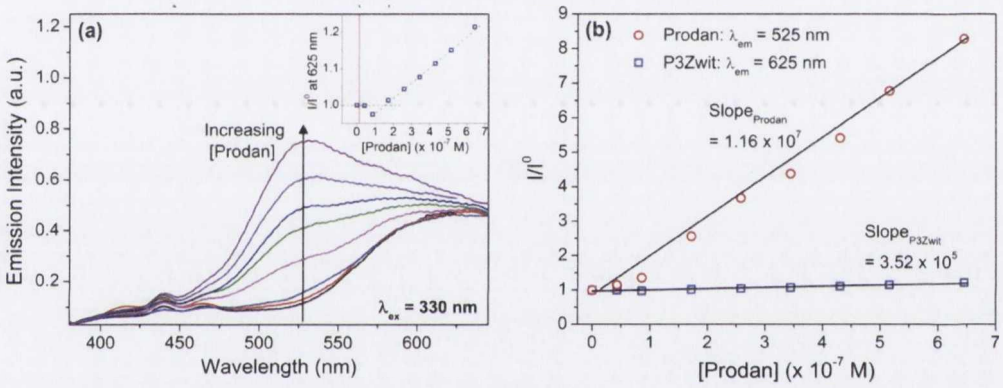


Figure 7.8 (a) Emission spectra of **P3Zwit** (1.93×10^{-5} M (r.u.)) upon addition of Prodan (0 – 6.5×10^{-7} M). λ_{ex} = 330 nm. Inset: Ratio of the **P3Zwit** emission intensity, I, to the initial intensity, I^0, at 625 nm, as a function of the concentration of Prodan. The red lines show the approximate concentration of Prodan used in the FRET experiments (2×10^{-8} M). (b) Ratio of emission intensity, I, over the initial intensity, I^0, at 525 and 626 nm, for Prodan and **P3Zwit** respectively, as a function of Prodan concentration (λ_{ex} = 330 nm).

In Förster theory,[47] the electronic coupling (V_{DA}) that promotes energy transfer from one molecule to another is usually calculated on the basis of a *point-dipole model*. This approach neglects the shapes of the donor and acceptor units and is valid if the size of the molecule is small with respect to intermolecular separations.[48] Therefore, the Förster equation for resonance energy transfer[47] has its limitations for linear conjugated systems as the point–dipole model cannot adequately account for the spatial distribution of excitations at short donor-acceptor distances.[48, 49] However, Förster theory can provide a useful tool to compare differences in the energy transfer efficiencies for each system. As the calculated Förster distances, R_0, are relatively similar for all the CPEs (see Table 7.2), and FRET efficiencies are highly dependent on the centre to centre *D-A* distance,[50] any differences in the K_{SV} values can be interpreted as the direct result of a change in distance between the Prodan donor and the CPE acceptor. The magnitude of the Stern-Volmer constants indicate that quenching of the Prodan emission by all three CPEs proceeds through a

static quenching mode.[51] Interestingly, **P3Zwit** has the highest K_p and yet the lowest K_{SV} (3.80 (±0.64) × 10^4 M (r.u.)$^{-1}$), suggesting that while this CPE is best incorporated within the **DPPC** bilayer, it is located at the greatest distance from the glycerol/lipid backbone (where the Prodan is located), potentially deep within the hydrophobic lipid tails. In comparison, the significantly lower K_{SV} for **P3TMAHT** and **P3Anionic** (5.55 (±1.64) × 10^4 and 6.38 (±2.22) × 10^4 M (r.u.)$^{-1}$, respectively) suggest that these poly(thiophene)s are in close proximity to Prodan and thus the glycerol/lipid backbone.

7.3.2.2 Particle Size and Surface Charge Studies

DLS has previously been used to confirm that the integrity of phospholipid vesicles is retained upon the addition of CPEs.[14] The *Z*-average hydrodynamic diameter of the phospholipid vesicles was measured before and after addition of the CPEs (summarised in Table 7.3). Pure **DPPC** vesicles have a narrow size distribution with a mean D_H of 115.3 (±2.0) nm and a PDI of 0.12 (±0.01). This size closely corresponds to the 100 nm diameter pore size of the polycarbonate filter used to prepare the vesicles. The vesicle size was unchanged when stored at 4 °C for 7 days. The pure CPE samples formed much larger aggregates in solution, with a mean D_H of 393.9 (±9.4), 382.8 (±36.6) and 244.7 (±2.5) nm for **P3Zwit**, **P3TMAHT** and **P3Anionic**, respectively, and large size distributions, with PDIs of 0.35 or greater.

Table 7.3 Hydrodynamic diameters (D_H) and polydispersities (PDI) of vesicle and vesicle-CPE mixtures (1:1 charge ratio) in HEPES buffer. Each value is the average of at least three measurements.

	D_H (nm)	PDI
DPPC	115.3 (±2.0)	0.12 (±0.01)
P3Zwit	393.9 (±9.4)	0.44 (±0.11)
P3TMAHT	382.8 (±36.6)	0.40 (±0.00)
P3Anionic	244.7 (±2.5)	0.35 (±0.06)
DPPC + **P3Zwit**	113.5 (±0.6)	0.11 (±0.01)
DPPC + **P3TMAHT**	119.3 (±1.5)	0.15 (±0.01)
DPPC + **P3Anionic**	130.0 (±4.5)	0.16 (±0.02)

Upon titration of the CPEs into a buffered solution of **DPPC** vesicles, a modest increase in D_H was observed, to 113.5 (±0.6), 119.3 (±1.5) and 130.0 (±4.5) nm for **P3Zwit**, **P3TMAHT** and **P3Anionic**, respectively. However, the size distributions remained narrow, with PDIs of 0.11 (±0.01), 0.15 (±0.01) and 0.16 (±0.02) for **P3Zwit**, **P3TMAHT** and **P3Anionic**, respectively. The DLS size measurements indicate that the **DPPC** vesicles break-up large CPE aggregates and that the vesicle structures are retained instead of being disrupted into smaller fragments.[6] It is well accepted that when CPEs (or other molecules) adsorb or penetrate vesicle surfaces there will be a moderate change in D_H of the particle.[14, 16, 40, 52, 53]

Zeta potential measurements were used to determine the effective charge of the vesicle surface, which will change depending on whether electrostatic associations between the CPE and **DPPC** occur at the vesicle surface or within the phospholipid bilayer.[54] The trends in ζ for **DPPC** vesicles, pure CPEs and CPE/**DPPC** mixtures at 1:1 charge ratio prepared in HEPES buffer, pH 7.3, are shown in Figure 7.9. The ζ of **DPPC** vesicles was -3.3 (±0.1) mV, close to the literature value of ~ -4.4 mV.[55] A comparable ζ for **P3Zwit** was recorded at -5.6 (±0.4) mV. As the surface charges of both materials are similar, it is unsurprising that upon combination a similar ζ of -7.9 (±3.7) mV was observed. In contrast, the cationic CPE, **P3TMAHT**, had a positive ζ of +12.5 (±2.8) mV. Upon addition of **P3TMAHT** to **DPPC** vesicles the ζ increased dramatically to +18.1 (±1.7) mV. Previously, the cationic CPE, poly(allyl-*N,N*-dimethyl-*N*-hexylammonium chloride) was absorbed onto zwitterionic phospholipid vesicles and the positively-charged ammonium ions of the CPE were shown to be exposed to the bulk solution, increasing the surface potential of the vesicles.[56] These results, thus, suggest that **P3TMAHT** covers the outer surface of the zwitterionic vesicle. Pure **P3Anionic** has a negative ζ of -28.1 (±5.2) mV, while the ζ of the **P3Anionic/DPPC** mixture lies between this value and that of **DPPC** at -25.4 (±1.0) mV. Since the **DPPC** vesicles only partially adopt the ζ of **P3Anionic**, it is reasonable to suggest that the CPE may be penetrating the phospholipid bilayer, with chains also protruding from the outer surface.[56]

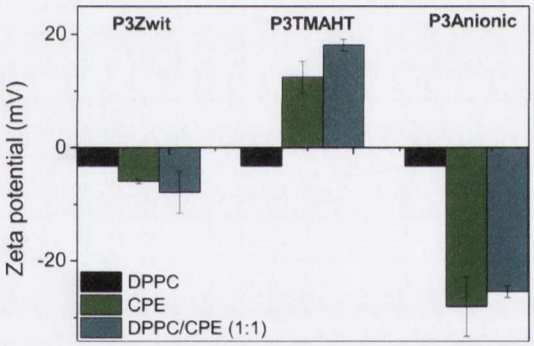


Figure 7.9 Zeta potentials of **DPPC** vesicles, CPEs and 1:1 CPE:**DPPC** charge ratio mixtures (conc. = 4.0×10^{-6} M (r.u.)) in HEPES buffer, 30 mM NaCl (pH 7.3). Each value is the average of at least three measurements.

7.3.2.3 Small-Angle Neutron Scattering

SANS experiments were performed on the CPE/**DPPC** vesicles (in 30 mM NaCl deuterated water solutions) to obtain deeper insight into the internal nanoscale organisation of the vesicle bilayers. The data were initially interpreted using scaling concepts to provide information about the CPE/**DPPC** aggregate shape (Figure 7.10a).[57] The observation window of the SANS experiments ranged from 3.0 to 69.8 nm, which is less than the diameter of isolated vesicles (~100 nm). However, it does cover the isolated chain length of the fully extended poly(thiophene)s (7.8-19.6 nm).[57] This means that fully dissolved rod-like polymers would be expected to exhibit a monatomic -1 decay, with a Guinier plateau in the low-q regime. This was not observed for any of the scattering curves, implying that the pure CPE solutions and the CPE/**DPPC** samples all

contained CPE associations (Appendix, Figure A.7.7). The low-q data ($q < 0.07$ Å^{-1}) arise from the structure of the vesicles themselves, while the high-q data ($0.07 < q$) originate from the internal structure of the bilayer[58] and can be used to probe changes in the structural organisation that result from interaction with the CPEs. The low-q regions for **DPPC** vesicles, **P3TMAHT/DPPC** and **P3Zwit/DPPC** mixtures decayed as $\sim q^{-2}$, which is typical of scattering from a flat rather than spherical bilayer.[59] This is to be expected considering that the radius of the vesicles is significantly greater than the thickness of the vesicle bilayer. In contrast, the **P3Anionic/DPPC** samples decayed as $q^{-1.6}$ in the low-q region, shifting to $q^{-4.1}$ in the high-q region. This excess scatter at $q = 0.05$ Å^{-1} could arise from a structure factor resulting from interparticle repulsion between similarly charged poly(thiophene) chains on the vesicle surfaces.[60, 61] Interestingly, the high-q "Porod" region ($q > 0.08$ Å^{-1}) of the **P3Anionic/DPPC** and **P3Zwit/DPPC** scattering profiles decays as $\sim q^{-4}$, consistent with scattering from smooth surfaces.[62] In contrast, the same region of the **P3TMAHT/DPPC** profile decays as $\sim q^{-3}$, indicating slightly rougher vesicle surfaces.

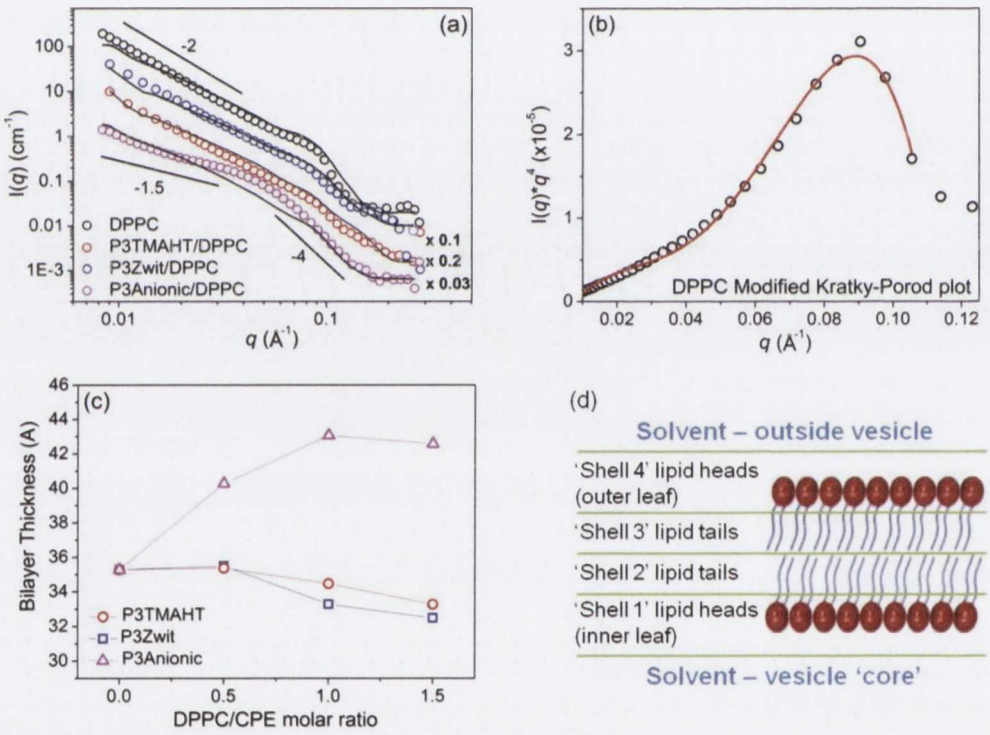


Figure 7.10 SANS data analysis to determine the nanoscale organisation of the CPE-**DPPC** systems. (a) SANS data for **DPPC** vesicles and mixtures of **P3TMAHT/DPPC**, **P3Zwit/DPPC** and **P3Anionic/DPPC** (1:1 charge ratio, 10 mg mL^{-1}) in D_2O, which have been offset for clarity. The solid lines show the fit to the data using a Core-Multi-Shell model as described in the text. (b) Modified Kratky-Porod (MKP) fit for **DPPC**. (c) MKP bilayer thicknesses of **DPPC** with increasing charge ratios of the CPEs. (d) Schematic of the phospholipid bilayer, defining the regions into which the Core-Multi-Shell model is divided.

The SANS data (0.009-0.27 Å^{-1}) were also fit to a Core-Multi-Shell model using a non-linear least-squares method, including polydispersity and q-resolution smearing.[22] The best fits for the **DPPC** vesicles and CPE/**DPPC** samples are shown in Figure 7.10a and the SLDs used for fitting are summarised in Table 7.4. In this model, four shells were used to represent the

phospholipid head-groups and the hydrophobic chains in the inner and outer regions of the bilayer (Figure 7.10d). The core of the vesicle is expected to contain the same solvent background as that outside of the vesicle. Due to the negligible binding constants of Na^+ and Cl^- ions (0.28 and 0.25 M^{-1}, respectively)[61] to zwitterionic vesicles, and the low concentration used (30 mM), ion associations are assumed to be unimportant and NaCl has not been included in the fits.[63]

The thickness of the bilayer was subsequently analysed using the modified Kratky-Porod (MKP) approach,[20] which relates the radius of gyration to the thickness of the bilayer and is independent of other model fitting. Pencer and Hallet found that the position of the first local maximum, q_{max}, in the $I(q)*q^4$ *vs.* q plot, could be used to obtain the bilayer thickness in unilamellar vesicles, if a homogeneous distribution of coherent neutron scattering length densities within the bilayer is assumed.[64] The MKP fit for pure **DPPC** (Figure 7.10b) gave a calculated bilayer thickness of 35.3 (±0.5) Å and the calculated thicknesses for all CPE/**DPPC** samples at different charge ratios are shown in Figure 7.10c. (MKP fits for the CPE/**DPPC** samples at different charge ratios are shown in Figure A.7.8.) The bilayer thicknesses for **P3Zwit/DPPC** and **P3TMAHT/DPPC** samples were found to decrease slightly to 33.3 (±0.1) and 34.5 (±0.1) Å, respectively, upon reaching a 1:1 charge ratio of CPE:**DPPC**. In contrast, the **P3Anionic/DPPC** samples increased in thickness to 43.3 (±0.1) Å at the same charge ratio.

Table 7.4 Structural parameters obtained from the SANS data using the MKP method and fitting to the Core-Multi-Shell model. The error values for the MKP fits were calculated from the goodness-of-fit R^2 values. φ_{dry} is the calculated percentage volume of dry material that each Core-Multi-Shell model fit represents, an ideal fit for these samples has a φ_{dry} of ~1 vol%.

Parameters		Blank DPPC vesicles	CPE:DPPC (1:1 charge ratio)		
			P3Zwit	P3TMAHT	P3Anionic
Bilayer thickness *via* MKP method (Å)		35.3 (±0.5)	33.3 (±0.1)	34.5 (±0.1)	43.3 (±0.1)
Core-Multi-Shell model:					
Inner leaflet	Head-group thickness (Å)	6.0	6.4	7.4	10.5
	Tail thickness (Å)	13.0	10.0	10.5	10.1
Outer leaflet	Tail thickness (Å)	13.0	10.0	10.5	10.1
	Head-group thickness (Å)	6.0	6.4	6.7	10.6
Total shell thickness (Å)		38.0	32.8	35.1	41.2
Radius of the vesicle core (Å)		481.3	504.0	483.0	489.9
Inner leaflet	Head-group SLD ($\times 10^{-6}$ Å^{-2})	2.44	2.43	1.38	0.96
	Tail SLD ($\times 10^{-6}$ Å^{-2})	0.11	0	0	-0.50
Outer leaflet	Tail SLD ($\times 10^{-6}$ Å^{-2})	0.11	0	0	-0.50
	Head-group SLD ($\times 10^{-6}$ Å^{-2})	2.35	2.27	1.38	0.96
φ_{dry} (%)		1.3	1.3	1.1	1.2

The total thickness of the blank **DPPC** vesicle bilayer with and without CPE using the Core-Multi-Shell model followed the same trend as the MKP fits (Table 7.4). The **DPPC** bilayer became slightly thinner upon addition of **P3TMAHT** from 38.0 to 35.1 Å. However, the head-group regions were thicker in comparison to pure **DPPC** vesicles. The SLD of the **DPPC** head-group regions is ~ 2.4 × 10^{-6} $Å^{-2}$, which decreased to ~1.4 × 10^{-6} $Å^{-2}$ upon addition of **P3TMAHT**. This may be attributed to the displacement of D_2O molecules from the head-group region by the cationic poly(thiophene), which has a much lower SLD of 0.44 × 10^{-6} $Å^{-2}$. The **P3TMAHT/DPPC** bilayers became slightly thinner and drier, but comparatively did not significantly change upon incorporation of the CPE. The **P3Anionic/DPPC** samples proved the most difficult to fit with the Core-Multi-Shell model. The excess scatter at 0.07 $Å^{-1}$ may be due to interparticle interactions between phospholipid vesicles or repulsion between similarly charged **P3Anionic** chains, however, the fits were not found to improve significantly upon the addition of a structure factor.[61] Nevertheless, fitting with this model gave vesicle bilayers with larger total thicknesses (41.2 Å) and larger head-group regions of ~10.5 Å. The SLDs of **P3Anionic** and the **DPPC** head-groups are both ~1.0 × 10^{-6} $Å^{-2}$, therefore, when intimately mixed the two species are expected to appear as one thicker 'shell'. In addition, when **P3Anionic** and **P3TMAHT** are mixed with the **DPPC** vesicles, the calculated radii of the vesicle cores were found to increase only moderately by ~7 and ~2 Å, respectively, in comparison to the **P3Zwit/DPPC** system which increased by 23 Å. For **P3Zwit/DPPC** samples the total bilayer thickness also decreased upon addition of **P3Zwit** decreasing to 32.8 Å, while the thickness of the head-group region remained relatively constant. The 'wetness' of the shells also remained effectively unchanged. These results suggest an increase in surface area of the vesicle bilayer upon addition of the **P3Zwit**, which may potentially be inserting throughout the **DPPC** bilayer, effectively spacing the phospholipids out, and thus increasing the overall surface area of the vesicle.

7.3.2.4 Imaging Studies

Epifluorescence microscopy was performed on a mixture of CPE/**DPPC** multilamellar vesicles (MLVs) to gain further insight into the incorporation of the CPEs within the phospholipid bilayers. Larger MLVs (5-20 μm in diameter) were used for epifluorescence microscopy measurements because of the limited size resolution of this technique. The **P3Zwit/DPPC** sample (Figure 7.11a) clearly shows red emission throughout the MLVs, suggesting the CPE is able to penetrate through multiple phospholipid bilayers. In contrast, the **P3TMAHT/DPPC** sample (Figure 7.11b) shows an uneven vesicle surface which may be attributed to aggregates of CPE on the vesicle, or potentially aggregation of the CPE/**DPPC** vesicles themselves.[9] The vesicle structure is most dominant in the **P3Anionic/DPPC** samples (Figure 7.11c), with the poly(thiophene) emission localised on the outer layers of the MLVs.

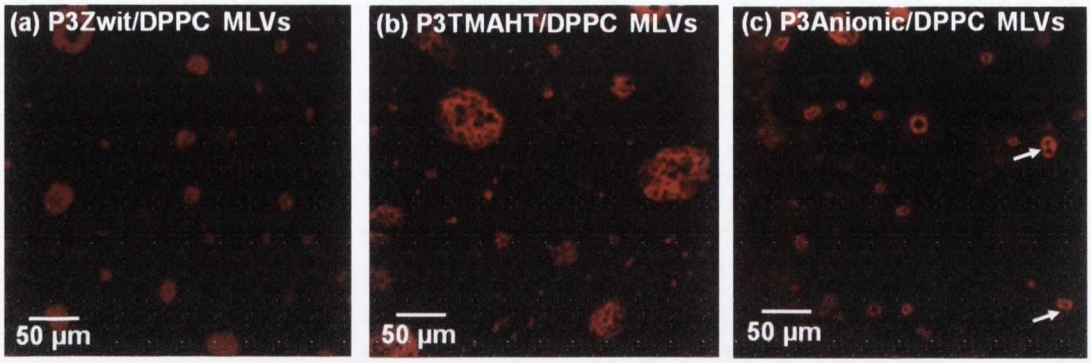


Figure 7.11 Epifluorescence images of **DPPC** multilamellar vesicles (MLVs) (2.6×10^{-3} M) titrated with (a) **P3Zwit** (1.3×10^{-3} M (r.u.)), (b) **P3TMAHT** (1.3×10^{-3} M (r.u.)) and (c) **P3Anionic** (1.3×10^{-3} M (r.u.)), λ_{ex} = 435 nm. Arrows highlight fused vesicles.

Atomic force microscopy was used to measure the surface topography of the **DPPC** LUVs, CPEs and their mixtures. AFM images of **DPPC** vesicles appeared as monodisperse spheres, 74 (±10) nm in diameter (Figure A.7.9a). The pure CPE samples gave large, amorphous aggregates which were 300-400 nm in diameter (Figure A.7.9b-d). Each CPE/**DPPC** sample contained features of two population sizes. In all cases there was no evidence of the pure CPE aggregates. The smaller populations were spheres of ~70 nm diameter, which potentially correspond to pure **DPPC** vesicles; however, it is more probable that these smaller features are **DPPC** vesicles which have only accommodated a few poly(thiophene) chains. The second, larger population in the **P3TMAHT/DPPC** sample (Figure 7.12a) featured spherical objects ~187 (±27) nm in diameter, with rough surfaces as indicated by SANS. A similar surface morphology has previously been reported for *E. coli* cells associated with cationic CPEs and was attributed to either a coating of CPE aggregates, disruption to the cell membrane, or a combination of both.[9] Since the DLS studies performed here suggest that the vesicle structure is retained, the roughening of the **DPPC** vesicles is most likely due to the formation of **P3TMAHT** clusters on the vesicle surface or aggregates of the CPE-**DPPC** vesicles. In contrast, the larger features in the **P3Zwit/DPPC** films (Figure 7.12b) were smooth spheres with diameters of 177 (±41) nm. The second population in **P3Anionic/DPPC** samples were aggregates ~158 (±78) nm in diameter, which clearly exhibit a multilayer effect (inset, Figure 7.12c). The outer shell has a thickness of ~30 nm, which could correspond to CPE chains extending from the vesicle surface, as suggested by the ζ measurements and the increase in head-group thickness observed using SANS. The large, smooth, spherical aggregates in the **P3Zwit**:**DPPC** and **P3Anionic**:**DPPC** samples are most likely the consequence of vesicle fusion. In particular, the appearance of fused vesicles is noted in the **P3Anionic/DPPC** AFM and epifluorescence images (white arrows in Figures 7.11c and 7.12c). Examples of such fused vesicle may be harder to identify in the **P3Zwit/DPPC** samples since the poly(thiophene) penetrates throughout the MLV bilayers, making it difficult to distinguish one adjacent vesicle from another in the epifluorescence images. CPE-induced fusion of phospholipid vesicles has previously been observed between the anionic poly(phenylene ethylene), poly-[5-methoxy-2-(3-sulfopropoxy)-1,4-phenylene-vinylene] (MPS-PPV), and the cationic phospholipid, dioleoyl-*sn*-glycero-3-

phosphocholine (DOPC).[15] It was postulated that partial penetration of the CPE chains within the DOPC bilayer induces strain, while CPE chains extending from the surface of the host vesicle are capable of bridging to an adjacent vesicle bilayer. When combined these two effects create the necessary proximity for fusion to occur. It is reasonable to assume a similar process also encourages the vesicle fusion observed here.

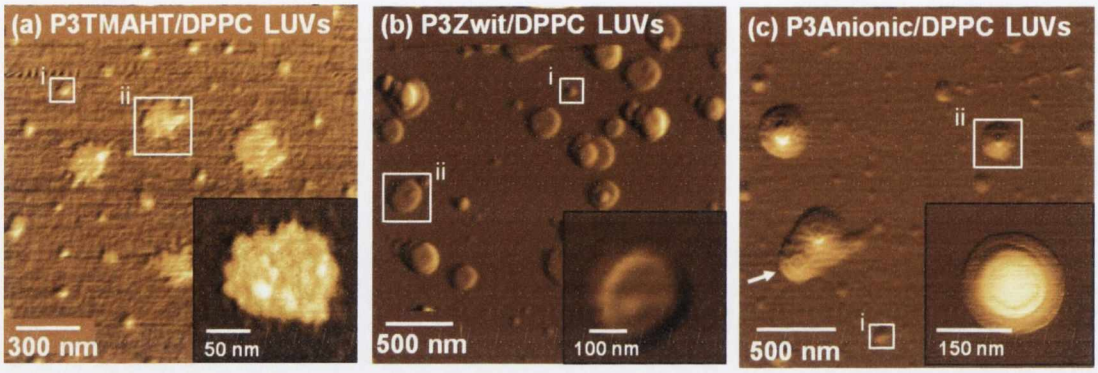


Figure 7.12 AFM tapping mode images of (a) **P3TMAHT/DPPC**, (b) **P3Zwit/DPPC** and (c) **P3Anionic/DPPC** LUVs at 1:1 charge ratio (2.0×10^{-5} M): (i) undoped **DPPC** vesicles, (ii) CPE-doped **DPPC** vesicle structures. Arrows highlight fused vesicles.

7.3.2.5 Mechanism of Interaction

From these studies three distinctive modes of interaction between each CPE and the **DPPC** vesicles are proposed, as shown by the schematic representation in Figure 7.13. The changes in the UV/Vis absorption and PL spectra confirm interaction between the CPEs and the vesicles. The calculated partition coefficients suggest the extent of incorporation follows the order **P3Zwit** › **P3Anionic** › **P3TMAHT**. In all cases an increase in size of the phospholipid vesicles was observed upon addition of the CPE (DLS, AFM, SANS); however, further inspection suggests that this is likely to be the result of different modes of interaction. Firstly, the global results suggest that **P3Zwit**, unrestricted by an overall charge, penetrates *throughout* the phospholipid bilayer. SANS revealed an increase in size of the vesicle including the core radius, suggesting an increase in the surface area of the phospholipid bilayer, which is to be expected if the CPE is incorporated throughout the thickness of the bilayer. In contrast, **P3Anionic** appears to only partially penetrate the phospholipid bilayer to localise within the phospholipid head-group region, encouraged by electrostatic attractive forces between the anionic sulfonate of the CPE and the outermost ammonium group of **DPPC**. This mechanism is supported by the increase in the phospholipid head-group thickness (SANS), efficient FRET with the membrane probe Prodan and localised changes to the outer surface of uni- and multi-lamellar vesicles (AFM, epifluorescence microscopy). Finally, the low K_p value suggests that **P3TMAHT** has minimal penetration within the **DPPC** bilayer, presumably due to electrostatic repulsion between the positively-charged ammonium groups on both the CPE and **DPPC**, which results in the formation of extended CPE structures on the surface of the vesicles (PL enhancement, SANS, zeta potential, AFM, epifluorescence). It is interesting to note that it was the steady-state emission of **P3Anionic** which

showed remarkable sensitivity to the phase transitions of **DPPC**, in contrast to **P3TMAHT** and **P3Zwit** which showed no significant sensitivity. This is an encouraging result that reflects the proposed assembly mechanisms adequately, since **P3Anionic** is the only poly(thiophene) to specifically localise within the **DPPC** head-group region, where sensitivity to membrane order is believed to be the greatest.[27]

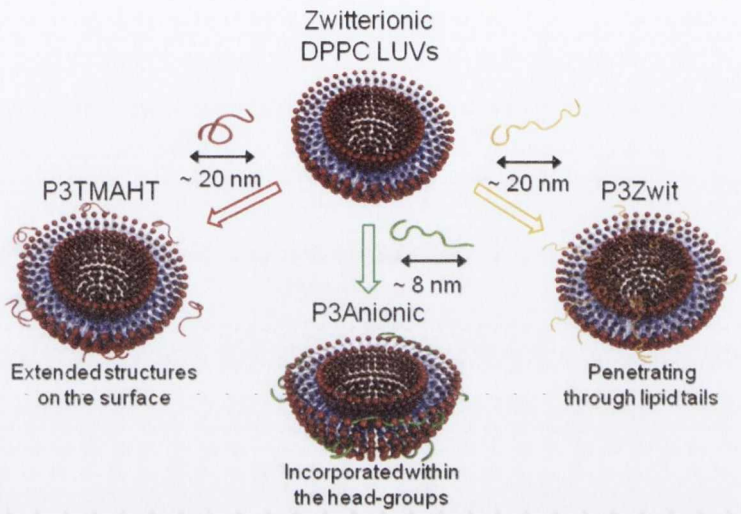


Figure 7.13 A schematic representation of the proposed CPE/**DPPC** vesicle interactions.

One potential reason for the observed difference in association between the charged poly(thiophene)s is their chain length. The anionic poly(thiophene) is approximately 21 r.u., whereas in comparison the cationic poly(thiophene) is 49 r.u. Wang *et al.* found that increasing the chain length of a cationic poly(phenylene ethynylene), decreased the degree of perturbation into the anionic phospholipid, DPPG, membrane.[16] However, it is important to note that **P3Zwit** has an identical chain-length to **P3TMAHT**, and yet is capable of burying deep within the bilayer, potentially suggesting that chain-length is not the mediating factor here. A further element to consider is the chemical structure of the **DPPC** phospholipid head-group, where the outermost group is a cationic trimethyl ammonium, as shown in Scheme 7.1. Repulsive forces are expected to exist between this group and the cation of **P3TMAHT**, which may be preventing **P3TMAHT** from penetrating further within the zwitterionic head-group region.

7.4 Conclusions

In summary, the red-emitting poly(thiophene), **P3Anionic**, has been shown to function as a fluorescent probe for the sequential identification of the three key phase transitions occurring within **DPPC** bilayers. **P3Anionic** is the first example of CPE probe capable of detecting the less energetically-demanding sub-transition, $T_{s,}$[30] highlighting its remarkable sensitivity to subtle changes in membrane order. This result may have important consequences for the detection of unsought changes in membrane permeability *via* phase transitions, which are thought to be behind a number of degenerative or life-threatening conditions.

In contrast to **P3Anionic**, the emission of conjugated poly(thiophene)s bearing cationic and zwitterionic pendant groups (**P3TMAHT** and **P3Zwit**) were found to not display any significant correlation to the membrane order. A series of binding mode studies were consequently performed to investigate whether this was an effect of the nature of association between each of the CPEs and the phospholipid vesicles. The strategic study comparing all three CPEs demonstrated that the penetration depth of the CPE within zwitterionic phospholipid bilayers could be controlled *via* charge-mediation. **P3Zwit**, with an overall neutral, zwitterionic side-group and hydrophobic poly(thiophene) backbone, can readily insert in between the **DPPC** zwitterionic head-groups, as well as within the hydrophobic phospholipid tails. In contrast, the charged poly(thiophene)s, **P3Anionic** and **P3TMAHT**, are unable to penetrate within the hydrophobic tails and localise around the zwitterionic head-groups of the phospholipid bilayers. **P3TMAHT** is believed to form extended structures on the vesicle surface, while **P3Anionic** burrows within the zwitterionic head-group region of the lipid bilayers where the sensitivity to membrane order is believed to be the greatest.[35]

Previously, CPEs have been somewhat disregarded as viable fluorescent membrane probes due to their relatively large size and lack of accurate localisation within the membrane bilayer. Yet this study has shown that through the strategic selection of the CPE charge, the nature of their interaction with cell membranes can be tuned, without the need for complex molecular probe design, and the associated time-consuming experimental procedures. This has important consequences for a variety of applications, such as in biosensing, where the location of the probe is explicitly linked to biophysical properties under investigation[13] and in drug delivery, where the presence of polymer shells has been shown to lead to prolonged drug delivery times.[65] Importantly, the **P3Zwit-DPPC** system also offers the unique advantage of a CPE-phospholipid system with the absence of mobile counterions. Such counterions are potentially problematic in biological sensing platforms due to their lack of biocompatibility or due to the possibility that their presence can result in undesirable side-reactions, such as fluorescence quenching by halide anions.[4]

The size of the large polymer is also known to advantageously inhibit cell internalisation,[32] which is a common problem for small molecule fluorescent dyes.[66] At the same time, at only <20 nm in length, these CPEs remain small enough to accurately probe the raft-like nanodomains in cell membranes (10-200 nm), whose role and impact in cell function remains a topic of wide debate.[2, 3] Finally, due their emission in the far-red region, poly(thiophene)s should be an ideal probe for *in-vivo/in-vitro* studies, since interference from tissue auto-fluorescence should be minimal. Therefore, CPEs combine a plethora of desirable properties for a membrane probe, which suggests that the selective engineering of CPE-phospholipid interfaces by strategic charge-mediation could play a key role in the design of superior biomedical and biotechnological devices.

7.5 References

1. R. B. Gennis, *Biomembranes: Molecular Structure and Function*, Springer-Verlag New York, Inc., 1989, pp. 1.
2. R. Marin, J. A. Rojo, N. Fabelo, C. E. Fernandez and M. Diaz, *Neuroscience*, 2013, **245**, 26-39.
3. W. Stillwell and S. R. Wassall, *Chem. Phys. Lipids*, 2003, **126**, 1-27.
4. S. M. Fonseca, R. P. Galvão, H. D. Burrows, A. Gutacker, U. Scherf and G. C. Bazan, *Macromol. Rapid Commun.*, 2013, **34**, 717-722.
5. S. Chemburu, E. Ji, Y. Casana, Y. Wu, T. Buranda, K. S. Schanze, G. P. Lopez and D. G. Whitten, *J. Phys. Chem. B*, 2008, **112**, 14492-14499.
6. Z. Kahveci, M. J. Martínez-Tomé, R. Mallavia and C. R. Mateo, *Biomacromolecules*, 2013, **14**, 1990-1998.
7. F. Jonsson, T. Beke-Somfai, J. Andréasson and B. Nordén, *Langmuir*, 2013, **29**, 2099-2103.
8. N. Anwar, A. Rix, W. Lederle and A. J. C. Kuehne, *Chem. Commun.*, 2015, **51**, 9358-9361.
9. L. E. Edens, Y. Wang, D. G. Whitten and D. J. Keller, *Langmuir*, 2014, **30**, 10691-10697.
10. J. Du, A. W. Thomas, X. Chen, L. E. Garner, C. A. Vandenberg and G. C. Bazan, *Chem. Commun.*, 2013, **49**, 9624-9626.
11. R. Koynova and M. Caffrey, *Biochim. Biophys. Acta, Biomembr.*, 1998, **1376**, 91-145.
12. Z. Kahveci, M. Martínez-Tomé, R. Esquembre, R. Mallavia and C. Mateo, *Materials*, 2014, **7**, 2120-2140.
13. A. P. Demchenko, Y. Mély, G. Duportail and A. S. Klymchenko, *Biophys. J.*, 2009, **96**, 3461-3470.
14. L. Ding, E. Y. Chi, S. Chemburu, E. Ji, K. S. Schanze, G. P. Lopez and D. G. Whitten, *Langmuir*, 2009, **25**, 13742-13751.
15. P. Karam, A. A. Hariri, C. F. Calver, X. Zhao, K. S. Schanze and G. Cosa, *Langmuir*, 2014, **30**, 10704-10711.
16. Y. Wang, E. M. Jones, Y. Tang, E. Ji, G. P. Lopez, E. Y. Chi, K. S. Schanze and D. G. Whitten, *Langmuir*, 2011, **27**, 10770-10775.
17. P. Vermette and L. Meagher, *Colloids Surf., B*, 2003, **28**, 153-198.
18. T. Costa, D. de Azevedo, B. Stewart, M. Knaapila, A. J. M. Valente, M. Kraft, U. Scherf and H. D. Burrows, *Polym. Chem.*, 2015, **6**, 8036-8046.
19. H. Matsuki, M. Goto, K. Tada and N. Tamai, *Inter. J. Mol. Sci.*, 2013, **14**, 2282-2302.
20. P. Balgavý, M. Dubničková, N. Kučerka, M. A. Kiselev, S. P. Yaradaikin and D. Uhríková, *Biochim. Biophys. Acta, Biomembr.*, 2001, **1512**, 40-52.
21. *http://www.sasview.org/index.html.*
22. S. Qian and W. T. Heller, *J. Phys. Chem. B*, 2011, **115**, 9831-9837.
23. K. A. Riske, R. P. Barroso, C. C. Vequi-Suplicy, R. Germano, V. B. Henriques and M. T. Lamy, *Biochim. Biophys. Acta, Biomembr.*, 2009, **1788**, 954-963.
24. K. K. Stokes, K. Heuzé and R. D. McCullough, *Macromolecules*, 2003, **36**, 7114-7118.
25. C. Tan, E. Atas, J. G. Müller, M. R. Pinto, V. D. Kleiman and K. S. Schanze, *J. Am. Chem. Soc.*, 2004, **126**, 13685-13694.
26. R. C. Evans, M. Knaapila, N. Willis-Fox, M. Kraft, A. Terry, H. D. Burrows and U. Scherf, *Langmuir*, 2012, **28**, 12348-12356.
27. S. Shrivastava, S. Haldar, G. Gimpl and A. Chattopadhyay, *J. Phys. Chem. B*, 2009, **113**, 4475-4481.

28. V. Kilin, O. Glushonkov, L. Herdly, A. Klymchenko, L. Richert and Y. Mely, *Biophys. J.*, 2015, **108**, 2521-2531.
29. R. Saxena, S. Shrivastava, S. Haldar, A. S. Klymchenko and A. Chattopadhyay, *Chem. Phys. Lipids*, 2014, **183**, 1-8.
30. M. Kinoshita, K. Ito and S. Kato, *Chem. Phys. Lipids*, 2010, **163**, 712-719.
31. A. A. Yaroslavov, T. A. Sitnikova, A. A. Rakhnyanskaya, E. G. Yaroslavova, D. A. Davydov, T. V. Burova, V. Y. Grinberg, L. Shi and F. M. Menger, *J. Am. Chem. Soc.*, 2009, **131**, 1666-1667.
32. M. J. Tapia, M. Monteserin, H. D. Burrows, J. A. S. Almeida, A. A. C. C. Pais, J. Pina, J. S. Seixas de Melo, S. Jarmelo and J. Estelrich, *Soft Matter*, 2015, **11**, 303-317.
33. M. Dal Molin, Q. Verolet, A. Colom, R. Letrun, E. Derivery, M. Gonzalez-Gaitan, E. Vauthey, A. Roux, N. Sakai and S. Matile, *J. Am. Chem. Soc.*, 2015, **137**, 568-571.
34. T. M. Swager, C. J. Gil and M. S. Wrighton, *J. Phys. Chem.*, 1995, **99**, 4886-4893.
35. M. Chevrier, J. E. Houston, J. Kesters, N. Van den Brande, A. E. Terry, S. Richeter, A. Mehdi, O. Coulembier, P. Dubois, R. Lazzaroni, B. Van Mele, W. Maes, R. C. Evans and S. Clement, *J. Mater. Chem. A*, 2015, **3**, 23905-23916.
36. A. Coutinho and M. Prieto, *Biophys. J.*, 1995, **69**, 2541-2557.
37. N. C. Santos, M. Prieto and M. A. R. B. Castanho, *Biochim. Biophys. Acta, Biomembr.*, 2003, **1612**, 123-135.
38. M. Vermeir, N. Boens and K. P. Heirwegh, *Biochem. J.* , 1992, **284**, 483-490.
39. A. I. Greenwood, S. Tristram-Nagle and J. F. Nagle, *Chem. Phys. Lipids*, 2006, **143**, 1-10.
40. A. T. Ngo and G. Cosa, *Langmuir*, 2009, **26**, 6746-6754.
41. T. Costa, L. E. Garner, M. Knaapila, A. W. Thomas, S. E. Rogers, G. C. Bazan and H. D. Burrows, *Langmuir*, 2013, **29**, 10047-10058.
42. M. E. H. Heeley, J. K. Gallaher, T. L. Nguyen, H. Y. Woo and J. M. Hodgkiss, *Chem. Commun.*, 2013, **49**, 4235-4237.
43. H. D. Burrows, M. a. J. Tapia, S. M. Fonseca, S. Pradhan, U. Scherf, C. u. L. Silva, A. A. C. C. Pais, A. J. M. Valente, K. Schillén, V. Alfredsson, A. M. Carnerup, M. Tomšič and A. Jamnik, *Langmuir*, 2009, **25**, 5545-5556.
44. K. A. Kozyra, J. R. Heldt, M. Engelke and H. A. Diehl, *Spectrochim. Acta Part A*, 2005, **61**, 1153-1161.
45. C. Ghatak, V. G. Rao, R. Pramanik, S. Sarkar and N. Sarkar, *Phys. Chem. Chem. Phys.*, 2011, **13**, 3711-3720.
46. T. Parasassi, E. Krasnowska, L. Bagatolli and E. Gratton, *J. Fluoresc.*, 1998, **8**, 365-373.
47. T. Förster, *Annalen der Physik*, 1948, **437**, 55-75.
48. D. Beljonne, G. Pourtois, C. Silva, E. Hennebicq, L. M. Herz, R. H. Friend, G. D. Scholes, S. Setayesh, K. Müllen and J. L. Brédas, *Proc. Nat. Acad. Sci.*, 2002, **99**, 10982-10987.
49. K. F. Wong, B. Bagchi and P. J. Rossky, *J. Mater. Chem. A*, 2004, **108**, 5752-5763.
50. J. R. Lakowics, *Principles of Fluorescence Spectorscopy*, Springer, 2006, pp. 443-475.
51. H. Jiang, P. Taranekar, J. R. Reynolds and K. S. Schanze, *Angew. Chem. Int. Ed.*, 2009, **48**, 4300-4316.
52. A. V. Sybachin, A. A. Efimova, E. A. Litmanovich, F. M. Menger and A. A. Yaroslavov, *Langmuir*, 2007, **23**, 10034-10039.
53. Y. Wang, Y. Tang, Z. Zhou, E. Ji, G. P. Lopez, E. Y. Chi, K. S. Schanze and D. G. Whitten, *Langmuir*, 2010, **26**, 12509-12514.
54. H. Y. Fan, M. Nazari, G. Raval, Z. Khan, H. Patel and H. Heerklotz, *Biochim. Biophys. Acta, Biomembr.*, 2014, **1838**, 2306-2312.
55. A. E. Wiącek, *Appl. Surf. Sci.*, 2011, **257**, 4495-4504.

56. M. Kepczynski, D. Jamróz, M. Wytrwal, J. Bednar, E. Rzad and M. Nowakowska, *Langmuir*, 2011, **28**, 676-688.
57. P. W. Schmidt, *Some Fundamental Concepts and Techniques Useful in Small-Angle Scattering Studies of Disordered Solids. In Modern Aspects of Small-Angle Scattering*, Kluwer Academic Publishers: Dordrecht, The Netherlands, 1995.
58. M. A. Kiselev, E. V. Zemlyanaya, V. K. Aswal and R. H. H. Neubert, *Eur. Biophys. J.*, 2006, **35**, 477-493.
59. I. Grillo, E. I. Kats and A. R. Muratov, *Langmuir*, 2003, **19**, 4573-4581.
60. A. Thomas, J. E. Houston, N. Van den Brande, J. De Winter, M. Chevrier, R. K. Heenan, A. E. Terry, S. Richeter, A. Mehdi, B. Van Mele, P. Dubois, R. Lazzaroni, P. Gerbaux, R. C. Evans and S. Clément, *Polym. Chem.*, 2014, **5**, 3352-3362.
61. M. Knaapila, R. C. Evans, A. Gutacker, V. M. Garamus, N. K. Szekely, U. Scherf and H. D. Burrows, *Soft Matter*, 2011, **7**, 6863-6872.
62. B. Hammouda, *J. Appl. Crystallogr.*, 2010, **43**, 716-719.
63. D. Uhríková, N. Kučerka, J. Teixeira, V. Gordeliy and P. Balgavý, *Chem. Phys. Lipids*, 2008, **155**, 80-89.
64. J. Pencer and F. R. Hallett, *Phys. Rev. E*, 2000, **61**, 3003-3008.
65. K. Mohr, S. S. Müller, L. K. Müller, K. Rusitzka, S. Gietzen, H. Frey and M. Schmidt, *Langmuir*, 2014, **30**, 14954-14962.
66. H.-Y. Wang, H.-R. Jia, X. Lu, B. Chen, G. Zhou, N. He, Z. Chen and F.-G. Wu, *J. Mater. Chem. B*, 2015, **3**, 6165-6173.

Chapter 8

The Development of Photodeformable Self-Assembly Templates using Photoactive Surfactants

8.1 Introduction

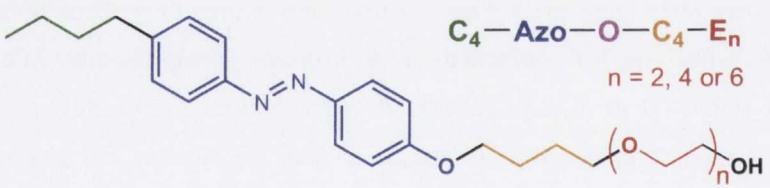
Photosurfactants (PS) are amphiphilic molecules which contain a light-responsive chromophore, such as an azobenzene group.[1] Photoisomerisation leads to a substantial change in the geometrical configuration of the molecule.[2] This results in a modification of the delicate hydrophilic-hydrophobic balance which has a significant impact on the shape and structure of supramolecular aggregates. For example, Hatton *et al.* found that the *trans*-isomer of the non-ionic azobenzene PS, diethylene glycol mono(4′,4-butyloxybutyl-azobenzene) ($C_4AzoOC_4E_2$), self-assembled into bilayer vesicles at high concentration. In contrast, the *cis*-isomer formed a bicontinuous phase which was attributed to the change in molecular architecture accompanying the *trans-cis* isomerisation.[3] Alternatively, photoisomerisation can result in complete loss of the micellar structure, typically when the surfactant concentration is above the *cmc* for the *trans*-isomer and below the *cmc* for the *cis*-isomer. For example, Lund *et al.* found from *in-situ* SAXS studies that the photoisomerisation of the cationic photosurfactant, 4-butyl-4′-(3-trimethyl-ammoniumpropoxy)phenylazobenzene (AzoTMA) led to the rapid dissolution of surfactant micelles (<1 s time scale).[4] It has previously been established that the change in shape and size of the azobenzene PS upon photoisomerisation was the driving force for such changes in their physicochemical behaviour.[5, 6] However, the *trans*-to-*cis* isomerisation of individual surfactant molecules, and their subsequent effect on the aggregate structure formed, is yet to be fully understood.

Surfactants which form lyotropic liquid crystalline phases have previously been employed as sacrificial, soft templates for ordered, nanostructured inorganic-organic polymeric materials in the bulk and as thin films.[7] PS systems which form LLC phases would theoretically have the combined ability to template inorganic sol-gel matrixes and change their shape upon irradiation with light. However, while "regular" surfactants are well-known to self-assemble into a variety of thermodynamically stable 2D or 3D LLC phases at concentrations significantly above the *cmc*, reports for the formation of extended LLC phases in pure PS systems are extremely rare.[8-10] Hughes *et al.* were the first to design azobenzene-containing PS capable of forming LLC phases.[8, 10] Two photoresponsive amphiphiles having comparable structures were reported which consisted of hydrophilic oligooxyetheylene units (E), hydrophobic alkyl chains and a light-sensitive azobenzene moiety ($C_{4+n}AzoC_mE_7$, where $n = 0$, $m = 5$ or $n = 5$, $m = 0$).[8] A combination of DSC, POM, SAXS and rheology studies were used to show that the nature of the LLC phases formed could be controlled by varying the position of the azobenzene moiety within the hydrophobic tail. Furthermore, *trans-cis* photoisomerisation of the PS with the azobenzene group localised in the middle of the alkyl chain induced significant changes in the self-assembled structure and its bulk properties. In contrast, when the azobenzene unit was directly attached to the hydrophilic domain there were no observable changes in the self-assembled structure upon photoisomerisation. To

date, this is the only reported azobenzene-containing PS found to form LLC phases contain ethylene glycol moieties.

8.1.1 Aims

Chapters 5 – 7 focused on the self-assembly of photoactive conjugated polymers with oppositely-charged species, such as surfactants, polyoxometalates and phospholipids, to design novel materials for energy and sensing applications. In this chapter an alternative approach will be taken, whereby surfactants which are inherently photoresponsive will be developed as templates for nanoporous polymeric materials. The goal for this chapter is to address the lack of photosurfactants which form photoresponsive LLC phases. The surfactants and the conditions identified as forming the desirable LLC phases will eventually be used to template inorganic sol-gel matrixes. The azobenzene-containing photosurfactant, diethylene glycol mono(4′,4-butyloxybutyl-azobenzene) (**$C_4AzoOC_4E_2$**), was previously reported by Hatton *et al.*[3, 5] *Trans*-**$C_4AzoOC_4E_2$** were found to assemble into bilayer vesicles, while upon *trans*-to-*cis* isomerisation with UV-light (λ_{ex} = 320 nm) a bicontinuous phase was formed.[3] However, no LLC phases were reported for this molecule. Given that the analogous neutral surfactants which do not contain an azobenzene moiety have shown LLC phase formation, it was anticipated that **$C_4AzoOC_4E_2$** should also form LLC phases at higher concentrations. Therefore, this surfactant with a diethylene glycol head-group, and two further PS with a four and six ethylene glycol units, **$C_4AzoOC_4E_4$** and **$C_4AzoOC_4E_6$**, respectively, were synthesised (Scheme 8.1). These PS will allow the impact of the size of the hydrophilic head-group, and the effect of photoisomerisation, on the self-assembly and growth of PS aggregates from isolated micelles to LLC phases to be determined.



Scheme 8.1 Chemical structure of the ethylene glycol photosurfactants studied in this chapter. **$C_4AzoOC_4E_n$**, where *n* is 2, 4 or 6 ethylene glycol units

The specific aims include:

- the synthesis of a series of ethylene glycol-containing azobenzene-PS predicted to form LLC phases and determine any structure-property relationships based on the size of the head-groups;
- to investigate the kinetics of photoisomerisation using UV/Vis absorption and ^{1}H NMR spectroscopy;
- to determine the critical micelle concentrations of the surfactants in both isomeric forms using dynamic light scattering;

- to study the size, shape and dimensions of the aggregates using multi-angle light scattering and SANS;
- to probe the phase behaviour of the PS at high concentrations using a polarised optical microscope equipped with a heat-stage to determine what, if any, LLC phases form, in addition to deducing the effect of photoisomerisation on any phase formed;
- to prepare preliminary binary (temperature-concentration) phase diagrams of the PS.

8.2 Experimental

8.2.1 Materials

4-butylaniline (97%), sodium nitrite (≥99.0%), 1,4-dribromobutane (99%), anhydrous potassium carbonate (≥99.0%), potassium iodide (99.0%), sodium sulfite (98%), copper sulfate pentahydrate (≥98.0%), ammonium hydroxide (5.01 N solution in water), hydroxylamine hydrochloride (98%), potassium hydroxide (≥85%), 1,6-dibromohexane (96%), 4-aminophenol (≥98.0%), diethylene glycol (99%), tetraethylene glycol (99%), hexaethylene glycol (97%) and hydrochloric acid (conc. 37%), ethanol (HPLC grade), tetrahydrofuran (HPLC grade), diethyl ether (≥99.5%), dichloromethane, acetone and hexane were purchased from Sigma Aldrich. Sodium hydroxide (≥97%) and chloroform (>99%) were purchased from Fisher Scientific and phenol (>99.0%) was purchased from BDH Chemical Ltd. England. Trimethylamine (24% weight in water) was purchased from ACROS. All reagents and solvents were used as received.

8.2.2 Instrumentation

The instrumentation for UV/Vis absorption, NMR, FTIR spectroscopy, mass spectrometry, MALS, SANS, cryo-SEM and POM are described in Chapter 3.

8.2.2.1 Light-stage set-up

Photoconversion of stable *trans*-surfactants to the *cis*-form was obtained by exposure to a UV light emitting diode (LED) (LedEngin®) with an illumination wavelength of 365 nm and a power output of 2.6 mW cm^{-2}, when placed at 4.5 cm from the sample. Reverse *cis*- to *trans*-isomerisation was performed using a blue LED (Prolight®) with an illumination wavelength of 465 nm and a power output of 2.4 mW cm^{-2}, when placed at 4.5 cm from the sample. The home-built light-stage set-up used for most of the photoirradiation experiments is shown schematically in Figure 8.1. The parameters for the LEDs used in this light-stage are summarised in Table 8.1.

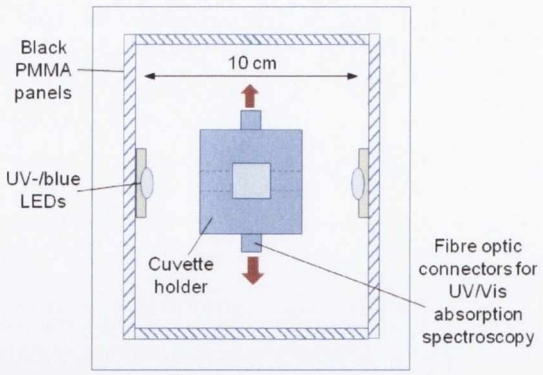


Figure 8.1 Schematic representation of the home-built light-stage used for photoisomerisaiton of the surfactants.

Table 8.1 Parameters of the LED used in the home-built light-stage, where i_f and V_f are the forward current and forward voltage, respectively.

LED	Brand	λ_{ex} (nm)	Power (W)	i_f(mA)	V_f(V)	Power supply (V)	Resistor (Ω)	Photon Flux (W m^{-2})
UV	LedEngin	365	3	700	4.88	9	6.8	1062.1
Blue	Prolight	465	1	350	3.5	9	18	1018.2

8.2.3 Methods

UV/Vis absorption spectroscopy: Solutions of each PS (9.7×10^{-5}, 8.0×10^{-5} and 3.4×10^{-5} M for **$C_4AzoOC_4E_2$**, **$C_4AzoOC_4E_4$** and **$C_4AzoOC_4E_6$**, respectively) were prepared in Millipore water.

Critical micelle concentration titrations: Stock solutions of each PS (9.7×10^{-4}, 8.0×10^{-4} and 6.8×10^{-4} M for **$C_4AzoOC_4E_2$**, **$C_4AzoOC_4E_4$** and **$C_4AzoOC_4E_6$**, respectively) were prepared in filtered Millipore water. All measurements were performed at 20 °C.

(*i*) *Surface tensiometry*: Aliquots of the stock solutions were added to Millipore water (1 mL). Surface tension was measured as function of concentration of the photosurfactants. Millipore water was used as a reference sample.

(*ii*) *Dynamic light scattering*: Aliquots of the stock solutions (0.5-1 μL) were added to filtered Millipore water (1 mL). The intensity of scattered light (kcounts) was measured as a function of concentration of photosurfactants.

Multi-angle dynamic light scattering: Dilutions of the pure PS samples in Millipore water (10 mL), above their *cmc*s, were filtered a minimum of ten times through a 0.2 μm syringe filter and sealed in 25 mL glass vials. To measure the hydrodynamic radii, R_H, DLS measurements were collected over series of angles (45-150°). The radii of gyration, R_g, was determined from the change in the scattering intensity as a function of the scattering angle. The correlation functions measured at each

angle were fit to a stretched exponential (Equation 2.18) using Origin 9.1, and the data was analysed as described in Section 2.2.3.2.

Polarised optical microscopy: A series of highly concentrated PS samples (10-100 *wt.*%) were prepared and deposited between two glass cover slips. These samples were imaged using a polarised optical microscope, equipped with a liquid nitrogen cooled heat-stage, in order to probe the LLC phases formed over a range of temperatures. Each sample was slowly heated and cooled between 5 – 100 °C, using a heating rate of 10 °C min^{-1}. Images were initially recorded in 5 °C intervals as the samples were heated. At temperatures where significant phase transitions were recorded, repeat measurements were performed at 1 °C intervals, with a slower heating rate of 1 °C min^{-1}. Photoisomerisation of the PS samples was achieved *via* 10 min of irradiation with a UV light emitting diode (λ_{ex} = 365 nm) for the *trans-cis* isomerisation and a blue light emitting diode (λ_{ex} = 465 nm) for the reverse *cis-trans* isomerisation. Control experiments were performed to ensure that no photoisomerisation would be triggered as a result of the halogen lamp used to power to POM. A number of *cis*-isomers were left on the light stage for ~2 h and no change in texture of the image was observed in this time.

Differential scanning calorimetry: A series of highly concentrated PS samples (10-100 *wt.*%) were sealed in aluminium crucibles. Samples were stored in the freezer prior to measurement. DSC measurements were performed in the range of 10-80 °C in a nitrogen atmosphere using a heating rate of 10 °C min^{-1}. Sample masses were ~5 mg.

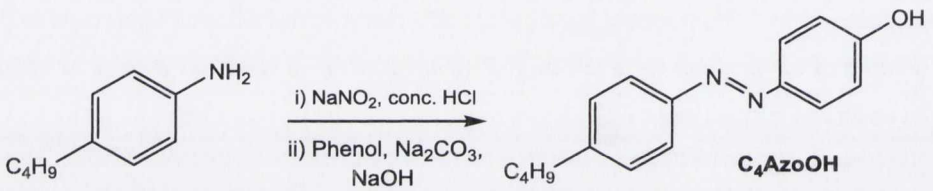
Small-angle neutron scattering: Photosurfactants were prepared in D_2O to provide good neutron scattering contrast. Heat studies were performed using a Jubalo water bath and 10 min. equilibration time between each temperature. Samples for the *cis*-isomer measurements were irradiated with UV-light (λ_{ex} = 365 nm) for a minimum of 20 min. directly before each measurement. UV/Vis absorption spectra were recorded before and after to ensure there had been no substantial thermal relaxation back to the *trans*-isomer during the measurement. The scattering functions were fit using non-linear least-squares analysis to the Sphere, Cylinder, Flexible Cylinder and Lamellar Sheet models using the SasView programme.[11, 12] Full details of the mathematical models can be found in Chapter 3. The fits were checked to have absolute SANS intensities consistent with the known sample concentrations.

Cryo-scanning electron microscopy: Approximately 50 μL of *trans*-**C_4AzoOC_4E$_2$** (1 mM) was plunged into sub-cooled N_2 and transferred *in-vacuo* to the cold-stage of the SEM cryo-preparation chamber.

8.2.4 Synthesis and Characterisation of Photosurfactants

8.2.4.1 Synthesis of the Bromide Precursor

The same bromide precursor, bromobutoxyphenyl-2-4-butylphenyldiazene (**C_4AzoOC_4Br**), was used for the synthesis of all photosurfactants. It was prepared using a slightly modified version of the previously synthesis by Tabor *et al.*[13] The synthesis of the first precursor, 4-butyl-4-hydroxy azobenzene (**C_4AzoOH**), involved an azocoupling reaction as shown in Scheme 8.2. The synthesis of the second precursor, 1-(4-(4-bromobutoxy)phenyl)-2-(4-butylphenyl)diazene (**C_4AzoOC_4Br**), involved a bimolecular nucleophilic substitution (S_N2) reaction with 1,4-dibromobutane, as shown in Scheme 8.3. All intermediates and the final products were characterised by ^{1}H NMR, ^{13}C NMR, ESI-MS, m.p. analysis and IR spectroscopy and compared to the literature data. The fully assigned ^{1}H and ^{13}C NMR spectra of the final products are shown in the Appendix (Figures A.8.1 – A.8.3). Spectroscopic and analytical data are summarised below.



Scheme 8.2 Synthetic route to the hydroxyl-azobenzene precursor **C_4AzoOH**.

Synthesis of (*E*)-4-((4-butylphenyl)diazenyl)phenol (C$_4$AzoOH): In a round-bottomed flask (250 mL), 4-butylaniline (6.0 g, 40 mmol) was dissolved in a 1:1 (*v*/*v*) acetone/H_2O mixture (100 mL) with HCl (37% conc., 10 mL)) and stirred for 20 min. in an ice bath. Separately, $NaNO_2$ (3.8 g, 40 mmol) was dissolved in distilled H_2O (50 mL) and cooled to 1-3 °C. To the cooled (*ca.* 2 °C) 4-butylaniline solution, the $NaNO_2$ solution was added slowly, and left for 20 min. to stir in an ice bath to produce the diazonium salt. Additionally, phenol (3.8 g, 40 mmol), NaOH (1.6 g, 40 mmol) and Na_2CO_3 (7.0 g, 40 mmol) were dissolved in distilled H_2O (100 mL), stirred for 5 min. and cooled to 1-3 °C. To this solution, the resultant diazonium salt was added dropwise and the temperature was maintained below 8 °C. The resulting yellow/brown precipitate was left to cool to room temperature, filtered and washed with minimum amounts of cold acetone. The product was recrystallised from chloroform to give 9.5 g (37.4 mmol) of yellow crystals of **C_4AzoOH** in a 93.4% yield.

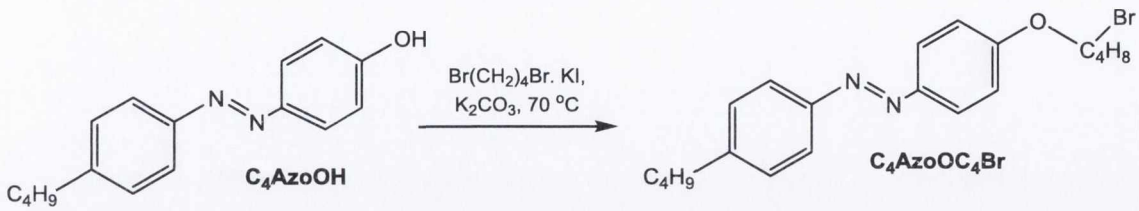
^{1}H NMR ($CDCl_3$, 400 MHz, 25 °C): δ = 0.93 (t, J = 8.0 Hz, 3H, CH_3); 1.30-1.43 (m, 2H, CH_2); 1.57-1.68 (m, 2H, CH_2); 2.71 (t, J = 8.0 Hz , 2H, CH_2); 5.17 (s, 1H, OH), 6.96 (d, J = 10.9 Hz, 2H, 2×CH); 7.32 (t, J = 10.9 Hz, 2H, 2×CH); 7.81 (d, J = 8.1 Hz, 2H, 2×CH); 7.88 (d, J = 8.1 Hz, 2H, 2×CH) ppm.

^{13}C NMR ($CDCl_3$, 100 MHz, 25 °C): δ = 13.98 (alkyl), 22.37 (alkyl), 33.51 (alkyl), 35.58 (alkyl), 114.69 (sp^2 Azo), 122.55 (sp^2 Azo), 124.67 (sp^2 Azo), 129.09 (sp^2 Azo), 145.89 (quart. Azo), 147.00 (quart. Azo), 150.94 (quart. Azo), 161.29 (quart. Azo) ppm.

ESI-MS (MeOH, *m/z*-ESI-): Found: 255.1485 $[M+H]^-$. Calculated: 255.1453 $[M+H]^-$.

FTIR ν_{max}: 3553 (s), 3180 (b), 2922 (b), 1748 (m), 1591 (m) cm^{-1}.

M.p.: 102-115 °C



Scheme 8.3 Synthetic route to the azobenzene bromide precursor **C_4AzoOC_4Br**.

Synthesis of 1-(4-(4-bromobutoxy)phenyl)-2-(4-butylphenyl)diazene (C_4AzoOC_4Br): In a round bottomed flask (50 mL), **C_4AzoOH** (4.0 g, 14 mmol) was dissolved in acetone (160 mL). To this solution, 1,4-dibromobutane (18 g, 9.8 mL, 69 mmol), anhydrous potassium carbonate (excess – 6.7 g, 47 mmol) and a catalytic amount of potassium iodide (2.0 g, 13.5 mmol) were added. The reaction mixture was refluxed at 65 °C and stirred for 20 h. The yellow/red solution was allowed to cool to RT, the excess salt was removed *via* filtration and the solvent removed under reduced pressure. The solid was dissolved in hexane (~30 mL) and washed with water until the washings became clear. The hexane was removed by rotary evaporation. The excess of 1,4-dibromobutane was removed using a silica plug and washed several times with cyclohexane. The product was collected with dichloromethane (DCM) and dried under vacuum. The product was recrystallised from ethanol to give yellow crystals (5.2 g, 13.4 mmol) of **C_4AzoOC_4Br** in a 96% yield.

^{1}H NMR (DMSO, 400 MHz, 25 °C): δ = 0.92 (t, J = 7.3 Hz, 3H, CH_3); 1.33-1.42 (m, 2H, CH_2); 1.60-1.67 (m, 2H, CH_2); 1.84-1.94 (m, 2H, CH_2) ; 1.96-2.05 (m, 2H, CH_2); 2.67 (t, J = 7.8 Hz, 2H, CH_2); 3.64 (t, 2H, J = 6.6 Hz, CH_2); 4.13 (t, 2H, J = 6.2 Hz, CH_2); 7.13 (d, 2H, J = 8.9 Hz, 2×CH); 7.39 (d, 2H, J = 8.3 Hz, 2×CH); 7.77 (d, 2H, J = 8.3 Hz, 2×CH); 7.87 (d, 2H, J = 9.0 Hz, 2×CH) ppm.

^{13}C NMR (DMSO, 100 MHz, 25 °C): δ = 14.24 (alkyl), 19.03 (alkyl), 22.22 (alkyl), 27.78 (alkyl). 33.39 (alkyl), 35.11 (alkyl), 56.49 (alkyl), 67.59 (alkyl), 115.50 (sp^2 Azo), 122.74 (sp^2 Azo), 124.86 (sp^2 Azo), 129.68 (sp^2 Azo), 146.17 (quart. Azo), 146.62 (quart. Azo), 150.74 (quart. Azo), 161.59 (quart. Azo) ppm.

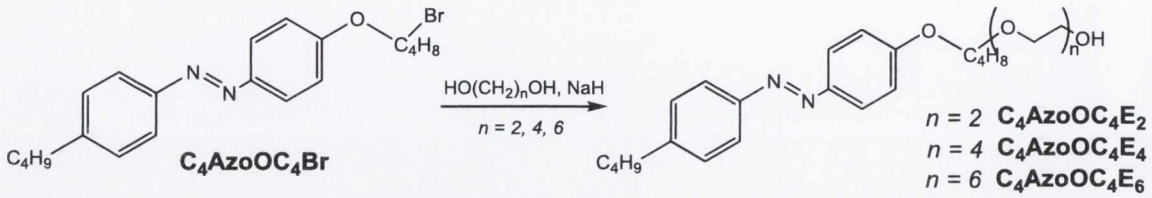
ESI-MS ($CHCl_3$, *m/z*-ESI+): Found: 389.1225 $[M+H]^+$. Calculated: 389.1223 $[M+H]^+$.

FTIR ν_{max}: 3462 (w), 2965 (br), 1765 (m), 1375 (m), 1208 (m) cm^{-1}.

M.p.: 62-64 °C.

8.2.4.2 General Procedure for the Synthesis of Neutral Photosurfactants

The same final general procedure was used to prepare all three neutral surfactants as shown in Scheme 8.4.



Scheme 8.4 Synthetic route to the neutral photosurfactants, **$C_4AzoOC_4E_2$**, **$C_4AzoOC_4E_4$** and **$C_4AzoOC_4E_6$**.

The corresponding ethylene glycol (~5 mL) was dried azeotropically by distillation with toluene (20 mL) at 170 °C. Sodium hydride (NaH, 60% in mineral oil) (1 molar equivalents (eq.)) was reacted with dry ethylene glycol (4 eq.) in dry tetrahydrofuran (THF) at room temperature for 2 h under N_2 protection. Upon addition of the NaH, the solutions immediately bubbled and became foamy. **C_4AzoOC_4Br** (0.1 eq.) was dissolved in dry THF and added dropwise to the reaction mixture, which turned yellow. The mixture was refluxed at 75 °C under N_2 for at least 48 h and monitored *via* thin layer chromatography (TLC) using ethyl acetate as the mobile phase. Ethylene glycol and product spots were developed on the TLC plate using potassium permanganate. Upon reaction completion, the solvent was removed by rotary evaporation. The dark red oil obtained was dissolved in dichloromethane and washed with water. The DCM layer was then dried with $MgSO_4$, filtered and the solvent removed by rotary evaporation. In some cases, unreacted **C_4AzoOC_4Br** was removed using a silica plug and washed several times with chloroform. The final products were washed thoroughly with methanol and the solvent was removed by rotary evaporation. The structures of the photosurfactants **$C_4AzoOC_4E_2$**, **$C_4AzoOC_4E_4$** and **$C_4AzoOC_4E_6$** were confirmed by ^{1}H NMR, ^{13}C NMR, ESI-MS and IR spectroscopy. The data for the known surfactant, **$C_4AzoOC_4E_2$**, was compared to the literature data.[3] Spectroscopic and analytical data are summarised below.

(E)-2-(2-(4-(4-((4-butylphenyl)diazenyl)phenoxy)butoxy)ethoxy)ethanol (**$C_4AzoOC_4E_2$**):[3]
Red oil (370 mg, 0.89 mmol) in a 35% yield.
^{1}H NMR ($CDCl_3$, 400 MHz, 25 °C): δ = 0.93 (t, 3H, J = 7.4 Hz, CH_3), 1.32-1.42 (m, 2H, J = 7.4 Hz CH_2), 1.59-1.67 (m, 2H, CH_2), 1.75-1.85 (m, 4H, 2×CH_2), 1.86-1.95 (m, 2H, J = 6.8 Hz, CH_2), 2.67 (t, 2H, J = 7.9 Hz, CH_2), 3.56 (t, 2H, J = 6.3 Hz, CH_2), 3.59-3.76 (m, 9H, 4×CH_2), 4.07 (t, 3H, J = 6.3 Hz, CH_3), 6.99 (d, 2H, J = 9.0 Hz, 2×CH), 7.29 (d, 2H, J = 8.3 Hz, 2×CH), 7.83 (d, 2H, J = 8.3 Hz, 2×CH), 7.93 (d, 2H, J = 9.3 Hz, 2×CH) ppm.
^{13}C NMR ($CDCl_3$, 100 MHz, 25 °C): δ = 14.07 (alkyl), 22.46 (alkyl), 33.57 (alkyl), 35.69 (alkyl), 61.96 (alkyl linker), 68.14 (alkyl linker), 71.09 (alkyl linker), 72.63 (alkyl linker), 70.41 (glycol

chain), 70.63 (glycol chain), 114.90 (sp^2 Azo), 122.69 (sp^2 Azo), 125.19 (sp^2 Azo), 129.24 (sp^2 Azo), 146.04 (quart. Azo), 146.66 (quart. Azo), 156.46 (quart. Azo), 161.62 (quart. Azo) ppm.

ESI-MS (MeOH, *m/z*-ESI+): Found: 437.2416 $[M+Na]^+$. Calculated: 437.2416 $[M+Na]^+$; Found: 415.2599 $[M+H]^+$. Calculated: 415.2597 $[M+H]^+$; Found: 452.2165 $[M+K]^+$. Calculated: 452.2156 $[M+K]^+$.

FTIR ν_{max}: 3462 (br), 2941 (s), 2867 (s), 1734 (s), 1599 (m), 1513 (m), 1376 (m), 1263 (s), 1094 (m), 835 (m) cm^{-1}.

(E)-16-(4-((4-butylphenyl)diazenyl)phenoxy)-3,6,9,12-tetraoxahexadecan-1-ol (**$C_4AzoOC_4E_4$**): Red oil (300 mg, 0.6 mmol) in a 23.0% yield.

^1H NMR ($CDCl_3$, 400 MHz, 25 °C): δ = 0.94 (t, 3H, J = 7.4 Hz, CH_3), 1.32-1.43 (m, 2H, J = 7.7 Hz, CH_2), 1.59-1.68 (m, 2H, CH_2), 1.75-1.84 (m, 4H, 2×CH_2), 1.86-1.95 (m, 2H, J = 6.8 Hz, CH_2), 2.68 (t, 2H, J = 7.9 Hz, CH_2), 3.56 (t, 2H, J = 6.7 Hz, CH_2), 3.58-3.75 (m, 16H, 2×4CH_2), 4.08 (t, 3H, J = 6.3 Hz, CH_3), 7.00 (d, 2H, J = 9.0 Hz, 2×Ar CH), 7.30 (d, 2H, J = 8.3 Hz, 2×CH), 7.83 (d, 2H, J = 8.3 Hz, 2×CH), 7.94 (d, 2H, J = 9.3 Hz, 2×CH).

^{13}C NMR ($CDCl_3$, 100 MHz, 25 °C): δ = 13.97 (alkyl), 22.36 (alkyl), 26.01 (alkyl), 26.11 (alkyl), 33.48 (alkyl), 35.59 (alkyl), 61.72 (alkyl linker), 68.08 (alkyl linker), 70.14 (glycol chain), 70.22 (glycol chain), 70.53-70.61 (glycol chain), 70.95 (glycol chain), 72.66 (glycol chain), 114.81 (sp^2 Azo), 122.58 (sp^2 Azo), 125.03 (sp^2 Azo), 129.13 (sp^2 Azo), 146.07 (quart. Azo), 146.51 (quart. Azo), 150.42 (quart. Azo), 161.78 (quart. Azo) ppm.

FTIR ν_{max}: 3457 (br), 2931 (s), 2861 (s), 1740 (s), 1603 (m), 1510 (m), 1364 (m), 1263 (m), 1115 (br), 831 (m) cm^{-1}.

ESI-MS (MeOH, *m/z*-ESI+): Found: 501.2959 $(M^+ -H)^+$. Calculated: 501.2965 $(M^+ -H)^+$; Found: 503.3128 $(M^+ +H)^+$. Calculated: 503.3121 $(M^+ +H)^+$; Found: 525.2930 $(M^+ +Na)^+$. Calculated: 525.2941 $(M^+ +Na)^+$.

(E)-22-(4-((4-butylphenyl)diazenyl)phenoxy)-3,6,9,12,15,18-hexaoxadocosan-1-ol (**$C_4AzoOC_4E_6$**): Orange oil (350 mg, 0.59 mmol) in a 37.0% yield.

^1H NMR ($CDCl_3$, 400 MHz, 25 °C): δ = 0.97 (t, 3H, J = 7.5 Hz, CH_3), 1.34-1.46 (m, 2H, CH_2), 1.62-1.72 (m, 2H, CH_2), 1.78-2.87 (m, 4H, 2×CH_2), 2.71 (t, 2H, J = 7.5 Hz, CH_2), 3.55-3.80 (m, 19H, 9×CH_2 and OH), 4.10 (t, 3H, J = 6.0 Hz, CH_2), 7.02 (d, 2H, J = 9.0 Hz, 2×CH), 7.33 (d, 2H, J = 9.0 Hz, 2×Ar CH), 7.84 (d, 2H, J = 6.0 Hz, 2×CH), 7.94 (d, 2H, J = 9.0 Hz, 2×CH).

^{13}C NMR ($CDCl_3$, 100 MHz, 25 °C): δ = 13.98 (alkyl), 22.35 (alkyl), 33.49 (alkyl), 35.56 (alkyl), 61.76 (alkyl linker), 68.06 (alkyl linker), 70.16 (alkyl linker), 72.68 (alkyl linker), 70.60 (glycol chain), 114.67 (sp^2 Azo), 122.51 (sp^2 Azo), 124.57 (sp^2 Azo), 129.06 (sp^2 Azo), 145.78 (quart. Azo), 147.00 (quart. Azo), 151.02 (quart. Azo), 161.36 (quart. Azo) ppm.

ESI-MS (MeOH, *m/z*-ESI+): Found: 589.3486 $[M-H]^+$. Calculated: 589.3489 $[M-H]^+$; Found: 591.3656 $[M+H]^+$. Calculated: 591.3645 $[M+H]^+$; Found: 613.3466 $[M+Na]^+$. Calculated: 613.3465 $[M+Na]^+$.

8.3 Results and Discussion

8.3.1 Observation of Photoisomerisation by UV/Vis Absorption Spectroscopy

Figure 8.2a shows the UV/Vis absorption spectra for the *trans*- and *cis*-isomers of **$C_4AzoOC_4E_6$** in H_2O at 20 °C. Similar optical properties were observed for the other surfactants (shown in the Appendix, Figure A.8.4) and the optical properties for all three PS are summarised in Table 8.2. The photograph in Figure 8.2b highlights the significant change in colour from yellow to orange induced by the *trans*-to-*cis* isomerisation.

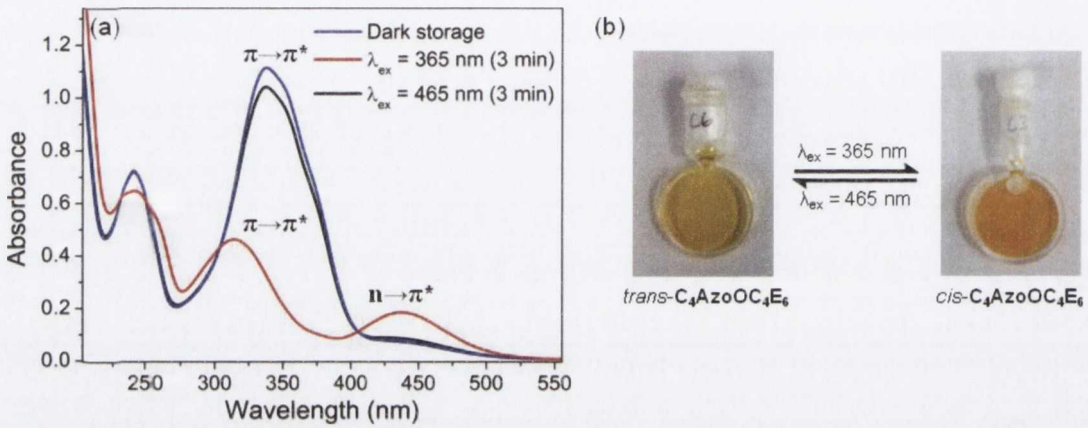


Figure 8.2 (a) UV/Vis absorption spectra of **$C_4AzoOC_4E_6$** in water (3.4×10^{-5} M) at 20 °C. The spectra correspond to the *trans*-form (stored in the dark, blue line), the photostationary state (after irradiation at λ_{ex} = 365 nm for 3 min., red line) and the reverse *cis*- to *trans*-isomerisation (after irradiation at λ_{ex} = 465 nm for 3 min., black line). (b) Photographs of a concentrated solution of **$C_4AzoOC_4E_6$** in water (2.0×10^{-2} M) before and after irradiation with UV light.

Table 8.2 UV/Vis absorption properties of the photosurfactants **$C_4AzoOC_4E_2$** (9.7×10^{-5} M), **$C_4AzoOC_4E_4$** (8.0×10^{-5} M) and **$C_4AzoOC_4E_6$** (3.4×10^{-5} M) at 20 °C. ε_{trans} is molar absorption coefficient for the *trans*-isomer, λ_{abs} is the absorbance maximum, $ID_{trans\text{-}cis}$ and $ID_{cis\text{-}trans}$ are the isomerisation degrees for the *trans-cis* and *cis-trans* processes, respectively, and k_{cis} and k_{trans} are the rate constants for *trans-cis* and *cis-trans* processes, respectively.

	ε_{trans} at 360 nm (M^{-1} cm^{-1})	*Trans*-λ_{abs} (nm)	*Cis*-λ_{abs} (nm)	$ID_{trans\text{-}cis}$ (%)	$ID_{cis\text{-}trans}$ (%)	k_{cis} [a] (s^{-1})	k_{trans} [a] (s^{-1})
$C_4AzoOC_4E_2$	10,714	324	313, 437	67.7	96.8	0.0035	0.0256
$C_4AzoOC_4E_4$	15,800	334	317, 438	85.1	87.4	0.0111	0.0514
$C_4AzoOC_4E_6$	14,806	337	314, 436	84.5	92.0	0.0152	0.0622

[a] The power outputs of the UV and blue LEDs were ~2.6 and 2.4 mW cm^{-2}, respectively, at a distance of 4.5 cm.

When stored in the dark, azobenzene-photosurfactants exist in the *trans*-form, which is thermodynamically more stable than the *cis*-form (>50 kJ mol^{-1}).[14] The *trans*-form of **$C_4AzoOC_4E_6$** exhibits a maximum absorbance at λ_{abs} = 337 nm (blue line, Figure 8.2a), which corresponds to the $\pi \rightarrow \pi^*$ transition.[2] The absorption maximum of the *trans*-isomer shifts to longer wavelengths with an increase in the length of the glycol head-group. This is consistent with the general observation

that the $\pi \rightarrow \pi^*$ transition of azobenzenes is sensitive to the nature of their substituents.[2] Electron donating groups (EDG) are known to cause the $\pi - \pi^*$ transition to shift to higher wavelengths because the EDG donates electron density to the molecule which leads to a less stable state. This causes the S_0-S_1 energy gap to become smaller as the size of the EDG (*i.e.* the ethylene glycol head-group) is increased, thus, causing the observed red-shift.[2] Upon irradiation with UV-light (λ_{ex} = 365 nm) for 3 min., the *trans*-absorption band decreases significantly and two new bands appear, which are both assigned to the *cis*-form (red line, Figure 8.2a) at λ_{abs} = 314 nm ($\pi \rightarrow \pi^*$ transition) and λ_{abs} = 436 nm ($n \rightarrow \pi^*$ transition) for **C_4AzoOC$_4$E$_6$**.[15] No further changes in the absorption spectra were observed at longer illumination times (up to 40 min.). However, it is important to note that the complete conversion to the *cis*-form cannot be obtained experimentally. An equilibrium known as the photostationary state (PSS) is obtained, which is comprised of a mixed population of *trans*- and *cis*-isomers.[8] Consequently, the *cis*-absorption spectrum contains a contribution from the *trans*-form. The *trans*-to-*cis* ratio in the PSS at λ_{abs} = 365 nm can be estimated by calculating the isomerisation degree (*ID*) from UV/Vis absorption spectroscopy using:[8]

$$ID = \frac{A_0(365) - A_i(365)}{A_0(365)} \times 100\% \qquad (8.1)$$

where $A_0(365)$ is the absorbance at λ_{abs} = 365 nm before UV-light irradiation and $A_i(365)$ is the absorbance at the same wavelength measured at the PSS after irraditation.[16] **C_4AzoOC$_4$E$_4$** and **C_4AzoOC$_4$E$_6$** gave *ID* of 85.1% and 84.5%, respectively, which correspond well to the literature values for similar non-ionic photosurfactants (86-89%).[8] Interestingly, the *ID* for **C_4AzoOC$_4$E$_2$** is slightly lower than expected at ~68%.

The reverse *cis*-to-*trans* isomerisation process was investigated by irradiation with blue light (λ_{ex} = 465 nm) for 3 min. (Figure 8.2a, black line). For all three PS, incomplete recovery of the *trans*-form was observed. The absorbances of each PS at λ_{abs} = 365 nm were found to only recover to 87-97% of their original values. This suggests the formation of a second PSS, where the *trans*-form is now the major isomer. However, these values remain quite high in comparison to other PSS, such as 4-alkylazobenzene-4'-(oxy-2-hydroxypropyl)-trimethylammoniummethylsulfate (AZMS) which had a *trans*-recovery of 70-80% upon irradiation with blue-light (λ_{ex} = 465 nm).[17]

8.3.2 Kinetics Study of Photo- and Thermal-Isomerisation Processes

The rates of the forward and reverse photoisomerisation processes were also investigated. The photosurfactants in their *trans*-form were illuminated with UV-light (λ_{ex} = 365 nm) and the absorption spectra were simultaneously recorded every 30 s for a total duration of 6 min. The resulting spectra of the *trans-cis* photoconversion are shown in Figure 8.3a for **C_4AzoOC$_4$E$_4$**. A rapid *trans-cis* isomerisation is observed within the first 100 s. Further illumination increased the concentration of the *cis*-form until the photostationary state is reached (at ~3 min.), thereafter, conversion remained constant. To induce the reverse *cis*-to-*trans* process, the photosurfactants in

the *cis*-form were illuminated with blue-light (λ_{ex} = 465 nm) and the absorption spectra were simultaneously recorded every 5 s over a total duration of 1 min. (Figure 8.3b for **C_4AzoOC_4E$_4$**).

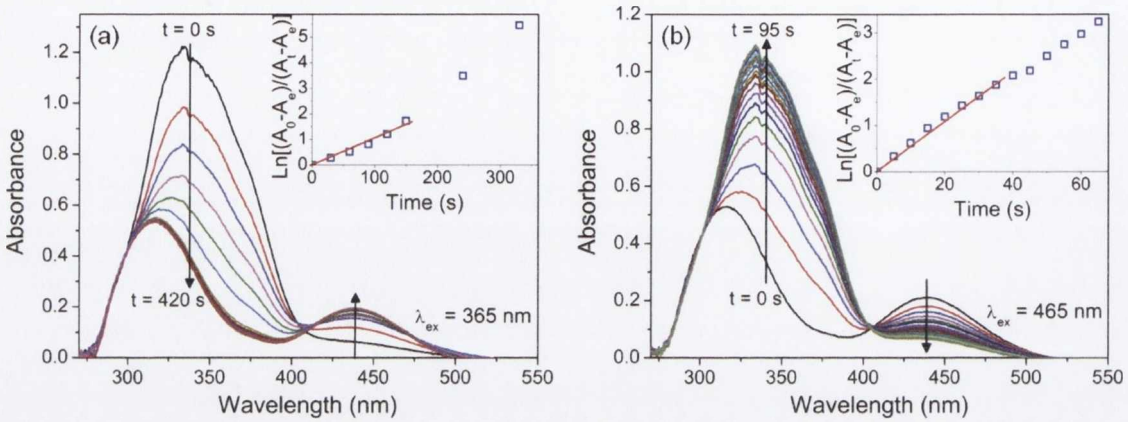


Figure 8.3 UV/Vis absorption spectra of **C_4AzoOC_4E$_4$** in water (8.0×10^{-5} M), at 20 °C as a function of time under (a) UV-light irradiation (λ_{ex} = 365 nm) and (b) blue light irradiation (λ_{ex} = 465 nm). The insets show the first order rate laws for the forward (*trans-cis*) and reverse (*cis-trans*) isomerisation, respectively. The corresponding rate constants, k_{cis}, and k_{trans}, were obtained as described in the text.

The *trans*-to-*cis* (and *cis*-to-*trans*) photoisomerisation obey first-order kinetics, whose rate constant is given by:[18]

$$k_{cis}t = \left[\frac{A_0(365) - A_\infty(365)}{A_t(365) - A_\infty(365)}\right] \tag{8.2}$$

where k_{cis} is the rate constant describing the *trans-cis* isomerisation, $A_0(365)$ is the absorption at λ_{abs} = 365 nm of the *trans*-isomer before UV irradiation, $A_\infty(365)$ is the absorbance at the photostationary state and $A_t(365)$ is the absorbance at time, t. Equation 8.2 can be used to yield k_{cis} for the isomerisation of the PS, as shown in the insets of Figure 8.3a for **C_4AzoOC_4E$_4$**. The reverse *cis*-to-*trans* isomerisation is described by the rate constant, k_{trans}, and can be determined experimentally by following the growth of the *trans*-isomer at λ_{abs} = 365 nm. The experimentally determined rate constants (k_{cis} and k_{trans}) obtained for the PS are listed in Table 8.2. Although the linear plot indicate first order kinetics, an in depth quantum yield study will be required to enable a definitive assignment.

The lifetime of photoconversion (τ) can be deduced from the rate constant (*i.e.* $\tau_{cis} = 1/k_{cis}$ and $\tau_{trans} = 1/k_{trans}$). The calculated values are, τ_{cis} = 285, 90 and 66 s and τ_{trans} = 39, 19 and 17 s for **C_4AzoOC_4E$_2$**, **C_4AzoOC_4E$_4$** and **C_4AzoOC_4E$_6$**, respectively. There is an obvious correlation between the length of the hydrophilic ethylene glycol head-group and the lifetime of photoconversion as both processes proceed the fastest for the longer **C_4AzoOC_4E$_6$**. Electron-donating groups, such as the oxyethylene units, result in a modest decrease in the energy barrier for isomerisation.[2] Thus, it is not surprising that the PS which the large EDG, **C_4AzoOC_4E$_6$** has the shortest lifetimes.

The reverse *cis*-to-*trans* process can also proceed thermally, which is why the *trans*-form will be recovered from a solution of *cis*-isomers after a couple of days of storage in the dark. To

quantify the thermal rate constant for *cis*-to-*trans* isomerisation, the UV/Vis absorption spectra of *cis*-**$C_4AzoOC_4E_6$** was measured as a function of time while being heated to 20 and 60 °C (shown in Appendix, Figure A.8.5). The calculated rate constants, k_{trans}^{T}, were 1.4×10^{-5} and 6.4×10^{-4} s^{-1} for 20 and 60 °C, respectively, both significantly lower than the rate of photoisomerisation (1.52×10^{-2} s^{-1}).

8.3.3 Critical Micelle Concentrations

The concentration at which surfactants form aggregates is a crucial parameter in the physical parameters of surfactants. The *cmc* represents the transition between unimers and micelles where the physicochemical properties (*i.e.* viscosity, surface tension, solubility) are changed. Surface tensiometry (ST) and DLS are two techniques that enable the *cmc* to be determined.

8.3.3.1 Dynamic light scattering

Dynamic light scattering measures the intensity of light scattered from a sample and can be used to determine the *cmc*. Below the *cmc*, unimers dispersed in solution are too small to be observed by DLS and so scatter very little light. As the concentration increases above the *cmc*, a rapid increase in the scattering intensity is observed, which indicates the formation of micelles. Figure 8.4 shows the intensity of scattering (kcounts) as a function of concentration for **$C_4AzoOC_4E_2$** before and after UV irradiation.

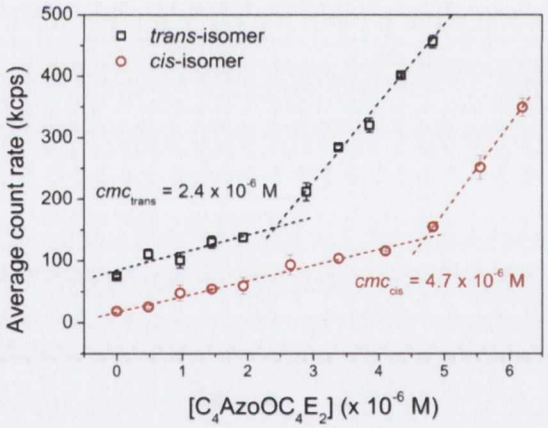


Figure 8.4 Effect of concentration on the intensity of scattered light of an aqueous solution of **$C_4AzoOC_4E_2$** in the *trans*- and *cis*-forms at 20 °C. The *cmc* values are obtained at the intersection between the two linear trend-lines. The error bars show the standard deviation of the mean average count rate obtained over 3 measurements.

In the *trans*-form, **$C_4AzoOC_4E_2$** exhibits a *cmc* of 2.4×10^{-6} M, is in reasonable agreement the value of 1.6×10^{-6} M reported by Hatton *et al.*[5] After illumination this value increases to 4.7×10^{-6} M. Similarly, the *cmc* values for **$C_4AzoOC_4E_4$** increased from 3.1×10^{-6} M to 3.4×10^{-6} M and **$C_4AzoOC_4E_6$** increased from 4.9×10^{-6} M to 5.4×10^{-6} M. In all three cases, the *cis*-forms exhibit a *cmc* greater than the *trans*-form. In addition, the values of *cmc* were found to increase with the length of the ethylene glycol head-groups. Therefore, these values are in good agreement with the fact that the *cis*-form and the surfactants with longer ethylene glycol head-groups are more

hydrophilic, which is expected to lead to higher solubility and therefore higher *cmc*s.[19] The plots for **$C_4AzoOC_4E_4$** and **$C_4AzoOC_4E_6$** are shown in Appendix Figure A.8.6 and the *cmc* values are summarised in Table 8.3.

Table 8.3 Critical micelle concentrations of the *trans*- and *cis*-isomers of the photosurfactants in water determined by DLS.

	***trans-cmc* (M)**	***cis-cmc* (M)**
$C_4AzoOC_4E_2$	2.4×10^{-6}	4.7×10^{-6}
$C_4AzoOC_4E_4$	3.1×10^{-6}	3.4×10^{-6}
$C_4AzoOC_4E_6$	4.9×10^{-6}	5.4×10^{-6}

8.3.3.2 Surface Tensiometry

Typically, critical micelle concentrations are determined by at least two methods as to ensure their validity.[20] Therefore, the surface tension (γ) of the PS in water at 20 °C were also investigated over a range of concentrations using pure water as the reference (γ_{water} = 72.80 mN m^{-1} at 20 °C).[21] Surface tension arises from the difference of interaction between the liquid-air medium.[21] At the liquid-air interface, the Gibb's absorption equation (Equation 8.3) relates the change of surface tension with concentration to the amount adsorbed at the interface:[22]

$$\Gamma_{ex} = \frac{-1}{R \cdot T} \cdot \left(\frac{d\,\gamma}{d\,ln\,c}\right) \tag{8.3}$$

where Γ_{ex} is the surface excess which represents the difference in concentration of a species adsorbed at an interface and the bulk. R is the gas constant, T is the temperature and c is the concentration of the surfactant. A surfactants possess the ability to lower the γ, as the concentration of the surfactant is increased, γ decreases linearly up to a critical concentration, beyond which it becomes constant. This means that the air-water interface has become saturated with surfactant. This saturation point represents the critical micelle concentration. After this point the γ becomes essentially constant and independent of concentration.[21]

Figure 8.5 shows the surface tension as a function of concentration for **$C_4AzoOC_4E_2$** in H_2O before and after UV irradiation. The *cmc* values are summarised in Table 8.4. Although these surface tension measurements support the values obtained from DLS, the data is preliminary and lack proper error bars, which could explain why some of the values are dramatically larger than those determined using DLS. Furthermore, previous surfactant typically level off above the cmc, which further suggests an issue with these measurements. Future work will involve repeating measurements, as well as *cmc* determination with an additional method, such as conductivity measurements[20] or the pyrene 1:3 ratio method[23].

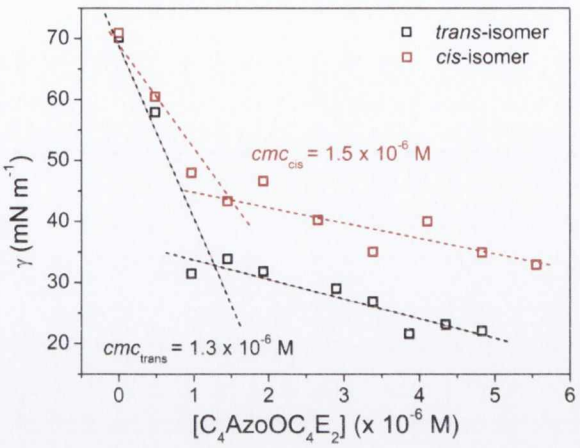


Figure 8.5 Effect of concentration on the surface tension of an aqueous solution of $\mathbf{C_4AzoOC_4E_2}$ in the *trans*- and *cis*-forms at 20 °C. The *cmc* values are obtained at the intersection between the two linear trend-lines.

Table 8.4 Critical micelle concentrations of the *trans*- and *cis*-isomers of the photosurfactants in water determined by surface tensiometry.

	trans-cmc (M)	*cis-cmc* (M)
$\mathbf{C_4AzoOC_4E_2}$	1.3×10^{-6}	1.5×10^{-6}
$\mathbf{C_4AzoOC_4E_4}$	2.6×10^{-6}	1.8×10^{-6}
$\mathbf{C_4AzoOC_4E_6}$	3.2×10^{-6}	25.0×10^{-6}

8.4 Micellar Solution-State Structures

8.4.1 Multi-Angle Light Scattering

MALS was used to determine the hydrodynamic radii (R_H) of the PS at concentrations slightly above their *cmc*. It is important to note, that these concentrations were still well below those required for the formation of LLC phases. Figure 8.6a shows the square of the correlation functions obtained for *trans*-$\mathbf{C_4AzoOC_4E_4}$ (2.0×10^{-4} M) over a range of angles (45-130°), given as a representative example. Equation 2.20 was then fit to the correlation function obtained at each angle (or q), C($q.t$), to yield the decay rate (Γ). A good fit to a mono-exponential decay, as shown in Figure 8.6b for the data obtained at 45°, suggests that the sample is monodisperse. Γ which is determined for each scattering angle was then plotted as a function of q^2. The slope of this plot yields the diffusion coefficient, D, which is related to Γ and q^2 by Equation 2.21. From D, R_H of the aggregate could be determined using the Stokes-Einstein equation (Equation 2.18). The plot of Γ *vs.* q^2 for *trans*-$\mathbf{C_4AzoOC_4E_4}$ is shown in Figure 8.6c and yielded an R_H of 55.3 (±2.5) nm.

Additionally, when R_H is greater than ~20 nm, the intensity of scattered light will vary as a function of angle (or q), which enabled R_g of the aggregate to also be determined (Equation 2.22). A plot of the natural logarithm of intensity of scattered light against q^2 yields a linear plot whose slope is equal to $-R_g^2/3$. The corresponding plot for *trans*-$\mathbf{C_4AzoOC_4E_4}$ is shown in Figures 8.6d and resulted in an R_g of 73.0 (±0.5) nm. The ratio of R_g to R_H has previously been used to yield

information about the aggregate shape.[24] Specifically, R_g/R_H values close to 0.8 indicate spherical aggregates, while the R_g/R_H value of 1.32 obtained for this system, suggests the formation of cylindrical rather than spherical aggregates. The calculated R_H and, where possible R_g and R_g/R_H values, for each of the PS in the *trans*- and *cis*-isomeric forms are summarised in Table 8.5.

Table 8.5 Hydrodynamic radii (R_H) and radii of gyration (R_g) for each of the photosurfactants in their *cis*- and *trans*-isomers.

Photosurfactant	Conc. (M)	Isomer	R_H (nm)	R_g (nm)	R_g/R_H
$C_4AzoOC_4E_2$	2.4×10^{-4}	*Trans*	124.9 ± 5.9	123.4	~1
		Cis	70.45 ± 3.0	86.8	1.23
$C_4AzoOC_4E_4$	2.0×10^{-4}	*Trans*	55.3 ± 2.5	73.0	1.32
		Cis	16.1 ± 0.6	-	-
$C_4AzoOC_4E_6$	1.7×10^{-4}	*Trans*	5.5 ± 1.2	-	-
		Cis	14.5 ± 0.2	-	-

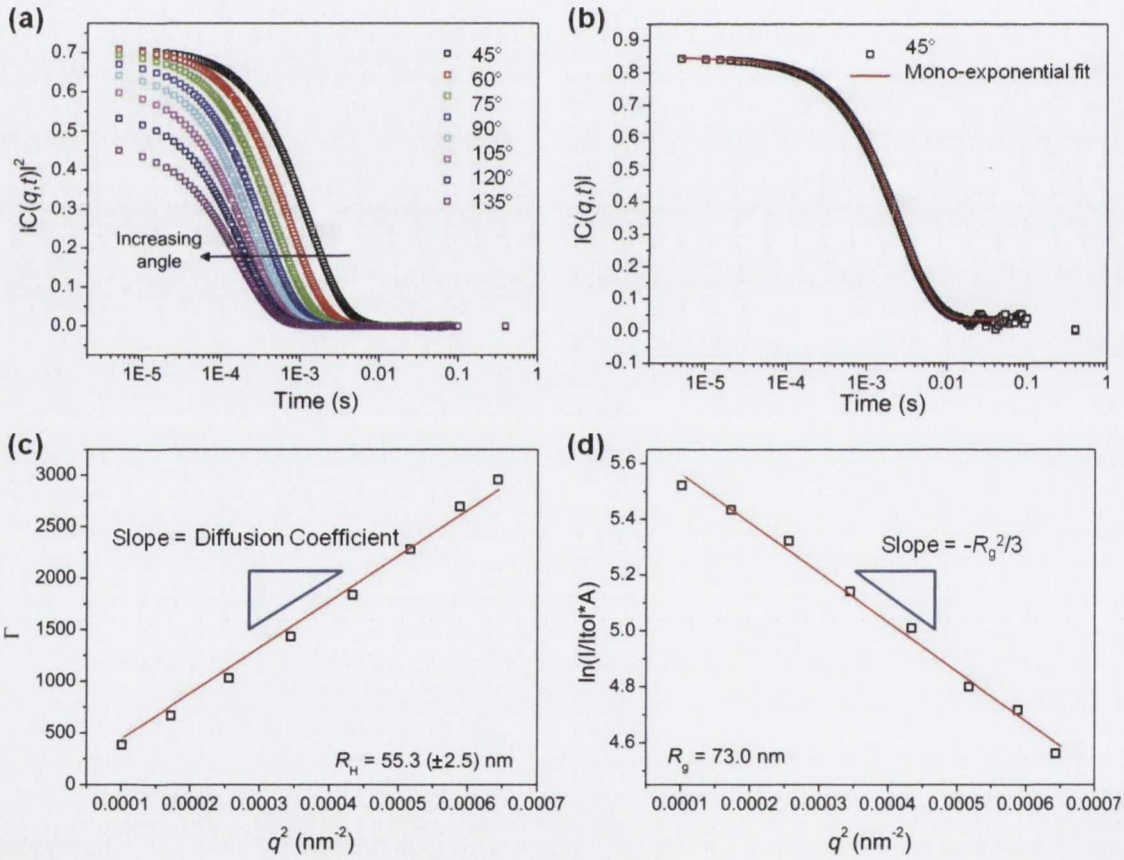


Figure 8.6 MALS data for the *trans*-**$C_4AzoOC_4E_4$** (2.0×10^{-4} M) in H_2O. (a) Correlation functions for *trans*-**$C_4AzoOC_4E_4$** (2.0×10^{-4} M) recorded over a range of angles at 25 °C. (b) Example of mono-exponential fit to the correlation function at 45°. (c) Gamma *vs.* wavevector plot for determining the hydrodynamic radius. (d) Scattering intensity *vs.* wavevector plot for determining the radius of gyration.

An increase in the size of the neutral head-group corresponds to a dramatic decrease in R_H in both the *trans*- and *cis*-isomeric forms. **$C_4AzoOC_4E_2$** and **$C_4AzoOC_4E_4$**, which formed

relatively large aggregates in the *trans*-form (R_H = 124.9 (±5.9) and R_H = 55.3 (±2.5) nm, respectively), underwent a significant decrease in size upon irradiation with UV-light. A similar decrease in size was previously observed for the cationic PS, AzoTMA, where photoisomerisation with UV-light induced the disassembly of the surfactant micelles.[4] This effect was attributed to less efficient packing of the "bent" *cis*-isomeric forms. Only the significantly smaller aggregates of *trans*-**C_4AzoOC$_4$E$_6$** (R_H = 5.5 (±1.2) nm) were found to increase in size upon photoisomerisation (R_H = 14.5 (±0.2) nm). Consequently, MALS clearly suggests that the size of the PS aggregates is dependent on both the size of the head-group and the isomeric form of the PS.

8.4.2 Small-Angle Neutron Scattering

8.4.2.1 Nanoscale Organisation and the Effect of Photoisomerisation

SANS was used to determine the nanoscale organisation of PS aggregates in D_2O. SANS is a useful method to deduce the shapes and dimensions of the individual micelles at low concentrations, as well as determining any interactions between the aggregates as the concentration is increased (*i.e.* the structure factor). Figure 8.7 shows the SANS data for the *trans*- and *cis*-isomers of each PS in D_2O, well-above their *cmc* (1 mM) at T = 20 °C. It is evident that there are significant differences in the scattering profiles for each surfactant and each isomeric form which suggests that their self-assembly processes are quite different. To confirm that there was no detrimental effect of neutron radiation on the isomeric form of the PS, UV/Vis absorption spectra were recorded before and after sample measurement. All the q-scaling and model fitting described below are summarised in Appendix Tables A.8.1-A.8.12.

Initially, SANS data were interpreted using scaling concepts. *Trans*-**C_4AzoOC$_4$E$_2$** in D_2O decays with q^{-2} at low q (q < 0.04 Å^{-1}) which suggests the formation of lamellar sheets (Figure 8.7a). A Lamellar Sheet Model[25, 26] fit to this is data to gives exceptionally dry sheets (6% D_2O) with a thickness (T_{sheet}) of 52.7 Å. Photoisomerisation to the *cis*-isomer resulted in a significant loss of the scattering intensity and a concominant change in the scattering profile to $q^{-3.9}$, which corresponds to the formation of smooth fractal aggregates.[27] Previously, *trans*-**C_4AzoOC$_4$E$_2$** was found to form bilayer vesicles at a similar concentration ([*trans*-**C_4AzoOC$_4$E$_2$**] = 0.7 mM) with a significantly larger T_{sheet} of 112 Å.[3] The structure changed to a bicontinuous phase following photoisomerisation to the *cis*-isomer.[3] This could potentially correspond to the smooth fractals that were identified in this study. It should be noted that the SANS data shown here and the SANS data shown in the study by Hatton *et al.* were performed at slightly different concentrations (1 *vs.* 0.7 mM, respectively) and over different q-ranges ($0.008 < q < 0.24$ Å^{-1} *vs.* $0.005 < q < 0.4$ Å^{-1}, respectively), may account for the difference in thicknesses and structure observed in the data analysis.

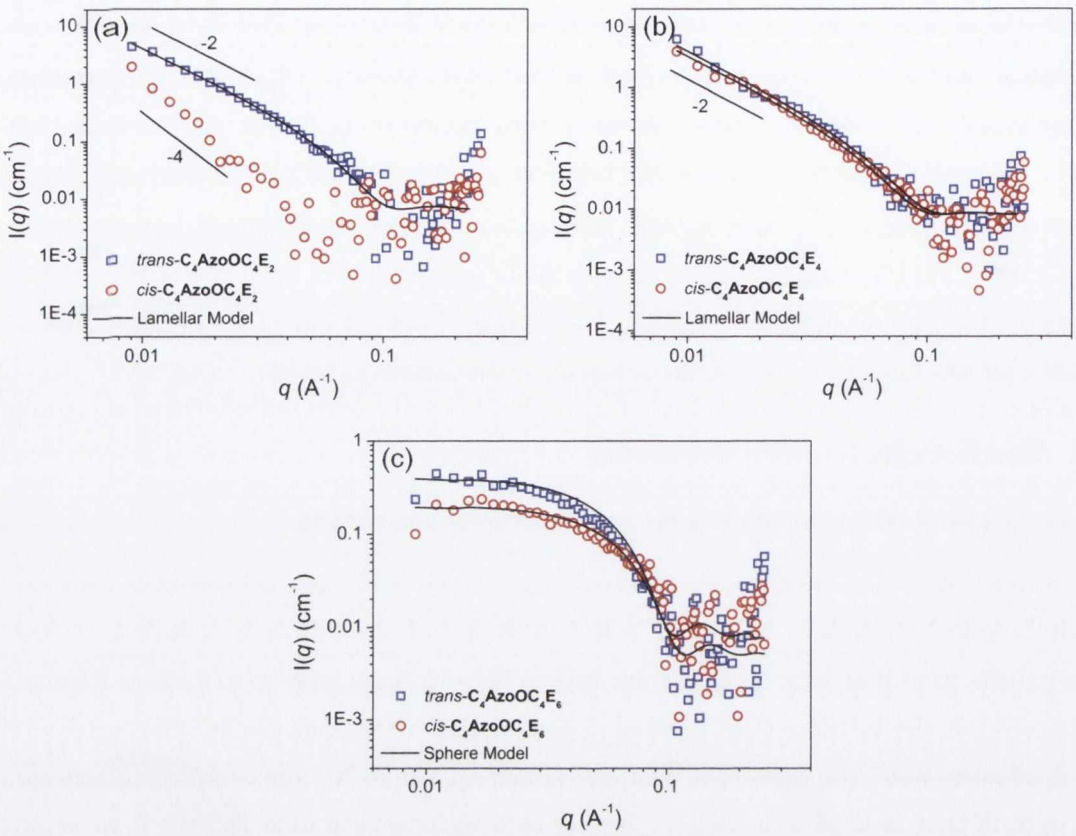


Figure 8.7 SANS data for the *trans*- and *cis*-isomers of (a) **C_4AzoOC$_4$E$_2$**, (b) **C_4AzoOC$_4$E$_4$** and (c) **C_4AzoOC$_4$E$_6$** in D_2O (1 mM) at T = 20 °C. Straight lines show -2 and -4 decays for comparison. Solid, dashed and dotted lines correspond to the fits to the models described in the text.

The SANS data of *trans*- and *cis*-**C_4AzoOC$_4$E$_4$** in D_2O show q-scalings at low q of $q^{-2.3}$ and $q^{-2.0}$, respectively, which again suggests the formation of lamellar sheets (Figure 8.7b). However, it should be noted that the SANS profiles in both these examples contained "bumps" at $q = \sim 0.02$ Å^{-1}. A similar effect was previously observed for **C_4AzoOC$_4$E$_2$** by Hatton *et al.*,[3] however, its precise origin was not assigned. This effect will be discussed in greater detail in Section 8.4.2.2. Nevertheless, fitting with the Lamellar Sheet Model[25, 26] yielded reasonable fits (Figure 8.7b) to the SANS data with a T_{sheet} of 53.4 and 55.5 Å and wetness of 50 and 34% for the *trans*- and *cis*-isomers, respectively.

In contrast, the scattering profiles for **C_4AzoOC$_4$E$_6$** are seen to plateau at low q (Figure 8.7c). The *trans*-data were best fit using the Sphere Model[28] which gave polydisperse aggregates with a radius (r) of 43.4 Å and wetness of 44%. Conversely, the *cis*-isomer was better fit using the Cylinder Model,[28, 29] which gave an r of 24.4 Å and a length (L) of 105.3 Å, without a significant change in the wetness of the aggregate being observed. These sizes correspond well to the radii of hydration measured using MALS, yielding 55 Å and 145 Å for *trans*- and *cis*-**C_4AzoOC$_4$E$_6$**, respectively.

8.4.2.2 Nanoscale Organisation and the Effect of Concentration

The "bumps" observed in the **$C_4AzoOC_4E_4$** samples at 1 mM (Figure 8.7b) could potentially be assigned to particle-particle interactions (*i.e.* the structure factor). To investigate this further, **$C_4AzoOC_4E_4$** was studied at significantly higher concentrations (20 and 200 mM) using SANS, as shown in Figure 8.8a. It was anticipated that any particle-particle interactions would be amplified in a more concentrated regime, thus, the contribution of the structure factor was also expected to increase. Therefore, it was promising that at higher concentrations of *trans*-**$C_4AzoOC_4E_4$**, there appears to be growth of a feature at $q = \sim 0.04$ Å^{-1}, particularly at a concentration of 200 mM. The growth of such features is typically attributed to interparticle interactions.[30] In both cases, the q-scaling resembles lamellar sheets ($q^{-2.1}$ and $q^{-1.7}$ for 20 and 200 mM, respectively). The 20 mM sample was fit with the Lamellar Sheet Model[25, 26] and gave slight thinner (T_{sheet} ~48.5 Å) and drier (36% D_2O) sheets than the 1 mM sample. It was not possible to fit the 200 mM sample using just the Lamellar Sheet Model[25, 26] due to a large contribution of the structure factor to the scattering profile. *Cis*-**$C_4AzoOC_4E_4$** also displayed a greater contribution of structure factor at a higher concentration ([*cis*-**$C_4AzoOC_4E_4$**] = 20 mM), as shown in Figure 8.8b. This feature is more pronounced for the *cis*-isomer than the *trans*-isomer. Therefore, although the scaling at low q once again indicated lamellar sheets ($q^{-1.9}$), model fitting could not be achieved at this time. Future work is required to determine appropriate methods and models to properly fit systems that display a lamellar form factor in combination with structure factor.

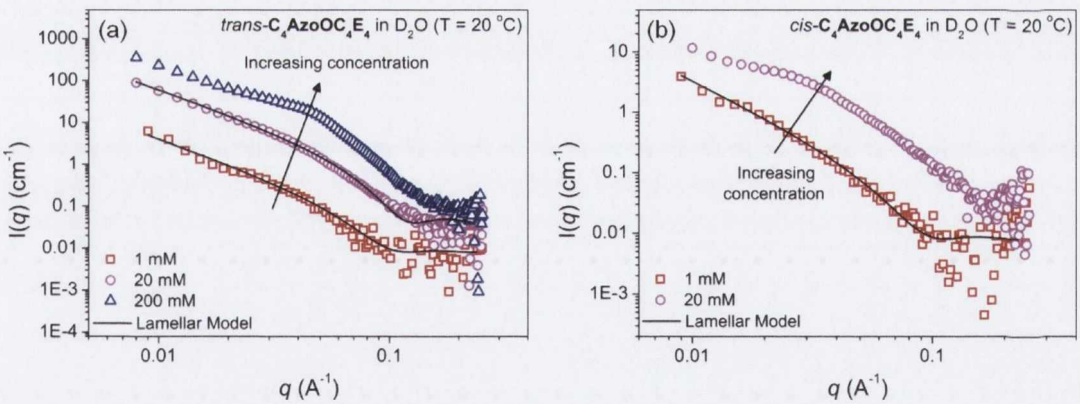


Figure 8.8 SANS data for (a) *trans*- and (b) *cis*-**$C_4AzoOC_4E_4$** in D_2O as function of concentration at T = 20 °C. The solid lines correspond to the fits to the models described in the text.

MALS studies for **$C_4AzoOC_4E_6$** suggested the formation of structures whose sizes (R_H = 5-15 nm) were within the observation window of these SANS experiments (2.6 – 70 nm), as highlighted by the appearance of a Guinier plateau in Figure 8.7c for the 1 mM samples. Therefore, SANS measurements are ideally suited to reveal any change in the overall aggregate shape and nanoscale morphology as a function of concentration (Figure 8.9). However, only slight changes were observed for *trans*-**$C_4AzoOC_4E_6$** in D_2O upon increasing the concentration from 1 to 200 mM (Figure 8.8a). For example, from 1 to 5 mM, there is a very subtle transformation from spherical to cylindrical aggregates (r = 32.1 Å, L = 120.6 Å, and wetness = 46%). These cylinders increased in both length and wetness up to 20 mM (r = 31.9 Å, L = 153.0 Å, and wetness = 57%). While at 40 mM, there was a reverse in trend as the cylinders appear to decrease in length (r = 31.9 Å, L = 127.5 Å, wetness = 33%). Finally, upon increasing the concentration further to 200 mM, the data is once again better fit by a Sphere Model, which resulted in wet, aggregates with a radius of 37.6 Å. It is worth noting that even at this high concentration regime, there appears to be no contribution of the interparticle structure which was observed for *trans*-**$C_4AzoOC_4E_4$**. This effect will be discussed in greater detail in Section 8.4.4.

Photoisomerisation to *cis*-**$C_4AzoOC_4E_6$** in D_2O resulted in the formation of longer cylindrical aggregates for concentrations between 5-200 mM (Figure 8.9b), in comparison to *trans*-**$C_4AzoOC_4E_6$**. The cylinder radius for all the concentrations investigated remained constant at ~25 Å, the wetness remained constant at ~50%, yet the length of the cylinder decreased progressively from 241.1 Å at 5 mM to 78.7 Å at 200 mM.

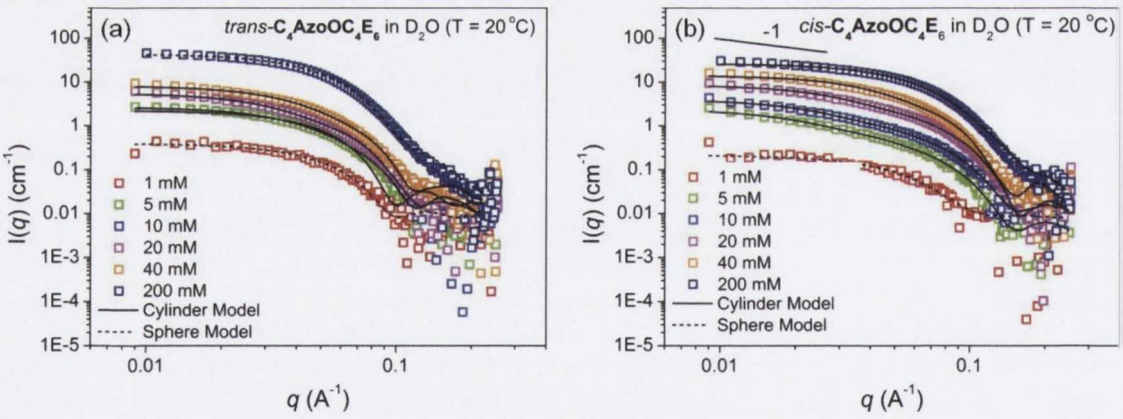


Figure 8.9 SANS data for (a) *trans*- and (b) *cis*-**$C_4AzoOC_4E_6$** in D_2O as function of concentration at T = 20 °C. The straight line shows a -1 decay for comparison. The solid and dotted lines correspond to the fits to the models described in the text.

8.4.2.3 Nanoscale Organisation and the Effect of Temperature

Temperature also plays a key role in controlling the structure and size of surfactant aggregates and will be particularly important later in the chapter when LLC phase formation is discussed. Thus, the SANS data for PS aggregates were also measured at one concentration (1 mM) as a function of temperature (20, 40, 60 and 80 °C), as shown in Figure 8.10 for the *trans*-isomers and Appendix Figure A.8.7 for the *cis*-isomers.

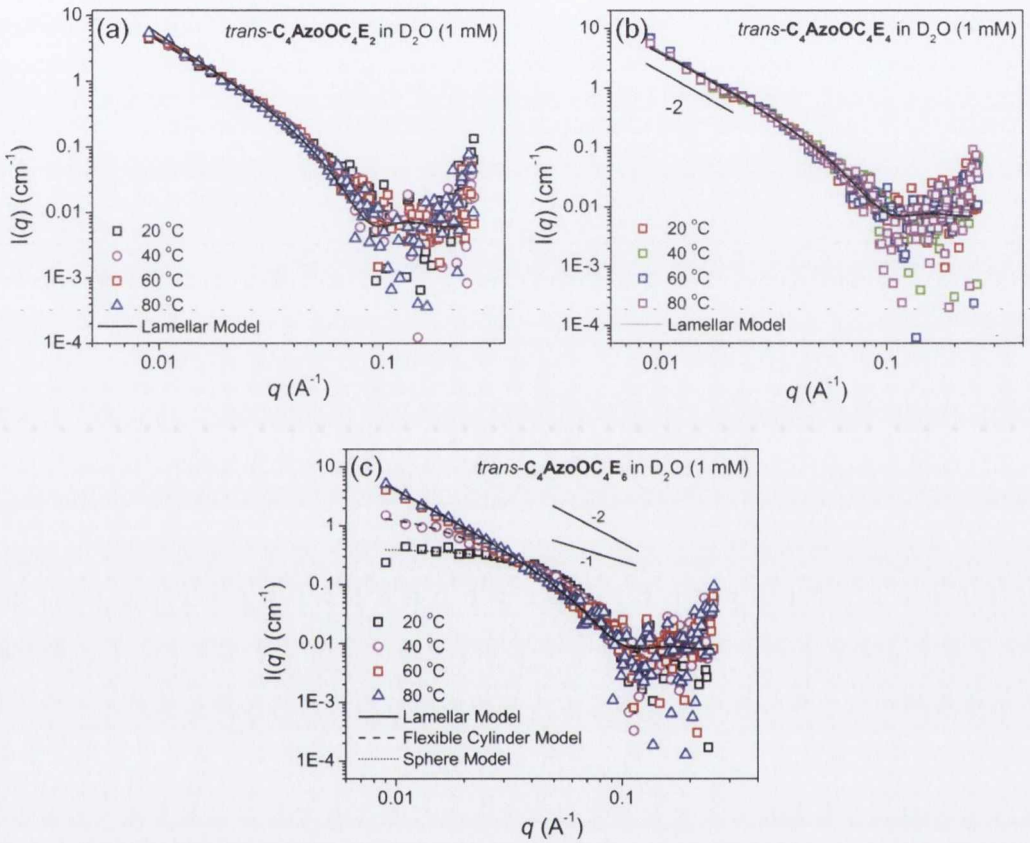


Figure 8.10 SANS data for the *trans*-isomers of (a) **$C_4AzoOC_4E_2$**, (b) **$C_4AzoOC_4E_4$** and (c) **$C_4AzoOC_4E_6$** in D_2O (1 mM) as a function of temperature. Straight lines show -1 and -2 decays for comparison. Solid, dashed and dotted lines correspond to the fits to the models described in the text.

Only subtle changes were observed for *trans*-**$C_4AzoOC_4E_2$** in D_2O as a function of temperature (Figure 8.10a). The scaling at low q remains constant at $q^{-2.0}$ and thus each scattering profile was fit to the Lamellar Sheet model. From 20 to 80 °C there is a slight increase in T_{sheet} from 52.7 to 60.6 Å, which is accompanied by a slight increase in wetness from 6 to 13%. More interestingly for the *cis*-isomer (see Appendix Figure A.8.7) which formed smooth fractal aggregates at T = 20 °C, the q-scaling decreases as the temperature increases, reaching $q^{-2.5}$ by T = 80 °C. Thus, this sample could be fit by the Lamellar Model, which produced an extremely wet (87%), thick (60.6 Å) sheet.

The *trans*- and *cis*-**$C_4AzoOC_4E_4$** samples were found to retain their interesting "bump" at higher temperatures (Figure 8.10b). This is slightly surprising as contributions to the SANS data by the structure factor is generally reduced at higher temperatures.[31] Nevertheless, these samples once

again could be reasonably well fit with the Lamellar Sheet Model.[25, 26] The sheet thicknesses ranged from 50-60 Å and the wetness varied around 60%. There was no obvious pattern to this data, which may be a result of the poor fits to the data in the mid-q region.

In contrast to **C_4AzoOC$_4$E$_2$** and **C_4AzoOC$_4$E$_4$**, the SANS data for **C_4AzoOC$_4$E$_6$** were found to change remarkably over the temperature range (Figure 8.10c). At T = 20 °C, the SANS data displayed a Guinier plateau, which increased to $q^{-0.9}$, $q^{-2.0}$ and $q^{-2.1}$ for T = 40, 60 and 80 °C, respectively. Such q-scalings correspond to a transformation from spheres, to cylinders to lamellar sheets.[32] Interestingly, T = 40 °C was better fit by the Flexible Cylindrical Model (r = 24.4 Å, L = 473.4 Å and Kuhn length (L_{Kuhn}) = 167.3 Å). At T = 60 °C and 80 °C, Lamellar Sheet Model fits gave T_{sheet} of 46.4 and 52.7 Å, respectively. The aggregate wetness was found not to change dramatically with temperature. Unlike at T = 20 °C where photoisomerisation results in a significant change from spherical to cylindrical aggregates (Figure 8.7c), the effect is significantly reduced at higher temperatures (Figure A.8.7 and Table A.8.6).

8.4.3 Cryo-Scanning Electron Microscopy (Cryo-SEM)

Some of the SANS data for the PS were best fit to lamellar sheets. Given the low concentration and the large R_H observed for **C_4AzoOC$_4$E$_2$** and **C_4AzoOC$_4$E$_4$** in the MALS experiments, it is likely these PS actually form vesicle-like structures, previously observed for **C_4AzoOC$_4$E$_2$**[3] and similar surfactants which do not contain azobenzene moieties.[33] If the diameter of the vesicles is outside the q-window of the SANS experiment (3.0 to 69.8 nm) then the scattering would appear to correspond to that of lamellar sheets (q^{-2}) as observed here. In this scenario, the sheet thickness determined from the SANS measurements would represent the thickness of the vesicle wall. In order to investigate whether the PS were in fact from vesicles in solution, preliminary cryo-SEM measurements were performed on *trans*-**C_4AzoOC$_4$E$_2$** (Figure 8.11). Low temperature cryo-SEM is an excellent technique for capturing and observing biological samples close to the natural state where critical point drying, using liquid N_2, prepares the sample for measurement without causing an unwanted change in the sample structure.

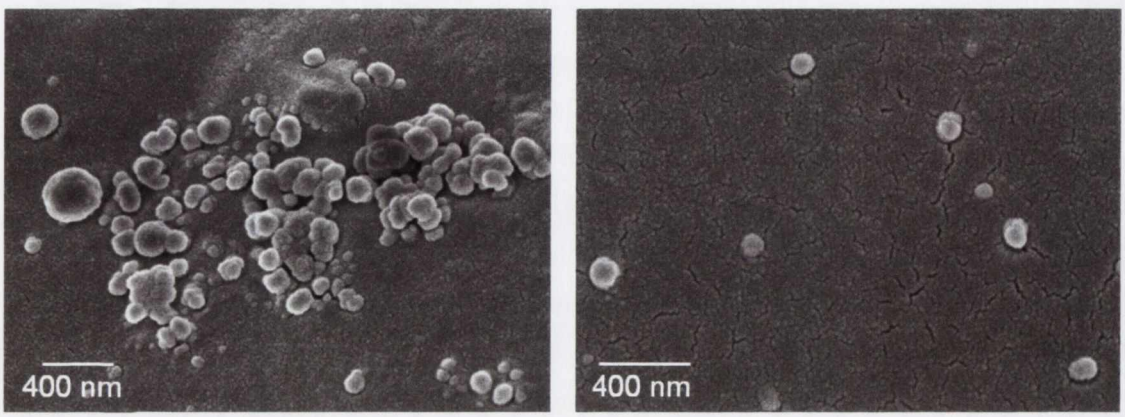


Figure 8.11 Cryo-SEM images of *trans*-**C_4AzoOC$_4$E$_2$** in D_2O (1 mM). Cryo-SEM measurements were performed by Dr Clodagh Dooley.

There is clearly the presence of multiple spheres in the frozen sample of *trans*-**$C_4AzoOC_4E_2$** shown in Figure 8.11. Although quite polydisperse, the size of these aggregates (150-300 nm) corresponds well to the R_H measured for using MALS (~125 nm). Unfortunately, only this one preliminary study has been performed to date, and the sample preparation procedure has yet to be optimised. Nevertheless, these images do confirm the formation of larger spheres in solution which support the formation of vesicles rather than simply lamellar sheets. Secondly, they also demonstrate the usefulness of cryo-SEM to image the solution-phase structure of soft matter materials.

8.4.4 Discussion of the Nanoscale Organisation of Dilute Solutions of PS

A combination of MALS, SANS and cryo-SEM have been used to investigate the nanoscale organisation of aggregates of the PS over a range of concentrations and temperatures, as well as, crucially, the effect of photoisomerisation of the azobenzene moiety. The PS with the shortest head-group length, **$C_4AzoOC_4E_2$**, was found to form vesicle aggregates with R_H ~125 nm at a concentration of 0.24 mM. At 1 mM, the SANS measurements have shown that the bilayer thickness of 52.7 Å (T = 20 °C) increases to 60.6 Å at higher temperature (T = 80 °C), although the sample remained relatively dry throughout. Photoisomerisation appeared to result in the destruction of these structures, as shown by the decrease in R_H from 125 to 70 nm and the appearance of smooth fractal aggregates in the SANS experiments.

The large R_H and lamellar sheet q-scaling in SANS also implied that *trans*-**$C_4AzoOC_4E_4$** forms vesicles at the concentrations investigated (1-200 mM). However, further work is required to: (1) image these vesicle structures (if they are in fact present); (2) fit the unusual mid-q data of the SANS. Higher concentration studies have suggested that the unusual mid-q data could be a result of particle-particle interactions. However, it could also be assigned to the formation of multilamellar vesicles.[3] Such structures would also display q-scaling which correspond to lamellar sheets, but would also be accompanied by subtle changes in the shape of the SANS profile, due to changes in the scattering length densities between the layers. Nevertheless, the fits to the SANS data, which still need to optimised, gave slightly thicker (53.4 Å) and significantly wetter (40% D_2O) sheets than **$C_4AzoOC_4E_2$**, which exhibited minimal structural rearrangement within the observation window of the SANS experiment (2.6 – 70 nm) upon photoisomerisation. The increase in thickness between the **$C_4AzoOC_4E_2$** and **$C_4AzoOC_4E_4$** is likely to be attributed to the increase in the length of the hydrophilic head-group.

Finally, **$C_4AzoOC_4E_6$** was the only PS found to form micelles at the concentrations investigated (1-200 mM). The radii determined using MALS (R_H ~55 Å) and SANS (r ~43.4 Å) for the 1 mM sample correspond well to the length of the molecule (~41 Å). Photoisomerisation at T = 20 °C resulted in a change in structure from spherical to cylindrical aggregates. For both isomers the precise dimension of the aggregates varied rationally with the concentration of the surfactant. Furthermore, even at high concentrations (*i.e.* 200 mM), interparticle interactions were

not observed in contrast to the higher concentrations of **$C_4AzoOC_4E_4$**. This may be explained by the difference in size of the aggregates of the PS that form. For example, **$C_4AzoOC_4E_4$** appears to form large, hollow vesicles which will occupy significantly more space than the compact micelles formed by **$C_4AzoOC_4E_6$**. Therefore, it is reasonable to assume that at the same concentration, the aggregates of **$C_4AzoOC_4E_4$** would be in closer proximity to each other than the aggregates of **$C_4AzoOC_4E_6$**. For aggregates in closer proximity to each other, the contribution of particle-particle interactions (*i.e.* structure factor) to the scattering data is expected to be greater, as seen here.

$C_4AzoOC_4E_6$ forms significantly smaller micelles than **$C_4AzoOC_4E_2$** and **$C_4AzoOC_4E_4$**. Previously, the neutral surfactant hexaethylene glycol mono-*n*-dodecyl ether ($C_{12}E_6$), which does not bear an azobenzene moiety, but has similar chain lengths in the glycol head-group and alkyl tail to that of the **$C_4AzoOC_4E_6$**, was found to form similarly sized ellipsoidal aggregates in D_2O (R_H ~53 Å).[33] In contrast, the analogous surfactant with a smaller head-group (E_5) formed much larger vesicles (R_H ~320 Å). The phase structure of such surfactants is expected to depend on the number of ethylene oxide units in the head-group,[34] which is related to the packing parameter (P) by V_c/a_0l_c, where V_c is the volume of the hydrophobic chain, a_0 is the mean cross-sectional surface area of the head-group and l_c is the critical chain length.[35] For the series of PS studied here, the tail length (~21 Å) and volume (~324 Å^3) are kept constant, only the head-group varies between 2, 4 and 6 ethylene glycol units (E_2, E_4 and E_6, respectively). (Full descriptions and references used for the calculation of the length and volume of the hydrophobic tail are given in the Appendix and Tables A.8.13 and A.8.14.) An increase in the head-group size while the hydrophobic portion of the molecule is kept constant will decrease P. This corresponds to an increase in the interfacial curvature of the aggregate. A small a_0 leads to a more planar interface, *e.g.* bilayers or vesicles, while a larger a_0 causes cylindrical or spherical aggregates to form.[35] This corresponds well to the observation here that as length of the head-group is increased from E_2 to E_4 to E_6, the structures transform from large vesicles, to smaller vesicles, to cylinders/spheres. Unfortunately it is difficult to determine the surface area of the head-group, a_0, of each PS as the longer ethylene glycol chains are unlikely to exist as extended chains. In addition, it was not possible to find an approximate value for the effective surface area of ethylene oxide units and, therefore, only a qualitative discussion about the effect of the size of the hydrophilic head-groups will be possible. This appears to be typical for studies in the literature involving the discussion of the relative sizes of neutral ethylene glycol head-groups.[34]

8.5 Lyotropic Liquid Crystalline Phase Formation

The formation of LLC phases by the photosurfactants is crucial if they are to be used as photoresponsive templates for inorganic sol-gel matrixes, as described in Chapter 1. Therefore, polarised optical microscopy has been used to identify whether the formation of LLC phases occurs. The phase formation has been investigated as a function of temperature and concentration. Any phases identified from the POM measurement will then be used to construct temperature-concentration phase diagrams.

8.5.1 Identification of LLC Phases using POM

The LLC phases for the PS-H_2O systems at high concentrations (*i.e.* >2 M) were probed using a polarised optical microscope equipped with a heat-stage. POM enables the spatial organisation of a sample to be observed with polarised light. The concentration used to form LLC phases is typically 10,000 times greater than the *cmc* values. Therefore, for simplicity, rather than working in molar concentrations, the surfactant concentrations will be expressed as weight percentages (*wt.*%). The surfactants were prepared in water at concentrations of 10-100 *wt.*% in 10% intervals. Brightness in the POM images is a clear indication that anisotropic LLC phases are present. Careful consideration of the POM texture allows the nature of the LLC phase to be assigned.

The neutral PS all showed promising LLC phase formation, corresponding well to previous studies on similar neutral surfactant systems.[8-10] Initially, all three PS were studied as a function of concentration at T = 20 or 30 °C. *Trans*-**C_4AzoOC$_4$E$_2$** at 30 °C is given as a representative example in Figure 8.12, while *trans*-**C_4AzoOC$_4$E$_4$** and *trans*-**C_4AzoOC$_4$E$_6$** are shown in Figures A.8.8 and A.8.9, respectively, in the Appendix. The lack of brightness at 20 *wt.*% *trans*-**C_4AzoOC$_4$E$_2$** suggests that no anisotropic LLC phases are present at this concentration. In contrast, at 30, 50, 60 and 90 *wt.*% the POM images display a smoke-like texture, consistent with the presence of normal hexagonal phases (H_1).[36] In contrast, lamellar mesophases (L_α), which exhibit a streaky or mosaic-like texture,[37] are seen for 40, 70 and 80 *wt.*% of *trans*-**C_4AzoOC$_4$E$_2$**.

Interestingly, the 100 *wt.*% *trans*-**C_4AzoOC$_4$E$_2$** (Figure 8.12i) and 100 *wt.*% *trans*-**C_4AzoOC$_4$E$_6$** (Appendix Figure A.8.9), without any solvent, also appear bright using POM. Such phases are termed *thermotropic* liquid crystalline phases.[9] The images have *pseudo*-isotropic regions separated by oily streaks, which is typically ascribed to a smectic phase (SmA) where the molecules are orientated normal to the plane.[9] Tschierske *et al.* previously reported that a neutral PS with 2 or 3 ethylene glycol units within the hydrophilic head-groups ($C_{12}OAzoE_n(OH)_2$, where n = 3 or 4), formed thermotropic liquid crystalline phases at high temperatures (100-170 °C), but were found to crystallise at lower temperatures.[9]

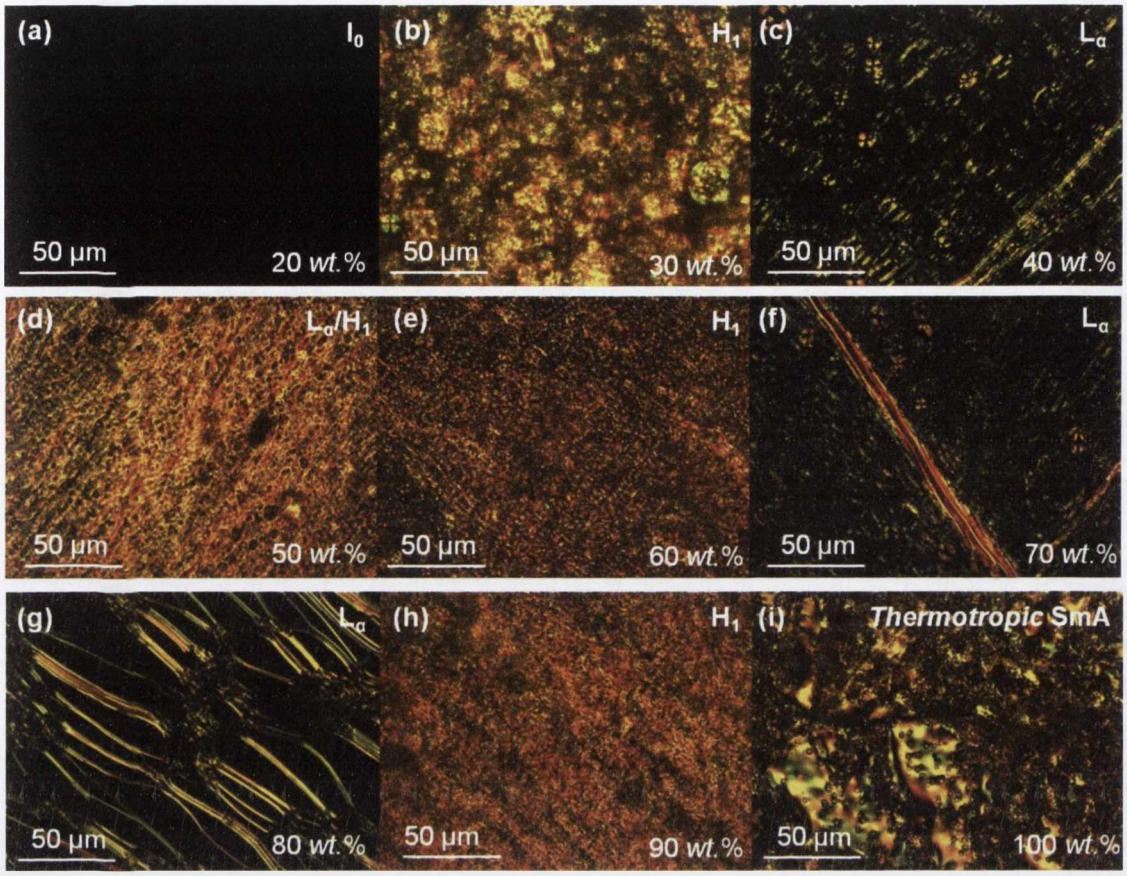


Figure 8.12 Polarised optical micrographs of *trans*-$\mathbf{C_4AzoOC_4E_2}$ as a function of concentration at T = 20 °C. I_0, H_1 and L_α represent isotropic, hexagonal and lamellar phases, respectively, and SmA is the thermotropic smectic phase.

The PS-H_2O compositions identified as forming LLC phases at T = 20 °C were also studied as a function of temperature. Each sample was slowly heated to 80 °C and then cooled to 15 °C. Typically only very minor changes to the structure of the LLC phases were observed upon increasing the temperature. For all concentrations, a temperature was reached in which any brightness previously attributed to the formation of anisotropic LLC phase was found to fade away. This is shown in Figures 8.13a-c for *trans*-$\mathbf{C_4AzoOC_4E_6}$, where complete loss of brightness is recorded at 37 °C. For all PS-H_2O compositions, brightness under POM was recovered upon cooling. It should be noted that on occasion the texture of the cooled sample was slightly dissimilar to the texture of the sample at the original temperature (Figure 8.13e). However, this can be attributed to an anchoring or organisation-inducing effect of the glass cover slips.[38] Gentle agitation of the glass slides recovered the original textures.

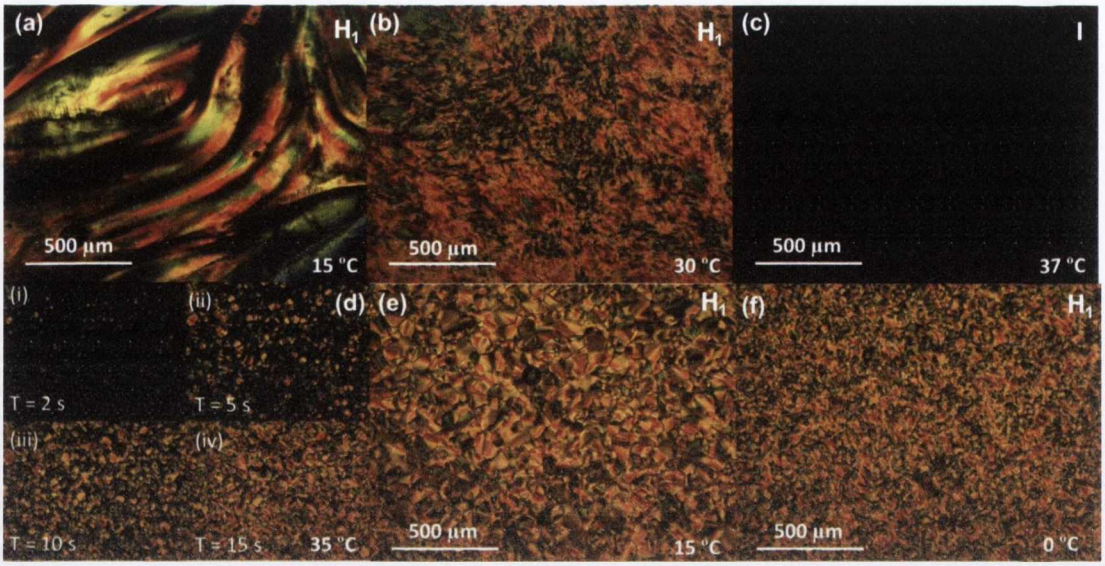


Figure 8.13 Polarised optical micrographs of *trans*-$\mathbf{C_4AzoOC_4E_6}$ (50 *wt.*%) as a function of heating and cooling. (a) 15 °C, (b) 30 °C, (c) 37 °C (loss of brightness), (d) cooled to 35 °C as a function of time, (e) cooled to 15 °C and (f) cooled to 0 °C. H_1 and I_0 represent hexagonal and isotropic phases, respectively.

This phase transition observed for *trans*-$\mathbf{C_4AzoOC_4E_6}$ corresponds well with the differential scanning calorimetry thermograms recorded at a range of compositions (20, 30, 40, 50, 80, 90 and 100 *wt.*%), as shown in the Figure 8.14. For 50 *wt.*% *trans*-$\mathbf{C_4AzoOC_4E_6}$ two endothermic peaks at recorded at 37 and 61 °C, the lower temperature corresponds very well the melting temperature observed in Figure 8.13 using POM. The higher the melting temperature the more stable the LLC phase is considered to be. This observation was noted for the rest of the *trans*-$\mathbf{C_4AzoOC_4E_6}$-H_2O compositions measured. Future work will involve trying to assign the origin of the second endothermic peaks at higher temperatures for the 20-80 *wt.*% samples. It is important to note that lack of brightness under POM only signifies that no anisotropic LLC phases are formed. However, it is possible that the phase transition at lower temperatures actually corresponds to a transition from an anisotropic to isotropic state, rather than strictly "melting" of all structural orientation. It is hoped that future small-angle X-ray scattering experiments will shed some light on the nature of the phases formed at higher temperatures.

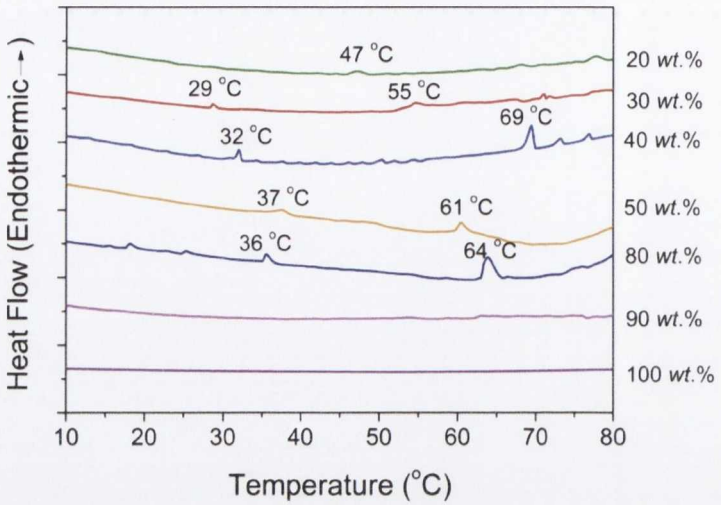


Figure 8.14 Differential scanning calorimetry thermographs of *trans*-C_4**AzoOC$_4$E$_6$** at a variation of concentrations (20, 60, 40, 50, 80, 90 and 100 *wt.*%) in H_2O. Heating rate of 10 °C min^{-1}. Sample masses were ~5 mg.

Finally, POM was used to determine the effect of photoisomerisation on any LLC phases formed. Where possible, all the experiments performed in this chapter were performed in the absence of external light sources, as to not induce any competitive photoisomerisation. However, a light source is obviously unavoidable with polarised optical microscopy, and, thus, it was important to check the effect of the emitted light (and heat from the lamp) on the *trans*- and *cis*-isomers. The polarised optical microscope used in these studies was equipped with a 50 W halogen reflector lamp. The emission spectrum of the lamp is shown in the Appendix, Figure A.8.10. The emission begins after λ_{em} = ~380 nm, and therefore there is no overlap with the π-π* band at ~350 nm of the *trans*-isomer. However, there does appear to be a small overlap between the n-π* band at ~450 nm of the *cis*-isomer and the emission of the lamp, which could induce isomerisation. To determine whether there was any photo- or thermal-isomerisation occurring as a result of the lamp, representative *trans*- and *cis*-samples of 60 *wt.*% **C$_4$AzoOC$_4$E$_6$** were left under the microscope for over 2 h. In this time no change in the texture of either sample was observed, which confirmed that there was little, if any, unintentional isomerisation induced by the lamp.

For all three neutral PS, photoisomerisation resulted in complete loss of brightness, as shown for 40 *wt.*% samples of each PS at T = 30 °C in Figure 8.15, which all displayed lamellar phases before photoirradiation with UV light. This suggests that the *cis*-isomers do not form anisotropic LLC phases. Hughes *et al.* previously observed a similar order-disorder transition (ODT) for the neutral PS, $C_4AzoC_5E_7$, which was found to form an ordered hexagonal phase at 50 *wt.*% surfactant before UV-irradiation.[8] The structure was assigned from POM and a SAXS pattern. Upon UV-irradiation, no brightness was visualised by POM and the SAXS pattern faded away to leave two broad peaks, which correlated to an isotropic state. LLC phases formed by *trans*-isomers are likely to be disrupted by the change in molecular geometry (rod-like to "bent") upon photoisomerisation. In addition, this effect is also likely to be a consequence of the difference

in hydrophobicity of the two isomers, with the *trans*-isomer being considerably more hydrophobic than the *cis*-state (the dipole moments across azobenzenes are ~0 D and ~3 D for *trans*- and *cis*-states, respectively).[14, 39]

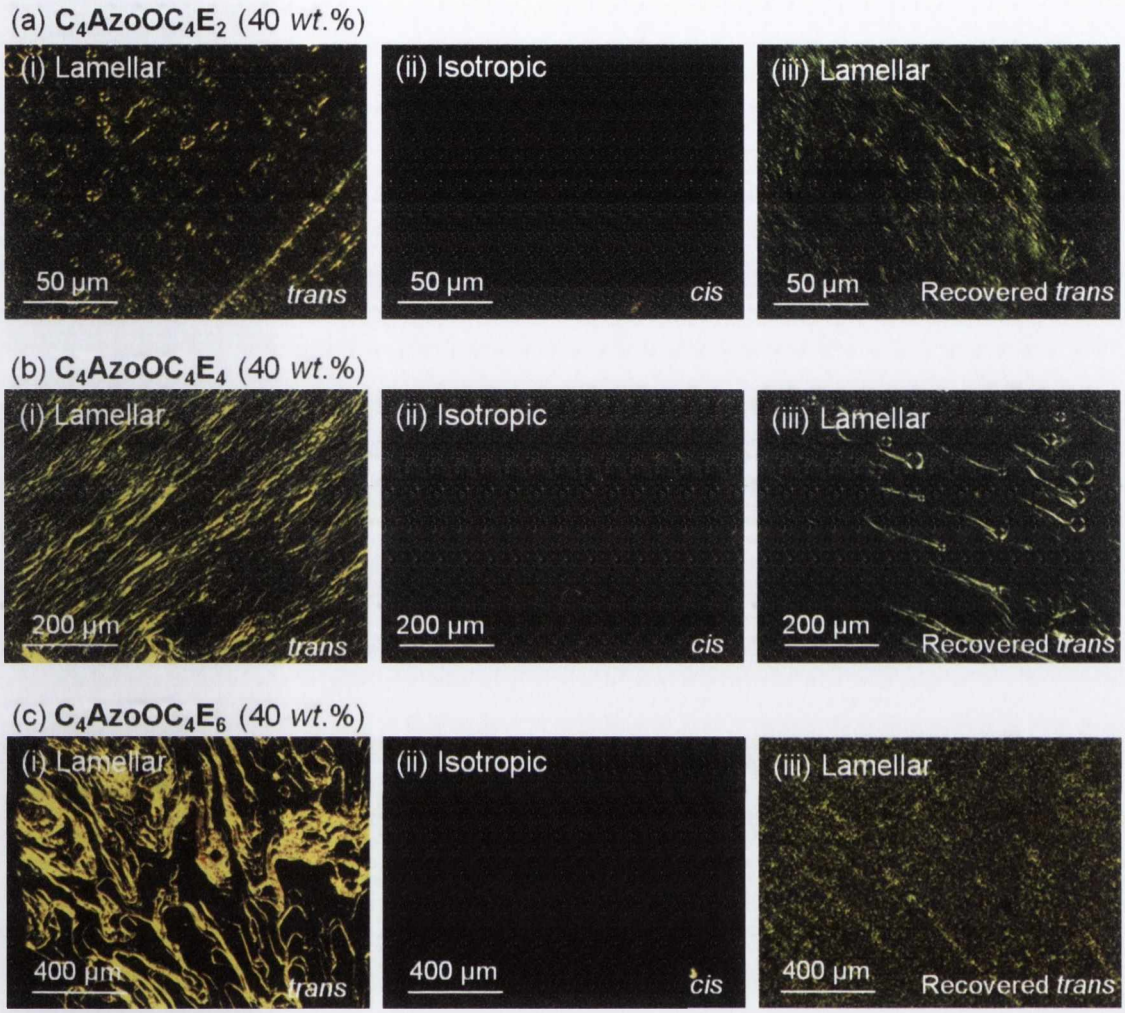


Figure 8.15 Polarised optical micrographs at T = 30 °C for (a) **$C_4AzoOC_4E_2$**, (b) **$C_4AzoOC_4E_4$** and (c) **$C_4AzoOC_4E_6$** at 40 *wt.*% in H_2O after (i) storage in the dark (*trans*-form), (ii) irradiation with UV-light (*cis*-form), and (iii) irradiation with blue light (*trans*-form recovered).

In some cases, a H_1 to L_α transition occurred, for example, for *trans*-**$C_4AzoOC_4E_6$** (60 *wt.*%) between 15 and 20 °C as shown in Appendix Figure A.8.11. H_1 to L_α phase transitions have previously been reported for poly(styrene-*b*-isoprene) diblock copolymers in selective solvents.[40] The order-order transition (OOT) is believed to be related to the fact that the selectivity of the water for hydrophilic oxyethylene units and the hydrophobic domains decreases as the temperature is increases. A similar phase transition was also observed for 55 *wt.*% of the neutral PS, $C_4AzoC_5E_7$.[8]

8.5.2 Proposed Binary Phase Diagrams

The preliminary binary concentration-temperature phase diagrams for each of the *trans*-PS are shown in Figure 8.16. The phases have been assigned by careful consideration of the POM images described in Section 8.1.5. From these preliminary phase diagrams it is clear that the length of the ethylene glycol head-group has a significant effect on the presence and nature of any LLC phases formed. Typically, as the concentration is increased there is a transition from a hexagonal to a lamellar phase, before reforming a hexagonal phase, which is likely to be a *reverse* hexagonal phase (H_{II}), however, this cannot be assigned from the POM images alone.[41]

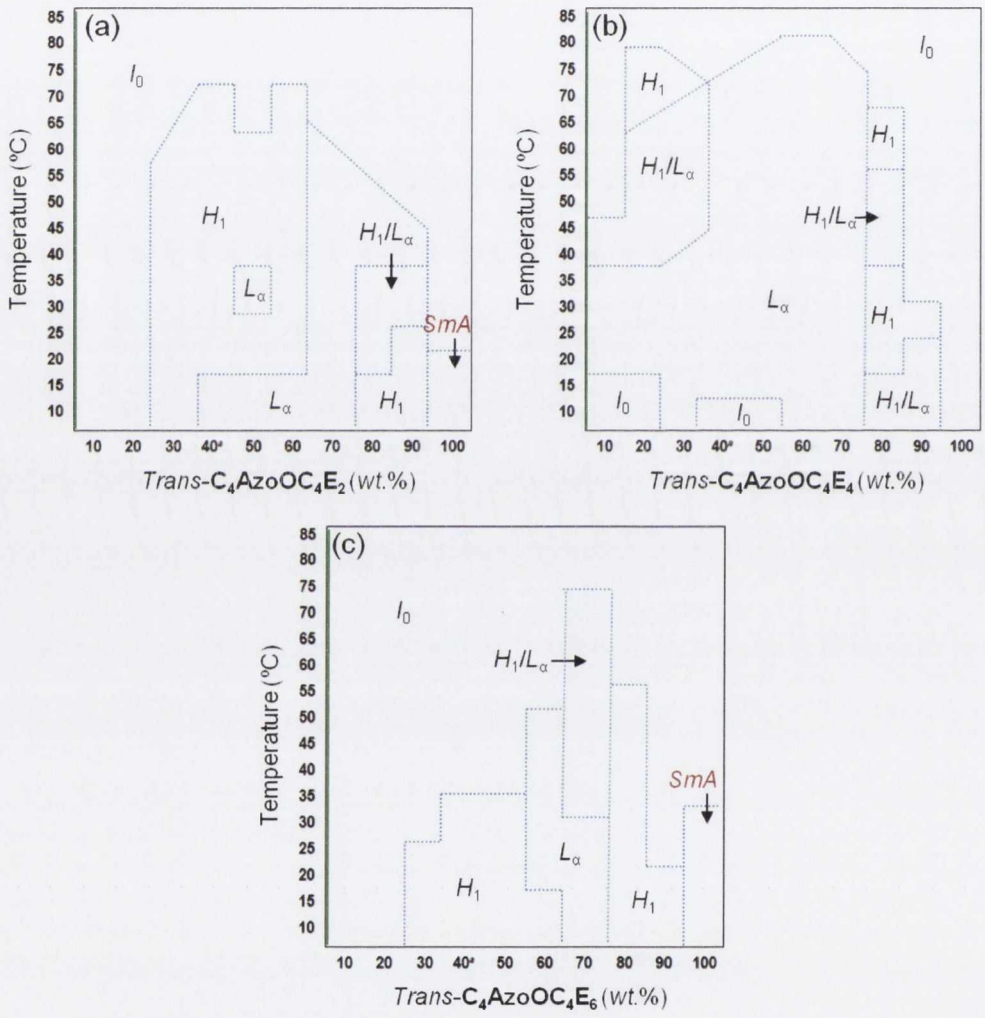


Figure 8.16 Preliminary temperature-concentration phase diagrams of (a) *trans*-**C_4AzoOC$_4$E$_2$**, (b) *trans*-**C_4AzoOC$_4$E$_4$** and (c) *trans*-**C_4AzoOC$_4$E$_6$** as a function of concentration and temperature. I_0, L_α and H_1 represent the isotropic, lamellar and hexagonal liquid crystalline phases, respectively and SmA is the smectic thermotropic liquid crystalline phase. The green line represents the approximate concentrations of the discrete aggregate studies (typically <0.1 *wt.*%).

Interestingly, *trans*-**C_4AzoOC$_4$E$_4$** appears to form lamellar sheets at 10 *wt.*%. This is a remarkably low concentration for a LLC phase to form. As a result, such L_α phases are typically referred to as *hyperswollen* lamellar phases.[42] Hyperswollen lamellar phases have previously been

reported for similar neutral surfactants when a certain alkyl chain (C)/ethylene glycol (E) ratio is reached (2.4 - 4).[42] For example, consider C_m/E_n, where m is the alkyl carbon number and n is the number of ethylene glycol units. The length of the alkyl chain (C_m) in each of the PS is approximately the same length of a 14 carbon alkyl chain. While the length of the ethylene glycol chain (E_n) varies from 2, 4 and 6 for **$C_4AzoOC_4E_2$**, **$C_4AzoOC_4E_4$** and **$C_4AzoOC_4E_6$**, respectively. Consequently, C_m/E_n = 7, 3.5 and 2.3 for **$C_4AzoOC_4E_2$**, **$C_4AzoOC_4E_4$** and **$C_4AzoOC_4E_6$**, respectively. Therefore, the head-to-tail ratio in **$C_4AzoOC_4E_4$** falls within the range required for the formation of hyperswollen lamellar sheets.[42] At around this ratio the head-group length to tail length is ~1:1, thus, favouring the formation of packed sheets.

8.6 Conclusions and Outlook

To summarise, the design, synthesis and characterisation of a series of non-ionic photosurfactants bearing azobenzene moieties has been achieved. While **$C_4AzoOC_4E_2$** is known in the literature,[5] **$C_4AzoOC_4E_4$** and **$C_4AzoOC_4E_6$** are novel compounds. This series of surfactants was selected to investigate the effect of photoisomerisation and the length (and surface area) of the hydrophilic head-group on the self-assembled formed structures in dilute (using MALS, SANS, cryo-SEM) and concentrated solutions (POM). Crucially it has been shown that the PS assemble into LLC phases at high concentrations, and that phase transformation occurs as a result of concentration, temperature and photoisomerisation. Future work will use the surfactants and the conditions identified here as forming desirable LLC phases as novel photoresponsive templates for inorganic sol-gel matrixes.

The results presented here have shown that varying the length of the ethylene glycol head-group is an effective method to control the structure of the self-assembled structures formed. The results suggest that the structures formed are dependent on the ratio between length of the hydrophilic head-groups and hydrophobic tails. It is therefore logical to assume that varying the length of the hydrophobic tail will also be an effective route to tune the self-assembled structures. In this study, the length of the alkyl substitute on the opposite side of the azobenzene has been kept constant as a butyl-chain. Future work, will involve the preparation of surfactants with a constant head-group size, such as tetraethylene glycol, and different lengths of alkyl chains (*e.g.* ethyl, butyl and octyl). Furthermore, it could also be interesting to synthesis "scaled" surfactants, whereby the ratio of the length of head-group to tail is kept constant, but both their sizes are increased proportionally. If the structures formed are largely dependent on just the head/tail ratio, then we would expect the phases to be maintained at the same PS-H_2O compositions but with proportionally larger dimensions.

Polarised optical microscopy has been used to probe the phase behaviour of the PS at high concentrations in water. It was shown that is possible to tune the nature of the LLC phase formed from isotropic, to hexagonal, to lamellar phases, depending on the concentration and temperature. Therefore, these results have enabled preliminary concentration-temperature phase diagrams to be

prepared. To date, the analysis of the POM images has focused on assigning phases according to the observed texture. However, the interference colours are known to depend on the birefringence of the crystal, its thickness, and the orientation of the molecules relative to the optical axis.[43] Therefore, future work will involve an in depth analysis of the colours formed to identify further information about the orientation of the molecules within the LLC phases.

Future studies, which are already underway, will use small-angle X-ray scattering to probe the nanoscale organisation of the PS in dilute and concentrated solutions. The extended *q*-range of a SAXS experiment, in comparison to SANS (particularly in the high-*q* region) will enable the full structure of the larger aggregates (**C_4AzoOC_4E_2** and **C_4AzoOC_4E_4**) to be identified. In addition, the contribution of structure factor in the more concentrated samples can be more clearly identified due to the superior resolution of SAXS. Thus, this technique should allow us to more effectively monitor the growth of individual micelles into larger aggregates as a function of concentration and temperature. Furthermore, SAXS will be used to quantitatively characterise the lyotropic liquid crystalline phases identified from the POM measurements. Liquid crystalline materials are known to form distinctive scattering patterns in SAXS.[44] Analysis of this data should enable the nature of the phase to be more conclusively identified, as well as the determination of the phase dimensions, such as the *d*-spacing within the lamellar phases. In particular, we hope to identify the formation of reverse hexagonal phases which are likely to be occurring at the lamellar-to-hexagonal phase transitions that coincide with increasing concentration, observed with POM. Lastly, phases which do not display optical textures using POM, such as bicontinuous mesophases which exhibit cubic symmetries,[38] will also be identified using SAXS.

Due to experimental limitations, the lowest concentration of PS probed in the SANS (and will be probed in future SAXS) experiments was ~1 mM. This is over a factor of a hundred times higher than the *cmc*s of the neutral surfactants ($2 - 6 \times 10^{-6}$ M). However, it is possible to monitor such low concentrations using ^{1}H NMR spectroscopy. Preliminary studies have shown that the ^{1}H NMR peaks in the aromatic region, which correspond to the azobenzene moiety, are sensitive to (a) packing of the molecules above the *cmc* (the peaks broaden) and (b) photoisomerisation of the azobenzene motif (the peaks shift). Future work will involve using ^{1}H NMR spectroscopy to obtain a more comprehensive understanding of the packing and dynamics of the molecules at concentrations around the *cmc*s of the surfactants. It should also be possible to trigger photoisomerisation and monitor the assembly/disassembly processes *in-situ* using ^{1}H NMR spectroscopy.

8.7 References

1. J. Eastoe and A. Vesperinas, *Soft Matter*, 2005, **1**, 338-347.
2. H. M. D. Bandara and S. C. Burdette, *Chem. Soc. Rev.*, 2012, **41**, 1809-1825.
3. T. Shang, K. A. Smith and T. A. Hatton, *Langmuir*, 2006, **22**, 1436-1442.
4. R. Lund, G. Brun, E. Chevallier, T. Narayanan and C. Tribet, *Langmuir*, 2016, **32**, 2539-2548.

5. T. Shang, K. A. Smith and T. A. Hatton, *Langmuir*, 2003, **19**, 10764-10773.
6. C. T. Lee, K. A. Smith and T. A. Hatton, *Macromolecules*, 2004, **37**, 5397-5405.
7. S. Besson, T. Gacoin, C. Ricolleau, C. Jacquiod and J.-P. Boilot, *J. Mater. Chem.*, 2003, **13**, 404-409.
8. S. Peng, Q. Guo, P. G. Hartley and T. C. Hughes, *J. Mater. Chem. C*, 2014, **2**, 8303-8312.
9. X. Tan, R. Zhang, C. Guo, X. Cheng, H. Gao, F. Liu, J. R. Bruckner, F. Giesselmann, M. Prehm and C. Tschierske, *J. Mater. Chem. C*, 2015, **3**, 11202-11211.
10. R. Yang, S. Peng, W. Wan and T. C. Hughes, *J. Mater. Chem. C*, 2014, **2**, 9122-9131.
11. *http://www.sasview.org/index.html.*
12. S. Qian and W. T. Heller, *J. Phys. Chem. B*, 2011, **115**, 9831-9837.
13. R. F. Tabor, R. J. Oakley, J. Eastoe, C. F. J. Faul, I. Grillo and R. K. Heenan, *Soft Matter*, 2009, **5**, 78-80.
14. K. G. Yager and C. J. Barrett, *J. Photochem. Photobiol. A*, 2006, **182**, 250-261.
15. Y. Zakrevskyy, J. Roxlau, G. Brezesinski, N. Lomadze and S. Santer, *J. Chem. Phys.*, 2014, **140**, 044906.
16. S. Guo, K. Matsukawa, T. Miyata, T. Okubo, K. Kuroda and A. Shimojima, *J. Am. Chem. Soc.*, 2015, **137**, 15434-15440.
17. H. C. Kang, B. M. Lee, J. Yoon and M. Yoon, *J. Colloid Interface Sci.*, 2000, **231**, 255-264.
18. P. Sierocki, H. Maas, P. Dragut, G. Richardt, F. Vögtle, L. De Cola, F. Brouwer and J. I. Zink, *J. Phys. Chem. B*, 2006, **110**, 24390-24398.
19. S. A. Buckingham, C. J. Garvey and G. G. Warr, *J. Phys. Chem.*, 1993, **97**, 10236-10244.
20. A. Dominguez, A. Fernandez, N. Gonzalez, E. Iglesias and L. Montenegro, *J. Chem. Educ.*, 1997, **74**, 1227-1231.
21. A. Czajka, G. Hazell and J. Eastoe, *Langmuir*, 2015, **31**, 8205-8217.
22. E. Alami, G. Beinert, P. Marie and R. Zana, *Langmuir*, 1993, **9**, 1465-1467.
23. J. Aguiar, P. Carpena, J. A. Molina-Bolívar and C. Carnero Ruiz, *J. Colloid Interface Sci.*, 2003, **258**, 116-122.
24. Y. Deng, Y. Li and X. Wang, *Macromolecules*, 2006, **39**, 6590-6598.
25. J. Berghausen, J. Zipfel, P. Lindner and W. Richtering, *J. Phys. Chem. B*, 2001, **105**, 11081-11088.
26. F. Nallet, R. Laversanne and D. Roux, *J. Phys. II France*, 1993, **3**, 487-502.
27. J. E. Martin and A. J. Hurd, *J. Appl. Crystallogr.*, 1987, **20**, 61-78.
28. A. Guinier and G. Fournet, *Small Angle Scattering of X-rays*, John Wiley and Sons, 1955.
29. A. A. Golosova, J. Adelsberger, A. Sepe, M. A. Niedermeier, P. Lindner, S. S. Funari, R. Jordan and C. M. Papadakis, *J. Phys. Chem. C*, 2012, **116**, 15765-15774.
30. L. Wang, R. Tabor, J. Eastoe, X. Li, R. K. Heenan and J. Dong, *Phys. Chem. Chem. Phys.*, 2009, **11**, 9772-9778.
31. J. Adelsberger, A. M. Bivigou-Koumba, A. Miasnikova, P. Busch, A. Laschewsky, P. Müller-Buschbaum and C. M. Papadakis, *Colloid. Polym. Sci.*, 2015, **293**, 1515-1523.
32. P. W. Schmidt, *Some Fundamental Concepts and Techniques Useful in Small-Angle Scattering Studies of Disordered Solids. In Modern Aspects of Small-Angle Scattering*, Kluwer Academic Publishers: Dordrecht, The Netherlands, 1995.
33. F. N. Padia, M. Yaseen, B. Gore, S. Rogers, G. Bell and J. R. Lu, *J. Phys. Chem. B*, 2014, **118**, 179-188.
34. H. N. Patrick, G. G. Warr, S. Manne and I. A. Aksay, *Langmuir*, 1997, **13**, 4349-4356.
35. J. N. Israelachvili, D. J. Mitchell and B. W. Ninham, *J. Chem. Soc., Faraday Trans. 2*, 1976, **72**, 1525-1568.
36. Y. Zhao, X. Yue, X. Wang and X. Chen, *J. Colloid Interface Sci.*, 2013, **389**, 199-205.

37. S. T. Hyde, *Handbook of Applied Surface and Colloid Chemistry* John Wiley & Sons, Ltd., 2001.
38. T. Ichikawa, T. Kato and H. Ohno, *J. Am. Chem. Soc.*, 2012, **134**, 11354-11357.
39. G. S. Hartley and R. J. W. Le Fevre, *J. Chem. Soc.*, 1939, 531-535.
40. T. P. Lodge, B. Pudil and K. J. Hanley, *Macromolecules*, 2002, **35**, 4707-4717.
41. M. Rappolt, A. Hickel, F. Bringezu and K. Lohner, *Biophys. J.*, 2003, **84**, 3111-3122.
42. Y. Uchida, T. Nishizawa, T. Omiya, Y. Hirota and N. Nishiyama, *J. Am. Chem. Soc.*, 2016, **138**, 1103-1105.
43. L. S. Hirst, *Fundamentals of Soft Matter Science* CRC Press, Taylor and Francis Group, Boca Raton, U.S.A., 2013.
44. S.-H. Ou, S.-C. Hung, G.-J. Wong and T.-M. Wu, *J. Mol. Liq.*, 2014, **199**, 190-195.

Chapter 9

Conclusions and Outlook

This thesis explored the self-assembly of conjugated polyelectrolytes and photoactive surfactants for the design of highly efficient energy and sensing devices.

The first part of this thesis focused on conjugated polyelectrolytes and their potential as materials for improving the efficiency of polymer photovoltaic cells. Significant enhancements can be achieved by careful control of the nanoscale organisation of the polymer donor materials or interfacial modifying layers. In **Chapter 4**, solvent mediation was used to control the aggregate morphology of all-conjugated poly(thiophene)-poly(thiophene) diblock copolymers. Optical studies revealed increased aggregation of the CPE chains in pure solvent, in comparison to the mixed solvent systems. In H_2O/MeOH mixtures, enhancements in the fluorescence quantum yields were accompanied by a corresponding trend in the *Z*-average particle diameter determined by DLS. SANS studies revealed that the **P3HT-*b*-CPEs** formed core-shell cylindrical aggregates in solution, where the relative thickness and "wetness" of the core and the shell was determined by the solvent system. Finally, AFM studies revealed that the aggregates formed in solution can be transferred as thin films. The thin-film nanoscale morphology of polymer-based devices is a critical component of device operation. The results shown here demonstrate that tuning the nanoscale organisation of aggregates of amphiphilic diblock copolymers in solution *via* solvent-mediation is a simple and effective method to control the morphology of subsequently prepared thin films.

In **Chapter 5**, it was shown that further control of the aggregate morphology could be achieved by the addition of oppositely charged surfactants. The role of the neutral P3HT block in the self-assembly of amphiphilic diblock copolymers was also investigated by direct comparison with the analogous homopolyelectrolyte. The optical properties of **P3HTPMe$_3$** and **P3HT-*b*-P3HTPMe$_3$** displayed a moderate dependence on the nature of the surfactant counterion, its concentration and the solvent. **P3HTPMe$_3$** was shown to freely transform from spheres or semi-flexible cylinders to rigid sheets upon association with anionic surfactants, the size and morphology of which was dependent on the surfactant charge density, tail length and stiffness and solvent. In contrast, complexation with SDS had only a limited effect on the solution structure of **P3HT-*b*-P3HTPMe$_3$**, with the hydrophobic P3HT core retaining the cylindrical morphology of the pure diblock copolymer. AFM studies revealed that the CPE-surfactant complexes formed films with distinctive surface morphologies from the pure parent polymers.

Poly(thiophene)-dodecyl sulfate complexes were also successfully incorporated as a cathodic interfacial layers in bulk heterojunction-polymer solar cells. Preliminary performance studies revealed a 20% increase in the power conversion efficiency of the devices upon addition of the CPE-SDS complexes, as well as a moderate difference between the homo- and diblock copolyelectrolytes. From this preliminary study, no concrete correlation between the solution-phase structure, the layer morphology and the observed enhancement in the device performance

has yet been identified. However, the degree of crystallinity of the polymers is expected to underpin the significant enhancement in the PCEs observed here.[1] Therefore, the ability to control the chain packing within the semi-crystalline P3HT blocks of the diblock copolymer may be an effective strategy to balance the charge carrier ability with other physical properties of the films.[1, 2]

Future work has already begun to investigate the nano-microstructural order of surfactant-ordered homo- and diblock-poly(thiophene) films using grazing-incidence small-/wide-angle X-ray scattering. GiSAXS will be used to probe the long-range connectivity and GiWAXS will investigate the relative degree of polymer crystallinity. Particular emphasis will be placed on identifying the role of the surfactant in controlling the nature and extent of face-to-face packing of the conjugated polymer backbones (π-π–stacking) and edge-to-edge packing of the conjugated polymer side chains (*lamellar*-stacking). These studies will also look investigate the effect of the deposition process and thermal annealing on the film organisation. These results will be correlated with complementary microscopy experiments (AFM, TEM) to probe the film morphology and, finally, OPV devices will be fabricated and characterised for the most relevant examples. Given the vast tuneability offered by homopolymer- and diblock copolymer-surfactant complexes, coupled with their solution processability, further significant enhancements in OPV device performance are to be expected once their structure-property relationships are better understood.

In **Chapter 6**, it was demonstrated for the first time that conjugated polyelectrolyte-polyoxometalate supramolecular networks can be formed *via* electrostatic associations. It was also shown that the dimensionality of the hybrid networks could be tuned by the chain length and steric charge distribution on the CPE. Specifically, **NET**, with a shorter chain length and two ammonium groups located on opposite sides of the CPE chain, formed alternating **NET-POM** 1D chain-like aggregates. In contrast, **PFP**, with a significantly longer chain length and charged groups on adjacent sides of the CPE chain, formed larger 2D plate-like arrays of **PFP-POM** complexes. Finally, AFM and SEM studies confirmed that the CPE-**POM** complexes could be transferred from solution to the solid-state with retention of their nanoscale organisation, which is critical for potential device applications.

Future work will involve extending the formation of CPE-**POM** hybrid materials to combine a variety of different **POMs** and CPEs, to exploit their range of molecular topologies, surface charge densities, chemical structures, redox and optical properties. The complexes formed are expected to yield a variety of well-defined, supramolecular architectures with enhanced functionality for potential applications as interfacial modifier layers and charge transport materials in OPV devices. Given that the optimisation of such devices is strongly correlated to the nanostructure of the material, hybrid systems of CPE-**POM**s could satisfy this requirement, while simultaneously offering enhanced functionality due to synergistic interactions between these two components.

CPEs also combine a plethora of desirable properties for membrane probes, including biocompatibility and environment-responsive fluorescence. In **Chapter 7**, a series of anionic, cationic and zwitterionic poly(thiophene)s were investigated as fluorescent probes for the sequential identification of the key phase transitions within model membrane bilayers. The anionic CPE was found to be uniquely capable of sensing subtle changes in membrane order, including the detection of the illusive sub-transition temperature, which highlights its remarkable sensitivity to subtle changes in membrane order.

A series of binding mode studies were performed to determine the origin of the difference in sensitivity demonstrated by each of the CPEs. This investigation indicated that the penetration depth of each CPE within the zwitterionic phospholipid bilayers was controlled *via* charge-mediation. Thus, the difference in sensitivity is likely to be a direct consequence of their localisation within the membrane bilayers. **P3Zwit**, with an overall neutral, zwitterionic side-group and hydrophobic poly(thiophene) backbone, could readily insert in between the **DPPC** zwitterionic head-groups, as well as within the hydrophobic phospholipid tails. In contrast, the charged poly(thiophene)s, **P3Anionic** and **P3TMAHT**, were unable to penetrate within the hydrophobic tails and localised around the zwitterionic head-groups of the phospholipid bilayers. **P3TMAHT** appeared to form extended structures on the vesicle surface, while **P3Anionic** localised within the zwitterionic head-group region of the lipid bilayers where the sensitivity to membrane order is believed to be the greatest. The selective engineering of CPE-phospholipid interfaces by strategic charge-mediation, as shown in **Chapter 7**, could play a key role in the design of superior biomedical and biotechnological devices.

The final part of this thesis involved the rational design of novel photoresponsive surfactants, which would self-organise into desirable patterns that could be controlled by light. In **Chapter 8**, the design, synthesis and characterisation of a family of non-ionic photosurfactants bearing azobenzene moieties was shown. **$C_4AzoOC_4E_2$** is known in the literature, while **$C_4AzoOC_4E_4$** and **$C_4AzoOC_4E_6$** were novel compounds. This series of surfactants was selected to investigate the effect of photoisomerisation and the length of the hydrophilic head-group on the self-assembled structures formed in dilute and concentrated solutions. Initially, the nanoscale organisation of aggregates of the PS over a range of concentrations and temperatures, as well as the effect of photoisomerisation of the azobenzene moiety, was investigated. **$C_4AzoOC_4E_2$** and **$C_4AzoOC_4E_4$** were found to self-assemble into lamellar sheets or vesicles, whose thickness and wetness depended on the concentration and temperature. In contrast, **$C_4AzoOC_4E_6$** was found to form micelles in the concentration regime 1-200 mM, which transformed from spheres to cylinders as the concentration or temperature were increased. The observed differences in the nanoscale organisation of each PS were attributed to the packing parameters of the surfactants, which corresponded well to the observation that as the length of the head-group was increased from E_2 to E_4 to E_6, the structures transform from large vesicles, to smaller vesicles, to cylinders/spheres.

Polarised optical microscopy was used to probe the phase behaviour of these PS at high concentrations in water. It was shown that is possible to tune the nature of the LLC phase formed between isotropic, hexagonal and lamellar phases, depending on the isomer, and the surfactant concentration and temperature. Finally, these results enabled preliminary binary phase diagrams to be assembled.

Future studies are already underway to use small-angle X-ray scattering to probe the nanoscale organisation of the PS in dilute and concentrated solutions. The extended q-range of a SAXS experiment will allow the full structure of the larger aggregates (**C_4AzoOC_4E_2** and **C_4AzoOC_4E_4**) to be better identified. This technique should also enable the growth of individual micelles into larger aggregates, as they begin to pack together, to be monitored. Furthermore, SAXS is a useful technique to quantitatively characterise any lyotropic liquid crystalline phases identified from the polarised optical microscopy measurements. Ultimately, the goal is to use the surfactants and the conditions identified as forming desirable LLC phases as novel photoresponsive templates for inorganic sol-gel matrixes.

The studies described in this thesis have demonstrated that self-assembly is an elegant method for the preparation of functional responsive materials. **Chapters 4-7** focused on the potential use of conjugated polyelectrolytes as materials for improving the efficiency of polymer photovoltaic cells and as bio-imaging and sensing devices. This work has been founded on the knowledge that the optoelectronic properties and nanoscale morphologies of CPEs are inherently linked. Since self-assembled systems, such as aggregates of CPEs, or the photosurfactants described in **Chapter 8**, are naturally dynamic it is possible to induce significant changes in the self-assembled structures formed by subtly altering environmental factors. The work in this thesis has focused on exploiting solvent, counterions, temperature and light to tune the aggregated structure of CPEs and surfactants in solution and thin films. Understanding the structure-property relationships within these systems is critical to direct future research.

9.1 References

1. S. Y. Son, Y. Kim, J. Lee, G.-Y. Lee, W.-T. Park, Y.-Y. Noh, C. E. Park and T. Park, *J. Am. Chem. Soc.*, 2016, **138**, 8096-8103.
2. H. Erothu, J. Kolomanska, P. Johnston, S. Schumann, D. Deribew, D. T. Toolan, A. Gregori, C. Dagron-Lartigau, G. Portale and W. Bras, *Macromolecules*, 2015, **48**, 2107-2117.

Appendix

Appendix Contents

Chapter 4

SANS Data Analysis of **P3HT-*b*-CPEs** III

Chapter 5

Optical Studies of **P3HTPMe$_3$**- and **P3HT-*b*-P3HTPMe$_3$**-Surfactant Complexes VI

SANS Data Analysis of CPE-Surfactant Complexes VII

AFM Images of CPEs and Surfactants XIII

Photoactive Layer Components XIV

Chapter 6

FTIR Spectra of **NET**, **PFP**, **NET-POM** and **PFP-POM** XV

AFM Images of **NET**, **PFP** and **POM** XVI

Chapter 7

Optical Studies of **DPPC**, CPEs and Prodan XVII

SANS Data for **P3Zwit**, **P3Anionic** and **P3TMAHT** XX

AFM Images of **DPPC**, **P3Zwit**, **P3Anionic** and **P3TMAHT** XXI

Chapter 8

Structural Characterisation of the Neutral Surfactants XXII

UV/Vis Absorption and Kinetics Studies XXVIII

SANS Data Analysis of the Neutral Surfactants XXIX

POM Images of the Neutral Surfactants XXXVII

POM Lamp Emission Spectrum XXXIX

Appendix – Chapter 4

Small-Angle Neutron Scattering Data Analysis

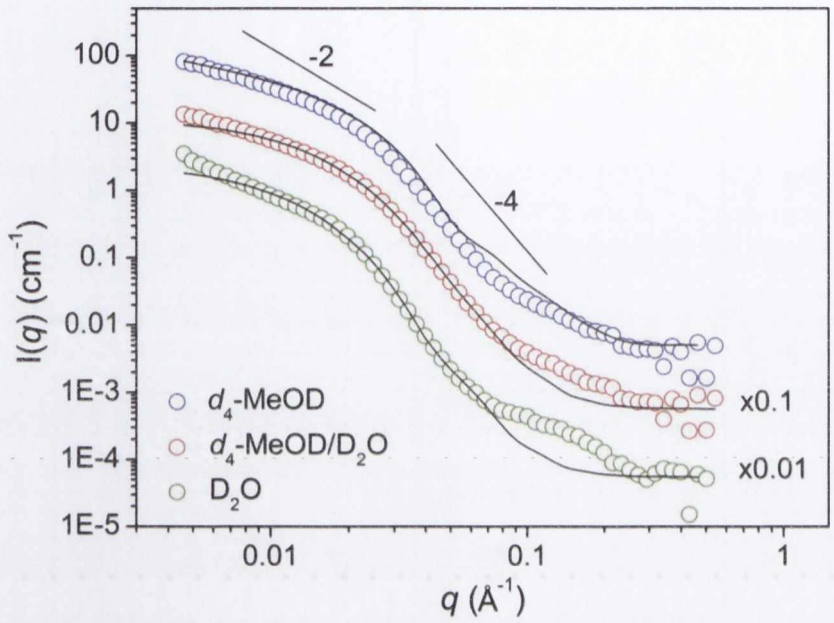


Figure A.4.1 SANS data for **P3HT-*b*-P3HTIm** in, d_4-MeOD, 20:80 (*v*/*v*) d_4-MeOD/D_2O and D_2O. For clarity, the d_4-MeOD/D_2O and D_2O data have been multiplied by 0.1 and 0.01, respectively. Curved lines show the best fits of the scattering profiles using the Core-Shell Cylinder Model. For comparison, the straight solid lines show -2 decay for a Guassian coil and -4 decay for Porod decay.

Table A.4.1 Structural parameters obtained SANS data for **P3HT-*b*-P3HTPy** and **P3HT-*b*-P3HTIm** in d_4-MeOD, D_2O and d_4-MeOD/D_2O mixtures: SLD_{sol} is the scattering length density of the solvent and α is the scattering power of the defined q region. L_{core}, r_{core} and T_{shell} are the core length, core radius and shell thickness, respectively, obtained from the best fits to the data using the Core-Shell Cylinder Model in SasView. $X_{sol\text{-}core}$ and $X_{sol\text{-}shell}$ are the calculated solvent fractions in the core and shell, respectively.

CPE	**Solvent**	**SLD_{sol} ($Å^{-2}$)**	**$q^{-\alpha}$ (q<0.2)**	**$q^{-\alpha}$ (0.2<q<0.7)**	**$q^{-\alpha}$ (q>0.7)**	**L_{core} (nm)**	**r_{core} (nm)**	**T_{shell} (nm)**	**$X_{sol\text{-}core}$**	**$X_{sol\text{-}shell}$**
P3HT-*b*-P3HTPy	d_4-MeOD	5.8×10^{-6}	-1.5	-4.2	-1.83	80	6	2	0.81	0.65
P3HT-*b*-P3HTPy	50:50 (*v*/*v*) d_4-MeOD/D_2O	6.09×10^{-6}	-1.38	-4.76	-1.78	11	7.5	9.5	0.31	0.87
P3HT-*b*-P3HTPy	D_2O	6.38×10^{-6}	-5/3	-5.21	-1.54	9	5.5	8	0.65	0.89
P3HT-*b*-P3HTIm	d_4-MeOD	5.8×10^{-6}	-0.93	-4.29	-1.79	93	5.4	2	0.79	0.62
P3HT-*b*-P3HTIm	20:80 (*v*/*v*) d_4-MeOD/D_2O	6.26×10^{-6}	-1.36	-4.47	-1.73	12	9	11	0.45	0.96
P3HT-*b*-P3HTIm	D_2O	6.38×10^{-6}	-1.72	-5.05	-1.63	23	13	11	0.69	0.97

Table A.4.2 Structural parameters obtained SANS data for **P3HT-*b*-P3HTPy** and **P3HT-*b*-P3HTIm** in D_2O and d_4-MeOD/D_2O mixtures: SLD_{sol} is the scattering length density of the solvent. r_{core} and T_{shell} are the core radius and shell thickness, respectively, obtained from the best fits to the data using the Core-Shell Sphere Model in SasView. $X_{sol\text{-}core}$ and $X_{sol\text{-}shell}$ are the calculated solvent fractions in the core and shell, respectively. The aggregation numbers: $N_{agg\text{-}cylinder}$ and $N_{agg\text{-}sphere,}$ have been calculated for the Core-Shell Cylinder Model and Core-Shell Sphere Model fits.

CPE	Solvent	SLD_{sol} ($Å^{-2}$)	r_{core} (nm)	T_{shell} (nm)	$X_{sol\text{-}core}$	$X_{sol\text{-}shell}$	$N_{agg\text{-}cylinder}$	$N_{agg\text{-}sphere}$
P3HT-*b*-P3HTPy	d_4-MeOD	5.8×10^{-6}	-	-	-	-	166	-
P3HT-*b*-P3HTPy	50:50 (*v*/*v*) d_4-MeOD/D_2O	6.09×10^{-6}	74	106	0.67	0.94	197	84
P3HT-*b*-P3HTPy	D_2O	6.38×10^{-6}	59	95	0.54	0.86	88	101
P3HT-*b*-P3HTIm	d_4-MeOD	5.8×10^{-6}	-	-	-	-	209	-
P3HT-*b*-P3HTIm	20:80 (*v*/*v*) d_4-MeOD/D_2O	6.26×10^{-6}	77	115	0.39	0.94	151	124
P3HT-*b*-P3HTIm	D_2O	6.38×10^{-6}	79	122	0.42	0.86	244	236

Appendix – Chapter 5

Sample Compositions

Table A.5.1 Composition of **P3HTPMe$_3$(SDS)$_x$** samples.

x	P3HTPMe$_3$ conc. (mg mL^{-1})	SDS conc. (mg mL^{-1})
0.2	8.48	1.52
0.5	6.91	3.09
1.0	5.27	4.73
2.0	3.58	6.42
5.0	1.82	8.18
20.0	0.53	9.47

Table A.5.2 Composition of **P3HT-*b*-P3HTPMe$_3$(SDS)$_x$** samples.

x	P3HT-*b*-P3HTPMe$_3$ conc. (mg mL^{-1})	SDS conc. (mg mL^{-1})
0.2	9.12	0.88
0.5	8.06	1.94
1.0	6.75	3.25
2.0	5.09	4.91
5.0	2.94	7.06
20.0	0.94	9.06

Optical Studies

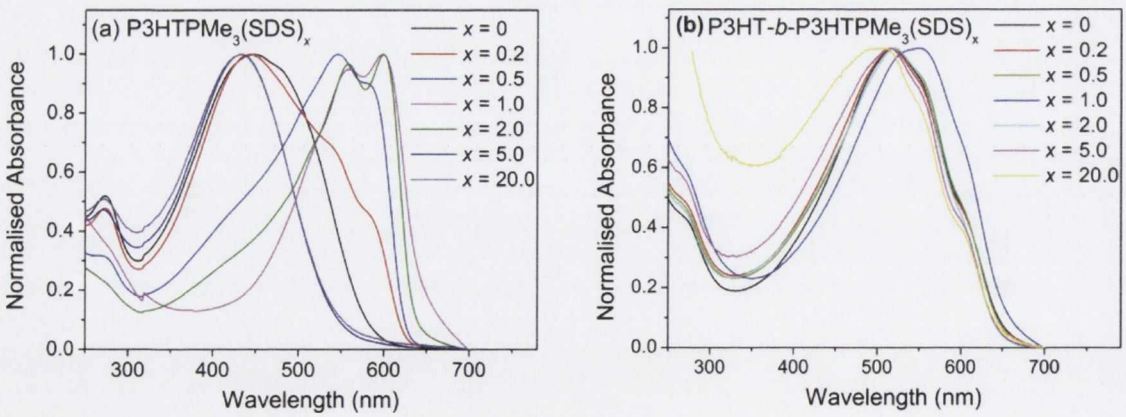


Figure A.5.1 Normalised UV/Vis absorption spectra for (a) **P3HTPMe$_3$(SDS)$_x$** and (b) **P3HT-*b*-P3HTPMe$_3$(SDS)$_x$** as a function of composition, x, at room temperature. Total sample concentration = 0.1 mg mL^{-1} in D_2O.

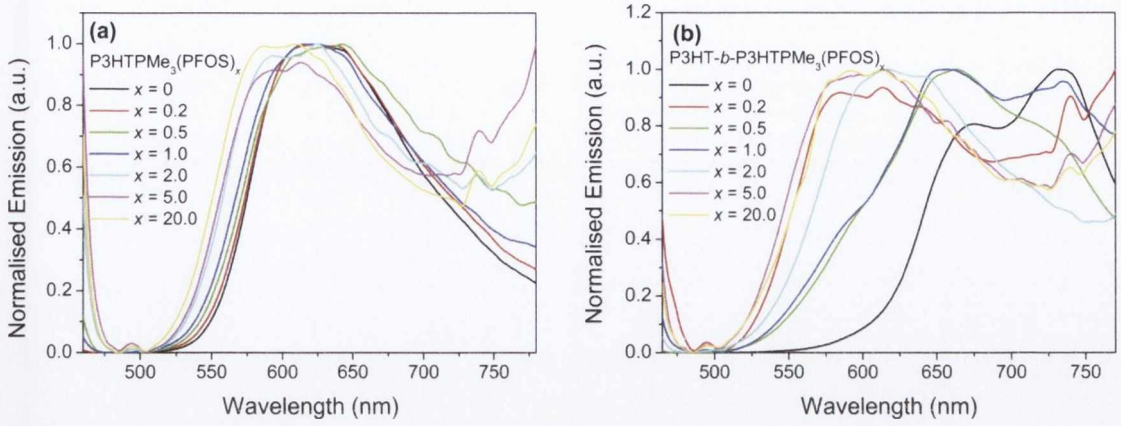


Figure A.5.2 Normalised steady-state emission spectra for (a) **P3HTPMe$_3$(PFOS)$_x$** and (b) **P3HT-*b*-P3HTPMe$_3$(PFOS)$_x$** as a function of PFOS composition, x, at room temperature. Total sample concentration = 10 mg mL^{-1} in D_2O. λ_{ex} = 450 nm.

Small-Angle Neutron Scattering Data Analysis

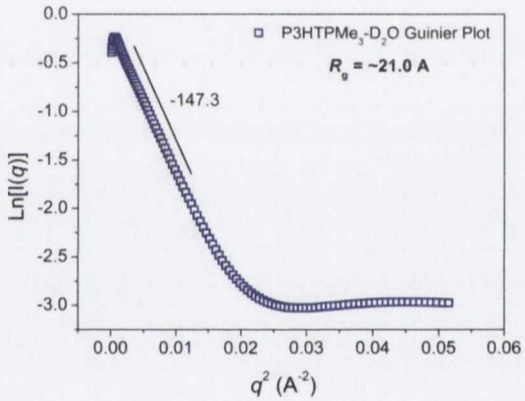


Figure A.5.3 Guinier plot of **P3HTPMe$_3$** in D_2O (10 mg mL^{-1}) at T = 25 °C. The Guinier plot involves plotting Ln[I(q)] *vs.* q^2. The slope = $R_g^2/3$, where R_g is the radius of gyration of the scattering objects.

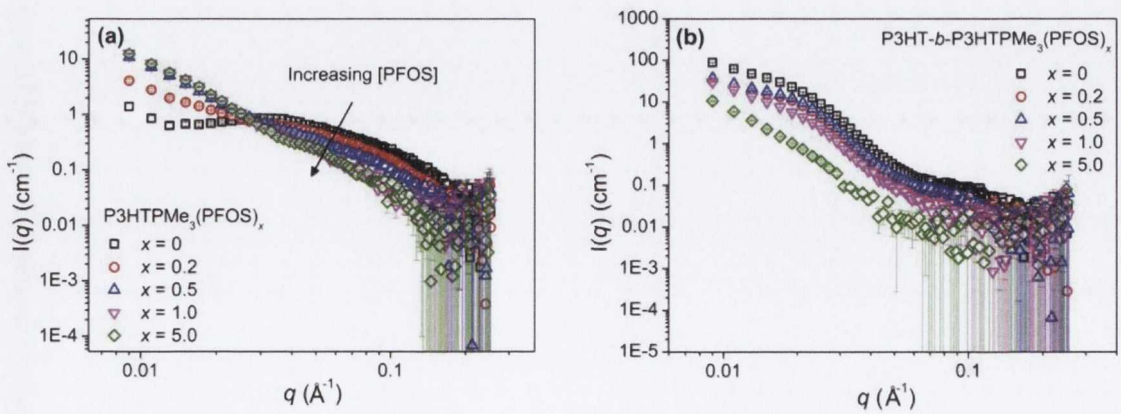


Figure A.5.4 SANS data of (a) **P3HTPMe$_3$** and (b) **P3HT-*b*-P3HTPMe$_3$** with selected charge ratios of PFOS in D_2O. The overall concentration was 10 mg mL^{-1}. T = 25 °C.

Table A.5.3 Structural parameters obtained from SANS data for **P3HTPMe$_3$(SDS)$_x$** in D_2O: α is the scattering power of the defined q region. R_g is the radius of gyration calculated from the corresponding Guinier plot. T_{sheet} is the sheet thickness, r is the radius of the sphere or cylinder and L is the length of the cylinder obtained from the best fit to the data using the Cylinder, Lamellar and Spherical Models in SasView. X_{sol} is the calculated solvent fraction in the aggregates.

Sample	$q^{-\alpha}$ (q<0.02)	Model	R_g (Å)	r (Å)	L (Å)	T_{sheet} (Å)	X_{sol}
P3HTPMe$_3$	-	Arbit.	21.0	-	-	-	-
x = 0.2	-1.71 ± 0.05	Rods	-	17.9	483.1	-	0.53
x = 0.5	-2.22 ± 0.05	Sheets	-	-	-	~10	-
x = 1.0	-2.61 ± 0.04	Sheets and spheres	-	-	-	18.0	-
x = 2.0	-1.83 ± 0.01	Sheets	-	-	-	13.7	-
x = 5.0	-0.46 ± 0.09	Spheres	-	24.8	-	-	0.34
x = 20.0	-0.26 ± 0.10	Arbit	19.4	-	-	-	-

Table A.5.4 Structural parameters obtained from SANS data for **P3HTPMe$_3$(d_{25}-SDS)$_x$** in D_2O: α is the scattering power of the defined q region. R_g is the radius of gyration calculated from the corresponding Guinier plot. T_{sheet} is the sheet thickness, r is the radius of the sphere or cylinder and L is the length of the cylinder obtained from the best fit to the data using the Cylinder, Lamellar and Spherical Models in SasView. X_{sol} is the calculated solvent fraction in the aggregates.

Sample	$q^{-\alpha}$ (q < 0.02)	Model	R_g (Å)	r (Å)	L (Å)	T_{sheet} (Å)
P3HTPMe$_3$	-	Arbit.	21.0	-	-	-
x = 0.2	-1.30 ± 0.11	Cylinder	-	17.0	105.9	-
x = 0.5	-1.97 ± 0.06	Lamellar	-	-	-	-
x = 1.0	-2.69 ± 0.02	Lamellar	-	-	-	34.0
x = 2.0	-1.96 ± 0.03	Lamellar	-	-	-	36.5
x = 5.0	-2.08 ± 0.12	Lamellar	-	-	-	25.9
x = 20.0	No scatter	-	-	-	-	-

Table A.5.5 Structural parameters obtained from SANS data for **P3HT-*b*-P3HTPMe$_3$(SDS)$_x$** in D_2O: α is the scattering power of the defined q region. L_{core}, r_{core} and T_{shell} are the core length, core radius and shell thickness, respectively, obtained from the best fits to the data using the Core-Shell-Cylinder Model in SasView. $X_{sol\text{-}core}$ and $X_{sol\text{-}shell}$ are the calculated solvent fractions in the core and shell, respectively.

Sample	$q^{-\alpha}$ (q<0.02)	$q^{-\alpha}$ (0.02<q<0.07)	$q^{-\alpha}$ (q>0.07)	Model	L_{core} (Å)	r_{core} (Å)	T_{shell} (Å)	T_{sheet} (Å)	$X_{sol\text{-}core}$	$X_{sol\text{-}shell}$
P3HT-*b*-P3HTPMe$_3$	-1.61 ± 0.15	-5.42 ± 0.08	-2.64 ± 0.72	Core-shell cylinder	517.8	47.2	69.5	-	0.05	0.82
***x* = 0.2**	-1.17 ± 0.05	-5.02 ± 0.08	-2.71 ± 0.35	Core-shell cylinder	580.7	34.3	75.9	-	0.09	0.76
***x* = 0.5**	-1.41 ± 0.06	-4.31 ± 0.10	-3.68 ± 0.32	Core-shell cylinder	541.2	49.2	86.9	-	0.01	0.79
***x* = 1.0**	-1.90 ± 0.04	-3.21 ± 0.16	-3.52 ± 0.30	Lamellar	-	-	-	59.4	0.60	-
***x* = 2.0**	-1.87 ± 0.08	-2.83 ± 0.13	-4.00 ± 0.18	Sheets and spheres	-	-	-	88.4	0.83	-
***x* = 5.0**	-1.68 ± 0.10	-1.97 ± 0.14	-4.00 ± 0.10	Sphere [a]	-	26.6	-	-	-	-
***x* = 20.0**	-	-	-4.00 ± 0.34	Sphere [a]	-	23.1	-	-	-	-

[a] This data was only fit between 0.027 and 0.24 Å^{-1} with fitted scattering length densities (SLDs) of 2.38 × 10^{-6} Å^{-2} and 3.63 × 10^{-6} Å^{-2} for x = 5.0 and x = 20.0, respectively. It was not possible to calculate the solvent fraction.

Table A.5.6 Structural parameters obtained from SANS data for **P3HT-*b*-P3HTPMe$_3$(d_{25}-SDS)$_x$** in D_2O: α is the scattering power of the defined q region. L_{core}, r_{core} and T_{shell} are the core length, core radius and shell thickness, respectively, obtained from the best fits to the data using the Core-Shell-Cylinder and Lamellar Models in SasView. $X_{sol\text{-}core}$ and $X_{sol\text{-}shell}$ are the calculated solvent fractions in the core and shell, respectively.

Sample	$q^{-\alpha}$ (q<0.02)	$q^{-\alpha}$ (0.02<q<0.07)	$q^{-\alpha}$ (q>0.07)	Model	L_{core} (Å)	r_{core} (Å)	T_{shell} (Å)	T_{sheet} (Å)	$X_{sol\text{-}core}$	$X_{sol\text{-}shell}$
P3HT-*b*-P3HTPMe$_3$	-1.61 ± 0.15	-5.42 ± 0.08	-2.64 ± 0.72	Core-shell cylinder	517.8	47.2	69.5	-	0.05	0.82
***x* = 0.2**	-1.49 ± 0.06	-5.41 ± 0.06	-2.16 ± 0.27	Core-shell cylinder	483.0	39.1	64.5	-	0.02	0.75
***x* = 0.5**	-1.74 ± 0.03	-4.95 ± 0.09	-1.71 ± 0.13	Core-shell cylinder	476.1	39.7	70.7	-	0.10	0.82
***x* = 1.0**	-1.97 ± 0.07	-4.64 ± 0.08	-3.07 ± 0.21	Core-shell cylinder	477.3	49.5	71.4	-	0.02	0.81
***x* = 2.0**	-1.58 ± 0.02	-4.06 ± 0.11	-1.97 ± 0.27	Lamellar	-	-	-	78.3	-	-
***x* = 5.0**	-1.54 ± 0.08	-4.04 ± 0.08	-3.19 ± 0.48	Lamellar	-	-	-	82.2	-	-
***x* = 20.0**	-1.51 ± 0.03	-3.89 ± 0.16	-1.42 ± 0.49	Lamellar	-	-	-	80.6	-	-

Table A.5.7 Structural parameters obtained from SANS data for pure **P3HTPMe$_3$** and **P3HTPMe$_3$** with a 1:1 charge ratio of PFOS, d_{25}-SDS and SDS in D_2O. α is the scattering power of the defined q region. R_g is the radius of gyration calculated from the corresponding Guinier plot. T_{sheet} is the sheet thickness, respectively, obtained from the best fits to the data using the Lamellar Model in SasView. X_{sol} is the calculated solvent fractions in the sheet.

Sample	$q^{-\alpha}$ ($q < 0.02$)	Model	R_g (Å)	T_{sheet} (Å)	X_{sol}
P3HTPMe$_3$	-	Arbit.	21.0	-	-
with **PFOS**	-2.31 ± 0.07	Lamellar	-	48.1	0.71
with **d_{25}-SDS**	-2.69 ± 0.02	Lamellar	-	34.0	0.6
with **SDS**	-2.61 ± 0.04	Lamellar	-	20.1	0.37

Table A.5.8 Structural parameters obtained from SANS data for pure **P3HT-*b*-P3HTPMe$_3$** and **P3HT-*b*-P3HTPMe$_3$** with a 1:1 charge ratio of PFOS, d_{25}-SDS and SDS in D_2O. α is the scattering power of the defined q region. L_{core}, r_{core}, T_{shell} and T_{sheet} are the core length, core radius, shell thickness and sheet thickness, respectively, obtained from the best fits to the data using the Core-Shell Cylinder and Lamellar Models in SasView. $X_{sol\text{-}core}$ and $X_{sol\text{-}shell}$ are the calculated solvent fractions in the core and shell, respectively.

Sample	$q^{-\alpha}$ (q<0.02)	$q^{-\alpha}$ (0.02<q<0.07)	$q^{-\alpha}$ (q>0.07)	Model	L_{core} (Å)	r_{core} (Å)	T_{shell} (Å)	T_{sheet} (Å)	$X_{sol\text{-}core}$	$X_{sol\text{-}shell}$
CPE	-1.61 ± 0.15	-5.42 ± 0.08	-2.64 ± 0.72	Core-shell cylinder	517.85	47.23	69.49	-	0.05	0.82
with **PFOS**	-2.23 ± 0.01	-4.81 ± 0.12	-2.77 ± 0.45	Core-shell cylinder	466.34	58.96	77.7	-	0.16	0.85
with **d_{25}-SDS**	-1.97 ± 0.04	-4.64 ± 0.08	-3.07 ± 0.21	Core-shell cylinder	477.3	49.5	71.4	-	0.02	0.81
with **SDS**	-1.90 ± 0.04	-3.21 ± 0.16	-3.52 ± 0.30	Lamellar	-	-	-	59.4	0.60	-

SANS data of CPEs and CPE-SDS mixtures in d_4-MeOD

Table A.5.9 Structural parameters obtained from SANS data for **P3HTPMe$_3$** and **P3HTPMe$_3$(SDS)$_1$** in d_4-MeOD: α is the scattering power of the defined q region. L, r and L_{Kuhn} are the length, radius and Kuhn length, respectively, obtained from the best fits to the data using the Cylinder, Flexible Rod and Lamellar Models in SasView. X_{sol} is the calculated solvent fraction in the aggregate.

Sample	$q^{-\alpha}$ ($q < 0.02$)	$q^{-\alpha}$ ($0.02 < q < 0.07$)	Model	L (Å)	r (Å)	L_{Kuhn} (Å)	T_{sheet} (Å)	X_{sol}
P3HTPMe$_3$	-1.22 ± 0.02	-1.22 ± 0.02	Cylinder	2865	12.9	-	-	0.79
			Flexible Cylinder	900.5	12.9	225.6	-	0.85
P3HTPMe$_3$(SDS)$_1$	-1.86 ± 0.04	-2.50 ± 0.04	Lamellar Sheet	-	-	-	47.2	~0.50

Table A.5.10 Structural parameters obtained from SANS data for **P3HT-*b*-P3HTPMe$_3$** and **P3HT-*b*-P3HTPMe$_3$(SDS)$_1$** in d_4-MeOD: SLD_{sol} is the scattering length density of the solvent, α is the scattering power of the defined q region. L_{core}, r_{core} and T_{shell} are the core length, core radius and shell thickness, respectively, obtained from the best fits to the data using the Core-Shell Cylinder Model in SasView. $X_{sol\text{-}core}$ and $X_{sol\text{-}shell}$ are the calculated solvent fractions in the core and shell, respectively.

Sample	$q^{-\alpha}$ (q<0.02)	$q^{-\alpha}$ (0.02<q<0.07)	$q^{-\alpha}$ (q>0.07)	L_{core} (Å)	r_{core} (Å)	T_{shell} (Å)	$X_{sol\text{-}core}$	$X_{sol\text{-}shell}$
P3HT-*b*-P3HTPMe$_3$	-1.81 ± 0.10	-4.39 ± 0.05	-1.90 ± 0.13	572.8	53.1	77.4	0.15	0.86
P3HT-*b*-P3HTPMe$_3$(SDS)$_1$	-1.82 ± 0.07	-4.93 ± 0.04	-1.64 ± 0.14	544.4	54.3	74.0	0.19	0.85

AFM Blank Images

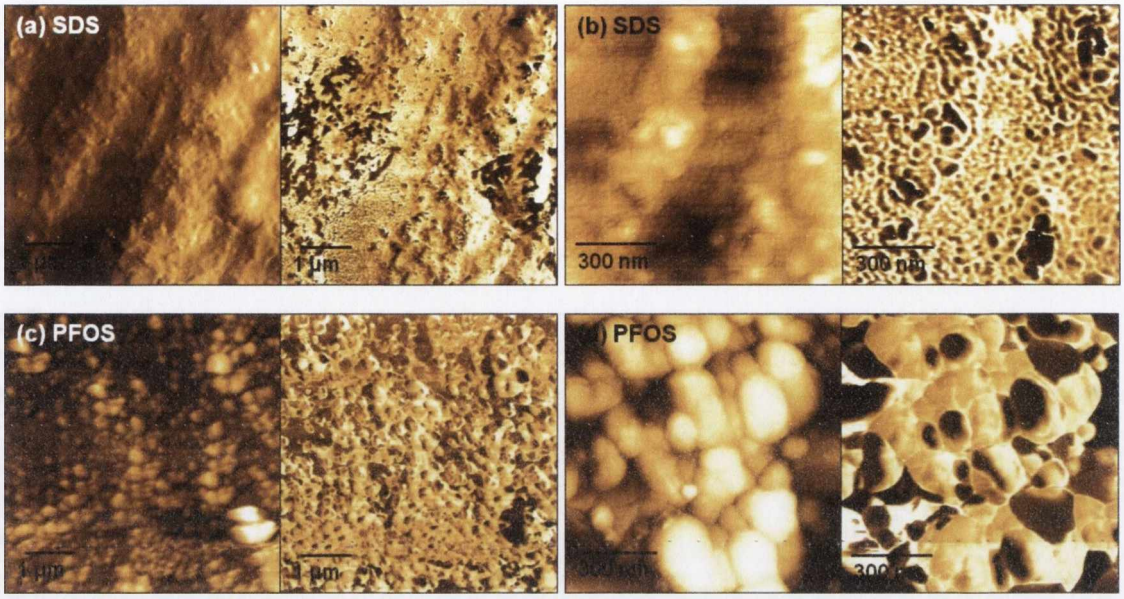


Figure A.5.5 AFM tapping mode images of (a,b) **SDS** and (c,d) **PFOS.** Drop-cast onto silicon from solutions of surfactants in D_2O (10 mg mL^{-1}). Left: height images; right: phase images.

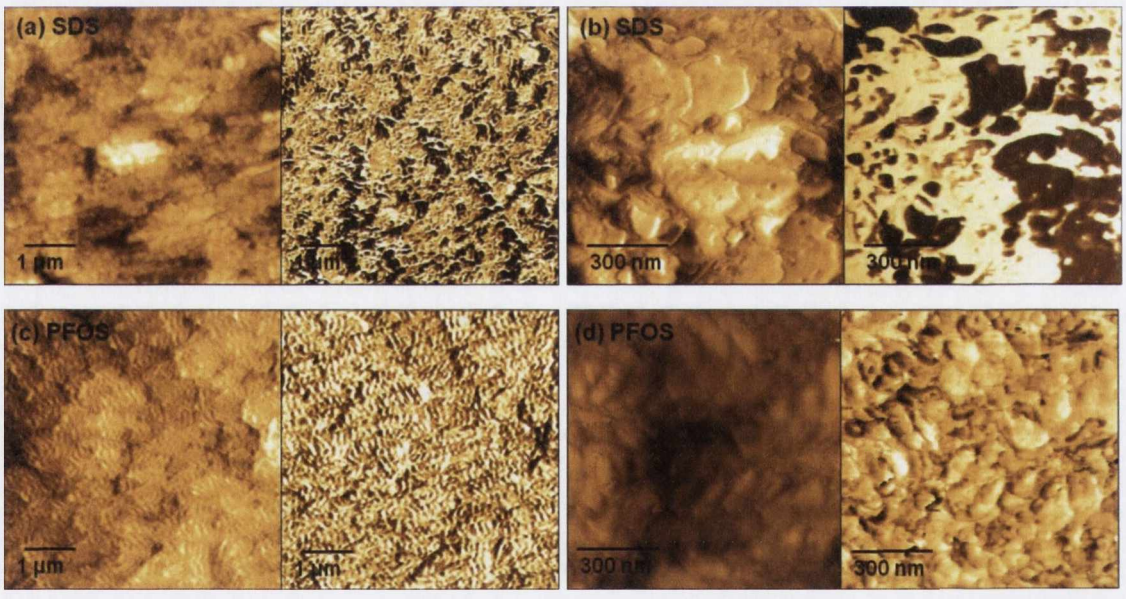


Figure A.5.6 AFM tapping mode images of (a,b) **SDS** and (c,d) **PFOS.** Spin-coated onto silicon from solutions of surfactants in MeOH (10 mg mL^{-1}). Left: height images; right: phase images.

OPV Device Fabrication and Characterisation

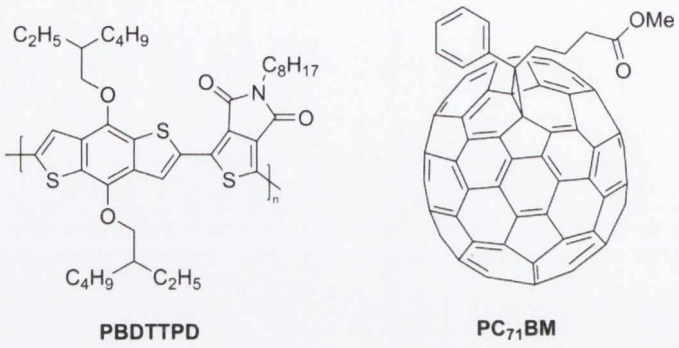


Figure A.5.7 Components of the photoactive layer.

Appendix – Chapter 6

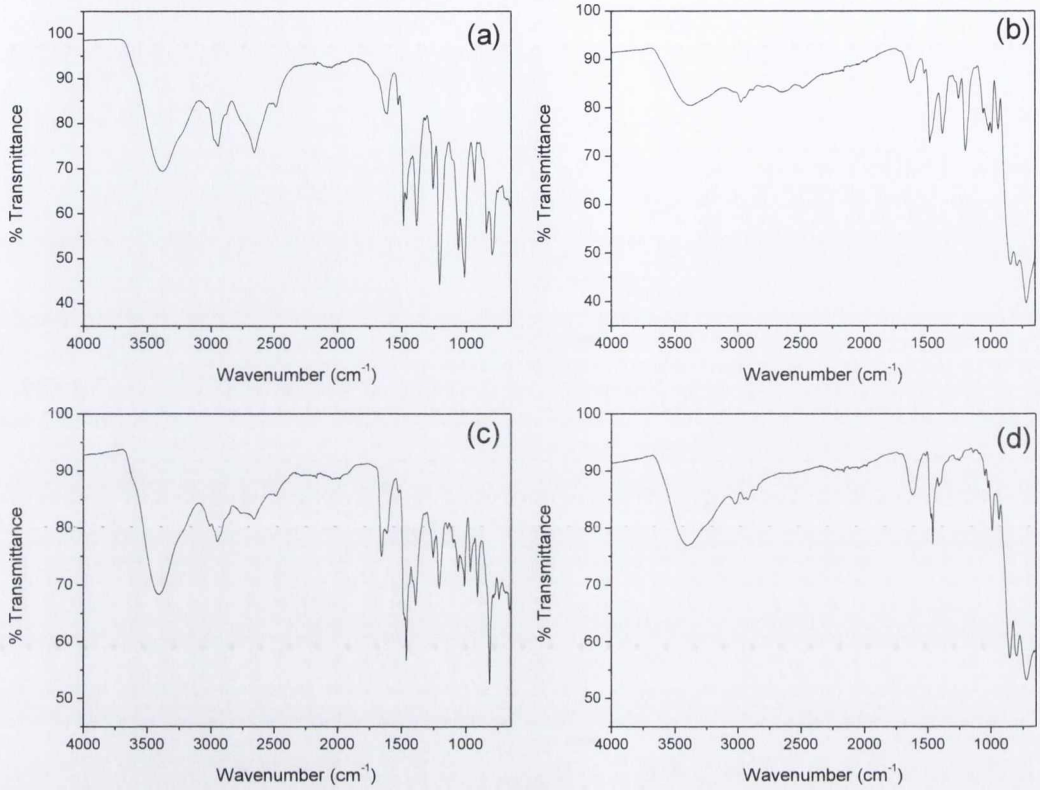


Figure A.6.1 FTIR spectra for (a) **NET**, (b) **POM/NET**=1, (c) **PFP** and (d) **POM/PFP**=1.

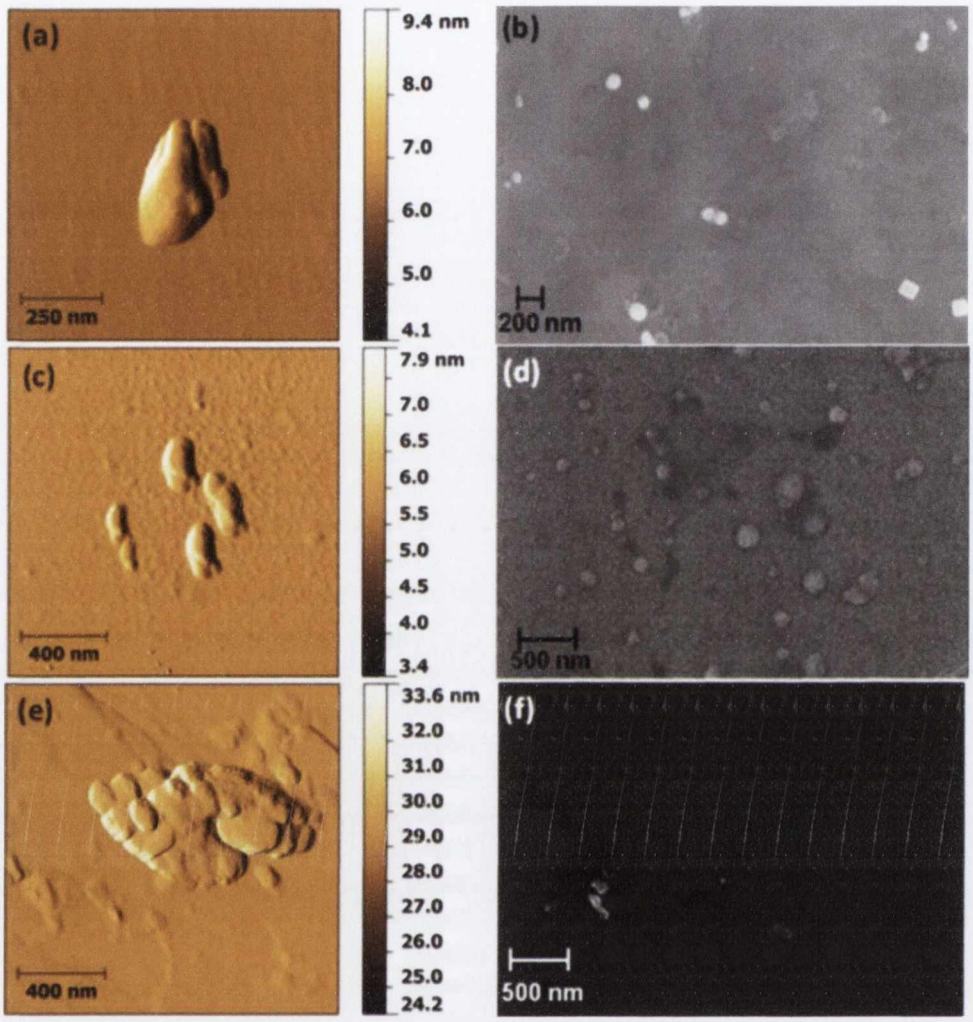


Figure A.6.2 AFM amplitude images of (a) **POM** (5×10^{-7} M), (c) **NET** (6.4×10^{-7} M (r.u.)) and (e) **PFP** (5×10^{-8} M (r.u.)) drop-cast onto freshly cleaved mica. SEM images of (b) **POM** (5×10^{-7} M), (d) **NET** (6.4×10^{-7} M (r.u.)) and (f) **PFP** (5×10^{-7} M (r.u.)) drop-cast onto silicon wafers. SEM measurements were performed by Dr Adam R. Patterson.

Appendix - Chapter 7

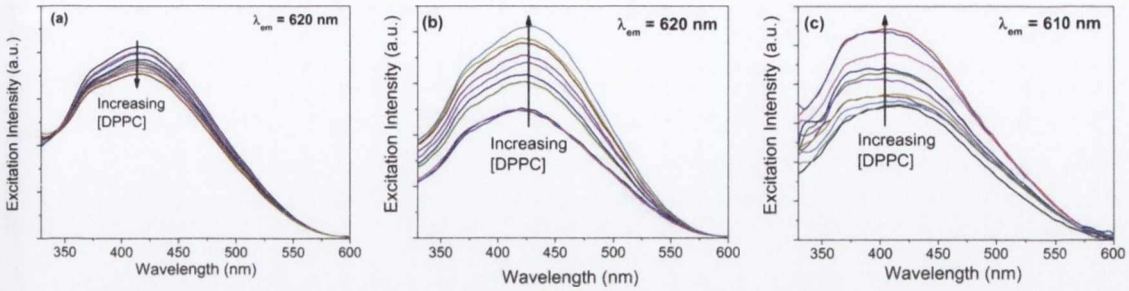


Figure A.7.1 Room temperature excitation spectra of (a) **P3Zwit** (1.29×10^{-5} M (r.u.)) titrated with **DPPC** vesicles (0 - 4.80×10^{-5} M), (b) **P3TMAHT** (3.94×10^{-5} M (r.u.)) titrated with **DPPC** vesicles (0 - 1.59×10^{-3} M) and (c) **P3Anionic** (1.93×10^{-5} M (r.u.)) titrated with **DPPC** vesicles (0 - 4.08×10^{-5} M) in pH 7.3 HEPES buffer.

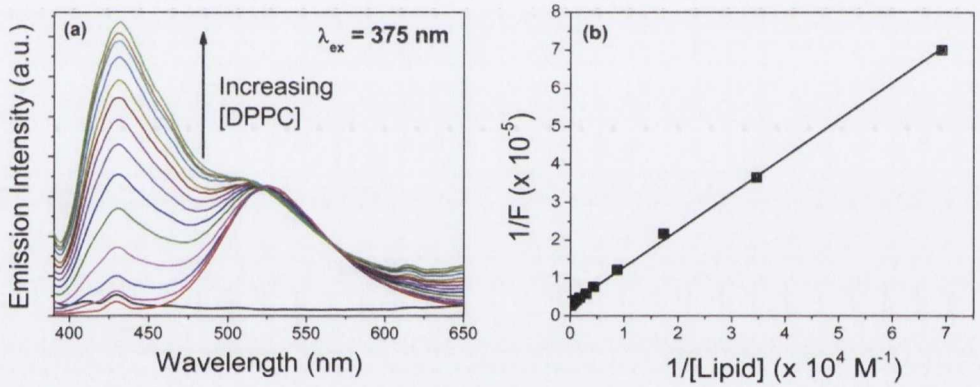


Figure A.7.2 (a) Emission spectra of Prodan (0.5 μM) at different concentrations of **DPPC** vesicles (0-1.62 mM). (λ_{ex} = 375 nm). (b) Double reciprocal plot of the intensity of Prodan at 430 nm with respect to different concentrations of **DPPC** vesicles. The partition coefficient (1.8×10^5) was calculated using $1/F = 55.6/(K_p F_0 L)$, where F_0 and F are the emission intensities of Prodan in aqueous and lipid phase, respectively (λ_{ex} = 435 nm).[1] L is the lipid concentration and 55.6 M is the considered molar concentration of water.

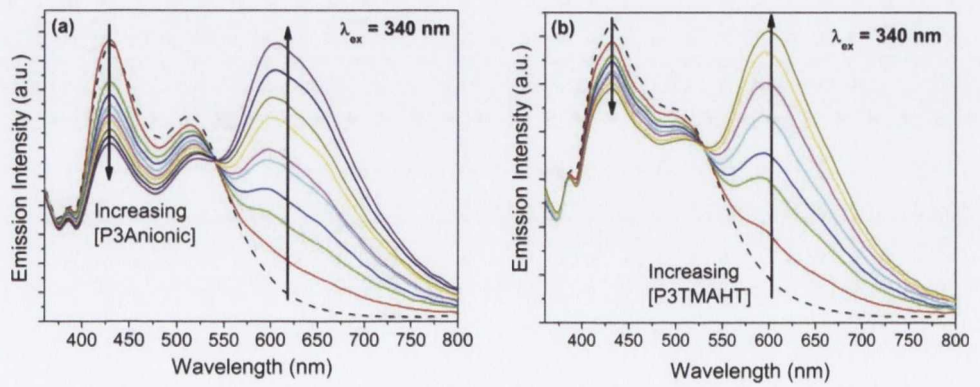


Figure A.7.3 Steady-state emission spectra of Prodan (2×10^{-8} M) in **DPPC** (1×10^{-4} M) vesicles upon the addition of (a) **P3Anionic** (0 - 1.5×10^{-5} M (r.u.)) and (b) **P3TMAHT** (0 - 7.9×10^{-6} M (r.u.)).

[1] N. C. Santos, M. Prieto and M. A. R. B. Castanho, *Biochim. Biophys. Acta*, 2003, **1612**, 123-135.

Calculation of Number of CPE Repeat Units (r.u.) and Number of Chains per DPPC Vesicle

For the sake of comparison, identical concentrations of CPE and **DPPC** were selected. The total concentration of CPE chosen was 1×10^{-5} M (r.u.) and the concentration of **DPPC** was 1×10^{-4} M, giving a 1:10 charge ratio of CPE:**DPPC**. When required the volume used was 2 mL. The total concentration of CPE in the system, $[CPE]_{total}$, is given by:

$$[CPE]_{total} = [CPE]_{DPPC} + [CPE]_{buffer} \quad (A.1)$$

where $[CPE]_{DPPC}$ is the concentration of CPE in **DPPC** vesicles and $[CPE]_{buffer}$ is the concentration of unassociated CPE in buffer solution. $[CPE]_{total}$ is taken as 1×10^{-5} M (r.u.). The partition coefficient, K_p, is described by:

$$K_p, = [CPE]_{DPPC}/[CPE]_{buffer} \quad (A.2)$$

which rearranges to:

$$[CPE]_{DPPC} = K_p[CPE]_{buffer} \quad (A.3)$$

Substituting (3) into (1) gives:

$$[CPE]_{total} = K_p[CPE]_{buffer} + [CPE]_{buffer} = (K_p + 1)[CPE]_{buffer} \quad (A.4)$$

Thus, as K_p and $[CPE]_{total}$ are known, Equation A.4 can be used to solve for $[CPE]_{buffer}$ and Equation A.3 can then be used to calculate $[CPE]_{DPPC}$ (Table A.1). The approximate number of repeat units in a solution of each CPE is given by:

$$\text{Number of CPE r.u.} = \text{volume} \times \text{concentration (r.u.)} \times N_A \quad (A.5)$$

where N_A is Avogadro's number and the volume selected is 2 mL. Division of the number of CPE r.u. by the approximate number of repeat units per individual CPE chain yields the approximate number of chains located in a population of **DPPC** vesicles.

The number of **DPPC** molecules in a large unilamellar vesicle (100 nm) can be calculated from the volume of a **DPPC** molecule (1148 $Å^3$)[1] and the volume of the vesicle (1.1×10^8 $Å^3$)[2], yielding ~8.8×10^4 molecules per **DPPC** vesicle. Given the concentration of DPPC in solution is 1×10^{-4} M, the calculated number of **DPPC** molecules is ~1.2×10^{17} and therefore the number of vesicles is ~ 1.4×10^{12}. Division of the number of CPE r.u. or chains by the approximate number of vesicles results in the approximate number of CPE r.u. (or chains) per **DPPC** vesicle.

[1] N. C. Santos, M. Prieto and M. A. R. B. Castanho, *Biochim. Biophys. Acta*, 2003, **1612**, 123-135

[2] C. Huang and J. T. Mason, *Proc. Natl. Acad. Sci.*, 1978, *75*, 308-310.

Table A.7.1 Summary of the values used and determined from the calculations of the number of CPE r.u. (and chains) per **DPPC** vesicle. K_p is the partition coefficient, $[CPE]_{DPPC}$ is the concentration of CPE in **DPPC** vesicles and $[CPE]_{buffer}$ is the concentration of unassociated CPE in buffer solution.

CPE	$[CPE]_{Total}$ ((r.u.) M)	K_p	$[CPE]_{buffer}$ ((r.u.) M)	$[CPE]_{DPPC}$ ((r.u.) M)	# of r.u. in DPPC
P3Zwit	1×10^{-5}	1.06×10^{5}	9.43×10^{-11}	9.99991×10^{-6}	1.20440×10^{16}
P3TMAHT	1×10^{-5}	1.28×10^{3}	7.81×10^{-9}	9.99219×10^{-6}	1.20346×10^{16}
P3Anionic	1×10^{-5}	4.86×10^{4}	2.06×10^{-10}	9.99979×10^{-6}	1.20438×10^{16}

Table A.7.1 *continued...*

CPE	Number of CPE r.u. per chain	# of chains in DPPC	# of r.u. in each DPPC vesicle	# of chains in each DPPC vesicle
P3Zwit	49	9.99999×10^{-2}	8800	180
P3TMAHT	49	9.99219×10^{-2}	8793	179
P3Anionic	21	9.99979×10^{-2}	8800	419

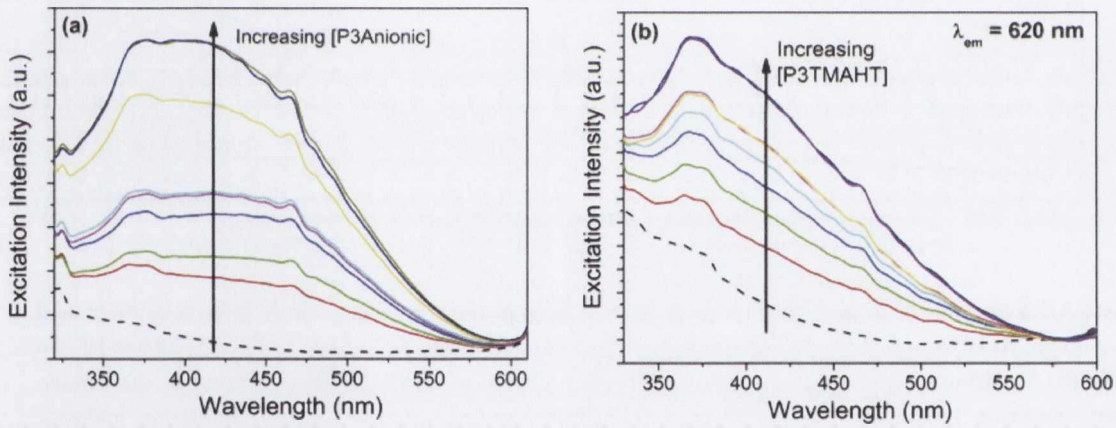


Figure A.7.4 Steady-state excitation spectra of Prodan (2×10^{-8} M) in **DPPC** (1×10^{-4} M) vesicles upon the addition of (a) **P3Anionic** (0 - 1.5×10^{-5} M (r.u.)) and (b) **P3TMAHT** (0 - 7.9×10^{-6} M (r.u.)).

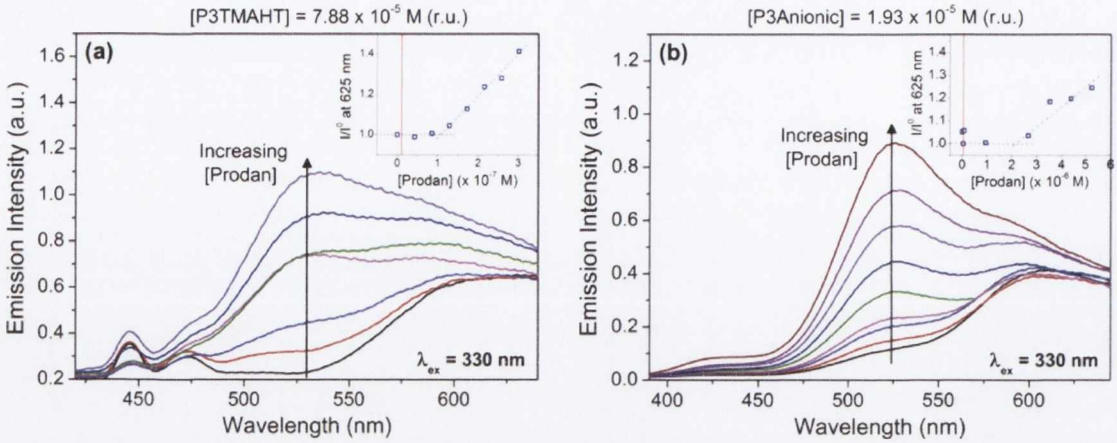


Figure A.7.5 (a) Emission spectra of **P3TMAHT** (7.88×10^{-5} M (r.u.)) upon addition of Prodan (0 – 2.94×10^{-7} M). (b) Emission spectra of **P3Anionic** (1.93×10^{-5} M (r.u.)) upon addition of Prodan (0 – 5.24×10^{-6} M). λ_{ex} = 330 nm. Insets: Ratio of the CPE emission intensity, I, to the initial intensity, I^0, at 625 nm, as a function of the concentration of Prodan. The red lines show the approximate concentration of Prodan used in the FRET experiments (2×10^{-8} M).

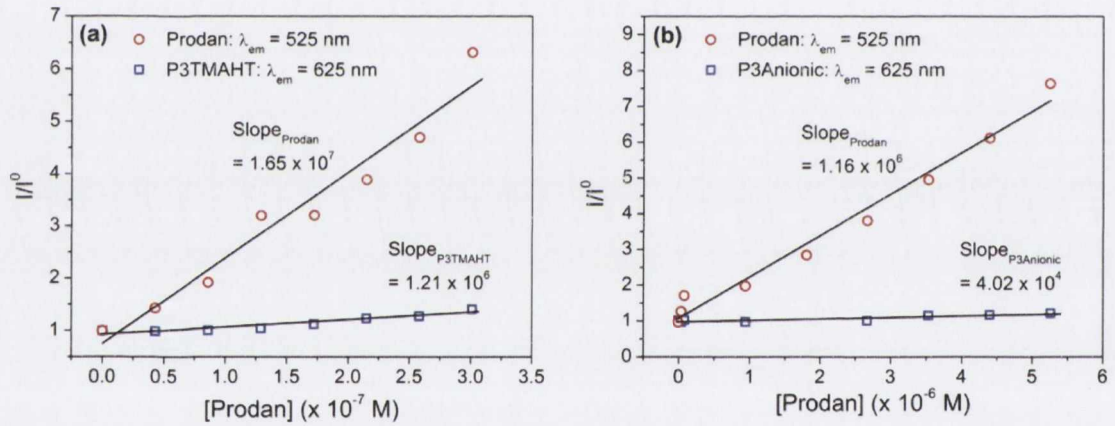


Figure A.7.6 Ratio of emission intensity, I, over the initial intensity, I^0, at 525 and 625 nm, for Prodan and CPEs respectively, as a function of Prodan concentration (λ_{ex} = 330 nm): (a) **P3TMAHT** (7.88×10^{-5} M (r.u.)); (b) **P3Anionic** (1.93×10^{-5} M (r.u.)). The solid trendlines reveal a linear increase in the Prodan (donor) emission intensity with increasing concentration, while the CPE (acceptor) emission intensity remains unaffected.

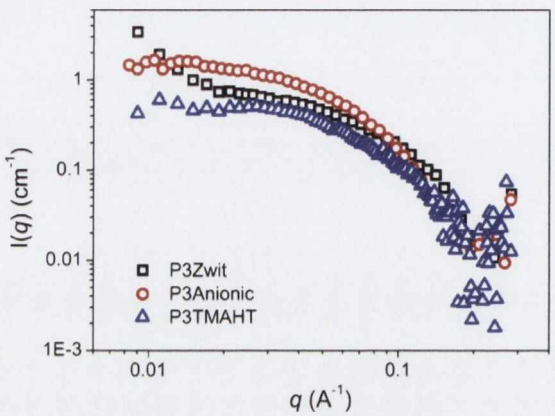


Figure A.7.7 SANS data of **P3Anionic**, **P3TMAHT** and **P3Zwit** in D_2O (10 mg mL^{-1}), 30 mM NaCl.

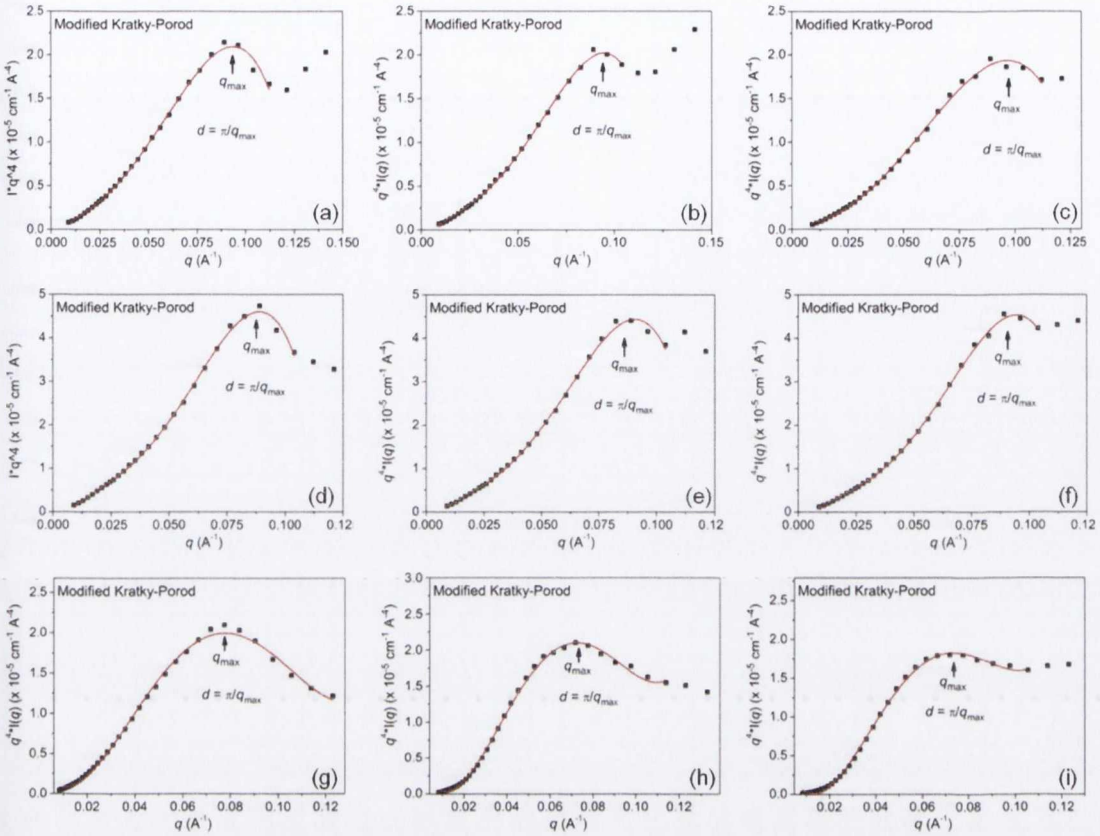


Figure A.7.8 Modified Kratky-Porod plots for CPE/**DPPC** SANS data. **P3Zwit**:**DPPC** at (a) 0.5:1, (b) 1:1 and (c) 1.5:1, **P3TMAHT**:**DPPC** at (d) 0.5:1, (e) 1:1 and (f) 1.5:1 and **P3Anionic**:**DPPC** at (g) 0.5:1, (h) 1:1 and (i) 1.5:1 molar ratios.

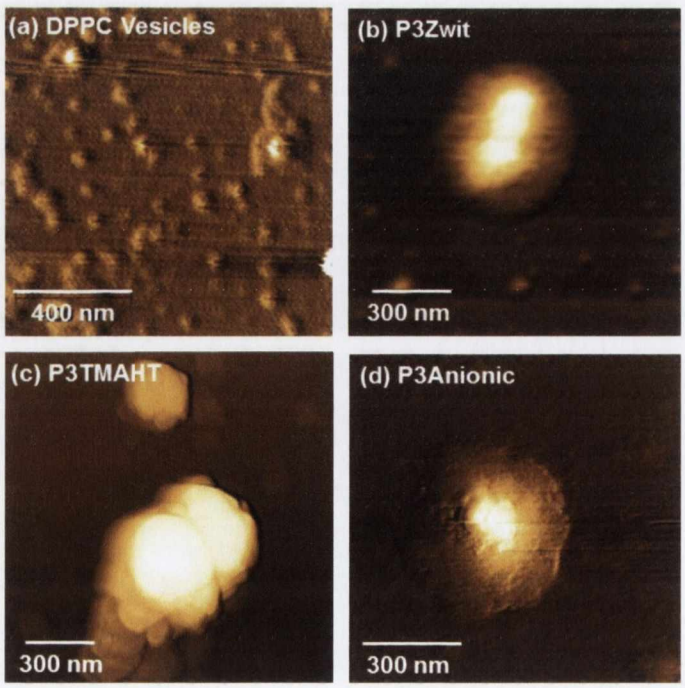
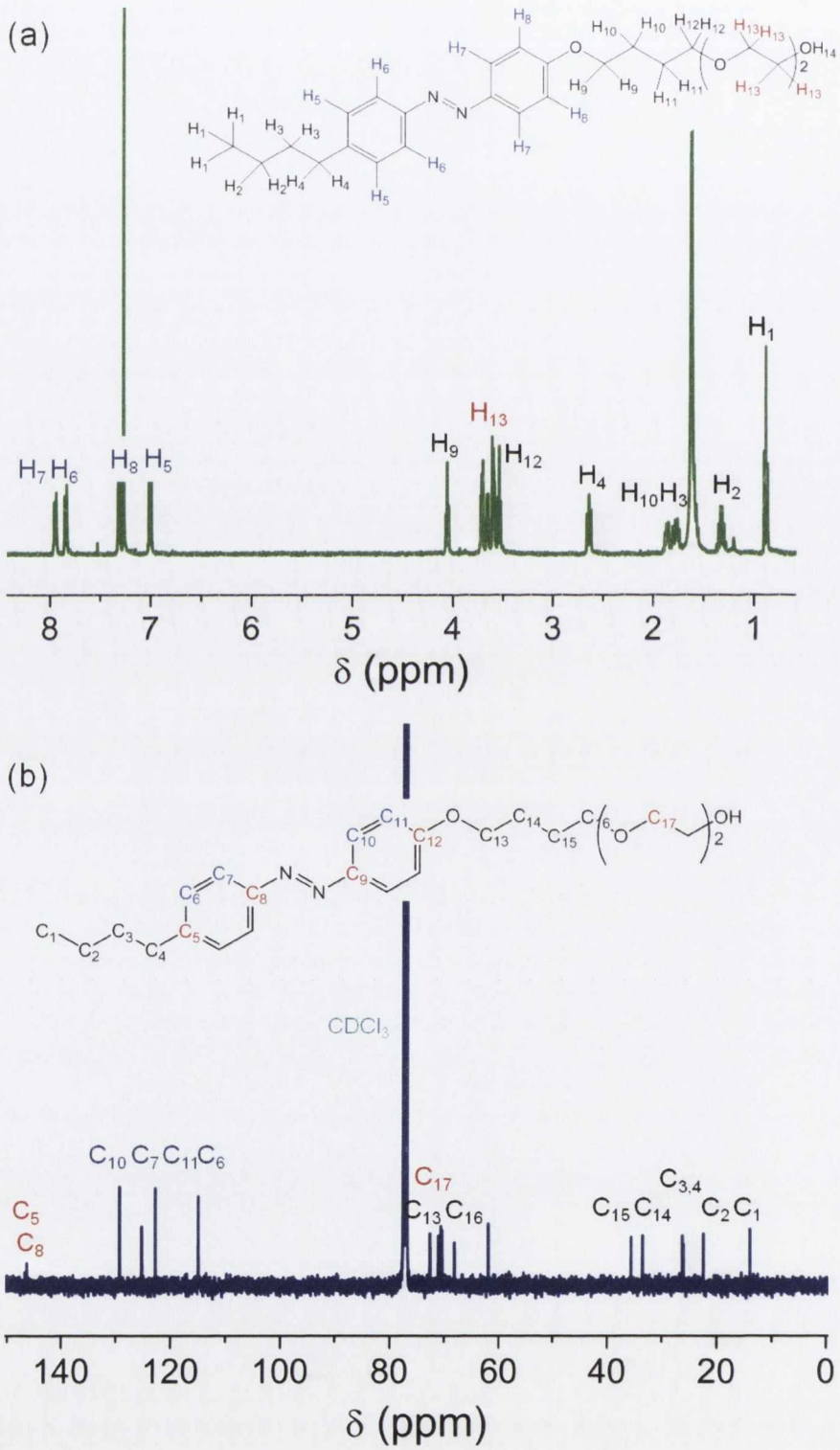


Figure A.7.9 Tapping mode AFM images of (a) **DPPC** vesicles (1.6×10^{-5} M), (b) **P3Zwit**, (c) **P3TMAHT** and (d) **P3Anionic** (1.0×10^{-5} M (r.u.)) drop-cast onto freshly cleaved mica.

Appendix - Chapter 8

Structural Characterisation of the Neutral Surfactants

The integration of the three peaks at ~3.6 ppm in each ^{1}H NMR spectra corresponds to the number of protons in the ethylene glycol chain of the surfactant: **$C_4AzoOC_4E_2$** = ~8H, **$C_4AzoOC_4E_4$** = ~16H, **$C_4AzoOC_4E_6$** = ~24H.



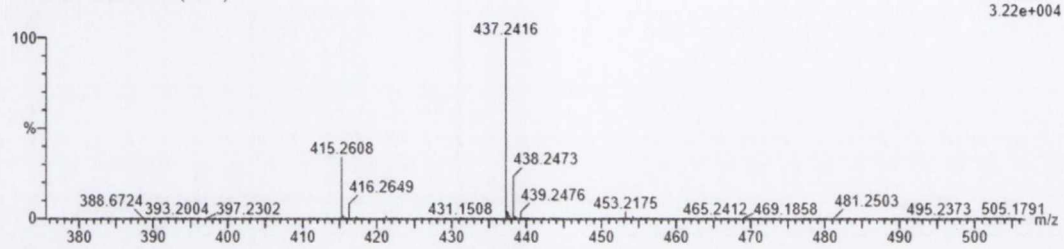
(c)

Single Mass Analysis
Tolerance = 10.0 PPM / DBE: min = 0.5, max = 100.0
Element prediction: Off
Number of isotope peaks used for i-FIT = 3

Monoisotopic Mass, Even Electron Ions
184 formula(e) evaluated with 1 results within limits (all results (up to 1000) for each mass)
Elements Used:
C: 0-24 H: 0-35 N: 0-2 O: 0-4 Na: 0-1 I: 0-2

Judith Houston (RE), JH009
LCT20150717MF012 92 (1.537)

TOF MS ES+
3.22e+004



Minimum:				0.5		
Maximum:		5.0	10.0	100.0		
Mass	Calc. Mass	mDa	PPM	DBE	i-FIT	Formula
437.2416	437.2416	0.0	0.0	8.5	147.6	C24 H34 N2 O4 Na

(d)

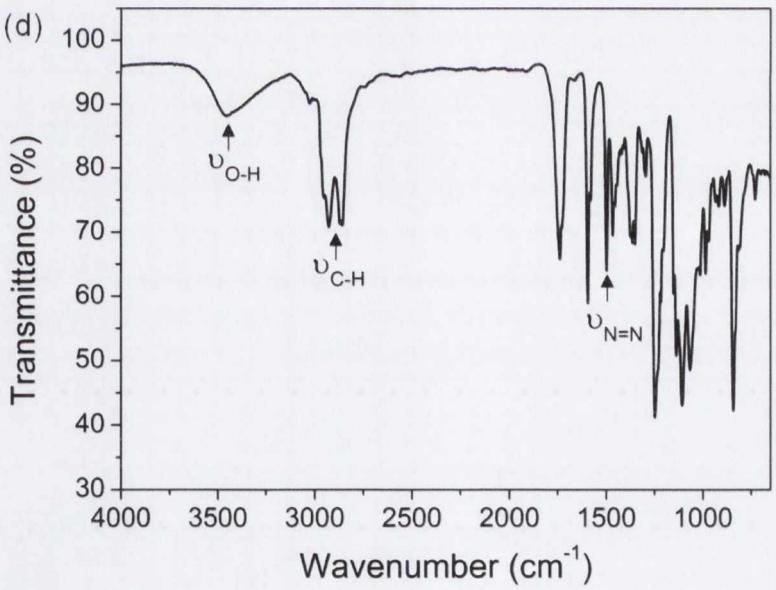
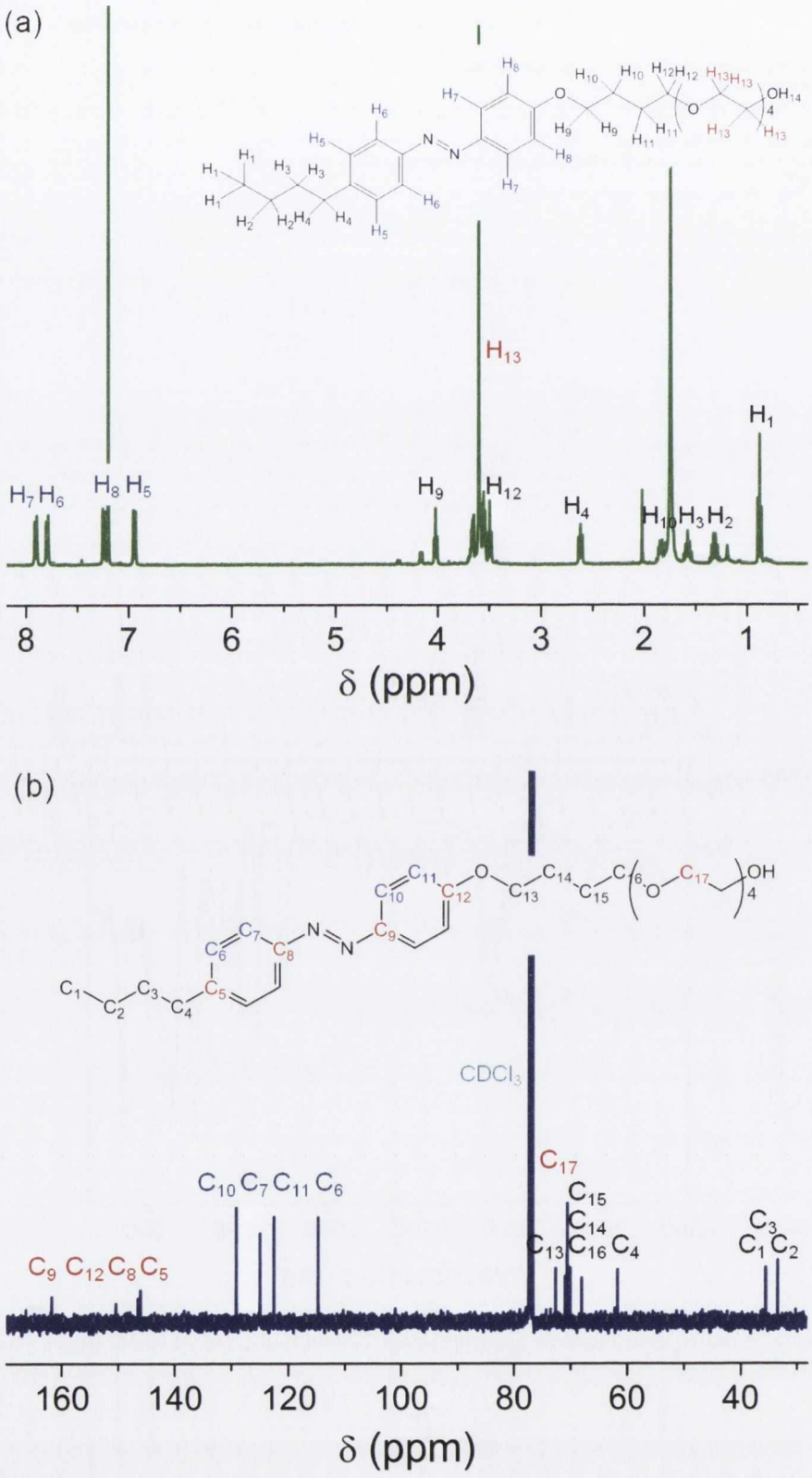


Figure A.8.1 Characterisation of azobenzene photosurfactant **C_4AzoOC_4E$_2$**: (a) ^{1}H NMR, (b) ^{13}C NMR, (c) HRMS and (d) FTIR.

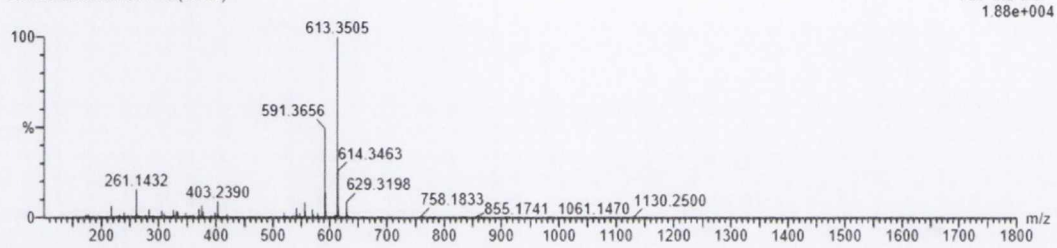

(a)
I
H13
H1
H7 H6
H8 H5
H9
H12
H4
H10 H3 H2
8
7
6
5
4
3
2
1
δ (ppm)
(b)
CDCl3
C17
C10 C7 C11 C6
C9 C12 C8 C5
C15
C14
C16
C13
C4
C3
C1 C2
160
140
120
100
80
60
40
δ (ppm)

(c)

Single Mass Analysis
Tolerance = 10.0 PPM / DBE: min = 0.5, max = 100.0
Element prediction: Off
Number of isotope peaks used for i-FIT = 3

Monoisotopic Mass, Even Electron Ions
25 formula(e) evaluated with 1 results within limits (all results (up to 1000) for each mass)
Elements Used:
C: 0-32 H: 0-51 N: 0-2 O: 0-8
Judith Houston (RE), JH010
LCT20150812MF011 45 (0.750)

TOF MS ES+
1.88e+004



Minimum:				0.5		
Maximum:		5.0	10.0	100.0		
Mass	Calc. Mass	mDa	PPM	DBE	i-FIT	Formula
591.3656	591.3645	1.1	1.9	8.5	89.4	C32 H51 N2 O8

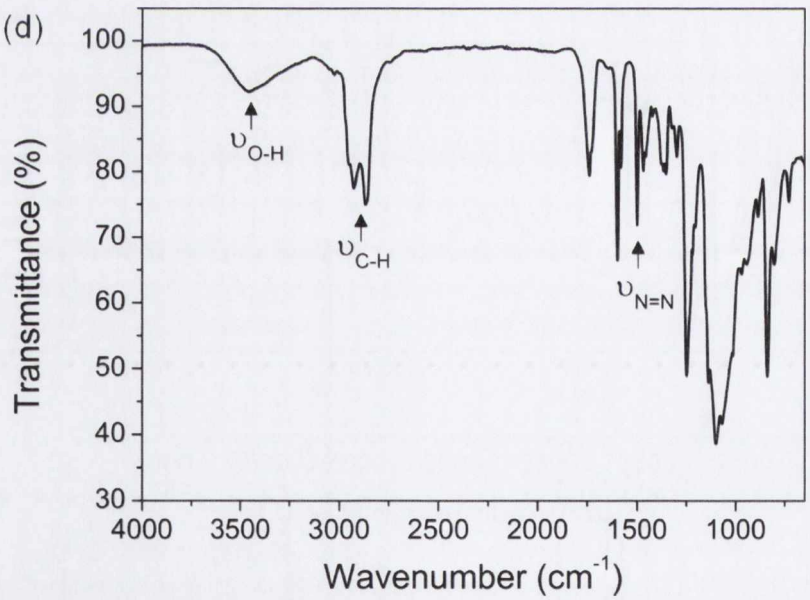
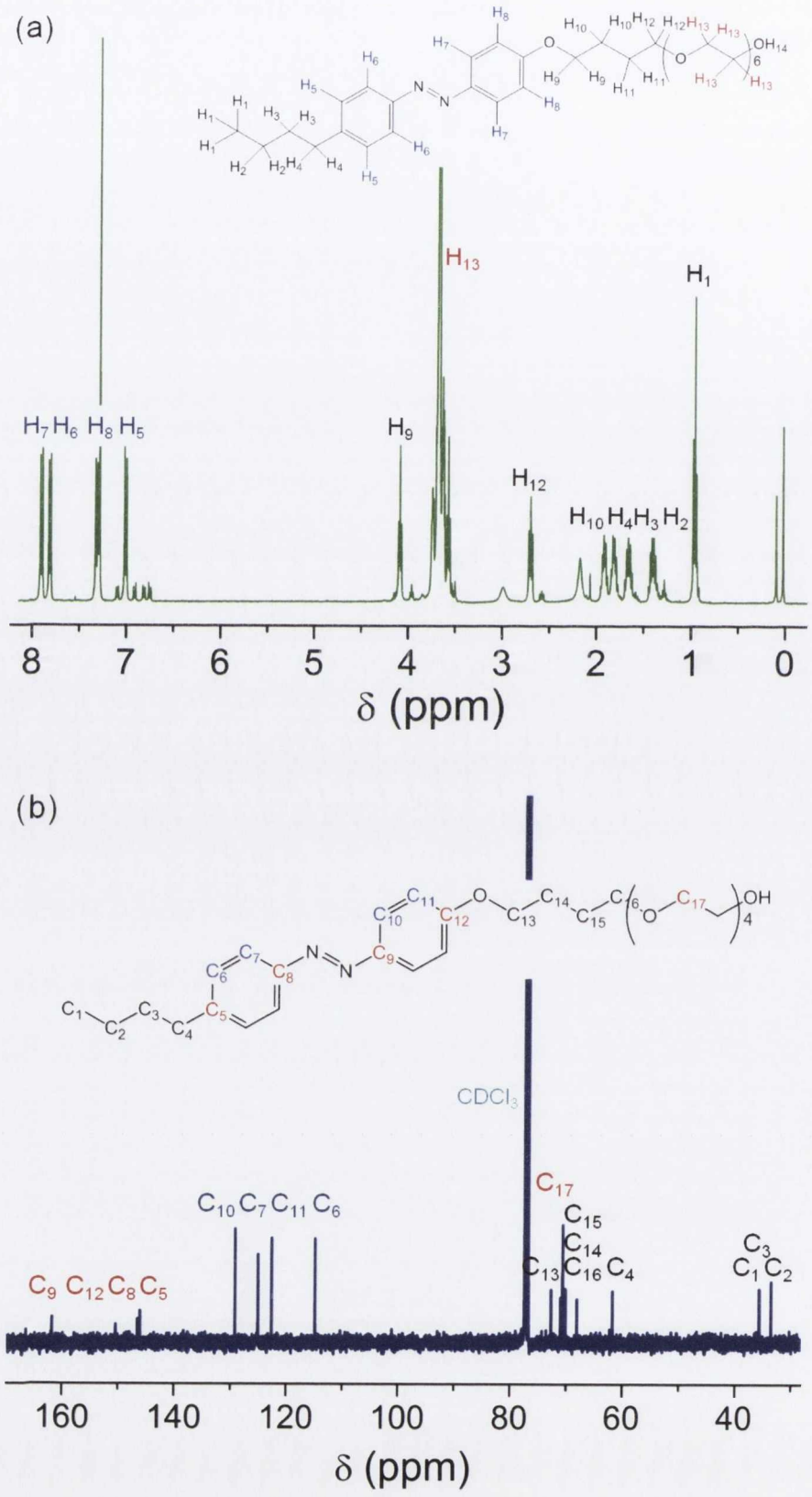


Figure A.8.2 Characterisation of azobenzene photosurfactant **C_4AzoOC_4E$_4$**: (a) ^{1}H NMR, (b) ^{13}C NMR, (c) HRMS and (d) FTIR.

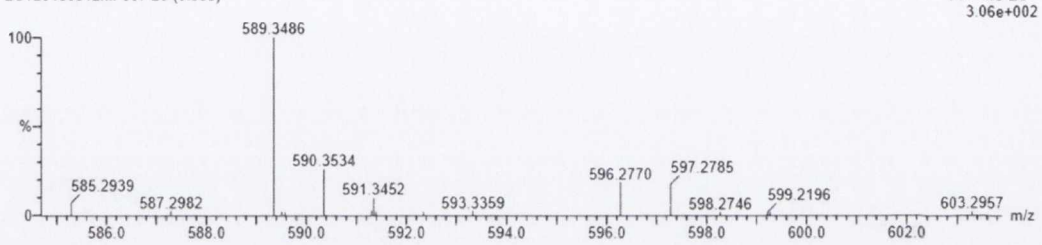

(a)
H7 H6 H8 H5
H9
H13
H12
H1
H10 H4 H3 H2
8 7 6 5 4 3 2 1 0
δ (ppm)
(b)
CDCl3
C10 C7 C11 C6
C9 C12 C8 C5
C17
C15
C14
C16
C13
C4
C3
C1 C2
160 140 120 100 80 60 40
δ (ppm)

(c)

Single Mass Analysis
Tolerance = 10.0 PPM / DBE: min = 0.5, max = 100.0
Element prediction: Off
Number of isotope peaks used for i-FIT = 3

Monoisotopic Mass, Even Electron Ions
25 formula(e) evaluated with 1 results within limits (all results (up to 1000) for each mass)
Elements Used:
C: 0-32 H: 0-50 N: 0-2 O: 0-8
Judith Houston (RE), JH010
LCT20150812MF007 20 (0.335)

TOF MS ES-
3.06e+002



Minimum:				0.5		
Maximum:		5.0	10.0	100.0		
Mass	Calc. Mass	mDa	PPM	DBE	i-FIT	Formula
589.3486	589.3489	-0.3	-0.5	9.5	5.8	C32 H49 N2 O8

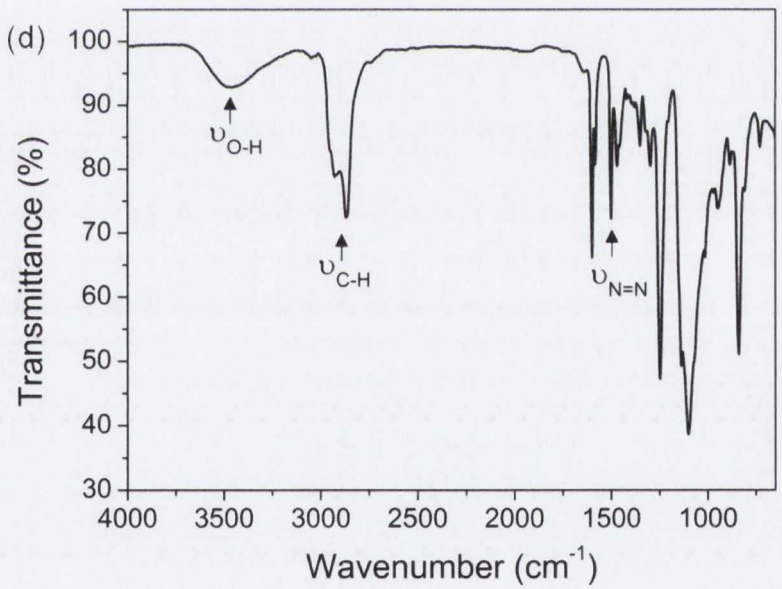


Figure A.8.3 Characterisation of azobenzene photosurfactant **C_4AzoOC_4E$_6$**: (a) ^{1}H NMR, (b) ^{13}C NMR, (c) HRMS and (d) FTIR

UV/Vis Absorption and Kinetics Studies

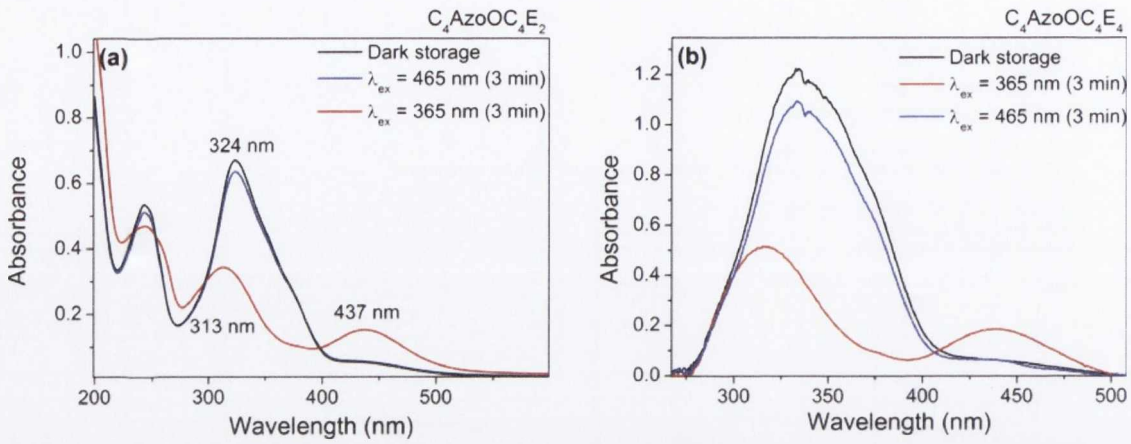


Figure A.8.4 UV/Vis absorption spectra of (a) **$C_4AzoOC_4E_2$** (9.7×10^{-5} M) and (b) **$C_4AzoOC_4E_4$** (8.0×10^{-5} M) at 20 °C. The spectra correspond to the *trans*-form (stored in the dark, black line), the photostationary state (after irradiation at λ_{ex} = 365 nm for 3 min, red line) and the reverse *cis*- to *trans*-isomerisation (after irradiation at λ_{ex} = 465 nm for 3 min, blue line).

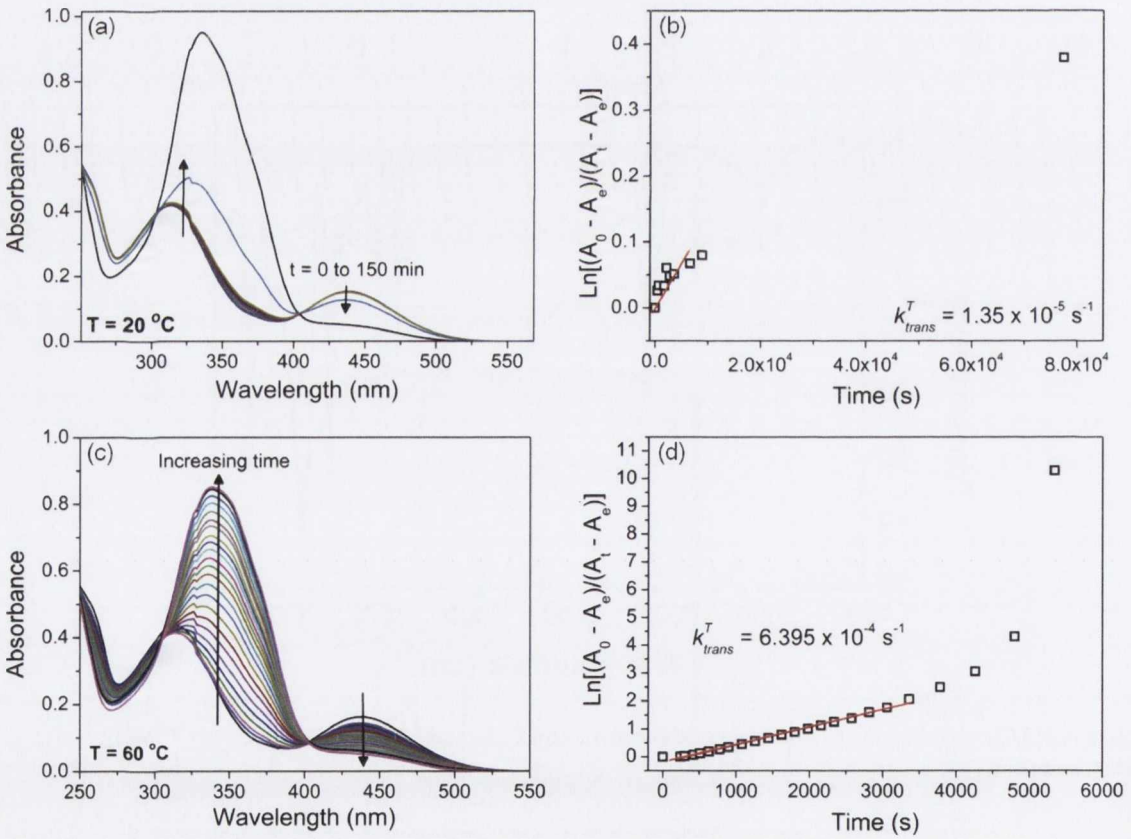


Figure A.8.5 Thermal *cis*-to-*trans* relaxation studies of **$C_4AzoOC_4E_6$**. UV/Vis absorption spectra of **$C_4AzoOC_4E_6$** in water (3.4×10^{-5} M) over time at (a) 20 °C and (c) 60 °C after illumination with λ_{ex} = 365 nm for 5 min to achieve maximum *cis*-isomer content. (b,d) Plots to show the first order rate laws for the thermally-induced reverse (*cis-trans*) isomerisation. k_{trans}^{T} is the corresponding rate constant.

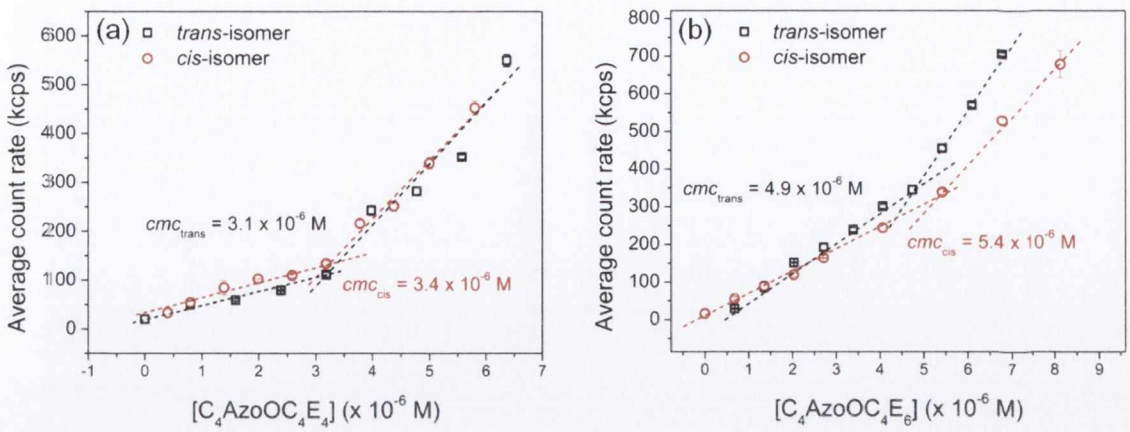


Figure A.8.6 Effect of concentration on the intensity of scattered light of an aqueous solution of (a) **$C_4AzoOC_4E_4$** and (b) **$C_4AzoOC_4E_6$** in the *trans*- and *cis*-forms at 20 °C. The *cmc* values are obtained at the intersection between the two trend-lines. The error bars show the standard deviation of the mean surface tension value obtained over 3 measurements.

Small-Angle Neutron Scattering Data Analysis

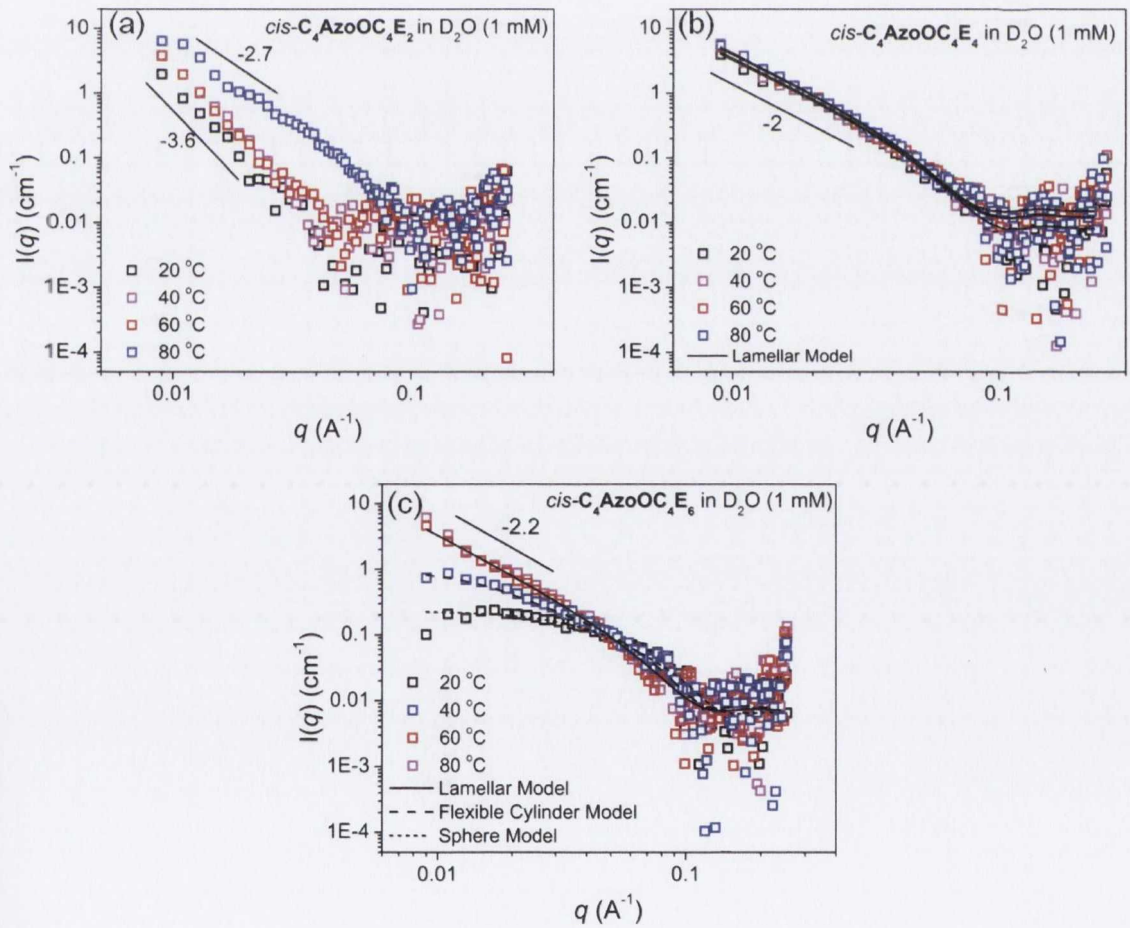


Figure A.8.7 SANS data for the *cis*-isomers of (a) **$C_4AzoOC_4E_2$**, (b) **$C_4AzoOC_4E_4$** and (c) **$C_4AzoOC_4E_6$** in D_2O (1 mM) as a function of temperature. Straight lines show -2, -2.2, -2.7 and -3.6 decays for comparison. Solid, dashed and dotted lines correspond to the fits to the models described in the main text.

Table A.8.1 Structural parameters obtained from SANS data for *trans*-$C_4AzoOC_4E_2$ in D_2O (1.0×10^{-3} M) as a function of temperature: α is the scattering power of the defined q region. T_{sheet} is the sheet thickness, obtained from the best fit to the data using the Lamellar Model in SasView. X_{sol} is the calculated solvent fraction in the aggregates. Each fit to the SANS data has been checked by calculating the theoretical volume mass of dry material the fit represents, φ_{dry}.

Temp. (°C)	$q^{-\alpha}$ ($q < 0.04$ Å^{-1})	Model	T_{sheet} (Å)	SLD ($\times 10^{-6}$ Å^{-2})	Scale	X_{sol}	φ_{dry}
20	2.02	Lamellar	52.7	1.40	0.00048	0.06	0.00065
40	2.01	Lamellar	57.5	1.49	0.00050	0.08	0.00065
60	2.02	Lamellar	58.6	1.53	0.00053	0.09	0.00065
80	2.03	Lamellar	60.6	1.75	0.00051	0.13	0.00065

Table A.8.2 Structural parameters obtained from SANS data for *cis*-$C_4AzoOC_4E_2$ in D_2O (1.0×10^{-3} M) as a function of temperature: α is the scattering power of the defined q region. L is the length, respectively, obtained from the best fit to the data using the Lamellar Model in SasView. X_{sol} is the calculated solvent fraction in the aggregates. Each fit to the SANS data has been checked by calculating the theoretical volume mass of dry material the fit represents, φ_{dry}.

Temp. (°C)	$q^{-\alpha}$ ($q < 0.04$ Å^{-1})	Model	T_{sheet} (Å)	SLD_{agg} ($\times 10^{-6}$ Å^{-2})	Scale	X_{sol}	φ_{dry}
20	3.91	-	-	-	-	-	-
40	3.73	-	-	-	-	-	-
60	3.89	-	-	-	-	-	-
80	2.48	Lamellar	60.6	4.71	0.0051	0.87	0.00065

Table A.8.3 Structural parameters obtained from SANS data for *trans*-**$C_4AzoOC_4E_4$** in D_2O (1.0×10^{-3} M) as a function of temperature: α is the scattering power of the defined q region. T_{sheet} is the sheet thickness, obtained from the best fit to the data using the Lamellar Model in SasView. X_{sol} is the calculated solvent fraction in the aggregates. Each fit to the SANS data has been checked by calculating the theoretical volume mass of dry material the fit represents, φ_{dry}.

Temp. (°C)	$q^{-\alpha}$ ($q < 0.04$ Å^{-1})	Model	T_{sheet} (Å)	SLD_{agg} ($\times 10^{-6}$ Å^{-2})	Scale	X_{sol}	φ_{dry}
20	2.26	Lamellar	53.4	3.648	0.00164	0.50	0.0008
40	2.27	Lamellar	50.7	4.280	0.0021	0.619	0.0008
60	2.33	Lamellar	62.3	4.83	0.0029	0.723	0.0008
80	2.21	Lamellar	53.8	4.43	0.0024	0.647	0.0008

Table A.8.4 Structural parameters obtained from SANS data for *cis*-**$C_4AzoOC_4E_4$** in D_2O (1.0×10^{-3} M) as a function of temperature: α is the scattering power of the defined q region. L is the length obtained from the best fit to the data using the Lamellar Model in SasView. X_{sol} is the calculated solvent fraction in the aggregates. Each fit to the SANS data has been checked by calculating the theoretical volume mass of dry material the fit represents, φ_{dry}.

Temp. (°C)	$q^{-\alpha}$ ($q < 0.04$ Å^{-1})	Model	T_{sheet} (Å)	SLD_{agg} ($\times 10^{-6}$ Å^{-2})	Scale	X_{sol}	φ_{dry}
20	2.03	Lamellar	55.5	2.799	0.0012	0.34	0.0008
40	2.31	Lamellar	57.6	3.729	0.00147	0.52	0.0008
60	2.27	Lamellar	61.7	3.787	0.00167	0.53	0.0008
80	2.30	Lamellar	60.4	3.500	0.0015	0.36	0.0008

Table A.8.5 Structural parameters obtained from SANS data for *trans*-$C_4AzoOC_4E_6$ in D_2O (1.0×10^{-3} M) as a function of temperature: α is the scattering power of the defined q region. L, r, L_{Kuhn} and T_{sheet} are the length, radius, Kuhn length and sheet thickness, obtained from the best fit to the data using the Sphere, Flexible Cylinder and Lamellar Models in SasView. X_{sol} is the calculated solvent fraction in the aggregates. Each fit to the SANS data has been checked by calculating the theoretical volume mass of dry material the fit represents, φ_{dry}.

Temp. (°C)	$q^{-\alpha}$ ($q < 0.04$ Å^{-1})	Model	r (Å)	L (Å)	L_{Kuhn} (Å)	T_{sheet} (Å)	SLD_{agg} ($\times 10^{-6}$ Å^{-2})	Scale	X_{sol}	φ_{dry}
20	-	Sphere[a]	43.4	-	-	-	3.36	0.0011	0.44	0.00065
40	0.92	Flexible Cylinder	31.3	473.4	167.3	-	3.15	0.0011	0.40	0.00065
60	2.02	Lamellar	-	-	-	46.4	2.82	0.001	0.35	0.00065
80	2.06	Lamellar	-	-	-	52.7	2.82	0.001	0.35	0.00065

[a] Fit improved with 0.2 polydispersity

Table A.8.6 Structural parameters obtained from SANS data for *cis*-$C_4AzoOC_4E_6$ in D_2O (1.0×10^{-3} M) as a function of temperature: α is the scattering power of the defined q region. L, r, L_{Kuhn} and T_{sheet} are the length, radius, Kuhn length and sheet thickness, obtained from the best fit to the data using the Sphere, Flexible Cylinder and Lamellar Models in SasView. X_{sol} is the calculated solvent fraction in the aggregates. Each fit to the SANS data has been checked by calculating the theoretical volume mass of dry material the fit represents, φ_{dry}.

Temp. (°C)	$q^{-\alpha}$ ($q < 0.04$ Å^{-1})	Model	r (Å)	L (Å)	L_{Kuhn} (Å)	T_{sheet} (Å)	SLD_{agg} ($\times 10^{-6}$ Å^{-2})	Scale	X_{sol}	φ_{dry}
20	-	Cylinder	24.4	105.3	-	-	3.10	0.0011	0.40	0.00065
40	1.25	Flexible Cylinder	28.5	419.5	182.0	-	3.34	0.0012	0.44	0.00065
60	2.14	Lamellar	-	-	-	46.0	3.18	0.0011	0.41	0.00065
80	2.21	Lamellar [a]	-	-	-	48.4	2.65	0.0012	0.31	0.00065

[a] T = 80 °C had "bumps" similar to the $C_4AzoOC_4E_4$ SANS data, thus the fits to Lamellar are not necessarily optimised.

Table A.8.7 Structural parameters obtained from SANS data for *trans*-$C_4AzoOC_4E_6$ in D_2O (T = 20 °C) as a function of concentration: α is the scattering power of the defined q region. L, r and T_{sheet} are the length and radius obtained from the best fit to the data using the Sphere and Cylinder Models in SasView. X_{sol} is the calculated solvent fraction in the aggregates.

Conc. (mM)	$q^{-\alpha}$ ($q < 0.04$ Å^{-1})	Model	r (Å)	L (Å)	X_{sol}	Vol_{dry}	N_{agg}
1	-	Sphere	43.4	-	0.44	150664	153
5	0.33	Cylinder	32.1	120.6	0.46	179583	182
10	0.47	Cylinder	31.8	144.1	0.50	2288956	232
20	0.61	Cylinder	31.9	153.0	0.57	278803	283
40	0.50	Cylinder	31.9	127.5	0.33	134510	137
200	0.40	Sphere	37.6	-	0.62	85623	87

Table A.8.8 Structural parameters obtained from SANS data for *cis*-$C_4AzoOC_4E_6$ in D_2O (T = 20 °C) as a function of concentration: α is the scattering power of the defined q region. L, r and T_{sheet} are the length and radius obtained from the best fit to the data using the Sphere and Cylinder Models in SasView. X_{sol} is the calculated solvent fraction in the aggregates.

Conc. (mM)	$q^{-\alpha}$ ($q < 0.04$ Å^{-1})	Model	r (Å)	L (Å)	X_{sol}	SLD ($\times 10^{-6}$ Å^{-2})	Vol_{dry}	N_{agg}
1	-	Sphere	39.4	-	0.302	2.67	77372.07	79
5	0.86	Cylinder	25.0	241.1	0.56	3.97	265103.3	269
10	0.72	Cylinder	24.5	210.2	0.74	4.92	293323.2	298
20	0.59	Cylinder	24.1	173.5	0.51	3.72	161455.8	164
40	0.44	Cylinder	26.7	121.9	0.52	3.74	141964.4	144
200	0.40	Cylinder	23.8	78.7	0.54		64772	66

Table A.8.9 Structural parameters obtained from SANS data for *trans*-$C_4AzoOC_4E_6$ in D_2O (T = 60 °C) as a function of concentration: α is the scattering power of the defined q region. T_{sheet} is the sheet thickness, obtained from the best fit to the data using the Lamellar Model in SasView. X_{sol} is the calculated solvent fraction in the aggregates. Each fit to the SANS data has been checked by calculating the theoretical volume mass of dry material the fit represents, φ_{dry}.

Conc. (mM)	$q^{-\alpha}$ ($q < 0.04$ Å^{-1})	Model	T_{sheet} (Å)	Scale	SLD ($\times 10^{-6}$ Å^{-2})	φ_{dry}
1	-2.21 ± 0.03	Lamellar	47.8	0.00378	4.52	0.0013
5	-2.14 ± 0.02	Lamellar	38.0	0.00799	3.60	0.0041
10	-2.24 ± 0.02	Lamellar	41.6	0.00903	2.85	0.0059
20	-2.19 ± 0.03	Lamellar	41.7	0.03237	4.36	0.0118
40	-2.26 ± 0.02	Lamellar [a]	42.3	0.04605	2.86	0.0321

Table A.8.10 Structural parameters obtained from SANS data for *cis*-$C_4AzoOC_4E_6$ in D_2O (T = 60 °C) as a function of concentration: α is the scattering power of the defined q region. T_{sheet} is the sheet thickness, obtained from the best fit to the data using the Lamellar Model in SasView. X_{sol} is the calculated solvent fraction in the aggregates. Each fit to the SANS data has been checked by calculating the theoretical volume mass of dry material the fit represents, φ_{dry}.

Conc. (mM)	$q^{-\alpha}$ ($q < 0.04$ Å^{-1})	Model	T_{sheet} (Å)	Scale	SLD ($\times 10^{-6}$ Å^{-2})	φ_{dry}
1	-2.13 ± 0.03	Lamellar	48.4	0.00084	2.67	0.0006
5	-2.18 ± 0.02	Lamellar	44.8	0.00534	3.07	0.0032
10	-2.18 ± 0.02	Lamellar	44.4	0.03294	4.37	0.012
20	-2.17 ± 0.02	Lamellar	42.6	0.04852	4.02	0.0209
40	-2.10 ± 0.12	Lamellar	41.7	0.04416	2.72	0.0298
		Lamellar[b]	40.4	0.07200	3.51	0.0379

[b] This fit was performed over the $q > 0.02$ Å^{-1}

Table A.8.11 Structural parameters obtained from SANS data for *trans*-$C_4AzoOC_4E_4$ in D_2O (1.0×10^{-3} M) as a function of temperature: α is the scattering power of the defined q region. T_{sheet} is the sheet thickness, obtained from the best fit to the data using the Lamellar Model in SasView. X_{sol} is the calculated solvent fraction in the aggregates. Each fit to the SANS data has been checked by calculating the theoretical volume mass of dry material the fit represents, φ_{dry}.

Conc. (mM)	$q^{-\alpha}$ ($q < 0.04$ Å^{-1})	Model	T_{sheet} (Å)	SLD ($\times 10^{-6}$ Å^{-2})	Scale	X_{sol}	φ_{dry}
1	2.26	Lamellar	53.4	3.648	0.001639	0.50	0.0008
20	2.05	Lamellar	48.5	2.90	0.017248	0.36	0.0111
200	1.68	[a]					

[a] Q -scaling suggested the Lamellar Model, however structure factor could not be applied to produce a reliable fit.

Table A.8.12 Structural parameters obtained from SANS data for *cis*-$C_4AzoOC_4E_4$ in D_2O (1.0×10^{-3} M) as a function of temperature: α is the scattering power of the defined q region. L is the length obtained from the best fit to the data using the Lamellar Model in SasView. X_{sol} is the calculated solvent fraction in the aggregates. Each fit to the SANS data has been checked by calculating the theoretical volume mass of dry material the fit represents, φ_{dry}.

Conc. (mM)	$q^{-\alpha}$ ($q < 0.04$ Å^{-1})	Model	T_{sheet} (Å)	SLD ($\times 10^{-6}$ Å^{-2})	Scale	X_{sol}	φ_{dry}
1	2.03	Lamellar	55.5	2.799	0.0012	0.34	0.0008
20	1.93	[a]					

[a] Q-scaling suggested the Lamellar Model, however structure factor could not be applied to produce a reliable fit.

Calculation of Molecule Volumes and Lengths

The volume and length of the hydrophobic 'C_4AzoOC_4' tail group of the neutral ethylene glycol photosurfactants were calculated from a combination of references outlined in Tables A.8.13 and A.8.14.

'C_4AzoOC_4' represents '$CH_3CH_2CH_2CH_2$-Azobenzene-O-$CH_2CH_2CH_2CH_2$'

Table A.8.13 Values used for the calculation of the volume of the hydrophobic tail of the PS.

Component	Volume (cm^3 mol^{-1})	Reference
Trans-azobenzene	106.2	Takeshita *et al.*[1]
$-CH_2CH_2CH_2CH_3$	3*28.2 + 42.6 = 127.2	Hirata *et al.*[2]
$-CH_2CH_2CH_2CH_2-$	4*28.2 = 112.8	Hirata *et al.*[2]
-O-	5.5	Durchschlag *et al.*[3]
Total Volume:	351.7	

Table A.8.14 Values used for the calculation of the length of the hydrophobic tail of the PS.

Component	Length (Å)	Reference
Trans-azobenzene	21.9	Xing *et al.*[4]
$-CH_2CH_2CH_2CH_3$	4*1.54 = 6.2	
$-CH_2CH_2CH_2CH_2-$	4*1.54 = 6.2	
-O-	1.2	
Total Length:	35.5	

[1] K. Takeshita, N. Hirota and M. Terazima, *J. Photochem. Photobiol. A,* 2000, **134**, 103-109.

[2] H. Hirata, N. Hattori, M. Ishida, H. Okabayashi, M. Frusaka and R. Zana, *J. Phys. Chem.*, 1995, **99**, 17778-17784.

[3] H. Durchschlag, P. Zipper, G. Purr and R. Jaenicke, *Colloid. Polym. Sci.*, 1996, **274**, 117-137.

[4] L. Xing and W. L. Mattice, *Langmuir*, 1996, **12**, 3024-3030.

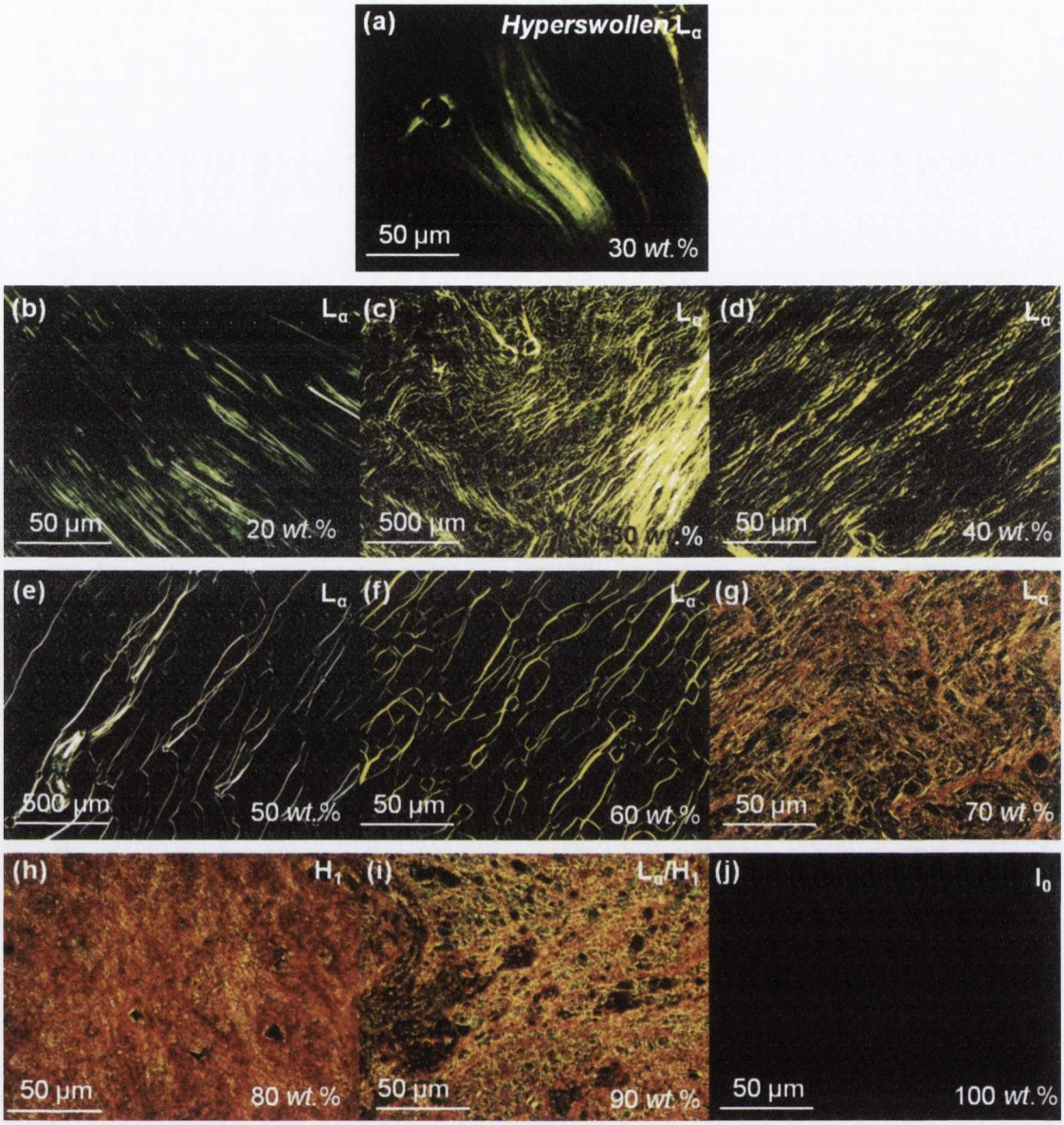


Figure A.8.8 Polarised optical micrographs of *trans*-C_4**AzoOC**$_4$**E**$_4$ as a function of concentration at T = 20 °C. I_0, H_1 and L_α represent isotropic, hexagonal and lamellar phases, respectively.

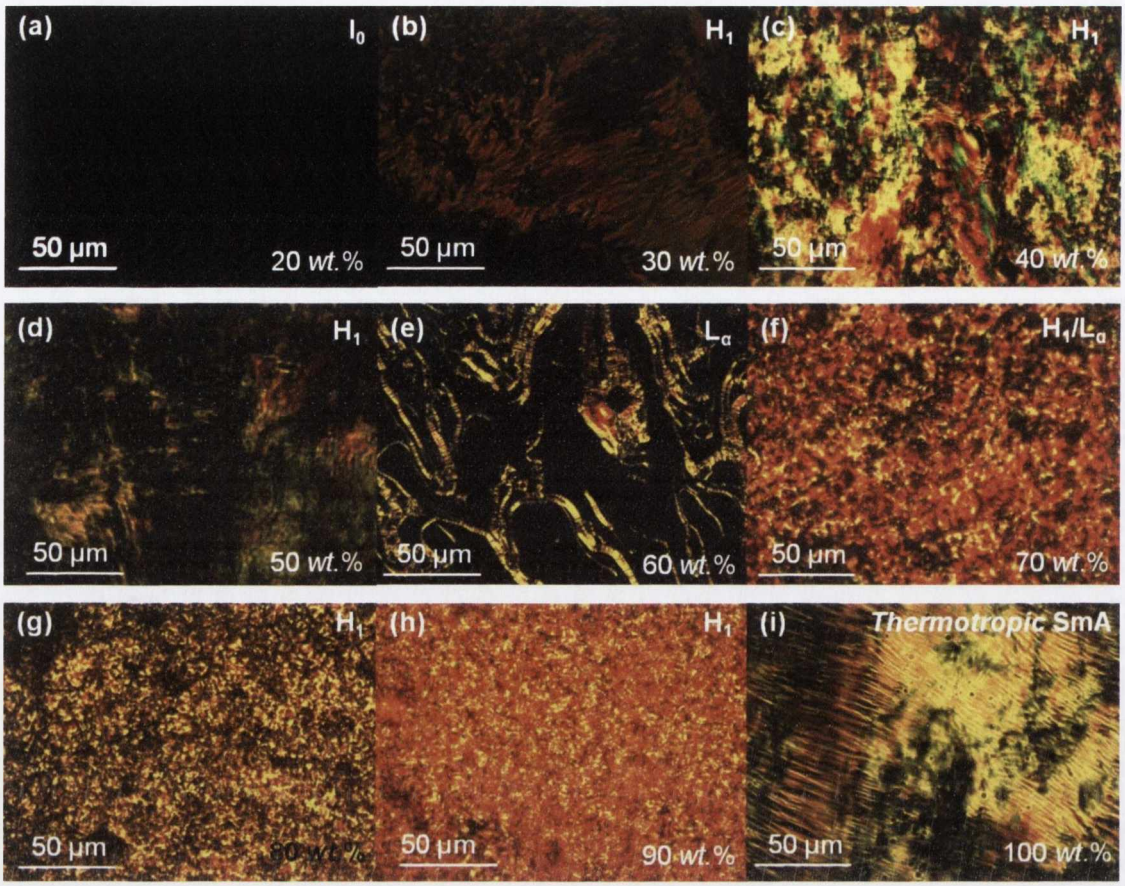


Figure A.8.9 Polarised optical micrographs of *trans*-C_4**AzoOC**$_4$**E**$_6$ as a function of concentration at T = 20 °C. I_0, H_1 and L_α represent isotropic, hexagonal and lamellar LLC phases, respectively, and SmA is the thermotropic smectic A phase.

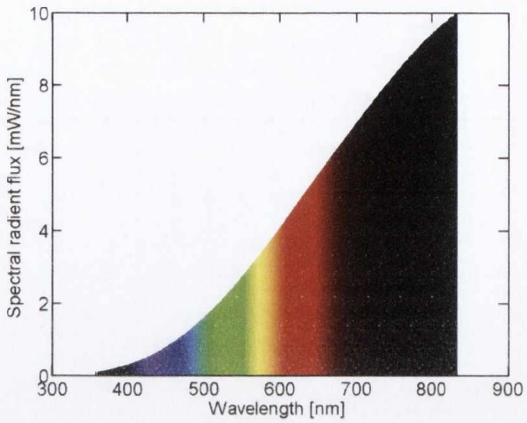


Figure A.8.10 Spectrum of the halogen lamp used by the polarised optical microscope.

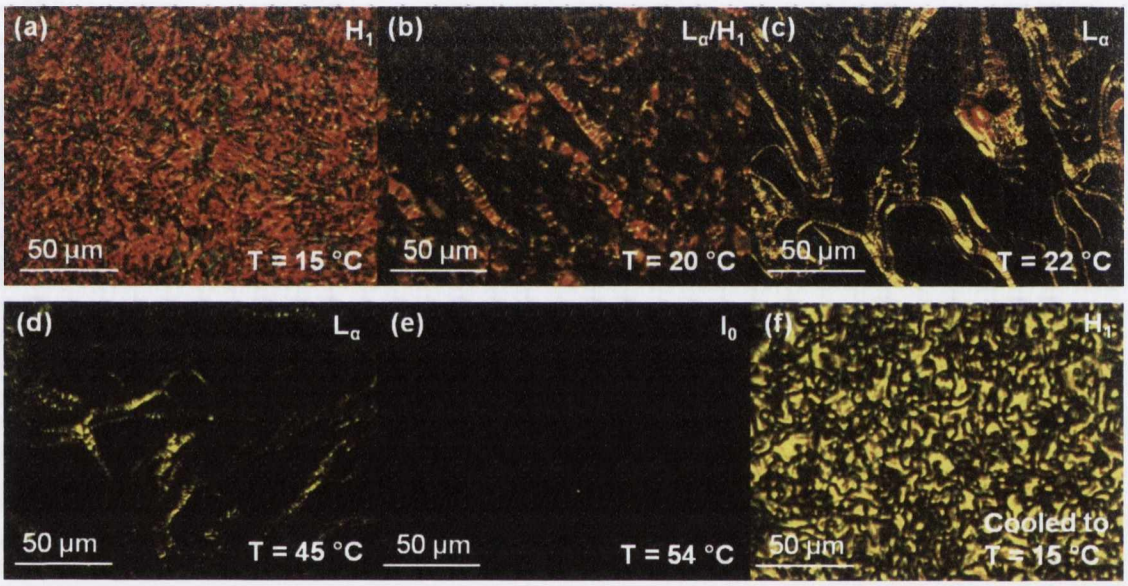


Figure A.8.11 Polarised optical micrographs of *trans*-$\mathbf{C_4AzoOC_4E_6}$ (60 *wt.*%) as a function of temperature. I_0, H_1 and L_α represent isotropic, hexagonal and lamellar LLC phases, respectively.